A STUDY OF SOME REACTIONS IN ANTIPROTON-PROTON ANNIHILATIONS NEAR 1.2 GeV/c WITH THE PRODUCTION OF AT LEAST ONE K_1^0 - MESON

Thesis submitted in accordance with the requirements of The University of Liverpool for the degree of Doctor of Philosophy

by

John Edward Galletly

Oliver Lodge Laboratory
University of Liverpool

September 1971

ABSTRACT

This thesis describes the study of antiproton annihilations in which at least one visible K_1^o was produced in the final state.

At 1.2 GeV/c, resonance production in the reactions $\bar{p}p \rightarrow K_1^o K^{\pm} \pi^{\mp}$, $\bar{p}p \rightarrow K_1^o K^{\pm} \pi^{\mp}(\pi^o)$, $\bar{p}p \rightarrow K_1^o K_1^o \pi^+ \pi^-$ and $\bar{p}p \rightarrow K_1^o(K^o) \pi^+ \pi^-$ is investigated.

The cross-sections for all reactions having a K_1^o are calculated at antiproton momenta between 1.28 and 1.47 GeV/c. A preliminary study of the cross-section for the reaction $\bar{p}p \rightarrow K_1^o K_1^o \omega^o$ is made at different antiproton momenta between 1.10 and 1.47 GeV/c.

The work concludes with a comparison of the reaction $\bar{p}p \rightarrow K_1^o K^{\pm} \pi^{\mp}$ at low energy with a Veneziano model.

ACKNOWLEDGEMENTS

I wish to thank:

Professor J.M. Cassels for the opportunity to carry out this research.

The Science Research Council for financial support during the first two years of this work.

Drs. R.A. Donald and D.N. Edwards for their constant advice, encouragement, hard work and patience throughout the course of the experiment.

Dr. W.H. Evans for his continuous interest.

Dr. N. West whose close co-operation has been invaluable throughout all stages of the experiment.

Our collaborators at I.P.N. for providing data and useful comments.

Drs. A. Poppleton and D. Waldren for many profitable discussions.

The various generations of postgraduate students for their friendship and help throughout.

The staff of the departmental computers.

Mr. L. Leech and the scanning and measuring staff.

Mrs. E.M. Crook for typing this thesis.

Mr. R. Barker for some of the diagrams.

Finally I would like to thank my wife, parents and family for their constant encouragement, patience and sacrifices without which this thesis would not have been possible.

TABLE OF CONTENTS

CHAPTER 1

INTRODUCTION

The annihilation of antiprotons in hydrogen at low energy provides an abundance of strange and non-strange meson resonances without the complication of baryon and hyperon excited states. Indeed antiproton-proton annihilations have provided a wealth of information on resonances such as the $\omega(780)$, $K^*(892)$, $\rho(760)$, $\phi(1019)$, $A_2(1300)$, etc.

An early experiment by CERN and the Collège de France (CDF) collaboration with stopped antiprotons found evidence for new structures viz the C(1250), E(1410) and an I = 1 $K\bar{K}$ interaction. In order to investigate these phenomena more fully, a new experiment at an antiproton momentum of 1.18 GeV/c (1964) was proposed by a collaboration between CERN, CDF, the Institut de Physique Nucléaire (IPN) and Liverpool. This experiment, however, showed no evidence for the production of the C^o meson and the study of the E^o meson was complicated by the strong production of K^*'s in the same final states. On the other hand, this experiment did produce some evidence for a new meson in the $(K\bar{K}\pi)^o$ system, called the D(1280). A collaboration between IPN and Liverpool put forward another proposal for further runs at antiproton momenta of 1.15 GeV/c (1967) and 1.10 GeV/c (1968) primarily to gain more statistics in order to investigate the spin-parity of this new object. A study of the D^o spin-parity has been completed[1] and this thesis is concerned with the study of some of the reactions at 1.10, 1.15 and 1.18 GeV/c in which at least one visible K_1^o is produced and in which there is little or no D^o production. In order to increase the statistics

the above three sets of data have been combined and will collectively be referred to as the 1.2 GeV/c data.

The reactions studied are

$$\bar{p}p \rightarrow K_1^o K^{\pm} \pi^{\mp}$$

$$\bar{p}p \rightarrow K_1^o K^{\pm} \pi^{\mp} (\pi^o)$$

$$\bar{p}p \rightarrow K_1^o K_1^o \pi^+ \pi^-$$

$$\bar{p}p \rightarrow K_1^o (K^o) \pi^+ \pi^-$$

The same collaboration also took part in another experiment at antiproton momenta of 1.28, 1.34, 1.39 and 1.47 GeV/c (1968). These data will be referred to as the formation data since the above range was chosen to investigate the formation of a direct channel resonance. (An enhancement in the $\bar{p}p$ total cross-section data of Abrams et al.[2] at this energy was attributed to a direct channel resonance) In this context the reaction $\bar{p}p \rightarrow K_1^o K_1^o \omega^o$ has been studied.

Table 1.1 gives a summary of the experiments involved in this work.

Beam Momentum (Nominal Value) GeV/c	Beam Momentum (Entrance Value) GeV/c	No. of Photographs (x 10^3)	Bubble Chamber	Beam Line
1.10	1.13 ± 0.03	190	2m	K8
1.15	1.18 ± 0.02	60	2m	M6
1.18	1.18 ± 0.05	300	81cm	K4
1.28	1.25 ± 0.01	37	2m	K8
1.34	1.32 ± 0.01	37	2m	K8
1.39	1.38 ± 0.01	37	2m	K8
1.47	1.45 ± 0.02	37	2m	K8

Table 1.1 Experiment Characteristics

Throughout this thesis, V^o is taken to mean the 2 charged pion decay of the K_1^o.

References

1. N. West Ph.D. Thesis, Liverpool (1970)

2. R.J. Abrams et al. Phys. ReV. Lett. 18 ,1209 (1967)

CHAPTER 2

I. THE COLLECTION OF THE DATA

II. THE EXTRACTION OF THE DATA

I. The collection of the data

The design and building of large bubble chambers and beam transport systems is a lengthy and involved task. In practice, the bubble chambers and beam lines are designed, built and maintained by specialist groups of physicists and engineers. They are then used almost continuously by different experimental groups for a variety of experiments involving a range of momenta and particles.

Since the data analysed in this thesis come from four experiments involving three different beam lines and two bubble chambers, only a general and simplified account of the experimental set-up will be given.

The CERN PS

Protons produced by an ion source are accelerated up to 50 MeV by a linac and are injected into the PS ring. The protons can be accelerated up to a momentum of 28 GeV/c. However, a convenient running momentum is about 19 GeV/c (The threshold labotatory momentum for antiproton production is 6.5 GeV/c.) The beam contains approximately 10^{12} protons grouped in 20 bunches about 10 nsec long and spaced from each other by about 100 nsec.

Bunches are extracted by bringing a kicker magnet close to the beam. When this magnet is pulsed, radial oscillations are induced in the beam and bunches are deflected in to a bending magnet (septum). The field of the septum deflects the protons out of the accelerator. These are then steered on to an external target, such as beryllium, producing a host of secondary particles.

Typically, the production ratio is :

$$\pi^- : K^- : \bar{p} = 2000 : 1000 : 1.$$

The antiprotons, together with the contaminating π^- and K^- mesons, are bent away down the beam line.

The beam line

The purpose of the beam line is to transport a beam of secondary particles (in this case, antiprotons) with well-defined momentum and minimum contamination from the primary target to the bubble chamber.

The beam line essentially comprises :

(a) Vertical and horizontal collimators to define the aperture and regulate the flux.

(b) Quadrupole magnets to focus the beam in both the vertical and horizontal planes.

(c) Bending magnets for momentum analysis. The beam is passed through a magnetic field causing a deflection in the horizontal plane, and a vertical slit placed after the bending magnet picks off the required momentum.

(d) Separators to perform a mass analysis. After the momentum analysis, all particles in the beam have about the same momentum. The "wanted particles" are separated from the others by either electrostatic or radio-frequency separators. In the experiments under consideration, electrostatic separation was used. The particles are passed through a vertical electric field between oppositely charged plates. so that different mass particles are deflected through different vertical distances. To keep the beam horizontal, the deflection of the wanted particles is compensated by a superimposed

magnetic field. A horizontal slit, called the "mass slit", then passes only the wanted particles.

Afterwards, another momentum analysis is done to remove the low momentum background (particles produced in the mass slit and muons from π-μ decays). A defocused quadrupole spreads the beam out just before entry into the bubble chamber. Then a final magnet deflects the particles into the chamber so they pass through the centre of the chamber despite its own strong magnetic field.

The bubble chamber

The bubble chamber is a pressure vessel containing a superheated liquid. In this case, it was liquid hydrogen. The front and back faces of the chamber have glass windows which enable the interactions in the chamber liquid to be illuminated and photographed. A large magnetic field surrounds the chamber so that the charge and momentum of any track can be measured from the track's curvature. This field has been accurately mapped out and can be calculated at any point to 0.1%.

The principle of operation of the bubble chamber is that a charged particle passing through a superheated liquid causes localised boiling along the particle's track. The exact mechanism is not fully understood but it is thought that δ-rays, produced by the incident particle, supply the energy to form unstable bubble nuclei.(1)

A schematic diagram of the CERN 2m H.B.C. is shown in Fig. 2A. In operation, the hydrogen is held at 27°K and 5 atms. i.e. just below its boiling point. To make

the liquid sensitive, the pressure is reduced to 2 atms. by raising a piston at the top of the chamber. The start of this expansion stroke is timed so that when a burst of particles enters the chamber, the liquid is in a uniformly superheated state. Bubbles then form along any unstable nuclei. When they have grown to a suitable size, 3 banks of flash tubes are triggered and illuminate the chamber from behind. Simultaneously, 4 cameras positioned in front of the chamber take photographs (or views) of the tracks. "Data box" quantities e.g. roll and frame number, etc. are also recorded on the beginning of each frame. The chamber is then recompressed and the film wound on for the next cycle. About 1500 such views constitute a roll of film.

Crosses (fiducials) etched on the back of the front glass and the front of the back glass serve as reference marks for the spatial reconstruction of the event. The coordinate system used is shown in Fig. 2B. The magnetic field acts along the Z - axis, which points towards the cameras. The X-Y plane (i.e.Z = 0) is on the back of the front glass. Particles enter along the X- axis and are spread out in the Y-direction to minimise confusion from overlapping tracks.

Before an exposure, physicists help to "tune" the beam i.e. make the fine adjustments to the magnet currents, etc. necessary to produce a beam of the desired momentum. During the run, physicists are present to ensure the magnet currents, etc. do not drift so that the correct number of particles of the correct momentum enter the chamber. Also test-strips from each roll are quickly developed for the physicists to check that the number of bubbles/cm, bubble size, etc. remain acceptable.

II. The extraction of the data

After the film has been developed, it is divided among the groups in the collaboration. It is then systematically searched or scanned for interesting events. These events are measured and then geometrically and kinematically reconstructed by computer, ready for identification by a physicist. In this instance, the standard CERN THRESH-GRIND-SLICE chain of programs was used.(2)

Scanning

An approximate life-size image of the film is projected via a mirror on to a white horizontal table top. It is scanned by two people, working side by side, looking at different views, but keeping approximately in step with each other. When one person finds a possible V^o event, this is checked by the other person on his view. If the event appears to be a "good" V^o event i.e. an annihilation apex with at least one associated V^o, in both views, then the roll and frame number, topology and approximate position of the event is noted. Any dubious events are noted and a decision is taken later. This procedure is repeated for each event found. In most instances, it was possible to eliminate "spurious" V^o events at this stage e.g. $\Lambda^o \rightarrow p\pi^-$, the proton being recognised from its heavily ionising track. All events within the visible region of the chamber were accepted, except those events for which the beam track was very much off beam i.e. the incident track not parallel with the rest of the beam.

The first scan was done using views 1 and 2, then a

rescan was made using views 3 and 4. In this way, events lost due to scanner inefficiency.confusion of tracks, etc. were reduced to a minimum. Afterwards, a measure list was made by combining the results of the scan and rescan lists.

Some common topologies are shown in Figs. 2C-F.

Measuring

The measuring machines at Liverpool are image plane digitisers, designed and built by Dr. W.H. Evans.

The machines consist of projectors, a digitiser and electronic equipment. A schematic diagram of a measuring engine is shown in Fig. 2G. There are 3 projectors which can produce an approximately life-size image of an event from any of 3 views on a large white table. The digitiser comprises a small stage mounted on an arm just above the table top. The stage is free to move along the arm and its movement defines the X-direction. The arm is also free to move along rails at right angles to the X-direction and this defines the Y-direction. The projected image is focussed so as to be in the plane of this moveable stage. A long diffraction grating is fixed along the arm while a smaller, slightly off-parallel grating is contained in the stage. Moiree fringes are formed and, when the stage is moved with respect to the arm, an illuminated photo-cell counts the number of fringes passing it. The photo-cell is connected to a Ferranti counter. There is a similar arrangement on the arm and one of the rails for the Y-direction.

By counting the number of fringes passing the X and Y photo-cells from some zero point, the coordinates of any point on the table can be determined. Each fringe count

represents 25μ on the table which is equivalent to 1.5μ on the film plane.

The console of the Ferranti counter displays the current (X,Y) coordinates. In addition, the console has space for the operator to set up the roll and frame number etc. for each event being measured. To save time labelling events at the measurement stage, each topology was assigned a type number which was also set up on the console.

To measure an event, an operator first measured 4 fiducials around the event. This was done by setting the cross-wires on the stage on the point of interest and pressing a button to record the information. Next, the primary and secondary apices were measured, followed by about 8 to 10 evenly-spaced points along the first 15 to 20 cms. of each track. For very slow tracks, even shorter distances were measured. Each event was measured on views 1,2, and 3.

All of this event information was transmitted to an on-line PDP-8 computer (later superceded by an IBM 1130), which was attached to all of the measuring engines. This computer made a simple circle fit to the track measurements to check on their accuracy, checked the fiducial measurements with an accurate, reference set of inter-fiducial distances and ensured that the correct number of apices and tracks had been measured for the specified type number.[3] If an error was detected, the operator was informed via the console and the track,view or whole event was remeasured as necessary. Satisfactorily measured events were written onto magnetic tape.

PLANT

Before the data output from the measuring machines could be used in the reconstruction program, they required a certain amount of re-organising and labelling. The program PLANT, written at Liverpool, performed this job.

Since the magnetic tapes from the PDP-8 contain the output from all the measuring machines, the program first sorts each event into the different experiments. The program next collates all the views for each event, identifies the fiducials against a reference set and labels them, and labels the apices and tracks consistent with the given type number. All this information is then written out on to a magnetic tape in a format acceptable to the reconstruction program. Also a listing is produced on which is printed the events processed and any errors.

PYTHON

Before the events can be processed through the reconstruction programs, it is also necessary to know such quantities as the camera and fiducial coordinates relative to the chamber, thicknesses of the various media between the cameras and the back of the chamber, and also the accurate refractive indices of the media. The program PYTHON calculates these constants.[4] The data required by the program are the spatial coordinates of the cameras and fiducials, the relative position of the fiducials on the different planes and the measured positions of all the fiducials on all views. The program transforms the film measurements to the bubble chamber system and compares the reconstructed and measured fiducial positions. Using an

iterative procedure, the optimum values of the camera coordinates, etc. are found.

THRESH

THRESH[5] is the geometrical reconstruction program and its purpose is to determine the curvature and direction in space of the tracks and the coordinates of the interaction points using the labelled set of film measurements output by PLANT.

The input data to THRESH consist of the following :-

i) Title block - camera and fiducial positions, refractive indices and thicknesses of the glass, air and liquid hydrogen layers, etc.

ii) Measurements of coordinate pairs of points on the film i.e. PLANT output.

iii) Tolerances on fiducials, reconstructed points, etc. to set criteria for the rejection of events as bad measurements.

Using the Title block information, the program first calculates the apparent positions on the back of the front glass of all fiducial marks, front and back.
These serve as a reference frame for the reconstruction of each event. For each view in turn, the transformation coefficients which relate the film fiducial measurements on that view to the apparent measurements on the back of the front glass are found. A minimum of 3 fiducials on each of 2 views is required but more fiducials are desirable to increase the reconstruction accuracy. The coordinates of all measured points can be transformed to the reference plane.

If the same point is measured on two or three views (e.g. the annhilation apex), then the spatial coordinates of that point are found from the intersection of the light rays through the point in the chamber from the camera lenses. The transformation coefficients are used to find the apparent coordinates of the point on the back of the front glass. The equations representing a light-ray through the point for each view may then be found. Measurements on two views are sufficient for the (X,Y,Z) coordinates of the point to be found.

Track reconstruction is more difficult since, normally, measurements of points along a track are non-corresponding for different views. Two views are selected, and points corresponding to measurements on one view are constructed by interpolation of measurements on the other view. THRESH assumes that the chamber is situated in a uniform magnetic field, perpendicular to the front glass, so that charged particles can be considered to describe helices. First approximations to the radius, tangent of dip angle ($\tan\lambda$) and azimuthal angle (ϕ) of the helix are obtained by fitting a circle to the reconstructed points projected on to the X-Y plane.

The last step is a final least-squares fit to the helix, this time using all views. Essentially, the set of deviations of the points from the light rays and from the helix equation, projected on to the appropriate film plane, are calculated. THRESH minimises the sum of all these deviations squared by expanding them in terms of small corrections to the helix parameters which are then

found by a least-squares fit in an iterative procedure. (Stopping tracks are labelled as straight).

The output from THRESH is written on to magnetic tape and consists of the (X,Y,Z) coordinates of all apices, the radius of curvature (ρ), dip (λ) and azimuthal (ϕ) angles of all tracks plus their associated errors. Any events failing to reconstruct are flagged. Also a listing is printed, containing a short summary of the events processed.

GRIND

The next link in the chain is the kinematical reconstruction of the event The purpose of GRIND[6] is to propose each possible hypothesis for the explanation of an event and give a measure of how likely each hypothesis is.

The input to GRIND consists of the following "titles":

i) Output tape from THRESH containing the geometry for each event.

ii) User- specified criteria governing the convergence of fits, etc.

iii) A magnetic field map and range-energy tables.

iv) The labelling scheme used in measuring each topology.

v) A list of mass assigments, called hypotheses, to be tested at each vertex in an event, i.e. a list of possible mass assignments (including neutral particles) for the interaction.

vi) General constants, e.g. multiple Coulomb scattering error and beam momentum.

GRIND first uses the magnetic field data to calculate

the momenta of all tracks. Later, a mass dependent correction allowing for energy loss is made for each particular mass hypothesis. The momenta of stopping tracks are found from the range-energy tables. Also at this point, the error on the track momenta is computed. This error derives from the measuring errors and uncertainties caused by multiple Coulomb scattering.

GRIND processes each event in turn. The event topology is implicit in the labels carried by the event. The program examines these labels and, by reference to the label block in the titles, builds up a vertex and assigns to each type a number (an integer) to describe the interaction. GRIND then inspects the mass assignments in the titles to see if the type number so constructed is present. If so, the program enters the hypothesis testing routines repeatedly, once with each combination of masses given for that type number. Fits are performed first at the secondary interactions and then this additional information is used in the fit at the annihilation apex.

A complete specification of an event satisfies the conservation of energy and momentum at each vertex. However, the raw measurements, because of measurement errors, do not exactly satisfy the 4 equations of energy and momentum. The corrections necessary to the measured quantities so that the event becomes physically possible are calculated by a least-squares fit. The "chi-squared" (χ^2) is defined as

$$\chi^2 = \sum_{\substack{\text{all} \\ \text{variables}}} \frac{(m_i - f_i)^2}{\sigma_i^2}$$

where m_i is the measured value of the i^{th} variable,

f_i is the fitted value of the i^{th} variable,

σ_i is the error of the i^{th} variable

and it is this quantity which is minimised in the fit.

The 4 equations of energy and momentum impose constraints on the system. If there is no missing neutral particle, the system is over-determined by these 4 equations and has 4 constraints. Such a fit is called a 4-C fit. When there is one missing neutral particle, the number of constraint equations reduces to one, since the 3 components of momentum of the missing particle have to be calculated. (A 1-C fit.) Events with 2 or more missing neutral particles require more constraint equations than physically available and so such events cannot be reconstructed in the manner of the other events. In this case, if the missing mass, M, of the event is positive then M is included in the mass assignment list of hypotheses. The program can then perform a pseudo 1-C fit to the event such that the missing neutral "particle" has mass M. No least-squares fit can be done and the fitted values of the track variables are taken as the measured values. Such events are termed "+ M" events.

If any of the measured variables, such as the momentum of one track, are badly measured then they are set as unknowns and the number of constraints drops accordingly.

The probability for each fit is calculated from the minimum χ^2 and number of constraints to give the "goodness" of the fit. If during the fit the χ^2 becomes too large, the fit is abandoned. Because of the errors on the measured variables, it is possible for each event to have been fitted to several different hypotheses.

The program also calculates for each fit an estimate of the bubble density of each track projected on to the reference frame using the fitted momenta and the relationship, ionisation is proportional to

$$\frac{1}{v^2} = 1 = \frac{m^2}{p^2},$$

where v is the particle's velocity,

p is the particle's momemtum,

m is the mass of the particle.

GRIND has 3 forms of output. On a magnetic tape, for each event, there is printed a complete copy of the geometry parameters, and also the masses, unfitted and fitted momenta. dip and azimuthal angles, error matrices, probability and χ^2 for each hypothesis. A card, called a SLICE card, is punched out for each successful fit. Paper output is also produced on which is printed the details of each successfully fitted hypothesis in an event, including the relative ionisations and probability.

Selecting the hypothesis

In order to check that each event had been successfully reconstructed and to resolve the ambiguities between different fits to the same event, each event was examined on the scanning table. This work was carried out by physicists.

Events failing to reconstruct were returned for remeasurement, unless they were immeasurable or not V^o events, in which case they were deleted. Even an event with a single successful fit was examined. If an event had several hypotheses for the same mass assignments of the charged tracks, then the fit with the highest number

of constraints was taken. To resolve the ambiguity between fits with different mass assignments, the ionisation data was used. In practice, given good, clear film, it is possible to distinguish between kaons and pions in the momentum range 150 - 700 MeV/c. by ionisation. (see Fig.2H.) Above 700 MeV/c, it is difficult to differentiate the two. Below 150 MeV/c the bubbles coalesce into a line. However, below about 200 MeV/c it is possible to deduce the mass of a particle by range (see Fig. 2I). If it was not possible to distinguish between the hypotheses, all were accepted and suitably flagged.

SLICE

SLICE computes the quantities necessary for the statistical analysis of the events e.g. resonance effective masses and momenta. The input to SLICE comprises the SLICE card for the appropriate chosen hypothesis and the GRIND output tape. The user specifies which quantities he wants calculated on data cards. The program extracts the necessary information from the flood of data on the GRIND tape and writes the desired quantities on to a Data Summary Tape (DST), event by event.

Library system

A copy of the combined measure list for each film was used as a library list. When a decision had been reached on an event, this was noted on the library list. In this way, a record was kept of all events and so minimised any losses.

References

1. D. Glaser et al. Phys. Rev. 87, 665 (1952)
   Phys. Rev. 97, 475 (1955)
2. THRESH Vol. II CERN- TC Program Library
   GRIND Vol. II CERN- TC Program Library
   SLICE Vol. II CERN- TC Program Library
3. R. Cooper Ph.D Thesis, Liverpool (1969)
4. PYTHON Vol. I CERN- TC Program Library
5. A. Moorhead CERN Yellow Report 60-33 (1960)
6. R. Bock CERN Yellow Reports 60-30 (1960); 61-29 (1961)

CHAPTER 3

PRELIMINARY OBSERVATIONS -- REACTION CONTAMINATION AND CROSS-SECTIONS

For each successfully reconstructed event which the physicist had to identify, there was usually more then one physical interpretation offered by GRIND. Thus there exists the possibility that the various reactions contain misclassified events which could lead to biases and misinterpretation of the data. Hence, before proceeding to the analysis of the reactions, the level of any contamination was investigated.

The following "loose" cuts were applied to the data.

1) Fiducial volume: to ensure that there was sufficient length of track for measurement and that the event was in the well-illuminated region of the chamber, the following volumes were taken.

a) 81 cm chamber : $-18\text{ cm} < X < 34\text{ cm}$

$-7\text{ cm} < Y < 5\text{ cm}$

$-19\text{ cm} < Z < -12\text{ cm}$

b) 2m chamber : $-75\text{ cm} < X < 66\text{ cm}$

$-20\text{ cm} < Y < 20\text{ cm}$

$-42\text{ cm} < Z < -8\text{ cm}$

2) Antiproton momentum : to preferentially remove badly measured events, the antiproton momentum p was selected as follows.

a) 1.18 GeV/c experiment $1.12 < p < 1.25$ GeV/c

b) 1.15 GeV/c experiment $1.09 < p < 1.20$ GeV/c

c) 1.10 GeV/c experiment $1.03 < p < 1.18$ GeV/c

3) Probability : Only events with probability greater than 2% were taken. This cut preferentially removes badly measured events and contamination.

The reaction $\bar{p}p \rightarrow K_1^o K^{\pm} \pi^{\mp}$

This reaction is a 4-C fit from the 2 prong, 1 V^o topology.

Possible sources of contamination are

a) events of the type $\bar{p}p \rightarrow K_1^o K^{\pm} \pi^{\mp} + m\,\pi^o$ ($m \geqslant 1$) i.e. 1-C or + M events which have been pulled into a 4-C fit and the missing pion(s) not fitted.

b) misidentified $K^{\pm}$ and $\pi^{\mp}$ tracks.

Above about 0.7 GeV/c, distinguishing between charged tracks on the basis of ionisation is not reliable (See Fig.2H).

Fig.3A displays the missing mass squared MM^2 for this reaction. MM^2 is defined as

$$MM^2 = \left[E_{\text{beam+target}} - \sum_i E_i\right]^2 - \left[P_{\text{beam}} - \sum_i P_i\right]^2 \qquad (3\text{-}1)$$

where E and P refer to energy and momentum respectively and the subscript i refers to the secondary particles. For 4-C events, MM^2 is zero. Naively, it might be expected that the experimental MM^2 distribution would be centred on zero, with a finite scatter around this value due to experimental errors. However, the MM^2 is skewed slightly negative. This feature is common to other experiments[1], some from other laboratories using different reconstruction programs. An explanation[2] has been given which takes into account the errors on the momentum (p), dip angle (λ) and azimuthal angle (ϕ). By expressing the MM^2 in terms of P, λ and ϕ and expanding MM^2 in a Taylor series about the true value, it is shown that the mean of the MM^2 is shifted towards negative values in cases where there are no missing particles. For the cases where missing particles exist, this effect is swamped out, and the MM^2 distribution

tends to be symmetric.

The positive side of the MM^2 distribution shows no great accumulation of entries as would be expected if the reaction contained excessive numbers of $K_1^o K^{\pm} \pi^{\mp} + m\,\pi^o$ events. It is concluded that the amount of this contamination is small.

The probability distribution for these events is shown in Fig.3B. The probability is calculated from the experimental χ^2 and the number of degrees of freedom n of the fit by using the theoretical χ^2 distribution, given by

$$f(\chi^2)\, d\chi^2 = \frac{(\chi^2)^{n/2}}{2^{n/2}\,\Gamma(\frac{n}{2})}\, e^{-x^2/2} \qquad (3\text{-}2)$$

where Γ is the Gamma function.

The probability to obtain a χ^2 value greater than or equal to a given value χ_o^2 (given by the fit) is

$$P_n\,(\chi^2 \geq \chi_o^2) = \int_{\chi_o^2}^{\infty} f_n\,(\chi^2)\, d\chi^2 \qquad (3\text{-}3)$$

Ideally, this distribution should be flat but, as Fig.3B shows, it has a peak at high probabilities, with a small excess at the low probability end. The bias towards high probability may be explained with the aid of the χ^2 used in the fits. This was defined in the previous chapter as,

$$\chi^2 = \sum_{\substack{\text{all} \\ \text{variables}}} \frac{(m_i - f_i)^2}{\sigma_i^2}$$

Thus a consistently small χ^2 and hence high probability is due to the external errors input to GRIND being overestimated.

This situation is not ideal since overestimation of the errors might lead to some 1-C events, for example ,

being pulled into the 4-C fit. However, it is hoped that the requirements of the constraint equation(s) will reduce this to a minimum. The excess at low probabilities is then possibly due to contamination. These events have been "pulled" a long way and so a high χ^2 and low probability results.

Even though the probability distribution is not flat, it should vary smoothly and so, assuming that the excess at the low probability end is due to contamination, an estimate of this number may be made. This was found to be of order 2%.

There is also the problem of misidentified $K^{\pm}$ and $\pi^{\mp}$ tracks. Fig.3C shows the laboratory momenta of those tracks with the second highest momentum in the event. There are 114 events, the $K^{\pm}$ and $\pi^{\mp}$ tracks of which both have a momenta greater than 0.7 GeV/c. Assuming that 50% of these were misidentified gives a contamination of approximately 3%. This number is an upper limit, since at least 50% of the events from this reaction had a unique fit.

Thus, it is concluded that the contamination in the $K_1^o K^{\pm} \pi^{\mp}$ channel is of order 4%.

<u>The reaction $\bar{p}p \longrightarrow K_1^o K_1^o \pi^+ \pi^-$</u>

This reaction consists of 4-C events from the 2 prong, 2 V^o topology.

Possible contamination can come from multineutrals of the type $K_1^o K_1^o \pi^+ \pi^- + m\pi^o$ $(m \geq 1)$.

The MM^2 distribution for these events is shown in Fig.3D. Again, the distribution is skewed slightly towards negative values. Examination of the plot reveals that there

is no excess of events on the positive side, so the amount of contamination is deduced to be small. Estimation of the contamination from the probability distribution (Fig.3E) gives a value of order 1%.

The reaction $\bar{p}p \longrightarrow K_1^o(K^o)\,\pi^+\pi^-$

These events are 1-C fits from the 2 prong, 1 V^o topology, which have a missing neutral kaon.

The sources of possible contamination are

a) multineutral events i.e. $K_1^o(K^o)\,\pi^+\pi^- + m\,\pi^o$ $(m \geqslant 1)$

b) $K^oK^{\pm}\pi^{\mp}\,(\pi^o)$ events which have a missing neutral pion and have been pulled into a $K_1^o(K^o)\pi^+\pi^-$ fit.

Fig.3F displays the MM^2 distribution for the $K_1^o(K^o)\,\pi^+\pi^-$ reaction. The plot peaks, as expected, at the mass squared value (0.25 GeV^2) of the kaon and has a reasonably symmetric spread about this point. There is no excessive accumulation of events on the upper half of the distribution, and so it is concluded that the amount of contamination from multineutral events is small. The small accumulation of events at 0.0 GeV^2 is due to events which have lost a constraint and become 0 - C events. For these, GRIND automatically sets the MM^2 to zero.

It is possible for events of the type $K_1^oK^{\pm}\pi^{\mp}\,(\pi^o)$ to have a fit to $K^o(K^o)\,\pi^+\pi^-$, and the event to go unrecognised at the decision-making stage. This could happen when both outgoing charged tracks are fast i.e.above 0.7 GeV/c when discrimination between tracks by ionisation is difficult. However, as Fig.3M shows, the number of identified $K_1^oK^{\pm}\pi^{\mp}(\pi^o)$ events with fast $K^{\pm}$ and $\pi^{\mp}$

tracks is very small. Thus, even taking a 50% misidentification, the number of $K_1^oK^{\pm}\pi^{\mp}(\pi^o)$ events that might be contaminating the $K_1^o(K^o)\pi^+\pi^-$ reaction is negligible. Moreover, there is no indication of any excess of events on the lower side of the MM^2 distribution, around 0.018 GeV^2 (= $M^2(\pi^o)$). This supports the conclusion reached above.

Again estimating the amount of contamination on the probability plot (Fig.3G), gives the contamination to be approximately 3%.

The reaction $\bar{p}p \longrightarrow K_1^oK^{\pm}\pi^{\mp}(\pi^o)$

This class of events belongs to the 2 prong, 1 V^o topology, having a 1-C fit and a missing neutral pion.

The reaction could possibly be contaminated by

a) $K_1^oK^{\pm}\pi^{\mp}(\pi^o) + m\pi^o$ ($m \geqslant 2$) events i.e. multineutral events

b) $K_1^o(K^o)\pi^+\pi^-$ events which have fitted to the $K_1^oK^{\pm}\pi^{\mp}(\pi^o)$ reaction and have been wrongly identified as such.

c) $K_1^oK^{\pm}\pi^{\mp}$ events i.e. the corresponding 4-C events which have fitted as 1-C events owing to measurement errors.

d) misidentified $K^{\pm}$ and $\pi^{\mp}$ tracks

The MM^2 distribution for this reaction is shown in Fig.3I. The figure is fairly symmetric about 0.018 GeV^2 with no surplus of events on the upper side, thus indicating that the number of contaminating multineutral events is low.

There is the possibilty of $K_1^o(K^o)\pi^+\pi^-$ with two fast π tracks being misidentified and contaminating the $K_1^oK^{\pm}\pi^{\mp}(\pi^o)$ events. However, as Fig.3H shows, the number of identified $K_1^o(K^o)\pi^+\pi^-$ events of this type is

very small so the contamination from this source can be assumed to be negligible.

If any 4-C $K^0_1K^{\pm}\pi^{\mp}$ events had fitted to the $K^0_1K^{\pm}\pi^{\mp}(\pi^0)$ reaction, then such events would be characterised by a low momentum neutral pion. Comparison of the momenta of $\pi^{\pm}$ and π^0 in Figs.3K,L shows that they are reasonably compatible at low momenta. Thus contamination is slight and is estimated to be 2%.

Misidentification of fast $K^{\pm}$ and $\pi^{\mp}$ tracks by ionisation is possible but, however, the number of such tracks with momenta above 0.7 GeV/c is very small (Fig.3M). Therefore such contamination was ignored.

Estimation of the excess of low probability events (Fig.3J) gave a value of order 2%.

Hence it is concluded that the total contamination for this reaction is of order 3%.

The reaction $\bar{p}p \rightarrow K^0_1K^0_1\pi^+\pi^-(\pi^0)$

These events have 1-C fits to the 2 prong, 2 V^0 topology. In the analysis of this reaction, the data from the formation experiment was included but the sample was divided up into C.M. energies rather than laboratory momenta. However, in the investigation of the contamination, the events were divided into 1.2 GeV/c data and formation data for convenience. The weak cut on the antiproton's laboratory momentum was relaxed.

Contamination may possibly come from

a) Multineutral events i.e. $K^0_1K^0_1\pi^+\pi^-(\pi^0)+m\,\pi^0(m\geqslant 2)$

b) 4-C events i.e. $K^0_1K^0_1\pi^+\pi^-$ which failed to get a 4-C fit.

The MM^2 distributions are presented in Figs.3N,O. Both plots are symmetric about the π^o mass squared value, with no evidence of large accumulations due to multineutral events. Estimation of the contamination from the probability distributions (Figs.3P and 3Q) yields values of order 2% and 3% for the 1.2 GeV/c and the formation experiments respectively.

If the event was really $K_1^oK_1^o\pi^+\pi^-$, then the fit to the 5-body reaction would have a low momentum neutral pion. Figs.3R,S and 3T,U show the momentum spectra of the charged and neutral pions for the 1.2 GeV/c and the formation experiments respectively. The distributions are compatible at low momenta for both sets of data, showing that contamination was slight. An upper limit of 2% was put on the estimate of the contamination from the 4-body final state.

Thus the total contamination was estimated to be approximately 3% and 4% for the 1.2 GeV/c and formation experiments respectively.

Summary

It is very difficult to give an accurate upper limit to the contamination but estimates have been made for the various reactions and are of order 1-4%. This was considered to be an acceptable level. In order to check that the cuts introduced did not produce any biases,parts of the subsequent analysis were performed on the full sample, and no significant differences in the results were found.

Cross-Sections

The cross-sections for the 1.2 GeV/c data have already been calculated [3] and the values for the reactions under consideration are reproduced in Table 3.1.

Reaction	Cross-Section μb
$K_1^o K^\pm \pi^\mp$	274 ± 14
$K_1^o K_1^o \pi^+ \pi^-$	187 ± 9
$K_1^o (K^o) \pi^+ \pi^-$	224 ± 10 *
$K_1^o K^\pm \pi^\mp \pi^o$	528 ± 22
$K_1^o K_1^o \pi^+ \pi^- \pi^o$	125 ± 8

Table 3.1 Cross-sections for 1.2 GeV/c data
(The neutral decay made of the K_1^o has been allowed for, except in the reaction asterisked)

However, the values for the formation experiment (1.28-1.47 GeV/c) have not been presented and so they will be dealt with in the next few sections.

The cross-section for an interaction is commonly stated as :

$$\sigma = \frac{\text{number of interactions/target particle/unit time}}{\text{number of incident particles/unit area/unit time}}$$

For stationary, free targets σ can be written as

$$\sigma = \frac{N}{L \left(\frac{A_N}{M_A} \right) \rho} \qquad (3\text{-}4)$$

where N is the number of interactions, L is the pathlength of the beam particles, A_N is Avogadro's number (= 6.023×10^{23} atoms/gm atom), M_A is the gram atomic weight (= 1.009 gm for hydrogen) and ρ is the target density (= 0.062 gm/cc for hydrogen at $26^{\circ}K$).

Defining the mean free path $\bar{\ell}$ by $\bar{\ell} = L/N$, then we can write for a hydrogen target,

$$\bar{\ell} = \frac{10^{30}}{N_A \rho} \mu b.cm = 2.77 \times 10^7 \mu b.cm. \qquad (3\text{-}5)$$

The task of calculating σ reduces to determining L and N, and to do this a fiducial volume must be defined to calculate the total pathlength. Only events within this volume are used in the calculation of N. The volume defined earlier for the 2m chamber was taken as the fiducial volume, with the extra condition that the Y coordinate of the $\bar{p}$ track at the volume entrance (X = -75cm) lay in the range

$$-12cm \leqslant Y \leqslant 17cm.$$

This cut ensured no track left the volume through the Y faces shortly after entering it. This was possible owing to the wide beam spread, and such short tracks hindered the accurate calculation of the average track length.

The Pathlength (L)

This is the total length of beam track within the fiducial volume for the whole exposure. It is given roughly by multiplying the total number of beam tracks entering the volume by the length of volume. The number of beam tracks entering the volume was estimated by counting the beam tracks crossing the volume entrance as defined above on every 20^{th} frame of each half-roll at each energy. From these numbers

the total number of beam tracks entering the volume was estimated. There are, however, some corrections to be made.

a) Curvature : the length of each beam track does not necessarily equal the length of the fiducial volume. The length depends on the track's curvature and at what angle the track enters the volume. This length (potential length) was found by taking each event in the volume and "floating" the beam track forwards and backwards to the limits from the annihilation point. An average length L_o was thus obtained.

b) Attenuation : Those tracks that interact traverse only part of the chamber. Owing to this attenuation, there will be a corresponding reduction in the pathlength and the effective length of track is

$$L_e = \int_0^{L_o} e^{-l/L_a}\, dl$$
$$= L_a(1-e^{-L_o/L_a})$$

where L_a is the attenuation length of a $\bar{p}$ track, which is equivalent to the attenuation cross-section, σ_a.

This cross-section is not equal to the total $\bar{p}p$ cross-section at each energy since the event sample contains some events with small elastic scatters on the $\bar{p}$ track. To find the fraction of elastic scatters which were to be taken as attenuation, the mean value of the dip angle λ and the mean variation of the azimuthal angle ϕ versus the X coordinate of the annihilation apex for the $\bar{p}$ tracks was calculated by plotting the relevant quantities at each energy. Knowing these results, the expected direction of any track could be found and hence the deviation Δ from this expected direction could be plotted. Fig.3V shows this deviation for the 1.28 GeV/c exposure. Most of the scatters

give rise to the long tail of this distribution. Those events with a deviation larger than a suitable cut-off (chosen as 0.07 rads. in the 1.28 GeV/c case) were taken as attenuation. From a knowledge of the $\bar{p}p$ elastic differential cross-section,[4] it is then possible to calculate the percentage α % of the elastic cross-section which attenuated the beam from the cut-off chosen. Then,

$$\sigma_a = (\sigma_{\bar{p}p_{TOT}} - \sigma_{\bar{p}p_{ELAS}}) + \alpha\% \times \sigma_{\bar{p}p_{ELAS}}$$

The values of the mean λ, the mean variation of ϕ. the cut-off chosen, and L_a for each momentum are given in Table 3.2.

So, from the spectrum of effective lengths, an average pathlength can be found.

c) Beam Contamination : Contamination by unwanted particles e.g. pions, kaons or muons, will give an incorrect value for the total $\bar{p}$ flux derived from a beam count. A measure of the contamination may be found from the distribution of δ-rays on the beam tracks.[5] For an incident particle of mass M_o and momentum P_o, the maximum momentum a δ-ray may have is approximately

$$P_{max} \approx \left(\frac{P_o}{M_o} \right)^2 \text{ MeV/c.}$$

Thus, a special scan is made for δ-rays with a radius of curvature greater than that possible due to antiprotons of given momentum. From this information, the contamination may be found.

Momentum GeV/c	$\overline{\lambda}$ rads	$\overline{\phi}$ rads	Δ rads	L_a cms
1.28	-0.003	3.04-0.0028X	0.070	259.5
1.34	0.0	3.04-0.0023X	0.060	260.8
1.39	-0.003	3.06-0.0026X	0.066	266.2
1.47	-0.003	3.06-0.0023X	0.068	274.6

Table 3.2 Data used in the calculation of cross-sections at each momentum.

The Number of Interactions (N)

The number of events which satisfied the above volume, entrance and deviation cuts was calculated from the D.S.T. This number has to be corrected for

a) Scanning Efficiency : Owing to film quality, density of tracks or just plain inefficiency, not all the V^o events on the film are found by the scanner. From a knowledge of the numbers of events found on the 1^{st} scan, 2^{nd} scan and on both 1^{st} and 2^{nd} scans, the overall efficiency may be calculated.

b) V^o Detection Efficiency : Besides scanner inefficiency, a V^o may be lost if it decays outside the visible region or else, if it decays so close to the annihilation apex, that it appears as a two prong.

The usual approach to remedy this loss is to choose an inner cut-off length L_o (e.g. 0.2cm) outside which it is assumed all events are found and weight the V^o events which decay outside this cut-off and within the potential

length L_p (maximum decay length available to the V^o - as defined by the fiducial volume) by the inverse of the probability that they decay between L_o and L_p. Other events are not used. This rejection of events can be criticised from the fact that it produces a momentum bias, particularly against low momentum events since rejection by the inner cut-off is the higher. The rejection due to the L_p cut-off is low and acceptable since, as the fiducial volume corresponds nearly to the whole well-illuminated region of the chamber, there were few events outside this volume.

In the case of the inner cut-off, the approach adopted at Liverpool[3] was to use an empirical weight W of the form (assuming a spherical cut-off)

$$W(p) = \frac{1}{e^{-mr/c\tau p}}$$

where m is the mass of the kaon, τ is the kaon lifetime, c is the velocity of light, p is the V^o momentum and r is the radius of the cut-off. The value of r was found by using all events and dividing the sample into 0.1 GeV/c momentum intervals. For each interval the decay length (distance between annihilation and V^o apices)was plotted and fitted to an exponential decay. Losses occuring near the annihilation apex were estimated by extrapolating the curve back to the origin and so a mean weight for each momentum interval was calculated. The above function was then fitted to a graph of mean weight versus mid-point of the momentum interval, giving a value for r .

If P_{in} is the probability that the kaon decays <u>outside</u> the inner cut-off and P_{out} is the probability that the kaon decays <u>outside</u> the potential length, the total weight is

then the inverse of the probability that it decays between the two cut-offs i.e.

$$W = \frac{1}{P_{in} - (1 - P_{out})}$$

The average corrections for V^o losses near the apex and outside the chamber were found to be 8% and 2% respectively.

c) Measure loss : Not all of the events measured reached the D.S.T. Events failed to reconstruct owing to dipping tracks, etc. or the event just got lost. With the aid of the library list, an estimate of the correction necessary for these events was made.

Tables 3.3 and 3.4 list the quantities used in the calculation of the mean free path ($\bar{l}$)

	Momentum GeV/c			
	1.28	1.34	1.39	1.47
Total No. of beam tracks within cuts	246408 ±3280	243798 ±3320	258105 ±3400	247812 ±3440
Contamination	5.1±0.7%	5.4±0.7%	8.1±0.7%	6.6±0.8%
Average Path-length cm	108.4±4.0	108.8±3.5	109.6±2.9	110.5±2.8
Total Path-length(L)cm	(2.535 ±0.101) x 10^7	(2.509 ±0.090) x 10^7	(2.617 ±0.081) x 10^7	(2.593 ±0.078) x 10^7

Table 3.4 Interactions data at each momentum

	Momentum GeV/c			
	1.28	1.34	1.39	1.47
Weighted sum of events within cuts	1291.3 ±35.9	1206.1 ±34.7	1212.8 ±34.8	1200.9 ±34.7
Measuring Efficiency	97±1%	97±1%	95.7±0.9%	94.8±0.9%
Scanning Efficiency	97.9 ±0.5%	98.6 ±0.7%	98.2 ±0.5%	98.7 ±0.5%
Number of Interactions (N)	1385.3 ±44.9	1282.7 ±41.6	1314.3 ±42.6	1314.0 ±42.4

Table 3.4 Interactions data at each momentum

Thus $\bar{l}$ (= L/N) at each momentum is

$(1.864 \pm 0.097) \times 10^4$ cm (1.28 GeV/c)

$(1.990 \pm 0.098) \times 10^4$ cm (1.34 GeV/c)

$(2.028 \pm 0.091) \times 10^4$ cm (1.38 GeV/c)

$(2.020 \pm 0.091) \times 10^4$ cm (1.47 GeV/c)

and so the cross-sections for the reaction

$\bar{p}p \longrightarrow$ Visible K^o + ··· are

= 1.486 ± 0.077 mb (1.28 GeV/c)

1.392 ± 0.068 mb (1.34 GeV/c)

1.366 ± 0.061 mb (1.38 GeV/c)

1.371 ± 0.062 mb (1.47 GeV/c)

These figures were calculated using the Liverpool data only since the scanning criteria, etc. were accurately known for these events. However, in the calculation of the

cross-sections for the various reactions (Tables 3.5,6,7,8), the full Liverpool and Paris sample was used, with only a volume cut, to increase the statistics. These weighted events were used to calculate the branching ratios to the different reactions from which the cross-sections were calculated using the above cross-sections and the K_1^o decay fraction ($K_1^o \to \pi^+\pi^-$ / $K_1^o \to$ total = 0.687). The errors quoted are mainly statistical and are given by the relationship: $\Delta\sigma = \dfrac{\sigma}{(\text{Number of events})^{1/2}}$ μb.

The variation of the cross-section with laboratory momentum is illustrated in Figs.3W,X,Y for the following reactions:

$$\bar{p}p \to K_1^oK_2^o\,\pi^+\pi^-$$

$$\bar{p}p \to K_1^oK^{\pm}\,\pi^{\mp}$$

$$\bar{p}p \to K_1^oK^{\pm}\,\pi^{\mp}(\pi^o)$$

$$\bar{p}p \to K_1^oK_1^o\,\pi^+\pi^-$$

$$\bar{p}p \to K_1^oK_1^o\,\pi^+\pi^-(\pi^o)$$

The reaction $\bar{p}p \to K_1^o(K^o)\,\pi^+\pi^-$ actually consists of two reactions: $\bar{p}p \to K_1^oK_1^o\,\pi^+\pi^-$ — where one of the K_1^o's has decayed via the neutral mode, and $\bar{p}p \to K_1^oK_2^o\,\pi^+\pi^-$.
If x is the branching ratio of the K_1^o(= 0.687), then we may write

$$\sigma_{K_1^o(K^o)\pi^+\pi^-} = x\sigma_{K_1^oK_2^o\pi^+\pi^-} + 2x(1-x)\sigma_{K_1^oK_1^o\pi^+\pi^-}$$

from which

$$\sigma_{K_1^oK_2^o\pi^+\pi^-} = \frac{\sigma_{K_1^o(K^o)\pi^+\pi^-} - 0.430\ \sigma_{K_1^oK_1^o\pi^+\pi^-}}{0.687}$$

Reaction	Weight sum of events on D.S.T.	% of Total	Cross-section μb
$K_1^o(K^o)$	27.4	0.88	13 ± 3 *
$K_1^o(K^o)M$	256.8	8.24	122 ± 10 *
$K_1^oK_1^o$	2.2	0.07	2 ± 2
$K_1^oK_1^o(\pi^o)$	44.2	1.42	45 ± 7
$K_1^oK_1^oM$	42.8	1.37	43 ± 7
$K_1^oK^\pm\pi^\mp$	387.1	12.42	269 ± 20
$K_1^o(K^o)\pi^+\pi^-$	540.3	17.33	258 ± 17 *
$K_1^oK^\pm\pi^\mp(\pi^o)$	761.1	24.42	528 ± 33
$K_1^o\pi^+\pi^-M$	291.2	9.34	202 ± 16
$K_1^oK^\pm\pi^\mp M$	166.1	5.33	115 ± 11
$K_1^oK_1^o\pi^+\pi^-$	178.3	5.72	180 ± 16
$K_1^oK_1^o\pi^+\pi^-(\pi^o)$	145.3	4.66	147 ± 14
$K_1^oK_1^o\pi^+\pi^-M$	14.3	0.46	15 ± 4
$K_1^oK^\pm\pi^\mp\pi^+\pi^-$	179.4	5.76	125 ± 11
$K_1^oK^\pm\pi^\mp\pi^+\pi^-(\pi^o)$	71.0	2.28	49 ± 6
$K_1^o(K^o)\pi^+\pi^+\pi^-\pi^-$	5.5	0.18	3 ± 1 *
$K_1^oK^\pm\pi^\mp\pi^+\pi^-M$	2.1	0.10	2 ± 1
$K_1^o\pi^+\pi^+\pi^-\pi^-M$	1.1	0.04	1 ± 1
Total	3117.2		

Table 3.5 Cross-section data for 1.28 GeV/c events

* These reactions have not been weighted by the K_1^o decay fraction

Reaction	Weight sum of events on D.S.T.	% of Total	Cross-section μb
$K_1^o(K^o)$	23.3	0.75	10 ± 2 *
$K_1^o(K^o)M$	247.5	7.93	110 ± 9 *
$K_1^oK_1^o$	2.1	0.07	2 ± 2
$K_1^oK_1^o(\pi^o)$	37.9	1.21	36 ± 6
$K_1^oK_1^oM$	45.9	1.47	43 ± 6
$K_1^oK^\pm\pi^\mp$	390.9	12.52	254 ± 18
$K_1^o(K^o)\pi^+\pi^-$	495.1	15.85	221 ± 15 *
$K_1^oK^\pm\pi^\mp(\pi^o)$	763.6	24.45	495 ± 30
$K_1^o\pi^+\pi^-M$	309.8	9.92	201 ± 15
$K_1^oK^\pm\pi^\mp M$	154.5	4.95	100 ± 9
$K_1^oK_1^o\pi^+\pi^-$	181.4	5.81	171 ± 15
$K_1^oK_1^o\pi^+\pi^-(\pi^o)$	157.8	5.05	149 ± 14
$K_1^oK_1^o\pi^+\pi^-M$	7.9	0.25	7 ± 3
$K_1^oK^\pm\pi^\mp\pi^+\pi^-$	209.7	6.72	136 ± 12
$K_1^oK^\pm\pi^\mp\pi^+\pi^-(\pi^o)$	83.8	2.68	54 ± 10
$K_1^o(K^o)\pi^+\pi^+\pi^-\pi^-$	7.1	0.23	3 ± 1 *
$K_1^oK^\pm\pi^\mp\pi^+\pi^-$ M	2.2	0.07	1 ± 1
$K_1^o\pi^+\pi^+\pi^-\pi^-M$	2.3	0.07	1 ± 1
Total	3122.8		

Table 3.6 Cross-section data for 1.34 GeV/c events

Reaction	Weight Sum of events on D.S.T.	% of Total	Cross-section μb
$K_1^o(K^o)$	10.3	0.34	5 ± 2 *
$K_1^o(K^o)M$	203.0	6.70	92 ± 9 *
$K_1^oK_1^o$	1.1	0.04	2 ± 2
$K_1^oK_1^o(\pi^o)$	38.0	1.25	36 ± 6
$K_1^oK_1^oM$	48.2	1.59	46 ± 6
$K_1^oK^\pm\pi^\mp$	313.8	10.36	206 ± 18
$K_1^o(K^o)\pi^+\pi^-$	484.3	15.98	218 ± 15 *
$K_1^oK^\pm\pi^\mp(\pi^o)$	720.4	23.78	473 ± 30
$K_1^o\pi^+\pi^-$ M	352.9	11.65	232 ± 15
$K_1^oK^\pm\pi^\mp$M	173.4	5.72	114 ± 9
$K_1^oK_1^o\pi^+\pi^-$	190.6	6.29	182 ± 15
$K_1^oK_1^o\pi^+\pi^-(\pi^o)$	167.1	5.52	160 ± 14
$K_1^oK_1^o\pi^+\pi^-$ M	10.9	0.36	10 ± 3
$K_1^oK^\pm\pi^\mp\pi^+\pi^-$	223.2	7.37	147 ± 12
$K_1^oK^\pm\pi^\mp\pi^+\pi^-(\pi^o)$	77.5	2.56	51 ± 9
$K_1^o(K^o)\pi^+\pi^+\pi^-\pi^-$	11.9	0.39	5 ± 1 *
$K_1^oK^\pm\pi^\mp\pi^+\pi^-$ M	2.2	0.07	1 ± 1
$K_1^o\pi^+\pi^+\pi^-\pi^-$ M	1.1	0.04	1 ± 1
Total	3029.9		

Table 3.7 Cross-section data for 1.39 GeV/c events

Reaction	Weight Sum of events on D.S.T.	% of Total	Cross-section b
$K_1^o(K^o)$	20.8	0.70	10 ± 2 *
$K_1^o(K^o)M$	197.6	6.61	91 ± 8 *
$K_1^oK_1^o$	2.1	0.07	2 ± 1
$K_1^oK_1^o(\pi^o)$	35.0	1.17	34 ± 6
$K_1^oK_1^oM$	55.9	1.87	54 ± 7
$K_1^oK^\pm\pi^\mp$	295.6	9.88	197 ± 14
$K_1^o(K^o)\pi^+\pi^-$	466.5	15.59	214 ± 14 *
$K_1^oK^\pm\pi^\mp(\pi^o)$	661.7	22.12	441 ± 27
$K_1^o\pi^+\pi^-M$	355.3	11.88	237 ± 17
$K_1^oK^\pm\pi^\mp M$	229.4	7.67	153 ± 12
$K_1^oK_1^o\pi^+\pi^-$	157.2	5.25	153 ± 14
$K_1^oK_1^o\pi^+\pi^-(\pi^o)$	149.9	5.01	146 ± 14
$K_1^oK_1^o\pi^+\pi^-M$	21.5	0.72	21 ± 5
$K_1^oK^\pm\pi^\mp\pi^+\pi^-$	210.4	7.03	140 ± 12
$K_1^oK^\pm\pi^\mp\pi^+\pi^-(\pi^o)$	111.8	3.74	75 ± 8
$K_1^o(K^o)\pi^+\pi^+\pi^-\pi^-$	7.8	0.26	4 ± 1 *
$K_1^oK^\pm\pi^\mp\pi^+\pi^-M$	9.8	0.33	7 ± 2
$K_1^o\pi^+\pi^+\pi^-\pi^-M$	3.2	0.11	2 ± 1
Total	2991.5		

Table 3.8 Cross-section data for 1.47 GeV/c events

References

1. D. Waldren Ph.D. Thesis Liverpool (1970), and references cited therein.
2. E. Fett "Methods in Subnuclear Physics", Vol.1, Gordon and Breach
3. N. West Ph.D. Thesis Liverpool (1970)
4. D.C. Howard Ph.D. Thesis Liverpool (1971)
5. M. Alston, J.V. Franck, L.T. Kerth "Bubble and Spark Chambers" Vol.II, p131, Academic Press
6. B. Lorstad, Ph.D. Thesis, Paris, 1969
7. J. Badier et al., Communication to Lund Conference (1969)

CHAPTER 4

ANALYSIS TECHNIQUES

In the absence of any theory describing the strong interaction, experimental analysis has been directed towards a determination of the parameters (e.g. mass, width) of the resonances which are so abundantly produced by the strong interaction.[1] Resonances are observed, for example, as enhancements in effective mass plots and their parameters are usually determined by comparing the experimental data with some theoretical prediction about the nature of the interaction e.g. phase space plus resonance production, and then varying the parameters and/or adding other parameters until the best agreement is reached. Such an approach is called phenomological and the process is called "fitting".

Choice of methods

In general, the two methods employed for fitting are least-squares (commonly referred to as minimum chi-squared (χ^2)) and maximum likelihood ($\mathcal{L}$). It can be shown that these two techniques are essentially equivalent for high statistics measurements (normally distributed) but in the case of poor statistics, the maximum likelihood method gives better results.

One way of proceeding is to fit the experimental distributions themselves e.g. effective mass plots. Thus for a (χ^2) fit, the quantity

$$\chi^2 = \sum_{\text{all bins}} \frac{(Th_i - E_i)^2}{\sigma_i^2},$$

(where Th_i and E_i are the number of events in the i^{th} bin

of the theoretical and experimental distributions respectively, and σ_i is the variance of E_i) would be minimised. This χ^2 distribution approaches the theoretical χ^2 distribution (defined in Chap.3) when the size of the sample is large. In practice, if one makes each Th_i and E_i at least 8 events then the sample will be big enough for the limiting distribution to be used. Assuming that there are many bins (in practice the number may be as small as 10) then we may write

$$\chi^2 = \sum_{\text{all bins}} \frac{(Th_i - E_i)^2}{Th_i},$$

where $\sigma_i^2 \approx Th_i$ has been used.[2] Thus, knowing the minimum chi-squared and the number of degrees of freedom of the fit (defined as the number of bins for which the theory is not constrained), the probability, or confidence level, of the fit can be found from statistical tables. If the theoretical distribution is normalised to the experimental distribution, then this introduces an extra constraint.

However, it may not be obvious which distributions need to be included in a fit and the best fit parameters can depend very much on which distributions are chosen for the fit. There is also the possibility of correlations existing between different distributions. For example, there is the problem of reflections - a resonance in one mass plot may distort other mass plots. This is difficult to take into account in χ^2 fits. Furthermore, as the experimental distributions are not always independent, it

is difficult to give a meaningful statement as to the probability of the fit. Another disadvantage is that of fitting associated resonance production e.g. $\bar{p}p \rightarrow K^{*}\bar{K}^{*}$. It is difficult to estimate the fraction of these processes since correlations between different effective masses in the same event cannot be easily examined. However, the χ^2 method has the advantages that it is visual and easy to use.

The following method does not have the above disadvantages. For an n-body final state, there are 3n-7 independent internal variables.[3] The technique consists of fitting the theoretical prediction in the space defined by these variables i.e. the density of events is evaluated in elementary volumes in the phase space of these variables. Thus, essentially, one is fitting to a density function over some region in a multi-dimensional space.

Again, a chi-squared function may be defined where now Th_i is the theoretical density of events in the i^{th} volume element and the summation is carried out over all such elements. There is, however, one serious drawback. Dividing the 3n-7 axes into m intervals gives m^{3n-7} volume elements. Thus, to have a reasonably small cell-size and enough events in each of the volumes to satisfy the χ^2 approximation, would require a large number of events, especially when $n \geqslant 4$.

This problem does not arise with the maximum likelihood technique. The method consists of setting up a likelihood function or estimator $\mathcal{L}$ and maximising $\mathcal{L}$ with respect to the unknown parameters. Thus $\mathcal{L}$ is defined by

$$\mathcal{L} = \prod_{i=1}^{N} L(x \mid \theta),$$

where $L'(x \mid \Theta)$ is a probability density function of Θ parameters, evaluated at each of the x experimental points of the multi-dimensional phase space. Also, $L(x \mid \Theta)$ must be normalised such that

$$\int_{\text{all phase space}} L'(x \mid \Theta)\,dx = 1, \text{ for all } \Theta.$$

In practice, a numerical normalisation is usually performed, based on an unormalised function L_o :

$$L'(x \mid \Theta) = \frac{L_o(x \mid \Theta)}{\int_{\text{all phase space}} L_o(x \mid \Theta)\,dx} \qquad (4\text{-}1)$$

Some Theoretical Considerations

To use the likelihood method, it is necessary to set up a probability density function in the space of the kinematic variables.

The cross-section for an n-body final state $|f\rangle$ from an initial state $|i\rangle$ may be written as [4]

$$d\sigma_{fi} = \text{const} \overline{\sum_i} \sum_f |T_{fi}|^2 \prod_{j=1}^{n} \frac{d^3\vec{p}_j}{2E_j}\, \delta(P_i - P_f) \qquad (4\text{-}2)$$

where $\vec{p}_j$, E_j are the 3-momentum and energy of the j^{th} final state particle;

P_i, P_f are the total 4-momenta of the initial and final states respectively;

T_{fi} is the Lorentz invariant matrix element for the process - the physics of the interaction is contained in this matrix element;

$\overline{\sum_i}$ is a suitable average over the initial states and

$\sum_f$ is a sum over all final states.

Integrating over continuous variables in the final state and incorporating any summation over discrete variables into $|T_{fi}|^2$ gives

$$d\sigma_{fi} = \text{const} \sum_i \int |T_{fi}|^2 \prod_{j=1}^{n} \frac{d^3\vec{p}_j}{2E_j} \delta(P_i - P_f)$$

$$= \text{const} \sum_i \int |T_{fi}|^2 \delta(P_i - P_f) \prod_{j=1} d^4 p_j \, \delta(p_j^2 - m_j^2) \quad (4\text{-}3)$$

where p_j and m_j are the 4- momentum and mass respectively of the j^{th} particle.

The term

$$Rn = \int \prod_{j=1}^{n} \frac{d^3\vec{p}_j}{2E_j} \delta(P_i - P_f) = \int d^{3n} Rn \quad (4\text{-}4)$$

is called the n-body Lorentz invariant phase space integral For n particles in the final state, the integration is carried out in the 3n-dimensional momentum space of the particles, over delta functions expressing conservation of energy and momentum and orientations of the entire system. The result is a distribution in 3n-7 independent internal variables.(3)

The 3n-7 variables were originally defined as 4-momenta. Now, the analysis consists of trying to find approximations to the matrix element which explain the observed effective mass distributions. Thus, it is convenient to transform from the 4-momenta variables into a new set involving effective masses and angles. Let these new variables be denoted by the vector variable $\underset{\sim}{M} = M_1, M_2, \cdots$ then

$$d\sigma_{fi} = \text{const} \sum_i \int |T_{fi}|^2 \; J \, d\underset{\sim}{M} \quad (4\text{-}5)$$

where $d\underset{\sim}{M} = dM_1 \, dM_2 \cdots$ and J is the Jacobian from the old to new system of variables.

The probability of finding the k^{th} event in the volume element $d\underset{\sim}{M}$ is just

$$P_k = \text{const}\left[\sum_i |T_{fi}|^2\right] J_k \, d\underset{\sim}{M}$$

and so the probability density D_k is

$$D_k = \frac{P_k}{d\underset{\sim}{M}} = \text{const}\left[\sum_i |T_{fi}|^2\right] J_k \qquad (4\text{-}6)$$

For N events the likelihood function ($\mathcal{L}$) is given by

$$\mathcal{L} = \prod_k^N D_k = \prod_k^N \text{const}\left[\sum_i |T_{fi}|^2\right] J_k \qquad (4\text{-}7)$$

In practice, since this function is rather small, the log of the function is maximised instead. Thus

$$L = \log \mathcal{L} = \sum_k \left[\log \sum_i |T_{fi}|^2 + \log J_k + \log \text{const}\right] \qquad (4\text{-}8)$$

The parameters of the fit are contained in the first term of the above expression and so the second and third terms can be ignored without affecting the results of the fit. Thus the quantity which is actually maximised is

$$L = \sum_k \log\left[\sum_i |T_{fi}|^2\right] \qquad (4\text{-}9)$$

The Form of the Matrix Element

As there are no detailed theories which describe the strong interaction, and, in particular, antiproton - proton annihilations, the best one can do is to look for a "good" approximation for the matrix element. The following discussion is by no means rigourous.

Figs. 5C and D of the following chapter show typical examples of effective mass distributions from the reactions under consideration. To a first approximation, these distributions deviate strongly from phase space only in the regions of resonance production. Thus, to describe the mass plots more accurately, it is necessary to consider a

matrix element which allows for this feature.

A resonance of mass M_r and width Γ_r decaying to particles i,j··n can be represented by a Breit-Wigner amplitude.(5)

$$B_r = \frac{\sqrt{\Gamma_r}}{M_o^2 - M_r^2 + i\,\Gamma_r\,M_r} \qquad (4\text{-}10)$$

Where M_o^2 is the effective mass squared of the group of particles i,j··n and is defined as

$$M_o^2 = \left[\sum E_k\right]^2 - \left[\sum P_k\right]^2 ,$$

E_k and P_k being the energy and momentum respectively of the k^{th} particle.

In some cases, the Breit-Wigner amplitude proposed by Jackson(6) is used.

$$J_r = \sqrt{\frac{M_o}{q_o}}\ \frac{\sqrt{\Gamma}}{M_o^2 - M_r^2 + i\,\Gamma\,M_r} \qquad (4\text{-}11)$$

$$\text{where}\quad \Gamma = \Gamma_r\ \frac{(q_o)}{(q_r)}^{2s+1}$$

q_o, q_r being the 3-momenta of the decay particles in the rest system of M_o and M_r respectively, s the spin of the resonance.

Another parameterisation used is that of a scattering length amplitude (7) of the form

$$SL = \frac{1}{1 - iAq} \qquad (4\text{-}12)$$

Where A is the scattering length and q is the 3-momentum of one of the particles in their C.M.S.

The simplest form for T_{fi} is(5)

$$T_{fi} = A_r \times B_r \qquad (4\text{-}13)$$

where A_r is an amplitude describing the effects of

all the other invariant quantities of the process, such as the angular variables.

If there is more than one interaction channel, then the individual amplitudes, appropriately normalised, should be added coherently with suitable phase factors between the channels to form the matrix element. However, at 1.2 GeV/c, the annihilation process is believed to take place from a number of $\bar{p}p$ initial angular momentum states.[8] A matrix element element constructed taking into account these facts would be very unwieldy. Thus, to make the analysis practicable, some simplifications are made.

When the square modulus of T_{fi} is taken, there will be leading terms of the type $|A_r|^2 \, |B_r|^2$ plus a string of interference terms such as would be seen between amplitudes from the same channel but different initial states etc. It is assumed that the phases of the interference terms are essentially randomly orientated and that summing over all the possible initial states will cause some cancellation of these terms. Thus they will be smaller than the leading terms and so are ignored. It is also assumed that after the summation the variables contained in $|A_r|^2$ etc. will tend to average out and can be replaced by a constant. or slowly varying, function $\overline{|A|^2}$. Furthermore since $\log \mathcal{L}$ is used this function can be ignored.

The ability of the matrix element to explain the experimental data will test the validity of the above assumptions.

As a simple example, consider the reactions

$$\bar{p}p \longrightarrow K_1^0 \; K_1^0 \; \pi^+ \pi^- \; \text{- phase space}$$

$$\bar{p}p \rightarrow A_2\,\pi^+\pi^- \;;\quad A_2 \rightarrow K_1^0\,K_1^0$$
$$\bar{p}p \rightarrow K_1^0\,K_1^0\,\rho^0 \;;\quad \rho^0 \rightarrow \pi^+\pi^-$$

Using the above reasoning, the approximate matrix element which will describe the effective mass plots is

$$\overline{\sum_i} |T_{fi}|^2 = \frac{f}{\bar{N}} + \frac{f_{A_2}}{\bar{N}_{A_2}} |B_{A_2}|^2 + \frac{f_\rho}{\bar{N}_\rho} |B_\rho|^2 \qquad (4\text{-}14)$$

where f, f_{A_2} and f_ρ represent the fraction of the channels present and N, N_{A_2} and N_ρ can be identified as the appropriate normalisation factors. They are defined as

$$N = \int d^{12}R_4 \;,\; N_{A_2} = \int |B_{A_2}|^2\, d^{12}R_4 \qquad (4\text{-}15)$$

(recall the equation $L'(x \mid \theta) = \dfrac{L_0(x \mid \theta)}{\int_{\text{all phase space}} L_0(x \mid \theta)\, dx}$)

Using the normalisation condition $\int d\sigma_{fi} = 1$ i.e. $f + f_{A_2} + f_\rho = 1$, a slight rearrangement gives the form usually used in the computations.

Thus,

$$L = \log \mathcal{L} = \sum_{\text{all events}} \log \left[\overline{\sum_i} |T_{fi}|^2 \right]$$

$$= \sum_{\text{all events}} \log \left[(1. - f_{A_2} - f_\rho) + f_{A_2} |B_{A_2}|^2 \frac{N}{N_{A_2}} + f_\rho |B_\rho|^2 \frac{N}{\bar{N}_\rho} \right] \qquad (4\text{-}16)$$

where the first term gives the phase space production of the final state.

This process can be extended to include more resonances.

For channels of the type $\bar{p}p \rightarrow K^{*\pm} K_1^0 \pi^{\mp}$; $K^{*\pm} \rightarrow K_1^0 \pi^{\pm}$, where there exists more than one effective mass combination (4 in this case), all the combinations must be included in T_{fi} since it is impossible to state which particular combination comes from the resonance. Thus using the above

arguments,

$$\sum_{i} |T_{fi}|^2 = \frac{f_{K^*}}{N_{K^*}} \sum_{i=1}^{4} |B_{K^*}^{i}|^2 \qquad (4\text{-}17)$$

where $N_{K^*} = \int \left[\sum_{i=1}^{4} |B_{K^*}^{i}|^2 \right] d^{12}R_4$

Associated resonance production e.g. $\bar{p}p \longrightarrow K^{*+} K^{*-}$; $K^{*+} \longrightarrow K_1^0 \pi^+$, $K^{*-} \longrightarrow K_1^0 \pi^-$ has a matrix element of the form

$$T_{fi} = A_{K^{*+}K^{*-}} B_{K^{*+}} B_{K^{*-}} \text{ and } \overline{\sum_{i}} |T_{fi}|^2$$

is written as

$$\overline{\sum_{i}} |T_{fi}|^2 = \frac{f_{K^*K^*}}{N_{K^*K^*}} \sum_{i=1}^{2} |B_{K^{*+}}^{i}|^2 |B_{K^{*-}}^{i}|^2 \qquad (4\text{-}18)$$

(the summation is included as there are two possible combinations of $K^{*+}K^{*-}$ from $K_1^0K_1^0\pi^+\pi^-$).

Resonances may also have a sequential or cascade decay made e.g. $\bar{p}p \longrightarrow E^0 \pi^0$; $E^0 \longrightarrow K^0K^{*0}$ or $K^{\pm}K^{*\mp}$; $K^{*0} \longrightarrow K^{\pm} \pi^{\mp}$, $K^{*\mp} \longrightarrow K_1^0 \pi^{\mp}$. T_{fi} will contain amplitudes for both the E^0 and K^* resonances. Thus

$$\overline{\sum_{i}} |T_{fi}|^2 = \frac{f_E}{N_E} |B_E|^2 \left[\left| Z B_{K^{*0}} + Z' B_{K^{*\mp}} \right|^2 \right] \qquad (4\text{-}19)$$

The K^* mesons are produced here from a state of definite spin and parity and cancellation of interference terms between the two possible K^* cannot be expected to occur. Hence suitable amplitudes Z and Z′ are included in the above expression to account for this situation.

The Fitting Procedure

The square modulus of the matrix element for any process consists of the appropriate combination of the above functions. In the likelihood fit, the log of this quantity is calculated for each event, one by one, and the negative sum (- L) is minimised by varying the resonance

parameters(e.g. mass, width, fraction) using the CERN minimisation program MINNOW.[9] Normalisation integrals are generated beforehand using the CERN Monte-Carlo program FOWL.[10] The parameter values at the minimum value of - L correspond to the best fit values. In essence, this corresponds to comparing each event to an average event and then varying the average event until it resembles the experimental situation as near as possible.

Since events are treated individually, any correlations within an event may be detected. Reflections are also automatically accounted for. The disadvantage of the likelihood method, apart from it being complicated and non-visual, is that it is difficult to attach a confidence level to a fit. It is however, possible to obtain a relative comparison between two fits using the likelihood ratio test: let L_1 and L_2 be two maximised likelihood functions for hypotheses H_1 and H_2, H_2 being determined from H_1 by the addition of r extra parameters. Then it can be shown that[11] the function $\Delta = 2 (\log L_2 - \log L_1)$ is distributed as a χ^2 with r degrees of freedom. Thus, if H_1 is the correct hypothesis, the confidence level, that the increase in the likelihood function for H_2 is purely statistical, can be obtained. The statistically expected value for Δ is r.

If, however, two hypotheses D_1, D_2 are independent such as a Breit-Wigner or scattering length fit to the same enhancement, it can be shown[12] that if Δ is at least equal to 4 then this corresponds to a 5% confidence level for a χ^2 distribution with one degree of freedom. Thus if $\Delta > 4$, hypothesis D_1 can be reasonably rejected compared with D_2. Precisely, however, χ^2 does not now

follow a χ^2 law.

When a fit is completed, the results of the fit are used to generate theoretical distributions, again using FOWL, and compared with the experimental data by a χ^2 test. Though the χ^2 obtained on each of these distributions may be used to give a relative comparison between different fits. a confidence level cannot be attached to any fit because of the correlations between distributions.

The Monte-Carlo Program - FOWL

In order to obtain normalisation integrals and theoretical distributions of a variable q ($= \frac{d}{dq}(Rn)$), it is necessary to calculate the phase space integral, Rn. Analytic expressions for this integral exist for 2,3 and 4-body final states. However, the required integrals were generated using FOWL since this method is much simpler.

In FOWL, the n-body phase space integral is decomposed into a successive product of pseudo 2-body systems (analytic) in terms of effective masses of these systems, using a recurrence relation for Rn. The program generates n-2 random numbers to calculate the R_2 terms in each of the appropriate C. of M. systems. The numbers are ordered in such a way that only physical events are generated. The phase space weight (called WT) is the product of these terms.

At each stage, the pseudo 2-body system is given two random rotations so the final event has an isotropic angular distribution.

Each event is weighted by its phase space weight and any phase space distributions may be calculated by histogramming the relevant quantities after generating many events. Distributions arising from any matrix element may

also be calculated in FOWL. This is done by multiplying the phase space weight by the square modulus of the matrix element for the event.

To calculate the normalisation integrals with FOWL, the sums

$$\sum_{j \text{ events}} |B_r|^2 \, WT_j \quad \text{and} \quad \sum_{j \text{ events}} WT_j$$

are kept, the contribution from each event being added. If a large number of events (typically 80,000) is generated then the ratio

$$\frac{N}{N_r} = \frac{\sum WT_j}{\sum |B_r|^2 \, WT_j}$$

is equivalent to the integrals over all the allowed regions of phase space.

If the masses and widths of the resonances are allowed to vary, then the normalisations must be recalculated at each stage. In practice, a grid of normalisations for differing masses and widths is generated and a particular value is found by interpolation. However, as this sharply increases both computer time and space, both in generation and during the fit, so most masses and widths are kept fixed.

References

1. Particle Data Group, Particle Properties (Jan 1971)
2. M.G. Kendall and A. Stuart "The Advanced Theory of Statistics", Vol.1, p356, Griffin.
   D. Drijard, W. Eadie, F. James, M. Roos, B. Sadoulet "Probability and Statistics applied to High Energy Physics" p7, Part3; p20, Part 6, CERN Report 1970
3. M. Block, Phys. Rev. 101, 796 (1956)
   P. Nyborg, Phys. Rev. 140, B921 (1965)
4. H. Muirhead "The Physics of Elementary Particles", p268, Pergamon
5. H. Pilkuhn "The Interactions of Hadrons" p36, North Holland
6. J.D. Jackson N.C. 34 1644 (1964)
   S. Margulies, J.J. Phelan N.C. 58 804 (1968)
7. H. Pilkuhn op. cit. p44
8. D.Q. Lamb M.Sc. Thesis, Liverpool (1969)
9. F. James and M. Roos MINNOW-CERN program library write-up D506
10. F. James FOWL-CERN program library write-up W505
11. A. Wald, Trans. Amer. Math. Society 54 (1943) p426
12. D. Drijard et al. op. cit. p4, Part 10
    B. Marechal Ph.D. Thesis, Paris (1969)

CHAPTER 5

A STUDY OF THE REACTIONS AND RESULTS

I. $\bar{p}p \rightarrow K_1^o K^{\pm} \pi^{\mp}$

II. $\bar{p}p \rightarrow K^o K^{\pm} \pi^{\mp} (\pi^o)$

III. $\bar{p}p \rightarrow K_1^o K_1^o \pi^+ \pi^-$

IV. $\bar{p}p \rightarrow K_1^o (K^o) \pi^+ \pi^-$

V. $\bar{p}p \rightarrow K_1^o K_1^o \omega$ $(\bar{p}p \rightarrow K_1^o K_1^o \pi^+ \pi^- (\pi^o))$

Since the required amount of computer time becomes prohibitive when the masses and widths of resonances are allowed to vary in the fits, the procedure adopted was to fix the masses and widths at their published values[1] and test if their presence was statistically significant - this means fitting the fraction of resonance present. However, the parameters of the $K\bar{K}$ threshold enhancements were allowed to vary since their situation is even more confused than the better known resonances.

Table 5.1 lists the resonance masses and widths used.

Resonance	Mass (MeV)	Width (MeV)
$K^*(892)$	892	50
$K^*(1420)$	1420	90
A_2 [a]	1318	40
ρ [b]	765	125
f^o	1264	151
f'	1514	73
D^o	1290	60
E^o	1410	70
ω^o [c]	783	20

Table 5.1 Resonance parameters used in the fits

a) Owing to statistical and resolution problems and also to the present confusion about the A_2 situation, no attempt was made to parameterise the A_2 by any amplitude other than the Breit-Wigner form. The values of the mass

and width taken are the averages for the $K\bar{K}$ decay mode. Indeed, in preliminary fits when the mass and width of the A_2 were allowed to vary, the values obtained were compatible with those used.

b) There are wide fluctuations in the measured values for the mass and width of the ρ meson due to differences in production mechanism, background behaviour, etc. and the numbers used represent average values.

c) The natural width of the ω meson is 13 MeV.[1] However, owing to experimental resolution, it is broadened and the value used is the result of a maximum likelihood fit to the reaction $\bar{p}p \rightarrow K_1^o K_1^o \pi^+ \pi^- \pi^o$ at 1.2 GeV/c.[2]

The fixed resonances were parameterised by the Breit-Wigner expression as this was computationally quicker and simpler to use. Indeed, Jackson[3] found that for resonances that are narrow and/or well above threshold the effect of the energy-dependence of the width is small.

By simulating V^o events with FOWL, allowing them to decay and checking to see if they would have been found on the film, a previous analysis[10] has shown that, while momenta spectra are improved, the inclusion of weights into effective mass distributions, etc. has no significant effect. Indeed, it was checked that the weighted and unweighted distributions for the reactions in this study were statistically compatible. Thus. though weights were used in cross-section calculations, they were not incorporated into the fits.

I. The reaction $\bar{p}p \longrightarrow K_1^o K^{\pm} \pi^{\mp}$

Figs. 5A and 5B show the Dalitz plot of the $K_1^o \pi^{\mp}$ and $K^{\pm} \pi^{\mp}$ effective mass squared for these events. The projections (in effective mass) are shown in Fig. 5C. Apart from the well-defined bands corresponding the $K^*(892)$ resonances, the Dalitz plots show

a) a band at 45^o (i.e. $K^oK^{\pm}$) around 1320 MeV, possibly corresponding to the A_2 meson.

b) smaller accumulations of events in $K\pi$ in the region 1420 MeV, possibly corresponding to $K^*(1420)$ meson production.

c) a possible band of events near the $K\bar{K}$ threshold.

d) a noticeable assymmetry with respect to the first diagonal.

The distribution of points on the Dalitz plot was fitted using the type of matrix element discussed in the previous chapter. The function used for the fits was of the form

$$\mathcal{L} = (1.- \sum_i f_i + \sum_i f_i N_i P_i)$$

where f_i are the fractions, N_i are the normalisations and P_i the parameterisations of the appropriate resonances. As indicated, the resonances' masses and widths were kept fixed and the statistical significance of the enhancements was investigated.

The production of other resonances not being as strong, the matrix element was first constructed to take into account $K^*(892)$ and then the influence of the other resonances was investigated. Using the above density function, the following possibilities were tested:

A) that only $K^*(892)$ resonances are produced

B) that only $K^*(892)$ and A_2 resonances are produced

C) that $K^*(892)$, A_2 and $K^*(1420)$ resonances are produced.

Introducing the notation B(i,j··n) for the square modulus of the Breit-Wigner amplitude

$$= |B_r|^2 = \frac{\Gamma_r}{(M_o^2 - M_r^2)^2 + \Gamma_r^2 M_r^2}$$

where r is a resonance of mass M_r and width Γ_r and M_o is the effective mass of the group particles i,j··n, and labelling the particles as follows: K_1^o-1, $K^{\pm}$-2, $\pi^{\mp}$-3, then the functions used in the fits were:

A) $(1.-f_1-f_2)+f_1N_1B_1(23)+f_2N_2B_2(13)$

B) $(1.-f_1-f_2-f_3)+f_1N_1B_1(23)+f_2N_2B_2(13)+f_3N_3B_3(12)$

C) $(1.-f_1-f_2-f_3-f_4-f_5)+f_1N_1B_1(23)+f_2N_2B_2(13)$
$+f_3N_3B_3(12)+f_4N_4B_4(23)+f_5N_5B_5(13)$

In the above the subscripts 1,2,3,4,5 refer to the $K^{*o}(892)$, $K^{*\pm}(892)$, A_2, $K^{*o}(1420)$, $K^{*\pm}(1420)$ resonances respectively and f_i and N_i the fraction and normalisation respectively for the i^{th} resonance.

The results of these fits are shown in Table 5.2. In this table, $\Delta = 2(\log \mathcal{L}_2 - \log \mathcal{L}_1)$ and the statistically expected Δ, $\langle\Delta\rangle$, are given for successive fits. For comparison, the value of $\log \mathcal{L}$ for phase space alone is also shown.

Fit	log $\mathcal{L}$	Δ	$\langle\Delta\rangle$
Phase Space	0.0	—	—
A	551.62	1103.24	2.0
B	570.52	38.20	1.0
C	580.48	19.92	2.0

Table 5.2 Results of the likelihood fits to $K^o K^{\pm} \pi^{\mp}$

Recalling that Δ is distributed as a χ^2 with r degrees of freedom, where r is the number of extra parameters in the likelihood function $\mathcal{L}_2$, then, assuming the extra parameters introduced in Fits A,B and C have no physical significance, the expected improvements in the respective Δ's are 2.0, 1.0 and 2.0 and the probabilities that improvements of 1103.24, 38.20 and 19.92 will result are all less than 0.01%. Thus, these results show that there is significant production of $K^*(892)$, A_2 and $K^*(1420)$ resonances i.e. the solution corresponding to Fit C is preferred. The results of this fit on the three mass spectra $M(K^{\pm} \pi^{\mp})$, $M(K_1^o \pi^{\mp})$, $M(K_1^o K^{\pm})$ are shown in Fig.5C, and they are tabulated in Table 5.3 together with the χ^2 evaluated on each of the above histograms between the experimental values and those predicted by Fit C. For comparison, the χ^2 evaluated with phase space is given as well.

Resonance	Fraction	Distribution	χ^2 for Phase Space	χ^2 for Fit C	No. of Bins
$K^{*o}(892)$	18 ± 2%	$K^{\pm}\pi^{\mp}$	419.2	54.1	48
$K^{*\pm}(892)$	30 ± 3%	$K_1^o\pi^{\mp}$	1303.3	69.3	48
A_2	4 ± 2%	$K_1^oK^{\pm}$	219.4	43.0	47
$K^{*o}(1420)$	4 ± 2%				
$K^{*\pm}(1420)$	3 ± 2%	Totals	1941.9	166.4	143

Table 5.3 Results of Fit C

It can be seen that Fit C describes the mass plots very well except in the region $M(K_1^oK^{\pm}) \sim$ 1700 MeV where there is an excess of events over the predicted number. Apart from being a statistical fluctuation, this effect could be a resonance. There are no well-defined resonances in this region, though the R(1750) has been reported.[1] Its partial decay modes are unknown. There is also the possibility that this effect is due to a complicated interference effect where the K^* bands cross. This has not been taken into account.

A study of the reaction $\bar{p}p \longrightarrow K_1^oK^{\pm}\pi^{\mp}$ at rest[4] showed that there was strong production of a I = 1 $K\bar{K}$ threshold enhancement and that a specific amplitude was required to reproduce the effect. The analysis, however, was unable to differentiate between three interpretations for this threshold enhancement viz. a narrow resonance around 972 MeV, a resonance at 1016 MeV with $\Gamma \sim 25$ MeV, or simply a scattering length of 2 fm. with no clear

relation to a resonating channel. Moreover, it was not possible to completely distinguish between J^P assignments 0^+ and 1^- for the resonance interpretations. Although the main information on the I =1 $K\bar{K}$ system comes from the above analysis, a similar enhancement has appeared in the reaction $\bar{p}p \rightarrow K\bar{K}\ 3\pi$ at rest[5] where it is associated with the decay of the E^o meson, in the reaction $\bar{p}p \rightarrow K_1^o K^\pm \pi^\mp \pi^o$ at 1.18 GeV/c[6] and in the reaction $\bar{p}p \rightarrow K\bar{K}\ 3\pi$ at 1.18 GeV/c where it is related to the decay of the D^o meson[7]. However, in the data of this reaction ($pp \rightarrow K^o K^\pm \pi^\mp$) at 1.18 GeV/c[6], there was no threshold enhancement observed. The increased statistics of the present study seem to be in agreement with this fact (see Fig.5C). Nevertheless, it is interesting to see if the introduction of an amplitude to describe any $K\bar{K}$ threshold effect improves the results of Fit C. Thus, four more likelihood fits were performed containing one of the following parameterisations:

D) a Breit-Wigner form

E,F) a Jackson form

$$J(i\ j) = |J_r|^2 = \frac{M_o}{q_o} \frac{\Gamma}{(M_o^2 - M_r^2)^2 + \Gamma^2 M_r^2}$$

$$\text{with } \Gamma = \Gamma_r \left(\frac{q_o}{q_r}\right)^{2s+1}$$

Since the data at rest were unable to determine the spin of the enhancement inambiguously, fits were tried with s = 0(FitE) and with s = 1(FitF). The distribution of the decay cosine ($\cos\Theta$ of the K_1^o with respect to the line of flight of the $K_1^o K^\pm$ system), for events with $M(K_1^o K^\pm) <$ 1080 MeV from the present data, is given in Fig.5C. This distribution was fitted with a zero and second order

polynomial. However, owing to the poor statistics in this region, the fits were of poor quality but the P-wave interpretation ($\chi^2 = 2.1/3$) gave a better fit than the S-wave interpretation ($\chi^2 = 5.0/3$).

G,H) a scattering length form

$$S(i\ j) = |SL|^2 = \frac{1}{1 + A^2 q^2}$$

where A is a real (= a) or complex (= a+ib) scattering length. For example, the function used in Fit E was written as: $(1.-f_1-f_2-f_3-f_4-f_5-f_6)+f_1N_1B_1(23)+f_2N_2B_2(13)$ $+f_3N_3B_3(12)+f_4N_4B_4(23)+f_5N_5B_5(13)+f_6N_6B_6(12)$.

When the terms were introduced into the matrix element from Fit C however, there was no significant improvement in $\log \mathcal{L}$. For Fits D,E,F,G and H respectively Δ was equal to 2.22, 2.24, 2.64, 0.18 and 0.30. If the extra parameters introduced were parameterising a statistical fluctuation, the expected Δ's would be 3.0, 3.0, 3.0, 2.0 and 3.0 respectively. The presence of a $K_1^0K^{\pm}$ threshold enhancement in this reaction is therefore doubtful and so Fit C is taken as the final fit.

It can be seen from the Dalitz plots (Figs.5A and B) and Table 5.3 that the amount of $K^{*\pm}(892)$ observed is roughly twice that of $K^{*0}(892)$. Two possible explanations have been given to interpret this effect. The first is in terms of interference between the isospin I = 0 and I = 1 states.[8] By expanding the $K\bar{K}\pi$ state into isospin vectors, it can be shown that if A and B are the amplitudes for KK^* in I = 0 and I = 1 respectively, the intensities of $K^+(\bar{K}^0\pi^-)$ and $K^0(K^-\pi^+)$ are proportional to $|A + B|^2$ and

$|A - B|^2$ respectively. The K^* bands on the Dalitz plot are therefore not necessarily symmetric with respect to the diagonal if interference takes place; the results suggest that it might. The interference may then also explain the peculiar structure of the Dalitz plot in the overlap region of the K^* bands. The second explanation of the observed effect is in terms of the interference of the KK^* amplitude for another process.[9] It is shown, for example, for KK^* proceeding from the $^3S_1$, I = 1 state, that the superposition of the resonant and non-resonant amplitudes leads to an interference term and an assymmetry whose importance depends on the relative magnitude and phase of the two amplitudes.

Summary

The study of the reaction $\bar{p}p \longrightarrow K_1^o K^{\pm} \pi^{\mp}$ has shown evidence for the production of K^{*o} (892) (18%), $K^{*\pm}$ (892) (30%), A_2 (4%), K^{*o} (1420) (4%), $K^{*\pm}$ (1420)(3%), but, however, the data do not really support the inclusion of a $K\bar{K}$ threshold effect. The difference in the observed amounts of K^* may be possibly explained by interference between KK^* amplitudes from different isospin states or interference between resonant and non-resonant KK^* amplitudes.

II The reaction $\bar{p}p \rightarrow K_1^o K^{\pm} \pi^{\mp} (\pi^o)$

The 2- and 3-body effective mass distributions for this reaction are shown in Fig.5D. In the $K\pi$ and $\pi\pi$ plots respectively, there is strong production of the $K^*(892)$ and ρ mesons while in the $K_1^o K^{\pm}$ distribution there is a small excess of events at threshold and at the position of the A_2 meson ($M(K_1^o K^{\pm}) \sim 1320$ MeV). In the 3-body mass spectra, there are no obvious enhancements visible, but, however, there are broad regions showing a distortion from phase space. In addition, the scatter plot diagrams (Fig.5E) provide evidence for the quasi 2-body processes $\bar{p}p \rightarrow K^{*o}\bar{K}^{*o}, K^{*+}K^{*-}$ and $\bar{p}p \rightarrow \rho^{\pm} A_2^{\mp}$. In particular, the strong accumulation of points at the crossing of the K^* bands is most striking. The first step in the construction of a matrix element for this reaction will therefore be the inclusion of the dominant K^* and ρ channels.

A likelihood analysis of the reaction was made with a matrix element successively taking into account the following channels with the phase space contribution.

A) $\bar{p}p \rightarrow K_1^o K^{\pm} \rho^{\mp}$ — $\rho^{\mp}$ production

B) $\bar{p}p \rightarrow K^* K^{\mp}(\pi^o), K^{*o} K_1^o(\pi^o),$
$K^{*o} K^{\pm} \pi^{\mp}, K^{*\pm} K_1^o \pi^{\mp}$ — K^* production

C) $\bar{p}p \rightarrow K^{*o}\bar{K}^{*o}, K^{*+}K^{*-}$ — associated K^* production

The likelihood function used was again of the form

$$= (1. - \sum_i f_i) + \sum_i f_i N_i B_i .$$

Labelling the particles as K_1^o - 1, $K^{\pm}$ - 2, $\pi^{\mp}$ - 3, π^o - 4,

the above channels can be written

A) $f_1 N_1 B_1(34)$

B) $f_2 N_2 (B_{2A}(13) + B_{2B}(24))$

$f_3 N_3 (B_{3A}(14) + B_{3B}(23))$

C) $f_4 N_4 (B_{2A}(13) \times B_{2B}(24))$

$f_5 N_5 (B_{3A}(14) \times B_{3B}(23))$

The results of these fits are shown in Table 5.4 and the projections of Fit C are given in Fig.5D.

Fit	log $\mathcal{L}$	Δ	$\langle \Delta \rangle$
Phase Space	0.0	-	-
A	127.30	254.60	1.0
B	635.70	1016.80	2.0
C	719.90	168.40	2.0

Table 5.4 Results of preliminary likelihood fits to the reaction $K_1^o K^{\pm} \pi^{\mp} (\pi^o)$

Thus the results confirm the presence of the above channels in the reaction $\bar{p}p \rightarrow K_1^o K^{\pm} \pi^{\mp} (\pi^o)$ since the probabilities that these improvements in log $\mathcal{L}$ are merely due to the increased number of parameters are less than 0.001%.

Inspection of Fig.5D shows that the $K\bar{K}$ effective mass distribution is still not fully explained with this matrix element , especially in the region close to threshold and around 1320 MeV. Therefore two more channels were included in the matrix element.

D) $\bar{p}p \rightarrow A_2^{\pm} \pi^{\mp} (\pi^o)$ — $A_2^{\pm}$ production

E) $\bar{p}p \rightarrow (K_1^o K^{\pm})_{Th} \pi^{\mp}(\pi^o)$ — $K_1^o K^{\pm}$ threshold effect

The function for A_2 production was of the usual form i.e. $f_6 N_6 B_4(12)$. When this channel was introduced, $\log \mathcal{L}$ increased to 727.23 (Δ = 14.66). The probability that this improvement is statistical is of order 0.02%. Thus the channel $\bar{p}p \rightarrow A_2^{\pm} \pi^{\mp}(\pi^o)$ is acceptable.

For the $K\bar{K}$ threshold effect, resonance and scattering length functions were successively tried to parameterise the effect. However in the case of the resonance forms, the mass was driven to below 992 MeV i.e. the $K_1^o K^{\pm}$ threshold. Thus these fits were discontinued. An analogous situation arose in the study of the 1.18 GeV/c data.[1] The study of the scattering length interpretation is incomplete but it is known that a scattering length parameterisation gives a significant increase in the likelihood function and that the scattering length is in the range 1.0 — 3.0 fm. However, it is possible to obtain some interesting results from the data using a fixed scattering length. This was taken as 2.0 fm. Preliminary fits using a complex scattering length showed that the complex part was very small ($\lesssim$ 0.00001). Therefore all the fits were carried out using a real scattering length.

When the scattering length channel was introduced, $\log \mathcal{L}$ increased to 762.60 (Δ = 68.74). The probability associated with the purely statistical interpretation of the improvement in Δ is less than 0.001%. Hence the presence of a I = 1 $K\bar{K}$ threshold effect in this reaction is substantiated and a real scattering length gives a good

account of this effect. Thus the inclusion of the A_2 and $(K_1^oK^\pm)_{SL}$ in the matrix element results in a better description of the $K\bar{K}$ spectrum. For example, the χ^2 over the $K_1^oK^\pm$ mass plot for Fits C and E respectively are 131.1 and 46.0 over 37 bins. Moreover, the reflection of these effects improves the $\pi\pi$ spectrum: 141.8 and 98.9 over 41 bins. The prediction of Fit E on the $K_1^oK^\pm$ mass plot is shown in Fig.5F. The distribution is well fitted. The 3-body spectra, which were distorted from phase space, are also reasonably well described.(Fig.5F).

The study of the 1.18 GeV/c data, however, gave some evidence for the production of the D^o meson in the $K_1^oK^\pm\pi^\mp$ plot of this reaction at a mass of 1280 MeV.[1]
The presence of the D^o at 1.2 GeV/c has been confirmed and analysed in detail with increased statistics in the reactions $\bar{p}p \to K_1^oK^\pm\pi^\mp\pi^+\pi^-$ and $\bar{p}p \to K_1^oK^\pm\pi^\mp\pi^+\pi^-(\pi^o)$.[2] The D^o was found to decay dominantly via a $K_1^oK^\pm$ scattering length i.e. threshold enhancement (decay fraction, $D^o \to (K_1^oK^\pm)_{SL} \,/\, D^o \to$ all decays $= 0.92$).[2] Fig.5G shows the effective mass distribution of the 3-body $(K_1^oK^\pm\pi^\mp)$ system when events with $M(K_1^oK^\pm) < 1080$ MeV are selected. (The dotted curve on this plot corresponds to the prediction of Fit E). It can be seen that this selection enhances the D^o signal. In this "cut" histogram, there is also some evidence of another enhancement near 1410 MeV. This accumulation of events could possibly correspond to the E^o meson which was observed in annihilations at rest, with a branching ratio $E \to K^*K^\pm(K^*K_1^o) \,/\, E \to (K_1^oK^\pm)_{SL} = 1$.[3] Indeed the earlier data at 1.18 GeV/c were inconclusive

regarding the production of this resonance.[1] This was mainly due to the difficulty in discriminating between E^o production and the reflection of $K^*\bar{K}^*$ in the $K_1^oK^\pm$ spectrum. (The data taken from the annihilation at rest associated the E^o decay with a $K_1^oK^\pm$ threshold enhancement). The use of the maximum likelihood fit to the overall reaction will solve this problem since reflections are automatically taken into account. The earlier study also found some weak evidence for the f'(1514) resonance in the $K_1^oK^\pm\pi^\mp$ distribution. This meson has a decay mode: $f' \longrightarrow K^*K^\pm(K^*K_1^o)$

In order to investigate the production of the D^o, E^o and f' mesons and also to test the possibility of the associated production: $\bar{p}p \longrightarrow \rho^\pm A_2^\mp$, four more likelihood fits were performed. Thus the matrix element of Fit E was taken as a basis and the following channels were successively added to it.

F) $\bar{p}p \longrightarrow D^o\pi^o$ — D^o production
$\hookrightarrow (K_1^oK^\pm)_{SL}\pi^\mp$ or others

G) $\bar{p}p \longrightarrow E^o\pi^o$ — E^o production
$\hookrightarrow (K_1^oK^\pm)_{SL}\pi^\mp$ or $K^*K^\pm(K^*K_1^o)$

H) $\bar{p}p \longrightarrow \rho^\pm A_2^\mp$ — associated A_2 production

I) $\bar{p}p \longrightarrow f'\pi^o$ — f' production
$\hookrightarrow K^*K^\pm(K^*K_1^o)$

In terms of Breit-Wigner intensities, the above channels are written:

$$F)\quad f_8B_8(123)\left[(1-f_D)N_{8A} + f_DS(12)N_{8B}\right]$$

where the term $B_8(123)$ represents the Breit-Wigner function for the D^o, while the first term in the square bracket

represents all D^o decays other than via $(K_1^o K^\pm)_{SL}$ and the second term represents D^o decays via $(K_1^o K^\pm)_{SL}$. In the above, the N's represent the appropriate normalisation factors and f_D = fraction $\dfrac{D^o \to K_1^o K^\pm \text{ scattering length}}{D^o \to \text{ all decays}}$

and was set to 0.92.[2]

G) $f_9 B_9(123)\left[f_E N_{9A} S(12) + (1-f_E) N_{9B}(B(13) + B(23))\right]$

$B_9(123)$ is a term describing E^o production while the decay of the E^o is described by the terms inside the square bracket. The first of these terms represents decays via $(K_1^o K^\pm)_{SL}$ and the second represents decays via $K^* K^\pm (K^* K_1^o)$. The fraction f_E = fraction $\dfrac{E^o \to (K_1^o K^\pm)_{SL}}{E^o \to (K_1^o K^\pm)_{SL} + K^* K^\pm (K^* K_1^o)}$

was set at 0.5.[3]

H) $f_{10} N_{10} B_{10}(34) B_6(12)$

where the Breit-Wigner functions describe the $\rho^\pm$ and $A_2^\mp$ mesons respectively.

I) $f_{11} N_{11} B_{11}(123)\left[B(13) + B(23)\right]$

where $B_{11}(123)$ characterises f' production and the terms in the square bracket specify the f' decay via $K^* K^\pm (K^* K_1^o)$.

Since the decays of the D^o, E^o and f' come from states of definite spin-parity, the decay functions for these mesons should contain factors to take this property into account i.e. Zemach coefficients[4] which depend on the spin-parity of the meson. Thus, for the E^o

$f_9 B_9(123)\left[f_E N_{9A} Z_A S(12) + (1-f_E) N_{9B} Z_B (B(13) + B(23))\right]$

However, anticipating the results of the fit presented later, all Zemach coefficients were set to unity in the fit, since there are relatively few D^o, E^o or f' events

produced.

The results of these fits are displayed in Table 5.5

Fit	log $\mathcal{L}$	Δ	$<\Delta>$
E	762.60	—	—
F	776.59	27.98	1.0
G	789.66	26.14	1.0
H	792.44	5.56	1.0
I	794.21	2.54	1.0

Table 5.5 Further fits to the reaction

$$\bar{p}p \rightarrow K_1^o K^{\pm} \pi^{\mp} (\pi^o)$$

The above results endorse the presence of the D^o and E^o channels since the probabilities that these Δ's result from the increased number of parameters are less than 0.001%. The inclusion of the associated production channel $\bar{p}p \rightarrow \rho^{\pm} A_2^{\mp}$ is also reasonable while the f'channel is a border-line case (probabilities of 1.8% and 11.1% respectively).

Table 5.6 lists the fractions of the resonances present from Fit I together with the χ^2 evaluated over the experimental distributions for phase space and Fit I. The predictions of this fit are given in Fig.5H(and on the cut distribution of Fig.5G).

Resonance	Fraction	Distribution	χ^2 for Phase Space	χ^2 for Fit I	No. of Bins
$\rho^{\pm}$	19±2%	$\pi\pi$	474.2	90.7	40
$K^{*\pm}$	19±2%	$(K\pi)^{\pm}$	1055.6	55.3	40
K^{*o}	15±2%	$(K\pi)^{o}$	276.0	57.9	40
$A_2^{\pm}$	3±1%	$K\bar{K}$	150.5	47.9	37
$K^{*\pm}K^{*\mp}$	12±1%	$(K\pi\pi)^{o}$	138.2	41.5	35
$K^{*o}\bar{K}^{*o}$	2.4±0.8%	$(K\pi\pi)^{\pm}$	91.9	64.0	37
$(K_1^oK^{\pm})_{SL}$	4.2±1.4%	$(K\bar{K}\pi)^{\pm}$	307.0	88.1	37
D^o	1.5±0.3%	$(K\bar{K}\pi)^{o}$	259.3	53.4	38
E^o	3±1%				
$\rho^{\pm}A_2^{\mp}$	2.2±0.7%	Totals	2752.7	498.8	304
f'	1.4±0.7%				

Table 5.6 Results of Fit I

It is interesting to note that most of the $K_1^oK^{\pm}$ threshold effect is involved in the $K\bar{K}\pi$ resonances D^o and E^o — the fraction of $(K_1^oK^{\pm})_{SL}$ falls from 11% to 4% when these resonances are introduced.

Summary

The study of the reaction $\bar{p}p \rightarrow K_1^oK^{\pm}\pi^{\mp}(\pi^o)$ at 1.2 GeV/c has provided evidence for the strong production of the ρ(19%) and K^*(34%) resonances. Also the associated production $\bar{p}p \rightarrow K^*\bar{K}^*$ is quite strong (14%). Indeed the production of these resonances account for 67% of this reaction. The presence of the D^o and E^o mesons in this reaction has been confirmed and most of the $K_1^oK^{\pm}$

threshold enhancement is involved in these resonances.

III The reaction $\bar{p}p \rightarrow K_1^o K_1^o \pi^+ \pi^-$

Examination of the effective mass spectra for this reaction in Fig.5I reveals strong production of the ρ^o and $K^*(892)$ mesons in the $\pi\pi$ and $K\pi$ distributions respectively. In the $K_1^o K_1^o$ system, there are excesses of events in the A_2 region and near threshold.

The scatter plot diagrams (Fig.5J) suggest there is abundant quasi 2-body annihilations of the form $\bar{p}p \rightarrow K^* \bar{K}^*$ but little, if any, of the form $\bar{p}p \rightarrow (K\bar{K})\rho$, where $(K\bar{K})$ represents a resonance in the $K_1^o K_1^o$ system. The 3-body $K\pi\pi$ mass plot shows no striking features whilst the $K\bar{K}\pi$ mass plot has broad regions showing a distortion from phase space.

Accordingly, the reaction was fitted by the maximun likelihood method assuming the following channels contribute in addition to phase space.

A) $\bar{p}p \rightarrow K_1^o K_1^o \rho^o$ — ρ^o production

B) $\bar{p}p \rightarrow K^{*+} K_1^o \pi^-$, $K^{*-} K_1^o \pi^+$ — K^* production

C) $\bar{p}p \rightarrow K^{*+} K^{*-}$ — associated K^* production

D) $\bar{p}p \rightarrow A_2^o \pi^+ \pi^-$ — A_2^o production

The function used in the fit was set up in the manner described in the previous sections e.g. the term for ρ production was of the form $f_1 N_1$ BW(34) while for K^* production the term used was $f_2 N_2 (BW(13) + BW(24) + BW(14) + BW(23))$. Here the particles have been labelled K_1^o - 1, K_1^o - 2, π^+ - 3, π^- - 4 and f_i and N_i represent the appropriate fraction and normalisation factor. The above channels were successively added to

the matrix element which was thus of the form

$$= (1. - \sum_i f_i) + \sum_i f_i N_i B_i$$

The results are summarised in Table 5.7

Fit	log $\mathcal{L}$	Δ	$\langle\Delta\rangle$
Phase Space	0.0	-	-
A	55.67	111.34	1.0
B	204.83	298.32	1.0
C	234.45	59.24	1.0
D	237.81	6.72	1.0

Table 5.7 Results of preliminary likelihood fit to the reaction $\bar{p}p \rightarrow K_1^o K_1^o \pi^+ \pi^-$

If the introduction of the above channels has no physical significance, the probability that the above Δ's result is less than 0.8%. The presence of these channels is thus reasonably established. The predictions of Fit D on the mass plots are shown in Fig.5I.

It can be seen that the matrix element containing only the above channels does not completely describe the $K_1^o K_1^o$ threshold region. The study of this reaction at 1.18 GeV/c showed evidence for a $K_1^o K_1^o$ threshold peak and the best interpretation favoured a resonance with a mass of 1045 MeV and a width of order 50 MeV, although a scattering length interpretation could not be completely excluded.(1)

A $K_1^oK_1^o$ threshold enhancement has been seen in the reactions $\pi^-p \rightarrow nK_1^oK_1^o$ and $K^-N \rightarrow YK_1^oK_1^o$, over a wide range of incident particle momenta.(2) These experiments, however, differ amongst themselves as to the correct interpretation for this enhancement, be it a scattering length or a Breit-Wigner amplitude. The resonance interpretations, referred to as the S^*, gave a mass of order 1070 MeV and a width greater than 80 MeV. The decay angular distributions for this $K_1^oK_1^o$ resonance are consistent with isotropy.

Other work on π^-p interactions observe a $\pi^+\pi^-$ enhancement with a mass of order 1050 MeV and a width less than 70 MeV.(3) However, this effect was not associated with the $K_1^oK_1^o$ enhancement because, apart from the mass and width discrepancies the decay distribution of the $\pi^+\pi^-$ effect favoured a 2^+ spin-parity assignment.

The results of an analysis of this reaction ($\bar{p}p \rightarrow K_1^oK_1^o\pi^+\pi^-$) at 0.7 GeV/c showed that a $K_1^oK_1^o$ threshold resonance was strongly produced (13%) with a mass and width of 1046 MeV and 40 MeV respectively. The decay distribution of this object favoured a D-wave.(4)

The situation regarding the $K_1^oK_1^o$ threshold enhancement is thus somewhat confused. In view of the general interest in the I = 0 $K\bar{K}$ threshold effect, the result of adding a term describing such an effect into the matrix element was investigated. Thus the following parameterisations of the $K_1^oK_1^o$ threshold region were tried.

E) a Breit-Wigner function

F) a Jackson function with s = 0. The decay

angular distribution (cos Θ of one K_1^o with respect to the line of flight of the $K_1^oK_1^o$ system) for events in the $K_1^oK_1^o$ threshold region ($1020 < M(K_1^oK_1^o) < 1070$ MeV) and with $\bar{p}p \rightarrow K^* \bar{K}^*$ events removed, was fitted with zero and fourth order polynomials. Though the fourth order polynomial gave the better χ^2 ($\chi^2 = 6.0/4$), the fit with the zero order polynomial could not be ruled out ($\chi^2 = 15.5/7$). Fig.5K shows the distribution. (It was later checked that a Jackson function with s = 2 in the likelihood fits gave similar results).

G) a scattering length function. In preliminary fits, a complex scattering length was tried in addition to a real scattering length. However, the complex part became so small ($\lesssim$ 0.00001 fm) that the complex scattering length fits were discontinued.

Table 5.8 lists the results of these fits.

Fit	log $\mathcal{L}$	Δ	$\langle\Delta\rangle$
D	237.81	-	-
E	252.09	28.56	3.0
F	252.09	28.56	3.0
G	250.56	25.50	2.0

Table 5.8 Results of including a $K\bar{K}$ threshold effect in the matrix element

Each fit shows a significant improvement in the likelihood function. For example, for Fit E the

probability is less than 0.001% that the improvement is statistical. Hence the above results endorse the presence of a channel $\bar{p}p \rightarrow (K\bar{K})_{th}\ \pi^+\pi^-$. It will be recalled that if D_1 and D_2 are two separate hypotheses for the same physical phenomenon, then if $\triangle = 2(\log D_2 - \log D_1)$ is greater than 4, hypothesis D_2 is more favourable than D_1 at a 5% confidence level. Computing twice the difference in $\log \mathcal{L}$ values between resonance interpretations (Fits E, F) and the scattering length interpretation shows the data are unable to discriminate between these interpretations for the $K_1^oK_1^o$ threshold effect. However, in the study of the 5-body reaction $\bar{p}p \rightarrow K_1^oK_1^o\pi^+\pi^-(\pi^o)$ at 1.2 GeV/c, the $K_1^oK_1^o$ threshold enhancement is produced more strongly (15%) and it was possible to exclude the scattering length interpretation in favour of the resonance one at a 1% confidence level.[5] Moreover, the decay angular distribution of this peak was well fitted by a zero order polynomial and no improvement was gained by adding up to fourth order terms. The predictions of Fits E and G on the $K_1^oK_1^o$ effective mass plot are given in Fig.5L.

In the study of this reaction at 0.7 GeV/c, evidence was found for the production of the f^o (1260) and f'(1514) resonances.[4] Inspection of Fig.5L shows that there appears to be a small excess of events in the region $M(K_1^oK_1^o) \sim 1514$ MeV, which may correspond to the $K_1^oK_1^o$ decay of the f'meson, and a small excess in the region $M(K_1^oK_1^o) \sim 1260$ MeV which could possibly correspond to the f^o meson. To test the significance of these effects, two

more likelihood fits were performed on the data, in which these resonances were successively added to the matrix element. The results of these fits taking Fit E as a basis are given in Table 5.9.

Fit	log $\mathcal{L}$	Δ	$\langle\Delta\rangle$
E	252.09	-	-
H	252.63	1.08	1.0
I	254.98	4.70	1.0

Table 5.9 Results of adding f^o and f' mesons to the matrix element

From the above results, the probability associated with the purely statistical increase in log $\mathcal{L}$ for Fit H(f^o) is of the order of 30% and so the presence of the f^o in this reaction should be considered doubtful. For Fit I (f' included), the probability for an increase in Δ of 4.70 when an increase of 1.0 was expected is 3%. Thus the channel $\bar{p}p \rightarrow f'\pi\pi$ is a borderline case.

Table 5.10 lists the fractions of the resonances obtained from Fit I together with the χ^2 evaluated on the experimental mass plots. The predictions of this fit are given in Fig.5M.

Resonance	Fraction	Distri-bution	χ^2 for Phase Space	χ^2 for Fit I	No of bins
ρ^0	30 ± 3%	$\pi\pi$	186.4	50.8	35
$K^{*\pm}$	30 ± 3%	$K\pi$	394.4	47.7	37
$K^*\bar{K}^*$	21 ± 2%	$K\bar{K}$	56.4	31.4	30
A_2^0	5 ± 3%	$K\pi\pi$	76.2	32.0	33
S^*	7 ± 1%	$K\bar{K}\pi$	154.3	41.0	34
f^0	4 ± 2%				
f'	3 ± 1%	Totals	867.7	202.8	169

Table 5.10 Results of Fit I

Similar results for the inclusion of the f^0 and f' mesons were obtained when Fits F and G were used as a basis. The values of $\log \mathcal{L}$ and the parameters of the $K_1^0K_1^0$ threshold enhancement for these final fits are summarised below.

Breit-Wigner form: $\log \mathcal{L} = 254.98$, S^* fraction $= 7 \pm 1\%$

$M_{S^*} = 1038^{+5}_{-8}$ MeV, $\Gamma_{S^*} = 44^{+18}_{-12}$ MeV

Jackson form: $\log \mathcal{L} = 253.55$. S^* fraction $= 6 \pm 2\%$

$M_{S^*} = 1043^{+5}_{-4}$ MeV, $\Gamma_{S^*} = 36^{+40}_{-14}$ MeV

Scattering length form: $\log \mathcal{L} = 252.32$, fraction $= 12 \pm 5\%$

$a = 2.6 \pm 1.7$

These results imply that now it is just possible to distinguish between the Breit-Wigner and scattering length interpretations in terms of differences in $\log \mathcal{L}$. This may, however, be due to slight inaccuracies in

interpolating the normalisations of the threshold enhancements and is being investigated further. It is interesting to calculate the expected f^o cross-section using data from other sources. From work on the reaction $\bar{p}p \rightarrow 4\pi$ at 1.2 GeV/c, it was found that $\sigma(f^o \rightarrow \pi\pi) = 0.30 \pm 0.13$mb.[6] Also, the branching ratio $f^o \rightarrow K\bar{K} / f^o \rightarrow \pi\pi$ is of order 6.3%![7] From these numbers it is possible to predict that $\sigma(f^o \rightarrow K_1^o K_1^o)$ at 1.2 GeV/c should be approximately 5 ± 2 μb. This compares with the value from Fit I of 8 ± 4 μb. These values are of the same order but the uncertainties involved make it difficult to draw any conclusions. For the f', there is no evidence for another decay mode at 1.2 GeV/c except $f' \rightarrow K^* \bar{K}$ (reaction III). However the ratio $f' \rightarrow K\bar{K} \,/\, f' \rightarrow K^* \bar{K}$ is very badly determined[7] and so again nothing conclusive can be said.

Summary

The study of the reaction $\bar{p}p \rightarrow K_1^o K_1^o \pi^+ \pi^-$ at 1.2 GeV/c has shown evidence for the copious production of the ρ (30%) and K^* resonances. The K^* production enters for more than 50% of the total, including 21% of the 2-body annihilations $\bar{p}p \rightarrow K^* \bar{K}^*$. The data do not give an unambiguous solution to the $K_1^o K_1^o$ threshold problem. For the resonance interpretations, though the values for the mass and width are smaller than found in other interactions, they are fairly compatible with values found in previous annihilation experiments. For the scattering length solution, this may correspond to the $I_3 = 0$ component of the $I = 1$ enhancement observed at the $K_1^o K^{\pm}$ threshold. There may of course be a combination of

scattering length and Breit-Wigner amplitudes. Better statistics and a more complete matrix element are needed to resolve the problem. The f^o- A_2 region is not completely described. This may be due to some f^o- A_2 interference which has not been taken into account.

IV The reaction $\bar{p}p \rightarrow K_1^o(K^o)\pi^+\pi^-$

Since a K_1^o may escape detection by decaying via $\pi^+\pi^-$ outside the volume of observation or via $\pi^o\pi^o$ anywhere, and since the long lifetime of the K_2^o prevents its frequent observation, the $K^o\bar{K}^o\pi^+\pi^-$ annihilations with only one K_1^o observed — $K_1^o(K^o)\pi^+\pi^-$ events — are a mixture of $K_1^oK_1^o\pi^+\pi^-$ and $K_1^oK_2^o\pi^+\pi^-$ final states.

The knowledge of the branching ratio of the K_1^o meson allows an estimate to be made of the number of events in these two reactions. To a first approximation, without the V^o weighting factors correcting for the finite size of the chamber, the number of $K_1^oK_1^o\pi^+\pi^-$ events in the $K_1^o(K^o)\pi^+\pi^-$ reaction is equal to the number of events where both K_1^o's are observed, reaction III. For taking the branching ratio into 2 charged pions as $^2/_3$, then starting with the production of two K_1^o's, the probability of observing both decays simultaneously is $^4/_9$ (i.e the product of the probabilities of each K_1^o being observed separately); and the probability of seeing either one is $^4/_9$ i.e. $2 \times {}^2/_3$ (probability of seeing $1^{\underline{st}}$ K_1^o) $\times$ $^1/_3$ (probability of not seeing $2^{\underline{nd}}$ K_1^o) = $^4/_9$. Thus the number of $K_1^oK_1^o\pi^+\pi^-$ events in the reaction $K_1^o(K^o)\pi^+\pi^-$ is equal to the number of events in reaction III. The $K_1^oK_2^o\pi^+\pi^-$ spectra can be obtained therefore by the suitable subtraction of the spectra of reaction III from the $K_1^o(K^o)\pi^+\pi^-$ spectra.

Fig.5N shows the 2- and 3-body mass distributions for the $K_1^o(K^o)\pi^+\pi^-$ reaction. In addition to effects coming from the $K_1^oK_2^o\pi^+\pi^-$ component, this reaction should

contain the same resonances as were found for reaction III. Strong production of the $K^*(892)$ resonance can be observed, while the ρ meson is also apparent. An effect of the $K_1^oK_2^o\pi^+\pi^-$ component is readily seen at the $K\bar{K}$ threshold where the $\phi(1019)$ meson is clearly produced. The natural width of the ϕ is of the order of 4 MeV[1]. Fig.50 shows the $(K^o\pi)^+$ versus $(K^o\pi)^-$ and K^oK^o versus $\pi^+\pi^-$ scatter plots. The former shows a high density of events in the $K^{*+}K^{*-}$ region. The 3-body mass plots show no strong features except for a general distortion from phase space.

A likelihood fit was made to this reaction and the matrix element was constructed as follows.
The reaction $\bar{p}p \longrightarrow K^o\bar{K}^o\pi^+\pi^-$ consists of three distinct modes, viz. $\bar{p}p \longrightarrow K_1^oK_1^o\pi^+\pi^-$, $K_1^oK_2^o\pi^+\pi^-$, $K_2^oK_2^o\pi^+\pi^-$. The last reaction is not observed as both K_2^o's go unseen. Using the experimental branching ratio of the K_1^o(=0.687[1]), then the probability of observing a $K_1^oK_1^o\pi^+\pi^-$ event (where one of the K_1^o's decays via the neutral mode) is $2 \times 0.687 \times (1.- 0.687) = 0.430$, while the probability of observing a $K_1^oK_2^o\pi^+\pi^-$ event is 0.687. Thus the matrix element, appropriately normalised, to be used in the fits can be written

$$= \frac{\frac{1}{2} \times 0.430 \times W_a}{(\frac{1}{2} \times 0.430 \times W_a + 0.687 \times W_b)} \times (1. - \sum_i f_i + \sum_i f_i N_i P_i)$$

$$+ \frac{0.687 \times W_b}{(\frac{1}{2} \times 0.430 \times W_a + 0.687 \times W_b)} \times (1. - \sum_j f_j + \sum_j f_j N_j P_j)$$

In the above expression f_i, N_i and P_i represent the fractions, normalisations and parameterisations respectively of the appropriate resonances. The first term

refers to the reaction $\bar{p}p \rightarrow K_1^0 K_1^0 \pi^+ \pi^-$ and the second term to the reaction $\bar{p}p \rightarrow K_1^0 K_2^0 \pi^+ \pi^-$. The factor $^1/2$ is included to take into account the fact that only $K_1^0 K_1^0 \pi^+ \pi^-$ (but not $K_2^0 K_2^0 \pi^+ \pi^-$) is observable, while the factors W_a and W_b represent the weights of the reactions $\bar{p}p \rightarrow K_1^0 K_1^0 \pi^+ \pi^-$ and $\bar{p}p \rightarrow K_1^0 K_2^0 \pi^+ \pi^-$ present. A priori, there is no information about the weights of the $K_1^0 K_1^0 \pi^+ \pi^-$ and $K_1^0 K_2^0 \pi^+ \pi^-$ events present in the $K_1^0(K^0)\pi^+\pi^-$ sample. Therefore in order to study the reaction $K_1^0(K^0)\pi^+\pi^-$ and in particular the $K_1^0 K_2^0 \pi^+ \pi^-$ component, it was assumed that W_a was equal to W_b. The ability of the above matrix element to describe the $K_1^0(K^0)\pi^+\pi^-$ mass plots will be a test of this assumption.

Thus the likelihood function for this reaction is composed of two distinct parts:

a) that corresponding to the reaction $\bar{p}p \rightarrow K_1^0 K_1^0 \pi^+ \pi^-$

b) that corresponding to the reaction $\bar{p}p \rightarrow K_1^0 K_2^0 \pi^+ \pi^-$

The parameters for parts a) and b) were alternatively kept fixed and free, respectively in a series of iterations to arrive at the best fit.

As a first step, the following channels were successively introduced to part b) in addition to the phase space contribution.

A) $\bar{p}p \rightarrow K_1^0 K_2^0 \rho^0$ — ρ^0 production

B) $\bar{p}p \rightarrow K^{*+} K^0 \pi^-$, $K^{*-} K^0 \pi^+$ — K^* production

C) $\bar{p}p \rightarrow K^{*+} K^{*-}$ — associated K^* production

D) $\bar{p}p \rightarrow \pi^+ \pi^- \phi$ — ϕ production.

The channels obtained from the fit (Fit I) to reaction III were assumed to contribute to part a) and the starting

values of the parameters for part a) were those obtained from that fit. These parameters were kept fixed at the starting values while $K_1^oK_2^o\pi^+\pi^-$ channels were introduced. Table 5.11 presents the results of these likelihood fits.

Fit	log $\mathcal{L}$	Δ	$\langle\Delta\rangle$
Phase Space $+K_1^oK_1^o\pi^+\pi^-$ contribution	287.60	—	—
A	296.41	17.62	1.0
B	574.11	555.40	1.0
C	627.69	107.16	1.0
D	678.63	101.88	3.0

Table 5.11 Results of the $K_1^oK_2^o\pi^+\pi^-$ contribution to the $K_1^o(K^o)\pi^+\pi^-$ matrix element

If the improvements in the above log $\mathcal{L}$ values are merely due to the increased number of parameters, then the probabilities that the above Δ's result are all less than 0.003%. Thus the $K_1^oK_2^o\pi^+\pi^-$ channels are reasonably justified.

The parameters for parts a) and b) were then alternatively kept fixed and free and the likelihood function was allowed to iterate to its best value. However, in the $K_1^oK_1^o\pi^+\pi^-$ component, the fraction of S^* was much reduced compared to the value found in reaction III and a determination of the mass and width was not possible. These parameters were therefore fixed at the values given

by reaction III. (M = 1038 MeV, Γ = 44 MeV). The results of the final fit are given in Table 5.12 and the projections are drawn on Fig.5N. Table 5.13 gives the χ^2 comparison between phase space and the final fit for these diagrams.

Part b) $K_1^oK_2^o\pi^+\pi^-$		Part a) $K_1^oK_1^o\pi^+\pi^-$	
Resonance	Fraction	Resonance	Fraction
ρ^o	5 ± 2%	ρ^o	33 ± 7%
$K^{*\pm}$	47 ± 4%	$K^{*\pm}$	31 ± 10%
ϕ	6 ± 1%	S^*	0 ± 3%
$K^*\bar{K}^*$	23 ± 2%	$K^*\bar{K}^*$	21 ± 7%
		A_2^o	2 ± 4%
		f^o	0 ± 5%
		f'	3 ± 4%

Table 5.12 Results of the final maximum likelihood fit to $K_1^o(K^o)\pi^+\pi^-$

Distribution	χ^2 for Phase Space	χ^2 for Final Fit	No. of Bins
$\pi\pi$	131.1	54.1	40
$K\pi$	1236.2	55.8	39
$K\bar{K}$	82.9	35.0	36
$K\pi\pi$	67.8	54.7	38
$K\bar{K}\pi$	325.0	60.8	37
Totals	1843.0	260.4	190

Table 5.13 Results of a χ^2 comparison between phase space and the final fit to the reaction $K_1^o(K^o)\pi^+\pi^-$

Inspection of Table 5.12 shows that results obtained for the $K_1^oK_1^o\pi^+\pi^-$ component are comparable, within the errors, to those obtained for reaction III. An outstanding feature of the $K_1^oK_2^o\pi^+\pi^-$ component is the suppression of ρ production: $\bar{p}p \rightarrow K_1^oK_2^o\rho$, although no obvious selection rule forbids its production. (This result was also observed in data at 0.7 GeV/c[2]). The mass and width of the ϕ meson given by the fit were 1018 ± 1 MeV and 10 ± 2 MeV respectively. The mass plots are reasonably described by the given matrix element and the distortions in the 3-body spectra are adequately explained by the reflections of the given resonances.

Finally, a fit was made in which the weights W_a and W_b were allowed to vary. The values obtained were both of the order 0.99, with the fractions similar to those given in Table 5.12.

Summary

For the $K_1^oK_2^o\pi^+\pi^-$ component of the $K_1^o(K^o)\pi^+\pi^-$ reaction, abundant production of K^* is observed (about 70%, including 23% of $\bar{p}p \rightarrow K^*\bar{K}^*$). The ϕ meson ($M \sim 1019$ MeV, $\Gamma \sim 10$ MeV) is produced (6%) but the ρ production (5%) is suppressed compared with ρ production (33%) in $K_1^oK_1^o\pi^+\pi^-$. The values of the fractions obtained for the $K_1^oK_1^o\pi^+\pi^-$ component are comparable with those given for reaction III.

V The reaction $\bar{p}p \longrightarrow K_1^0 K_1^0 \omega^0$ ($\bar{p}p \longrightarrow K_1^0 K_1^0 \pi^+\pi^-(\pi^0)$)

As soon as the mass of a meson exceeds two nucleon masses and if it is coupled to the $\bar{p}p$ system, it is possible to study its properties in formation experiments via the reactions

$$\bar{p}p \longrightarrow \text{meson} \longrightarrow \bar{p}p$$
$$\longrightarrow \text{other states}$$

The total cross-section measurements of Abrams et al.[1] gave evidence for a possible direct channel resonance at a mass of 2190 MeV and width 85 MeV. The magnitude of this effect was of order 5mb. The missing mass spectrometer experiment of Chikovani et al.[2] also gave evidence for a resonance in this region ($M \sim 2195$ MeV) but the width was found to be less than 13 MeV. The large number of open channels in antiproton-proton interactions, however, makes a study of a direct channel effect via the total cross-section difficult and so, a priori. it is more promising to look for such an effect in one of the well-defined annihilation reactions. In this context, two reports have been presented which have tentatively given evidence for the formation of a resonance ($M \sim 2180$ MeV, $\sigma \sim 200\mu b$) in the reaction $\bar{p}p \longrightarrow K\bar{K}\omega^0$[3].

In view of the general interest aroused by these experiments, a preliminary study of the reaction $\bar{p}p \longrightarrow K_1^0 K_1^0 \pi^+\pi^-(\pi^0)$, in which the channel $\bar{p}p \longrightarrow K_1^0 K_1^0 \omega^0$ is present[4], has been made in the C.M. energy range 2.10 - 2.24 GeV (approximately corresponding to the 1.10 - 1.47 GeV/c experiments)

The data was divided into seven intervals of C.M.

energy in this range viz 2.10 - 2.12, 2.12 - 2.14 ··· 2.20 - 2.24 GeV in steps of 20 MeV and the cross-section for $\bar{p}p \longrightarrow K_1^o K_1^o \omega^o$ calculated for each of these intervals.

For the present study, the cross-section data for the reaction $\bar{p}p \longrightarrow K_1^o K_1^o \pi^+ \pi^- (\pi^o)$ given in Fig.3X has been used. These data however were calculated by ignoring the energy loss of the antiproton as it moved through the hydrogen. A study is presently going on in which this energy loss is being taken into account—at least for the 1.10 - 1.47 GeV/c experiments. However, the final errors are such that this approximation is reasonable. The data have been fitted by linear and quadratic variations using the χ^2 method. Both forms gave comparable fits (χ^2 = 10.5/5 and 9.7/4). These are shown in Fig.5P The cross-sections for $\bar{p}p \longrightarrow K_1^o K_1^o \pi^+ \pi^- (\pi^o)$ at momenta corresponding to the mid-points of the above energy intervals were read off from the straight-line graph. These values are given in Table 5.14 below.

In order to calculate the cross-sections for $\bar{p}p \longrightarrow K_1^o K_1^o \omega^o$ from the $\bar{p}p \longrightarrow K_1^o K_1^o \pi^+ \pi^- (\pi^o)$ cross-section, the fraction of the channel $\bar{p}p \longrightarrow K_1^o K_1^o \omega^o$ present in the reaction $\bar{p}p \longrightarrow K_1^o K_1^o \pi^+ \pi^- (\pi^o)$ must be known. To find this maximum likelihood fits were made to the $K_1^o K_1^o \pi^+ \pi^- (\pi^o)$ data in each of the seven C.M. energy intervals. The reaction $\bar{p}p \longrightarrow K_1^o K_1^o \pi^+ \pi^- (\pi^o)$ has been studied at 1.2 GeV/c and the following channels were found to be present.[4]

$$\bar{p}p \longrightarrow \rho^o \; K_1^o K_1^o (\pi^o) \qquad \text{— } \rho \text{ production}$$
$$\rho^\pm \; K_1^o K_1^o \; \pi^\mp$$

$\bar{p}p \longrightarrow K^{*\pm}K^{*\mp}(\pi^o)$ — $K^*\bar{K}^*$ production
$K^{*\pm}K^{*o}\pi^{\mp}$

$\bar{p}p \longrightarrow S^*\pi^+\pi^-(\pi^o)$ — S^* production

$\bar{p}p \longrightarrow \omega^o K_1^o K_1^o$ — ω^o production

$\bar{p}p \longrightarrow D^o\pi^+\pi^-$ — D^o production

$\bar{p}p \longrightarrow E^o\pi^+\pi^-$ — E^o production

In the likelihood fits to the seven energy intervals, these channels were assumed to contribute. The fraction of the channel $\bar{p}p \longrightarrow K_1^o K_1^o \omega^o$ in each of these intervals is given in Table 5.14.

The predictions of these fits on the $\pi^+\pi^-\pi^o$ mass plots are shown in Fig.5Q. The cross-section for $\bar{p}p \longrightarrow K_1^o K_1^o \omega^o$ is also given in Table 5.14 and Fig.5R.

Energy Interval GeV	Cross-section for $\bar{p}p \to K_1^o K_1^o \pi^+\pi^-(\pi^o)$ μb	Number of events	Fraction of $\bar{p}p \to K_1^o K_1^o \omega^o$ %	Cross-section for $\bar{p}p \to K_1^o K_1^o \omega^o$ μb
2.10-2.12	144.2	263	40±4	58±6
2.12-2.14	143.7	330	42±4	60±6
2.14-2.16	143.2	195	42±6	60±9
2.16-2.18	142.7	106	38±6	54±9
2.18-2.20	142.2	153	30±6	43±9
2.20-2.22	141.8	128	24±5	34±7
2.22-2.24	141.3	103	30±6	42±9

Table 5.14 Data for the reaction $\bar{p}p \longrightarrow K_1^o K_1^o \omega^o$
(The errors given on $\sigma(\bar{p}p \longrightarrow K_1^o K_1^o \omega^o)$ are errors from the maximum likelihood fits only)

Though Fig.5R shows an interesting variation, it is not possible in this preliminary study to say much because of the limited statistics. The data available show no significant enhancement in the region 2.16 - 2.20 GeV and a linear variation for $\sigma(\bar{p}p \rightarrow K_1^o K_1^o \omega^o)$ gives an acceptable fit. ($\chi^2 = 2.6/5$).

Obviously more data are required in this region before a thorough study can be completed. It would also be interesting to fill in the energy band corresponding to the momentum range 0.7 to 1.10 GeV/c. The momentum range 1.5 - 2.0 GeV/c is presently being examined.[5] Studies of other $\bar{p}p$ reactions in the energy region of 2180 GeV have produced interesting results, but none has given evidence for the formation of a direct channel resonance.[6]

Summary

A preliminary study of the reaction $\bar{p}p \rightarrow K_1^o K_1^o \omega^o$ shows that the limited data do not need the introduction of a direct channel effect.

References

Section I

1. Particle Data Group, Particle Properties (Jan 1971)
2. J. Duboc et al., "Analysis of $K\bar{K}$ and $K\bar{K}\pi$ Resonances Produced in $\bar{p}p$ Annihilations at 1.2 GeV/c", Kiev Conference report (1970)
   B. Makowski, private communication
3. J.D. Jackson, N.C. 34, 1644 (1964)
4. B. Conforto et al., Nucl. Phys. B3, 469 (1967)
5. P. Baillon et al., N.C. 50, 393 (1967)
6. J. Barlow et al., N.C. 50, 701 (1967)
7. Ch. D'Andlau et al., Phys. Lett. 17 347 (1964)
8. J. Vandermeulen, "Protonium Anninilation", Herceg-Novi lecture (1966)
9. J. Vandermeulen, op. cit.
   N. Barash et al., Phys. Rev. 139, B1659 (1965)
10. N. West, Ph.D. Thesis, Liverpool, (1970)

Section II

1. J. Barlow et al., op. cit.
2. N. West, op.cit.
3. P. Baillon et al., op. cit.
4. C. Zemach, Phys. Rev. 133, B1201 (1964)
   Phys. Rev. 140, B97 (1965)
   Phys. Rev. 140, B109 (1965)

Section III

1. J. Barlow et al., op. cit.
2. G. Alexander et al., Phys. Rev. Lett. 9, 460 (1962)

D.J. Crennell et al., Phys. Rev. Lett, 16, 1025 (1966)

R.J. Hess et al., Phys. Rev. Lett. 17, 1109 (1966)

W. Beusch et al., Phys. Lett. 25B, 357 (1967)

T.F. Hoang et al., Phys. Rev. Lett. 21, 316 (1968)

J. Alitti et al., Phys. Rev. Lett. 21, 1705 (1968)

3. C. Whitehead et al., N.C. 53A, 1057 (1968)

D.H. Miller et al., Phys. Rev. Lett. 21, 1469 (1968)

D.H. Miller et al., Phys. Lett. 28B, 51 (1968)

4. M. Aguilar - Benitez et al., Phys. Lett. 29B, 241 (1969)

5. J. Duboc et al., op. cit.

B. Makowski, private communication

6. R.S. Moore, Ph.D. Thesis, Liverpool, 1968

7. Particle Data Group, Particle Properties.

Section IV

1. Particle Data Group, Particle Properties.

2. M. Aguilar - Benitez et al., Nucl. Phys. B14, 195 (1969)

Section V

1. R.J. Abrams et al., Phys. Rev. Lett. 18, 1209 (1967)

2. G. Chikovani et al., Phys. Lett. 22, 233 (1966)

3. W.A. Cooper et al., Communication to Vienns Conference (1968)

W.A. Cooper et al., Bull. Am. Phys. Soc. 13, 1441 (1968)

M. Baubillier et al., Communication to Lund Conference (1969)

4. J. Duboc et al., op. cit.

B. Makowski, private communication.

5. R.A. Donald, D.N. Edwards, private communication

6. J.K. Gibbins, M.A. Houlden, D.C. Howard, Ph.D. Theses, Liverpool, 1971.

CHAPTER 6

APPLICATION OF A VENEZIANO MODEL TO THE REACTION $\bar{p}p \longrightarrow K_1^o K^{\pm} \pi^{\mp}$

I INTRODUCTION AND THEORY OF THE VENEZIANO MODEL

II APPLICATION TO THE REACTION $\bar{p}p \longrightarrow K_1^o K^{\pm} \pi^{\mp}$

I. Introduction and theory of the Veneziano Model

The theoretical description of multiparticle reactions is one of the most important tasks of present-day hadron physics. From the intense amount of work put into the subject a qualitative picture of the 2-hadron collision amplitude has evolved. This amplitude has supposedly the following properties:[1]

a) analyticity: if collision amplitudes are derived from potential theory or from quantum field theory, it is found that they are analytic functions of certain physical parameters. In the relativistic case these parameters are the Mandelstam invariants s,t,u (the Mandelstam Hypothesis[2]). The analytic behaviour of collision amplitudes plays a major role both in establishing results at high energies and providing a basis for approximation procedures.

b) crossing symmetry: This is perhaps most easily described with the Mandelstam variables.[2] Consider the reaction $1 + 2 \longrightarrow \bar{3} + \bar{4}$ for particles of mass m, with respective 4-momenta p_1, p_2, p_3 and p_4 (taken as ingoing). The Mandelstam variables are defined as (see Fig.6A)

$$s = (p_1+p_2)^2 = (p_3+p_4)^2 \qquad (6\text{-}1)$$

$$t = (p_2+p_3)^2 = (p_1+p_4)^2 \qquad (6\text{-}2)$$

$$u = (p_2+p_4)^2 = (p_1+p_3)^2 \qquad (6\text{-}3)$$

with $s + t + u = 4m^2$. The reaction corresponding to particles 1 and 2 in the initial state. (and its CPT conjugate with particles 3 and 4 in the initial state) is called the s-channel. This name derives from the fact that s is the square of the C.M. energy in this channel. Thus

$$s = 4(q^2+m^2) \qquad (6\text{-}4)$$

$$t = -2q^2(1-\cos\Theta) \qquad (6\text{-}5)$$

$$u = -2q^2(1+\cos\Theta) \qquad (6\text{-}6)$$

where q is the 3-momentum and Θ the scattering angle in the s-channel C.M. system. The physical region for the s-channel is characterised by $s \geqslant 4m^2$, $t \leqslant 0$, $u \leqslant 0$. The t- and u- channels are defined similarly. If an amplitude describing an s-channel process is continued (extrapolated) into the region $s \leqslant 0$, $u \leqslant 0$, $t \geqslant 4m^2$ (i.e. the physical region of the t-channel) for example, then the principle of crossing symmetry asserts that this amplitude will describe the t-channel process i.e. the interaction in the s-channel and those in the t and u channels are described by the same analytic function. The continuation of an s-channel amplitude into the t-channel, for example, is called "crossing" and the t- and u- channels are then called the "crossed" channels.

c) low energy resonance contributions: in the range of C.M. energies below approximately 2 GeV, cross-sections typically present the appearance indicated in Fig.6B. This behaviour may be understood in terms of a few partial waves dominated by resonance contributions. The amplitude of this low energy behaviour may be written as

$$A(s,t) = \sum A_J^s(s,t)$$

where $$A_J^s(s,t) = (2J+1)\, f_J P_J(\cos\Theta) \qquad (6\text{-}7)$$

and $$f_J = \frac{m_r \Gamma_r}{m_r^2 - s - i\, m_r \Gamma_r} \qquad (6\text{-}8)$$

for a resonance of mass m_r, width Γ_r and spin J.

d) Regge asymptotic behaviour:[3] above C.M. energies of about 5 GeV, the variation of cross-section with energy is far smoother than in the low energy range and a different parameterisation is used to describe the amplitude. A basic feature of these high energy reactions is that they have a peripheral nature i.e. $d\sigma/d\Omega$ is peaked near $\cos\theta = \pm 1$. This forward (backward) peaking near $t = 0$ ($u = 0$) suggests that the amplitude may be dominated by singularities which occur near $t = 0$ ($u = 0$) but in the kinematically forbidden region of t and u. Therefore, if the t-channel contains a singularity near $t = 0$ at a value of t which is non-physical for the s-channel, such that the t-channel amplitude has a maximum, it might be expected that the analytically continued s-channel amplitude will be dominated by the t-channel singularity for small values of $|t|$. Thus these reactions are studied in terms of t-(or u-) channel parameters. For example, for the reaction $\pi^- p \rightarrow \pi^0 n$, $d\sigma/dt$ was fitted to an equation of the form $d\sigma/dt = f(t)s^{2\alpha(t)-2}$ with $\alpha(t) = \alpha_o + \alpha' t$. When $\alpha(t)$ was extrapolated from $t < 0$ (s-region) into the unphysical s-region, $t > 0$, $\alpha(t)$ was found to pass through positive integral values $\alpha(t_o) = 0 \cdots \alpha(t_J) = J$ and these values corresponded to known particles of spin J and mass $m_J^2 = t_J$. (see Fig.6c). Thus the t-channel singularities appear not to be fixed in the J-plane but move in such a way that, when projected into the region $t > 0$, they intercept integer values of J which correspond to the physical resonances which can be exchanged in the t-channel. This concept of moving poles

was demonstrated in potential scattering by Regge[5] and extended to high energy interactions by Chew and others.[6] The resulting model is known as the Regge-pole model.

In this model, it is assumed that the amplitude which describes peripheral processes is dominated by a crossed-channel singularity which moves in the J-plane. The locus of these poles is described by $\alpha(t)$ (or $\alpha(u)$) which is called the Regge trajectory. Each trajectory possesses a definite set of quantum numbers such as isospin, parity,etc. For a specific reaction, $\alpha(t)$ for $t \leqslant 0$ determines the s-channel scattering and when $\alpha(t)$ is extended to $t > 0$, it intercepts integer (for mesons) or half-integer (for baryons) values of α at $t = t_R$, where t_R is the mass squared of resonances having the quantum numbers of the crossed channel. The concept of signature[4] actually limits the poles to appear in steps of $\Delta J = 2$. Thus a high energy s-channel process can be regarded as the exchange of virtual "particles" in the t-channel. From the theory of complex angular momentum[7], the Regge amplitude for large s is given by

$$A^t(s,t) = \frac{\beta(t)}{\Gamma(\alpha + 1)\sin \pi\alpha(t)} s^{\alpha(t)} \quad (6\text{-}9)$$

From this it can be shown that $d\sigma/dt \sim s^{2\alpha(t)-2}$

e) duality: using finite energy sum rules (FESR), Dolen, Horn and Schmid[8] showed that an amplitude describing high energy behaviour, due to t-channel exchanges, if analytically continued to the low energy region, will show the s-channel resonance behaviour.[9] This property is known as duality — s-channel resonances and t-channel Regge poles

appear as two complementary ways to describe the amplitude.

f) unitarity: reactions are connected via unitarity— even the simplest 2-body collision is strongly influenced by what happens in the many-particle channels.

g) Pomeron contribution: as far as is known the reactions which are dominated by Pomeron exchange (e.g. elastic pp and K^+p scattering) do not contain s-channel resonances. Thus the effective Pomeron trajectory cannot be built up from resonances as are normal Regge trajectories. Indeed, it is found that the Pomeron trajectory has little in common with the other trajectories, and so the Pomeron is thought to be really something outside the framework of duality. In such reactions that contain parts due to vacuum exchanges and ordinary Regge exchanges, the amplitude is thought to be a superposition of the respective Regge and Pomeron amplitudes.

No one has yet put forward a function which satisfies all of the above stringent conditions. However, in 1968, Veneziano[10] proposed a model which did satisfy conditions a) $\longrightarrow$ e).

Considering the scattering of scalar, neutral mesons, Veneziano wrote down the following amplitude

$$T_4 = \beta \left[V(1234) + V(2134) + V(2314) \right] \qquad (6\text{-}10)$$

with constant β and with

$$V(1234) = B_4(-\alpha_{12}, -\alpha_{23}), \text{ etc.} \qquad (6\text{-}11)$$

$$B_4(x,y) = \int_0^1 du\, u^{x-1} (1-u)^{y-1} = \frac{\Gamma(x)\,\Gamma(y)}{\Gamma(x+y)} \qquad (6\text{-}12)$$

where $\alpha_{12} = \alpha_{34} = \alpha_0 + \alpha' s_{12}$ are Regge trajectories with intercept α_0 and slope α' and $s_{12} = (p_1+p_2)^2 \equiv s$, $s_{23} = (p_2+p_3)^2 \equiv t$, etc. (see Fig. 6D)

The properties of this amplitude may be found with the following properties of the Γ function.

1) $\Gamma(Z)$ is analytic in Z on the whole complex Z plane except for poles at Z =0, -1, -2,··.(for example, see Fig.6E[11]). Also $\Gamma(Z)$ has no zeros anywhere.

2) as $Z \to \infty$, $\Gamma(Z) \sim Z^Z$

Thus it can be noted in particular that:

a) B_4 as defined in (6-12) is symmetric in x and y, which by (6-11) implies V(1234) is invariant under cyclic and anticyclic permutations of the external lines. The $4! = 24$ permutations of $p_1 \cdot\cdot p_4$ are thus divided into three $(24/(4+4)=3)$ classes – the three terms in (6-10) corresponding to the three possible non-equivalent orderings of the external lines. The symmetry properties of B_4 thus imply that the amplitude T_4 is completely crossing symmetric.

b) V(1234), being a ratio of Γ's, must be analytic except possibly where the Γ functions in the numerator have poles i.e. at $\alpha_{12} = 0, 1, 2, \cdot\cdot$ and $\alpha_{23} = 0,1, 2,\cdot\cdot$. It does not have double poles, since when α_{12} and α_{23} are both non-negative integers, the denominator $(-\alpha_{12} - \alpha_{23})$ also has a pole to cancel it. Similarly for V(2134) and V(2314) and so for T_4.

B_4 can be expanded as a sum of poles in $\alpha_{12} \equiv \alpha(s)$

$$B_4(\alpha(s)) = \sum_{J=0}^{\infty} \frac{\Gamma(J+1+\alpha(t))}{J!\,\Gamma(1+\alpha(t))} \frac{1}{J-\alpha(s)} \qquad (6\text{-}13)$$

and similarly in terms of poles in $\alpha_{23} \equiv \alpha(t)$. The residue at the pole $\alpha(s) = J$ is

$$R_J(\alpha(t)) = \frac{\Gamma(J+1+\alpha(t))}{J!\,\Gamma(1+\alpha(t))}$$

$$= \frac{1}{J!} \left(\alpha(t)+J\right)\left(\alpha(t)+J-1\right)\cdots\left(\alpha(t)-1\right) \qquad (6\text{-}14)$$

Thus the residue of the pole in B_4 at $\alpha(s) = J$ is a polynomial in $\alpha(t)$ of degree J and so a polynomial in t. It can be decomposed into a series of Legendre polynomials of degree J, J-1, ·· 0 and so the pole at $\alpha(s) = J$ is thus associated with a family of resonances of spin $1 \leqslant J$.(see Fig.6F)

c) To investigate the asymptotic s behaviour of the amplitude for fixed t, consider, for example, the term

$$B_4(-\alpha(s),-\alpha(t)) = \frac{\Gamma(-\alpha(s))\,\Gamma(-\alpha(t))}{\Gamma(-\alpha(s)-\alpha(t))}$$

Then as $s \longrightarrow \infty$, it is possible to write

$$B_4(-\alpha(s),-\alpha(t)) \approx (-\alpha(t))\,(-\alpha(s))^{\alpha(t)}$$

Using $\Gamma(Z)\,\Gamma(1-Z) = \frac{\pi}{\sin \pi Z}$

it follows that $\Gamma(-\alpha(t)) = \frac{-\pi}{\Gamma(1+\alpha(t))\sin \pi\alpha(t)}$

$$\text{so } \lim_{s\to\infty} B_4(-\alpha(s),-\alpha(t)) \approx \frac{-\pi}{\Gamma(1+\alpha(t))} \cdot \frac{(-\alpha(s))^{\alpha(t)}}{\sin \pi\alpha(t)}$$

Also using $\alpha(s) \approx s$ as $s \longrightarrow \infty$

$$\text{then } \lim_{s\to\infty} B_4(-\alpha(s),-\alpha(t)) \approx \frac{-\pi(-1)^{\alpha(t)}}{\Gamma(1+\alpha(t))} \cdot \frac{s^{\alpha(t)}}{\sin \pi\alpha(t)}$$

This is of the form of the usual Regge expression (6-9)

Having shown the Regge behaviour and also the existence of resonance poles in the amplitude, duality automatically follows, since the same function has been shown explicitly to contain both low energy resonance and high energy Regge behaviour.

There are however various shortcomings of the

Veneziano amplitude which may be enumerated as follows.

a) the Pomeron is not included in the model. So far no satisfactory solution for its inclusion has been put forward.

b) the amplitude is not unitary. This arises because the trajectories are real and so the amplitude has poles only on the real axis. A unitary amplitude should have cuts corresponding to thresholds of elastic and inelastic channels while its poles corresponding to resonances should move off the real axis. For phenomenological purposes, the effects of unitarity are simulated by artificially introducing an imaginary part to the trajectory function $\alpha(s)$.

$$\alpha(s) = \alpha_o + \alpha' s + i\,\Theta(s-s_{th}).\ \mathrm{Im}\,\alpha(s) \qquad (6\text{-}15)$$

where Θ is a step-function to ensure the imaginary part of the trajectory is zero below the threshold s_{th} for the 2-particle state to which it couples. Near $s = m_r^2$, $\alpha_o + \alpha' m_r^2 = n$ so (c.f. equation (6-13))

$$\frac{1}{n-\alpha(s)} = \frac{1}{n-\alpha_o-\alpha' s - i\ \mathrm{Im}\,\alpha(s)} = \frac{1/\alpha'}{m_r^2 - s - i(1/\alpha')\,\mathrm{Im}\,\alpha(s)}$$

Comparing this with (6-8), it can be seen that Im(s) may be determined by

$$\mathrm{Im}\,\alpha(m_r^2) = \alpha' m_r \Gamma_r \qquad (6\text{-}16)$$

This leads to a convenient representation of Im $\alpha(s)$ viz. Im $\alpha(s) = k(s-s_{th})$ where k is a constant chosen that the first few resonances above threshold on the trajectory have approximately the correct width.

This trick moves the poles of (6-12) off the real axis, but now the residues will not in general be

polynomials in $\cos\theta$ and ancestor states (states with spin $l > J$) arise.

c) it is possible to replace $B_4(x,y)$ by

$$\tilde{B}_4(x,y) = \int_0^1 du\ f(u)u^{x-1}\ (1-u)^{y-1}$$
$$= \sum_{m=0}^{\infty} \sum_{n=0}^{\infty} \beta_{mn}\ B_4(x+m,y+n) \qquad (6\text{-}17)$$

(where m and n are integers) and not alter the properties of the Veneziano amplitude, provided $f(u) = f(1-u)$ and $f(u)$ is well-behaved at $u = 0$ and 1. The series in (6-17) contains $B_4(x,y)$ as the first term; the absence of the higher ("satellite") terms in (6-11) is thus only a hopeful assumption.

d) the model makes no provisions for the spin and isospin of the external particles. A related problem is how to incorporate baryons into the model.

In spite of these difficulties the Veneziano model has met with an enthusiastic response and much effort is being made to try to overcome these problems.

Accordingly the model has been generalised to processes with any number of external lines.[12] In this context is the Veneziano amplitude for 3-particle final states. It was found by Bardakci and Ruegg[13] and independently by Virasoro[13] that there was an essentially straightforward generalisation of the amplitude to 5-particle reactions ($1+2 \rightarrow 3+4+5$). In analogy with the 4-particle case, the amplitude is written as a sum of terms over all permutations of the five external lines.

$$T_5 = \sum_{1,2,3,4,5} V(12345) \qquad (6\text{-}18)$$

Introducing the generalised Mandelstam variables

$$s_{12} = (p_1+p_2)^2 = (p_3+p_4+p_5)^2$$

$$s_{23} = (p_2+p_3)^2 = (p_4+p_5+p_1)^2 \text{ etc,}$$

V(12345) for the scattering of scalar, neutral mesons is defined as

$$V(12345) = \beta B_5(-\alpha_{12},-\alpha_{23},-\alpha_{34},-\alpha_{45},-\alpha_{51}) \qquad (6\text{-}19)$$

where $\alpha_{ij} = \alpha_o + \alpha' s_{ij}$ and $B_5(x_1,x_2,x_3,x_4,x_5)$

$$= \int_0^1\int_0^1 du_2 du_4 (1-u_2)^{x_1-1} u_2^{x_2-1} (1-u_2u_4)^{x_3-x_1-x_5} u_4^{x_4-1} (1-u_4)^{x_5-1}$$

In the above, u_i are generalisations of the integration variable u in (6-12). They are called conjugate variables to the x_i, and satisfy the following constraints:

$$u_i = 1-u_{i-1}u_{i+1}, \quad i=1,\cdots 5, \quad u_6 \equiv u_1$$

The function B_5 is called the generalised beta-function of the fifth order, and bears a close resemblance to the ordinary beta-function given in (6-12). It is possible to show that B_5 satisfies all requirements of the Veneziano model.[14] In particular, as with B_4, B_5 is required to be invariant under cyclic or anticyclic permutations of the external lines. The number of non-equivalent permutations is thus $5!/5.2 = 12$.

II Application to the reaction $\bar{p}p \rightarrow K_1^0 K^{\pm} \pi^{\mp}$

The first application of the five-point function B_5 was made by Petersson and Tornqvist to the reaction $K^-p \rightarrow \pi^+\pi^-\Lambda^0$.[15] The success of this work led Chan, Raitio, Thomas and Tornqvist[16] to extend the model and they wrote down an amplitude to describe (in principle) the reactions

$$K^+p \rightarrow K^0\pi^+p \qquad (1)$$

$$K^-p \rightarrow \bar{K}^0\pi^-p \qquad (2)$$

$$\pi^-p \rightarrow K^0K^-p \qquad (3)$$

$$\bar{p}p \rightarrow K^0K^-\pi^+ \qquad (4)$$

which are related by crossing.

Some qualitative features of these reactions are known. From the analysis of K^* production in reactions (1) and (2) at high energy, it is found that the Pomeron contribution is suppressed and that the reactions are dominated by "ω exchange". Ignoring any Pomeron contribution, Chan et al. made the assumption that a reasonable description of the above reactions would be given by a vector exchange model. This is only an approximation and any possible "π exchange" is neglected. Moreover, since there is no reliable method for dealing with fermions, these are dealt with in a very approximate fashion and treated as bosons.

Essentially the amplitude is written as a five-point function B_5 multiplied by a kinematic factor K and the expression is summed over all 12 non-cyclic permutations of the external particles represented by the graph of Fig.6G.

$$A = \sum_{\text{perm}}^{12} K.B_5 \qquad (6\text{-}20)$$

The lines are taken as ingoing for convenience. Now the arguments of B_5 are given in terms of the Regge trajectories of the corresponding resonances between neighbouring pairs of external lines in each graph (recall (6-19)). However because of the quantum numbers, many of the graphs obtained by permuting the external lines give rise to "exotic" resonances e.g. the K^+p combination. The terms in the amplitude representing such graphs can to a first approximation be neglected. Excluding such cases, only four terms remain in (6-20), corresponding to the orderings of the four diagrams in Fig.6H. The trajectories inserted by Chan et al. are dictated by the empirical evidence available and are believed to be the dominant ones. It will be recalled that a Regge trajectory has a definite signature i.e. resonance poles along a trajectory appear in steps of $\Delta J = 2$. Thus a boson trajectory with even (odd) signature will have physical particles at $J = 0,2,4 \cdots$ ($J = 1,3,5 \cdots$). However some trajectories appear to coincide almost exactly with trajectories of opposite signature. These are said to be "exchange degenerate". Experimental evidence points to the ω-A_2, the Λ ($\equiv Y_0^*$) and the Y_1^* trajectories being exchange degenerate. Thus the ω with $J = 1$ is the first pole on the ω- A_2 trajectory and the A_2 with $J = 2$ is the second pole.

In the graphs of Fig.6H all channels have a P-wave resonance corresponding to the first pole. Now formula

(6-19) (and the original Veneziano formula) was written down for the case of the scattering of scalar mesons with the exchange of Regge trajectories having a leading spin zero pole. Thus to apply the model to the present case the formula needs modifying. This can be done by writing the arguments of B_5 as $1 - \alpha_{mn}$ since then the poles will occur when $1 - \alpha_{mn} = 0, -1, -2 \cdots$, i.e. when $\alpha_{mn} = 1,2,3 \cdots$. However, this shift in arguments alters some of the properties of the amplitude.

To compensate for this the kinematic factor is introduced. The one used was proposed by Bardakci and Ruegg[17] and is

$$K = \varepsilon_{\mu\nu\rho\sigma}\, p_1^{\mu} p_2^{\nu} p_3^{\rho} p_4^{\sigma}$$

where $\varepsilon_{\mu\nu\rho\sigma}$ is the totally antisymmetric tensor and p_i the 4-momentum of the i^{th} external particle. Thus (6-19) becomes

$$V(12345) = \beta \varepsilon_{\mu\nu\rho\sigma}\, p_1^{\mu} p_2^{\nu} p_3^{\rho} p_4^{\sigma}\; B_5 \qquad (6\text{-}21)$$

This amplitude can be shown to have all the Veneziano properties.[18]

For the baryons, however, the terms $1 - \alpha_{mn}$ in B_5 would not give resonances at the correct masses. Therefore above threshold the arguments corresponding to baryon trajectories are shifted by a half-integer. However to ensure the correct Regge behaviour for baryon exchange, the arguments of the baryon trajectories below threshold are taken as $1 - \alpha_{mn}$.[19]

The amplitudes for each of the graphs in Fig.6H are given below.

$$\left.\begin{aligned} P &= K\, B_5(1-\alpha_{K^*}, 1-\alpha_{A_2}, {}^1/2-\alpha_\Lambda, 1-\alpha_\omega, {}^1/2-\alpha_N) \\ Q &= K\, B_5(1-\alpha_{K^*}, {}^1/2-\alpha_\Lambda, 1-\alpha_\omega, {}^3/2-\alpha_{Y^*}, 1-\alpha_{K^*}) \\ R &= K\, B\,(1-\alpha_{K^*}, 1-\alpha_{A_2}, {}^3/2-\alpha_{Y^*}, 1-\alpha_\omega, {}^3/2-\alpha_\Delta) \\ S &= K\, B_5({}^3/2-\alpha_\Delta, {}^1/2-\alpha_\Lambda, 1-\alpha_{A_2}, {}^3/2-\alpha_{Y^*}, {}^1/2-\alpha_N) \end{aligned}\right\} \quad (6\text{-}22)$$

with $K = \varepsilon_{\mu\nu\rho\sigma}\, p_\pi^\mu p_{\bar{K}}^\nu p_K^\rho p_{\bar{p}}^\sigma$

The trajectory parameters are summarised in Table 6.1. These parameters are determined from the Chew-Frautschi plot of the known resonances using the masses given in the Particle Data Group's tables.[20] The imaginary part of α above threshold is obtained from the total widths of known resonances using the formula $\mathrm{Im}\,\alpha = \alpha' m_r \Gamma_r$

The full amplitude T is written as a linear combination of the four graphs.

$$T = aP + bQ + cR + dS \quad (6\text{-}23)$$

where a,b,c and d are parameters giving the relative strengths of the respective amplitudes. These parameters may be fixed with an approximate exchange degeneracy argument. In the four-point case, it can be shown that the residues at $\alpha(s) = J$ for V(1234) and V(2134) differ only by a sign $(-1)^J$ in the leading term.[21] Thus with V(1234) alone, the leading trajectory has particles for every J and is thus exchange degenerate. However with V(1234) + V(2134) then all particles with odd J on the leading trajectory are removed so that the trajectory has a definite signature. Moreover it is noticed that V(1234) and V(2134) differ only by interchanging 1 and 2.
A similar situation holds for the five-point amplitude.

Since graphs R and S differ only by the interchange

of the π^- and $\bar{p}$ lines, |d| is zero or equal to |c| according as the trajectory in the $\pi^- \bar{p}$ channel is or is not exchange degenerate. Since there is no experimental evidence for a $J^P = \frac{5}{2}^-$ recurrence on the Δ trajectory, graphs R and S should be combined to cancel all wrong-signature poles. Thus for R and S as defined in (6-22), c:d = 1:1. Similarly, graphs P and S differ only by the interchange of the π^- and p lines. If the N_α trajectory is to have definite signature (absence of a N_α recurrence with $J^P = \frac{3}{2}^-$) then this requires a:d = 1:1. However, graph Q differs only from graphs P and R by the interchange of the $\pi^- \bar{K}^0$ and $\pi^- K^+$ lines respectively. Now experimental evidence points to the K^* trajectory being exchange degenerate and so graph Q is omitted from the full amplitude. If these crude arguments are accepted, then the full amplitude is

$$T = \beta \left[P + R + S \right]$$

where β is the only free parameter.

Indeed with such an amplitude Chan et al. were able to give a reasonable global description (cross-sections, mass plots, angular distributions, etc.) of reactions (1), (2), (3). The model was not applied to the reaction $\bar{p}p \rightarrow K_1^0 K^\pm \pi^\mp$ in general, but it was found that the predicted cross-section at 3.7 GeV/c was too large by an order of magnitude. Indeed, as the baryon trajectories have been treated in a very approximate way, this might be expected. In the present study the model is applied to the reaction at 1.1, 2.5[22] and 5.7[23] GeV/c. In calculating the predictions of the model, the Monte-

Carlo program FOWL was used to generate events and the B_5 function was evaluated by means of a program written by Hopkinson.(24)

The experimental data show evidence for the production of $K^{*o}(892)$, $K^{*\pm}(892)$ and of A_2. The relative amounts of $K^{*\pm}$ and K^{*o} vary with energy, the $K^{*\pm}$ percentage remaining approximately constant, while that of K^{*o} decreases.(25) The angular distributions also vary with energy, being rather flat at 1.1 GeV/c and strongly peaked at the higher energies.

Cross-sections

Using the model as prescribed by Chan et al., the cross-sections for the reaction $\bar{p}p \rightarrow K_1^o K^{\pm} \pi^{\mp}$ were calculated at 1.1, 2.5 and 5.7 GeV/c. Since the prediction of the amplitude (normalised to $K^+p \rightarrow K^o\pi^+p$ at 5 GeV/c) was not in good agreement with experiment at 3.7 GeV/c, the prediction in this study was normalised to the $\bar{p}p \rightarrow K_1^o K^{\pm} \pi^{\mp}$ cross-section at 2.5 GeV/c and the energy dependence of this prediction was investigated. However the agreement is poor, there being a discrepancy of a factor of 3 at 1.1 GeV/c. The predictions of the amplitude on the effective mass plots at 1.1 GeV/c are encouraging but there is bad disagreement with the C.M.S. production angles (Figs.6I,J). The shape of the theoretical angular distributions is governed to a large extent by the kinematic factor $\varepsilon_{\mu\nu\rho\sigma} p_\pi^\mu p_{\bar{K}}^\nu p_K^\rho p_{\bar{p}}^\sigma$. Since the kinematic factor neglects baryon spin, difficulty might be expected for baryon exchange where this might be important. However some kinematic factor is certainly necessary since its omission

produces a discrepancy in the cross-section in the opposite direction. It has been found that a good description of the cross-section in the range 1.1 - 5.7 GeV/c can be obtained by using another kinematic factor. The new factor is

$$K = \left| \vec{p}_{K^\pm} \wedge \vec{p}_{\pi^\mp} \right|$$

where the $\vec{p}_{K^\pm}$ and $\vec{p}_{\pi^\mp}$ are the vectorial momenta of the $K^\pm$ and $\pi^\mp$ in the $\bar{p}p$ C.M. system. The agreement obtained is shown in Fig.6K. It should be stressed that this factor is purely empirical and no theoretical basis for its use is known.

Mass and angular distributions

a) 1.1 GeV/c

Using the same graphs and relative weights of Chan et al. and the new kinematic factor, a reasonable description of the effective mass plots can be obtained. However, in the angular distributions, the pion C.M.S. production angle is too strongly peaked in the backward direction (here forward is defined as the π^- going in the $\bar{p}$ direction and the π^+ in the direction of the proton). This can be corrected by lowering the intercept of the trajectory by 1/2. Such a procedure has been used by Chan et al. and by Raitio[26] to improve the agreement in reactions (2) and (3) and $K^+n \rightarrow K^o\pi^+ n$. (This modification suppresses the Δ exchange - it has been suggested that the Δ residue has an extra zero at the wrong-signature point with $\alpha_\Delta = 1/2$[27]). The predictions of the model with this modification are shown in Figs.6L,M,N. It can be seen

that there is a reasonable agreement with the effective mass distributions and the production and decay angular distributions at this energy.

It was found that it is possible to slightly improve the overall agreement by altering the relative weights of the contributing graphs. Writing $T = \beta \left[P + \gamma R + \delta S \right]$, the parameters γ and δ were determined by a maximum likelihood fit to the experimental data at 1.1 GeV/c.
The likelihood function used was

$$\mathcal{L} = \sum_{\text{all events}} \log \frac{|T|^2}{\int_{\substack{\text{all} \\ \text{phase} \\ \text{space}}} |T|^2}$$

The values of γ and δ obtained from this fit were of order 0.94 and 0.59 respectively. However in view of the results obtained at 2.5 and 5.7 GeV/c, it cannot be claimed that such changes are significant.

b) 2.5 GeV/c

The new kinematic factor and the Chan parameters were again used to compare the predictions of the model with the experimental mass and angular distributions. However the model predicts too much K^{*o} and A_2 and not enough $K^{*\pm}$. In order to obtain a reasonable agreement between the model and the experimental mass plots at this energy, it was found necessary to lower the Λ intercept by approximately $^1/2$ (from -0.68 to -1.1). The resulting prediction is shown in Fig.60. It can be seen that there are indications of high mass $K\pi$ and $K\bar{K}$ resonances in the experimental data and the model reproduces them well.

However the angular distributions are badly described. (Fig.6P).

c) 5.7 GeV/c

A very bad disagreement was obtained at this energy when the initial comparison was made as in sections a) and b). Hardly any $K^{*\pm}$ and too much K^{*o} was predicted. By lowering the $\wedge$ intercept again to -1.1 the agreement is improved slightly (Fig.6Q).

Since the 2.5 and 5.7 GeV/c mass plots were improved by lowering the $\wedge$ intercept, the same procedure was tried at 1.1 GeV/c. However such a modification results in too much A_2 production and destroys the previous agreement obtained for the angular distributions.

Summary

By introducing an entirely empirical kinematic factor, it has been possible to give a good description of the energy variation of the cross-section for the reaction $\bar{p}p \rightarrow K_1^o K^{\pm} \pi^{\mp}$. With the new kinematic factor a reasonable agreement with the mass and angular distributions at 1.1 GeV/c can also be obtained. However the same model does not give a good description of the 2.5 and 5.7 GeV/c data. It is possible to describe the mass distributions at these energies by altering the parameters of the $\wedge$ trajectory in an arbitary manner, but no method of describing the angular distributions at 2.5 GeV/c has yet been found. A new model for $\bar{N}NK\bar{K}$ processes including spin and isospin has recently been published[28] and it would be very interesting to compare the results of this model with the data.

$$\alpha(x) = \theta(x_{th}-x)(\alpha_0+\delta+\alpha'_-x) + \theta(x-x_{th})((\alpha_0+\alpha'_+x)+ia(x-x_0))$$

Trajectory	α_0	δ	α'_+	α'_-	a	x_0
$\omega - A_2$	0.48	0	0.9	0.9	0.07	0.18
K^*	0.35	0	0.82	0.9	0.07	0.29
N	-0.37	$-1/2$	1	0.9	0.14	1.0
$\triangle$	0.13	$1/2$	0.9	0.9	0.14	1.0
$\wedge$	-0.68	$-1/2$	0.95	0.9	0.14	2.1
Y_1^*	-0.22	$-1/2$	0.9	0.9	0.4	1.57

Table 6.1 Trajectory parameters below and above the threshold x_{th}

References

1. Chan H-M., "Multi-Particle Phenemenology", Herceg Novi lecture (1969)

2. S. Mandelstam, Phys. Rev. 112, 1344 (1958)
Phys. Rev. 115, 1741, 1752 (1959)

3. This section relies heavily on the report by H.J. Lubatti, "Theory and Phenomenology in Particle Physics", Part B, p318, Academic Press.

4. For example, see H. Muirhead, "The Physics of Elementary Particles" p454, Pergamon.

5. T. Regge, N.C. 14, 951 (1959).
N.C. 18, 947 (1960).

6. G.F. Chew, S.C. Frautschi, Phys. Rev. Lett. 7, 394 (1961)
Phys. Rev. Lett. 8, 41 (1962)
R. Blankenbecler, M.L. Goldberger, Phys. Rev. 126, 766 (1962)

7. H. Muirhead, op. cit., p451.

8. R. Dolen, D. Horn, C. Schmid, Phys. Rev. 166, 1768 (1968)

9. D. Amati, "An Introduction to Dual Theory", Lectures given at Latino-American School of Physics, La Plata, Argentina (1970).

10. G. Veneziano. N.C. 57A, 190 (1968)

11. E. Jahnke, F. Emde "Tables of Functions", p13, Dover.

12. Chan H-M, Phys. Lett. 28B. 425 (1968)

13. K. Bardakci, H.Ruegg, Phys. Lett. 28B, 343 (1968)
M. Virasoro, Phys. Rev. Lett. 22, 37 (1969)

14. Chan H-M. "Multi-Particle Phenomenology", op. cit.

15. B. Petersson, N.A. Tornqvist, Nucl. Phys. B13. 629 (1969)

16. Chan H-M, R.O. Raitio, G.H. Thomas, N.A. Tornqvist, Nucl. Phys. B19, 173 (1970)

17. K. Bardakci, H. Ruegg, Phys. Lett. 28B, 267 (1968)

18. Chan H-M, "Multi-Particle Phenomenology", op. cit.

19. P. Hoyer, B. Petersson, N. Tornqvist, CERN Preprint TH. 1159 (1970)

20. Particle Data Group, Particle Properties

21. Chan H-M, "Multi-Particle Phenomenology", op. cit.

22. M. Baubillier and M. Rivoal (IPN), private communication

23. B. French et al., Nucl. Phys. B19, 173 (1970)

24. J. Hopkinson, Daresbury Preprint DNPL/P21 (1969)

25. M. Rivoal, private communication.

26. R. Raitio, Nucl. Phys. B21, 427 (1970)

27. K. Igi et al., Phys. Rev. Lett. 21, 580 (1968)

28. G. Benfatto, M. Lusignoli, F. Nicolo, N.C. 4A, p209 (1971)

CHAPTER 7

CONCLUSION

A study of the reactions $\bar{p}p \rightarrow K_1^o K^{\pm} \pi^{\mp}$, $\bar{p}p \rightarrow K_1^o K^{\pm} \pi^{\mp}(\pi^o)$, $\bar{p}p \rightarrow K_1^o K_1^o \pi^+ \pi^-$ and $\bar{p}p \rightarrow K_1^o(K^o)\pi^+ \pi^-$ at 1.2 GeV/c has shown that there is abundant resonance production. In particular $K^*(892)$ production, including associated K^* production in the 4-body final states, is dominant. Another resonance which plays a major role in the 4-body reactions is the ρ meson, though it is suppressed in $\bar{p}p \rightarrow K_1^o K_2^o \pi^+ \pi^-$. There is evidence also for the production of the A_2, ϕ, D^o and E^o mesons and $K\bar{K}$ threshold enhancements.

The cross-sections for the production of the various resonances in the reactions are presented below. These cross-sections have been calculated from the values in Table 3.1 and the appropriate resonance fraction.

I $\bar{p}p \rightarrow K_1^o K^{\pm} \pi^{\mp}$ (Fit C)

$\bar{p}p \rightarrow K^{*o}(892)K^o$	49 ± 6 μb
$K^{*\mp}(892)K^{\pm}$	82 ± 9 "
$A_2 \pi^{\mp}$	11 ± 6 "
$K^{*o}(1420)K_1^o$	11 ± 6 "
$K^{*\mp}(1420)K^{\pm}$	8 ± 5 "

II $\bar{p}p \rightarrow K_1^o K^{\pm} \pi^{\mp}(\pi^o)$ (Fit I)

$\bar{p}p \rightarrow \rho^{\mp} K_1^o K^{\pm}$	100 ± 12 μb
$K^{*\pm} K\pi$	100 ± 12 "
$K^{*o} K\pi$	79 ± 10 "
$A_2^{\pm} \pi^{\mp} \pi^o$	16 ± 5 "
$K^{*\pm} K^{*\mp}$	63 ± 6 "
$K^{*o} \bar{K}^{*o}$	13 ± 4 "
$(K_1^o K^{\pm})_{SL} \pi^{\mp} \pi^o$	22 ± 7 "
$D^o \pi^o$	8 ± 2 "

$E^0 \pi^0$	16 ± 5 μb
$A_2^{\pm} \rho^{\mp}$	12 ± 4 "
$f' \pi^0$	7 ± 4 "

III $\bar{p}p \rightarrow K_1^0 K_1^0 \pi^+ \pi^-$ (Fit I)

$\bar{p}p \rightarrow \rho^0 K_1^0 K_1^0$	56 ± 6 μb
$K^{*\pm} K_1^0$	56 ± 6 "
$K^{*\pm} K^{*\mp}$	39 ± 4 "
$A_2^0 \pi^+ \pi^-$	9 ± 5 "
$S^* \pi^+ \pi^-$	13 ± 2 "
$f^0 \pi^+ \pi^-$	8 ± 4 "
$f' \pi^+ \pi^-$	6 ± 2 "

The data do not give a clear solution to the $K_1^0 K_1^0$ threshold problem.

IV $\bar{p}p \rightarrow K_1^0 K_2^0 \pi^+ \pi^-$

$\bar{p}p \rightarrow \rho^0 K_1^0 K_2^0$	10 ± 4 μb
$K^{*\pm} K \pi$	98 ± 12 "
$\phi \pi^+ \pi^-$	13 ± 3 "
$K^{*\pm} K^{*\mp}$	48 ± 6 "

V $\bar{p}p \rightarrow K_1^0 K_1^0 \omega^0$

The variation of the cross-section for $\bar{p}p \rightarrow K_1^0 K_1^0 \omega^0$ with the $\bar{p}p$ C.M.S. energy can be adequately described by a straight line fit and so the limited data do not need the introduction of a direct channel effect.

The model of Chan et al. was compared with experiment using the reaction $\bar{p}p \rightarrow K_1^0 K^{\pm} \pi^{\mp}$ at 1.1, 2.5 and 5.7 GeV/c. A new kinematic factor is necessary to correctly describe the energy dependence of the cross-section. No general agreement over all energies has been found. However, it

is possible to obtain reasonable agreement at 1.1 GeV/c and partial agreement at 2.5 and 5.7 GeV/c by altering trajectory parameters.

LIST OF DIAGRAM CAPTIONS

Figure

2A Schematic diagram of the bubble chamber

2B Definition of bubble chamber coordinate system

2C 0 prong V^0 event

2D 0 prong V^0V^0 and 2 prong V^0 events

2E 2 prong V^0V^0 event

2F 4 prong V^0 event

2G Schematic diagram of a measuring engine

2H Relative ionisation versus momentum for π, K

2I Range in liquid hydrogen versus momentum for π, K

3A Missing mass squared distribution for $K_1^0 K^\pm \pi^\mp$

3B Probability distribution for $K_1^0 K^\pm \pi^\mp$

3C Second highest momentum distribution for $K_1^0 K^\pm \pi^\mp$

3D Missing mass squared distribution for $K_1^0 K_1^0 \pi^+ \pi^-$

3E Probability distribution for $K_1^0 K_1^0 \pi^+ \pi^-$

3F Missing mass squared distribution for $K_1^0 (K^0) \pi^+ \pi^-$

3G Probability distribution for $K_1^0 (K^0) \pi^+ \pi^-$

3H Second highest momentum distribution for $K_1^0 (K^0) \pi^+ \pi^-$

3I Missing mass squared distribution for $K_1^0 K^\pm \pi^\mp (\pi^0)$

3J Probability distribution for $K_1^0 K^\pm \pi^\mp (\pi^0)$

3K Momentum distribution of $\pi^\mp$ from $K_1^0 K^\pm \pi^\mp (\pi^0)$

3L Momentum distribution of π^0 from $K_1^0 K^\pm \pi^\mp (\pi^0)$

3M Second highest momentum distribution for $K_1^0 K^\pm \pi^\mp (\pi^0)$

3N Missing mass squared distribution for $K_1^0 K_1^0 \pi^+ \pi^- (\pi^0)$ (1.2 GeV/c events)

3O Missing mass squared distribution for $K_1^0 K_1^0 \pi^+ \pi^- (\pi^0)$ (Formation expt. events)

3P Probability distribution for $K_1^0K_1^0\,\pi^+\,\pi^-(\pi^0)$ (1.2 GeV/c events)

3Q Probability distribution for $K_1^0K_1^0\,\pi^+\,\pi^-(\pi^0)$ (Formation expt. events)

3R Momentum distribution of π^0 from $K_1^0K_1^0\,\pi^+\,\pi^-(\pi^0)$ (1.2 GeV/c events)

3S Momentum distribution of $\pi^\pm$ from $K_1^0K_1^0\,\pi^+\,\pi^-(\pi^0)$ (1.2 GeV/c events)

3T Momentum distribution of π^0 from $K_1^0K_1^0\,\pi^+\,\pi^-(\pi^0)$ (Formation expt. events)

3U Momentum distribution of $\pi^\pm$ from $K_1^0K_1^0\,\pi^+\,\pi^-(\pi^0)$ (Formation expt. events)

3V Deviation from expected beam direction for 1.28 GeV/c events

3W Cross-section variation with incident $\bar{p}$ lab momentum for the reaction $\bar{p}p \rightarrow K_1^0K_2^0\,\pi^+\,\pi^-$

3X Cross-section variation with incident $\bar{p}$ lab momentum for the reactions

1) $\bar{p}p \rightarrow K_1^0K^\pm\,\pi^\mp$

and 2) $\bar{p}p \rightarrow K_1^0K_1^\pm\,\pi^\mp(\pi^0)$

3Y Cross-section variation with incident $\bar{p}$ lab momentum for the reactions

1) $\bar{p}p \rightarrow K_1^0K_1^0\,\pi^+\,\pi^-$

and 2) $\bar{p}p \rightarrow K_1^0K_1^0\,\pi^+\,\pi^-(\pi^0)$

5A Dalitz plot for reaction $\bar{p}p \rightarrow K_1^0K^\pm\pi^\mp$

5B Dalitz plot (contour) for reaction $\bar{p}p \rightarrow K_1^0K^\pm\pi^\mp$

5C $K_1^0K^\pm\,\pi^\mp$ distributions

1) $K^\pm\pi^\mp$ effective mass spectrum

2) $K_1^0\pi^\mp$ " " "

3) $K_1^0K^\pm$ " " "

The dotted curve corresponds to phase space

The full curve corresponds to Fit C

4) Angular distribution ($\cos\Theta$) of the K_1^o with respect to the line of flight of the $K_1^oK^\pm$ system for events with $M(K_1^oK^\pm) < 1080$ MeV.

The dotted curve corresponds to a zero order polynomial fit.

The broken curve corresponds to a second order polynomial fit.

5D $K_1^oK^\pm\pi^\mp(\pi^o)$ distributions

1) $\pi^\mp\pi^o$ effective mass spectrum
2) $K_1^o\pi^\mp(K^\pm\pi^o)$ " " "
3) $K_1^o\pi^o(K^\pm\pi^\mp)$ " " "
4) $K_1^oK^\pm$ " " "
5) $K^\pm\pi^\mp\pi^o$ " " "
6) $K_1^o\pi^\mp\pi^o$ " " "
7) $K_1^oK^\pm\pi^o$ " " "
8) $K_1^oK^\pm\pi^\mp$ " " "

The dotted curve corresponds to phase space.

The full curve corresponds to Fit C.

5E Scatter plots for $K_1^oK^\pm\pi^\mp(\pi^o)$

1) $K_1^o\pi^\mp$ effective mass versus $K^\pm\pi^o$ effective mass
2) $K_1^o\pi^o$ " " " $K^\pm\pi^\mp$ " "
3) $K_1^oK^\pm$ " " " $\pi^\mp\pi^o$ " "

5F $K_1^oK^\pm\pi^\mp(\pi^o)$ distributions

1) $K_1^oK^\pm$ effective mass spectrum
2) $K^\pm\pi^\mp\pi^o$ " " "
3) $K_1^o\pi^\mp\pi^o$ " " "
4) $K_1^oK^\pm\pi^o$ " " "
5) $K_1^oK^\pm\pi^\mp$ " " "

The full curve corresponds to Fit E

5G $K_1^o K^{\pm} \pi^{\mp}$ effective mass spectrum for events with $M(K_1^o K^{\pm}) < 1080$ MeV.

The dotted curve corresponds to Fit E.

The full curve corresponds to Fit I.

5H $K_1^o K^{\pm} \pi^{\mp}(\pi^o)$ distributions

1) $\pi^{\mp} \pi^o$ effective mass spectrum

2) $K_1^o \pi^{\mp}(K^{\pm} \pi^o)$ " " "

3) $K_1^o \pi^o(K^{\pm} \pi^{\mp})$ " " "

4) $K_1^o K^{\pm}$ " " "

5) $K^{\pm} \pi^{\mp} \pi^o$ " " "

6) $K_1^o \pi^{\mp} \pi^o$ " " "

7) $K_1^o K^{\pm} \pi^o$ " " "

8) $K_1^o K^{\pm} \pi^{\mp}$ " " "

The full curve corresponds to Fit I

5I $K_1^o K_1^o \pi^+ \pi^-$ distributions

1) $\pi^+ \pi^-$ effective mass spectrum

2) $K_1^o \pi^{\pm}$ " " " (4 combinations)

3) $K_1^o K_1^o$ " " "

4) $K_1^o \pi^+ \pi^-$ " " " (2 combinations)

5) $K_1^o K_1^o \pi^{\pm}$ " " " (2 combinations)

5J Scatter plots for $K_1^o K_1^o \pi^+ \pi^-$

1) $K_1^o \pi^+$ effective mass versus $K_1^o \pi^-$ effective mass

2) $K_1^o K_1^o$ " " " $\pi^+ \pi^-$ " "

5K Angular distribution ($\cos \Theta$) of one K_1^o with respect to line of flight of the $K_1^o K_1^o$ system for events with $1020 < M(K_1^o K_1^o) < 1070$ MeV and with $K^{*-} K^{*}$ events excluded.

The dotted curve corresponds to a zero order

polynomial fit.

The dashed curve corresponds to a fourth order polynomial fit.

5L $K_1^oK_1^o$ effective mass spectrum

The dotted curve corresponds to a scattering length fit (Fit G)

The full curve corresponds to the Breit-Wigner fit (Fit E)

5M $K_1^oK_1^o\pi^+\pi^-$ distributions

1) $\pi^+\pi^-$ effective mass spectrum
2) $K_1^o\pi^\pm$ " " " (4 combination)
3) $K_1^oK_1^o$ " " "
4) $K_1^o\pi^+\pi^-$ " " " (2 combinations)
5) $K_1^oK_1^o\pi^\pm$ " " " (2 combinations)

The full curve corresponds to Fit I

5N $K_1^o(K^o)\pi^+\pi^-$ distributions

1) $\pi^+\pi^-$ effective mass spectrum
2) $K^o\pi^\pm$ " " " (4 combinations)
3) $K_1^o(K^o)$ " " "
4) $K^o\pi^+\pi^-$ " " " (2 combinations)
5) $K_1^o(K^o)\pi^\pm$ " " " (2 combinations)

The dotted curve corresponds to phase space.

The full curve corresponds to the final fit.

5O Scatter plots for $K_1^o(K^o)\pi^+\pi^-$

1) $K^o\pi^+$ effective mass versus $K^o\pi^-$ effective mass
2) $K_1^o(K^o)$ " " " $\pi^+\pi^-$ " "

5P Cross-section variation with incident $\bar{p}$ lab momentum for the reaction $\bar{p}p \rightarrow K_1^oK_1^o\pi^+\pi^-(\pi^o)$

The full curve corresponds to a linear fit

The dotted curve corresponds to a quadratic fit.

5Q $\pi^+ \pi^- \pi^o$ effective mass distributions in the energy intervals

1) $2.10 < E < 2.12$ GeV

2) $2.12 < E < 2.14$ GeV

3) $2.14 < E < 2.16$ GeV

4) $2.16 < E < 2.18$ GeV

5) $2.18 < E < 2.20$ GeV

6) $2.20 < E < 2.22$ GeV

7) $2.22 < E < 2.24$ GeV

The full curve corresponds to the maximum likelihood fit.

5R Cross-section variation with $\bar{p}p$ CMS energy for the reaction $\bar{p}p \rightarrow K_1^o K_1^o \omega^o$.
The full curve corresponds to a linear fit.

6A Diagram depicting the Mandelstam variables, s and t

6B Typical variation of the cross-section with energy at low energy.

6C A Chew-Frautschi plot showing a Regge trajectory.

6D Diagrams for the Veneziano amplitude.

6E Relief diagram of the complex gamma function.

6F A Regge trajectory with the daughter sequence.

6G The general class of reactions described by the model of Chan et al.

6H The four diagrams that contribute to the amplitude of Chan et al. The resonances shown represent the trajectories used.

6I The predictions of the model on the $K_1^o K^{\pm} \pi^{\mp}$ mass

plots at 1.1 GeV/c.

6J The predictions of the model on the C.M.S. production angles at 1.1 GeV/c.

6K The variation of the cross-section for $\bar{p}p \rightarrow K_1^o K^{\pm} \pi^{\mp}$ with $\bar{p}$ lab momentum, showing the prediction of the modified model.

6L The predictions of the modified model on the $K_1^o K^{\pm} \pi^{\mp}$ mass plots at 1.1 GeV/c.

6M The predictions of the modified model on the C.M.S. production angles at 1.1 GeV/c.

6N The predictions of the modified model on the resonance decay angles at 1.1 GeV/c.

6O The predictions of the modified model on the $K_1^o K^{\pm} \pi^{\mp}$ mass squared plots at 2.5 GeV/c.

6P The predictions of the modified model on the C.M.S. production angles at 2.5 GeV/c.

6Q The predictions of the modified model on the $K_1^o K^{\pm} \pi^{\mp}$ mass squared plots at 5.7 GeV/c.

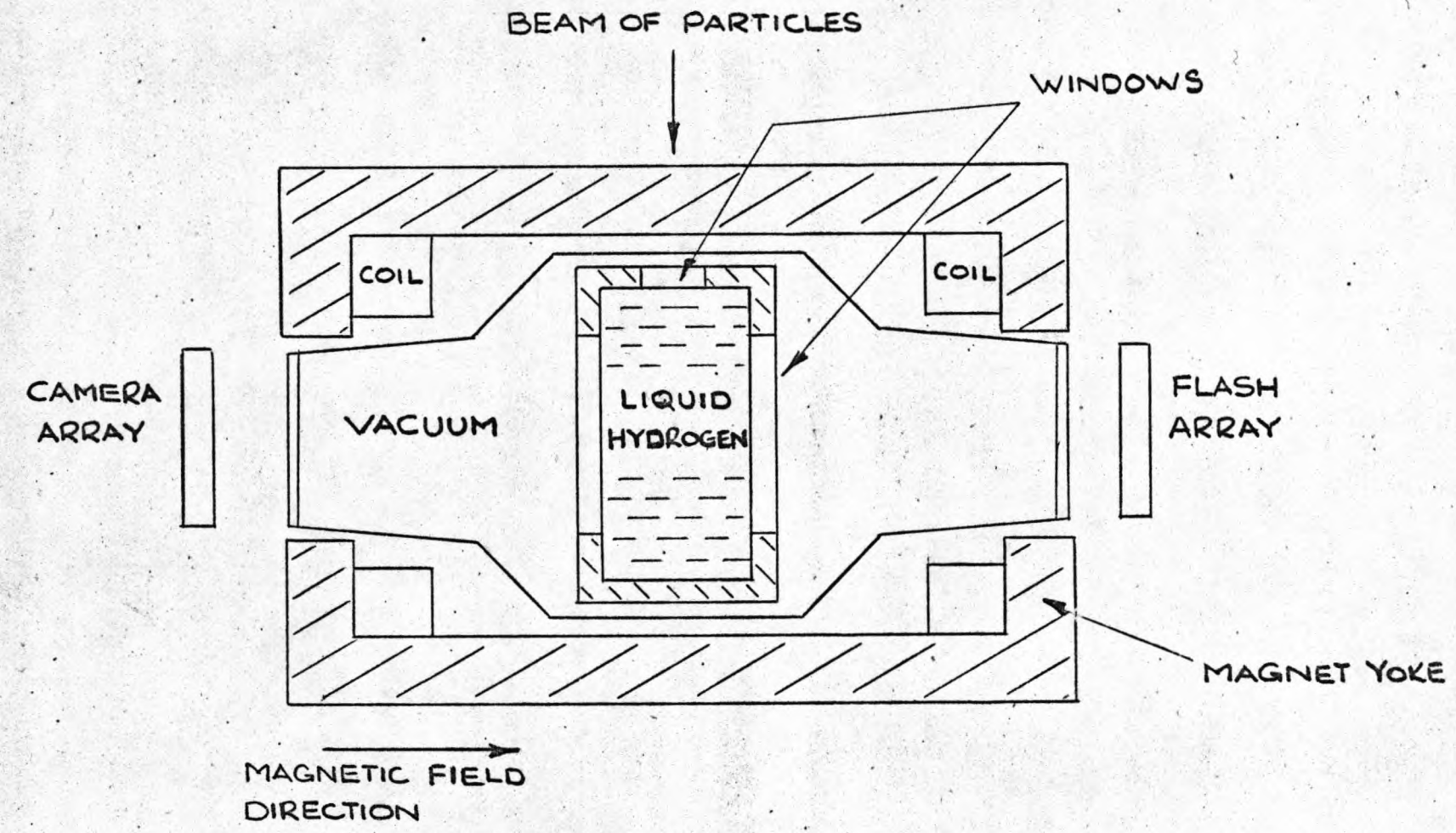

FIG. 2A SCHEMATIC DIAGRAM OF THE BUBBLE CHAMBER

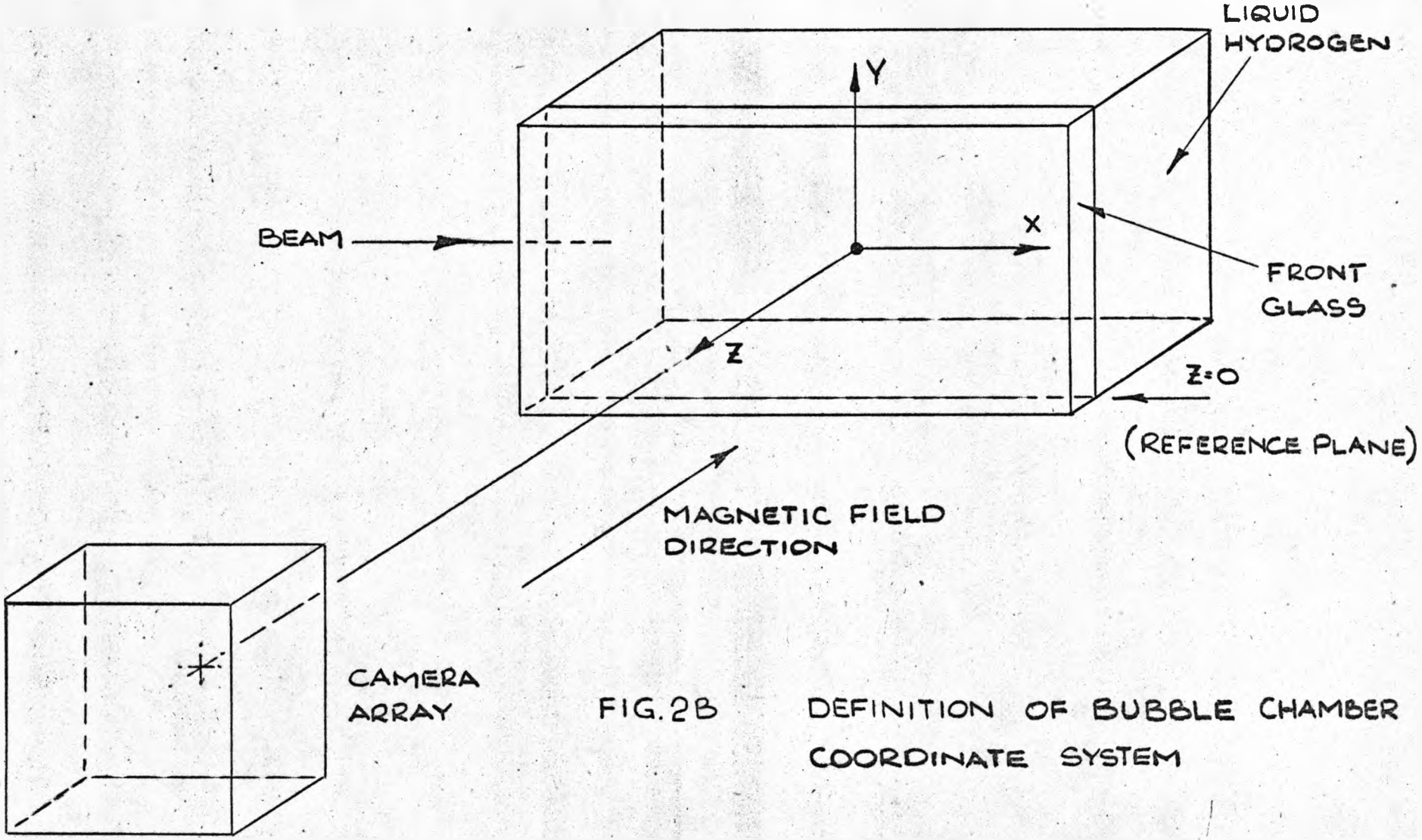

FIG. 2B DEFINITION OF BUBBLE CHAMBER COORDINATE SYSTEM

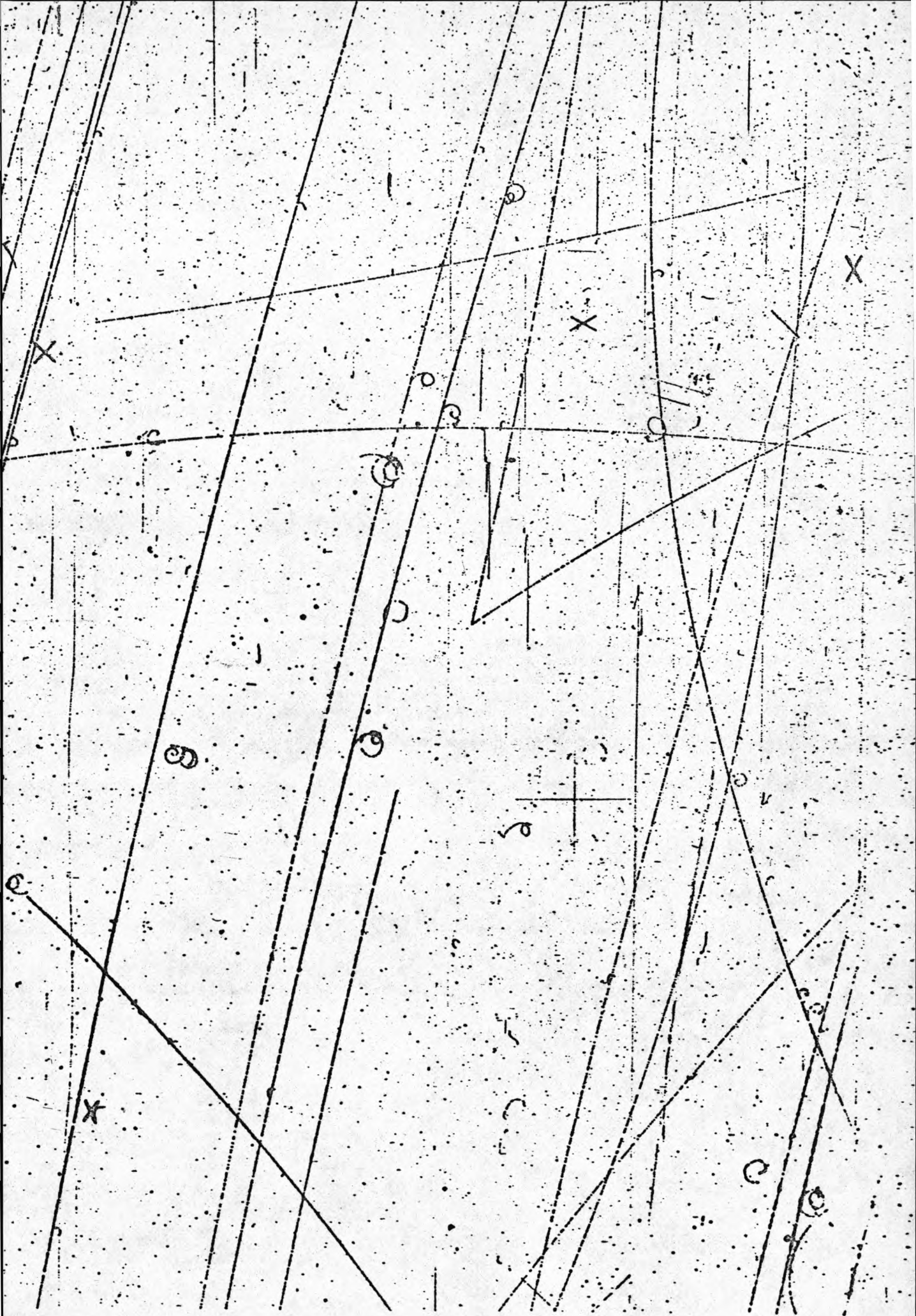

Fig. 2C 0 Prong V°

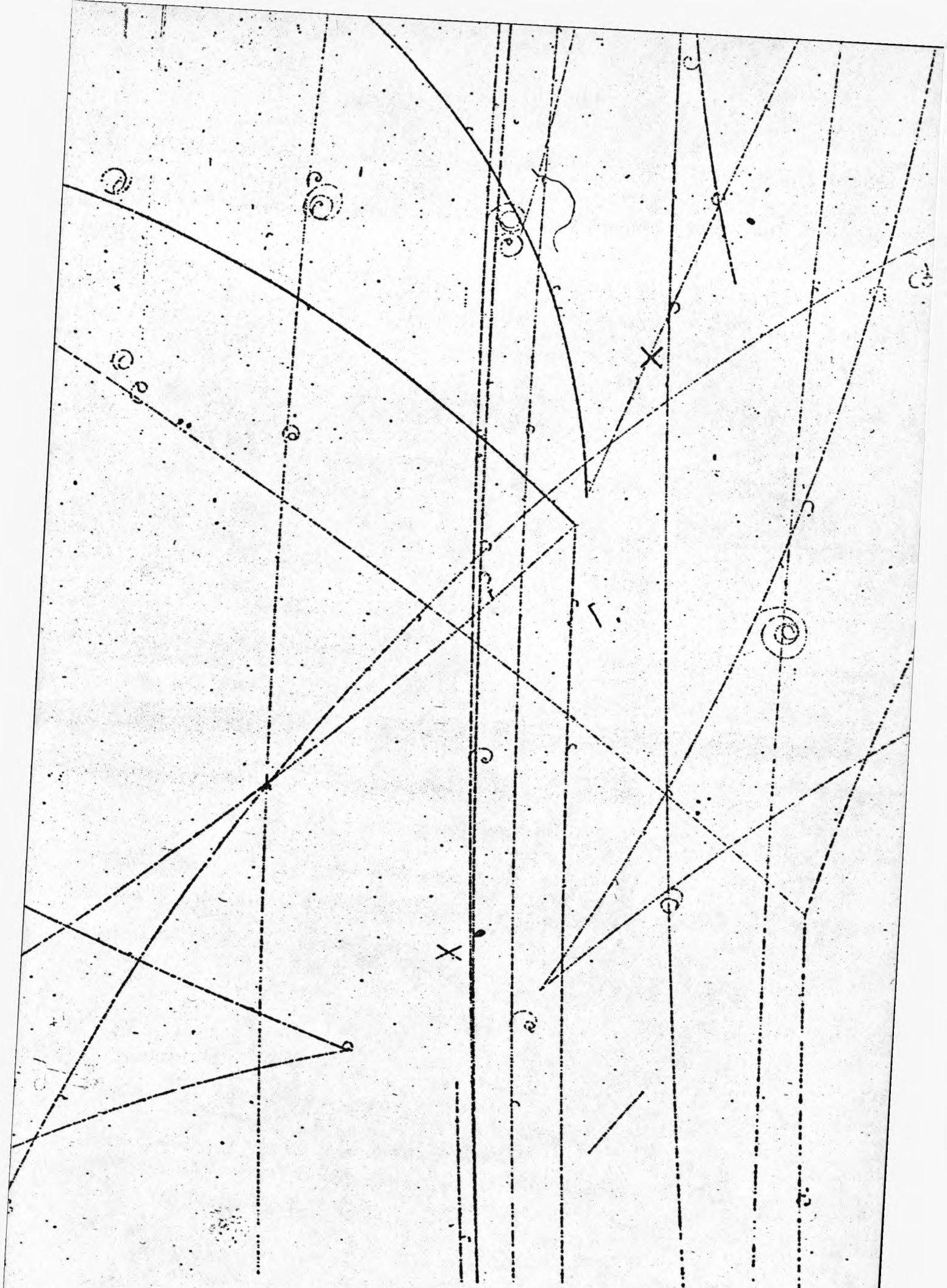

Fig. 2D 0 Prong V^oV^o and 2 Prong V^o

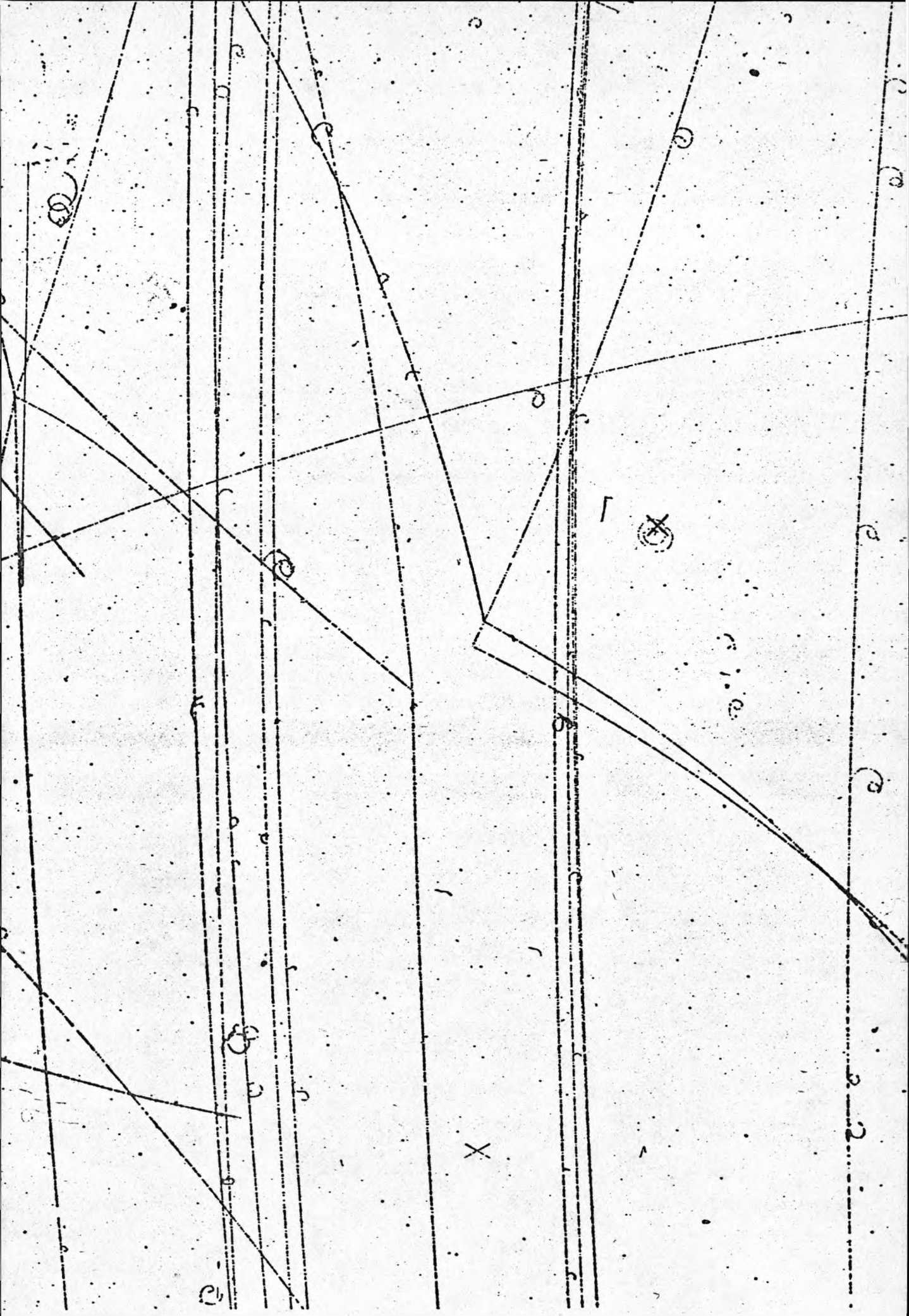

Fig. 2E 2 Prong $V^{o}V^{o}$

Fig. 2F 4 Prong V°

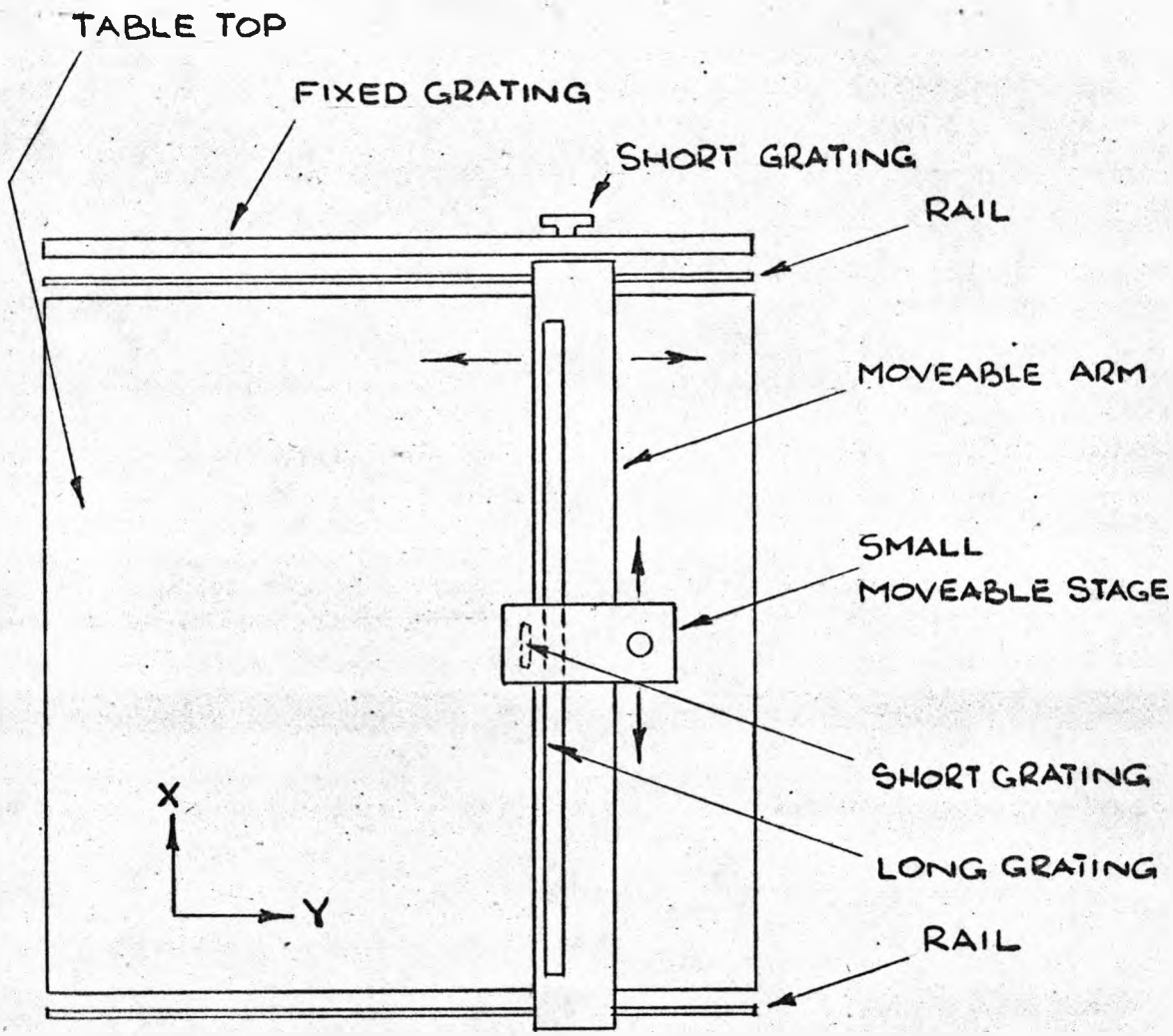

FIG. 2G SCHEMATIC DIAGRAM OF MEASURING ENGINE

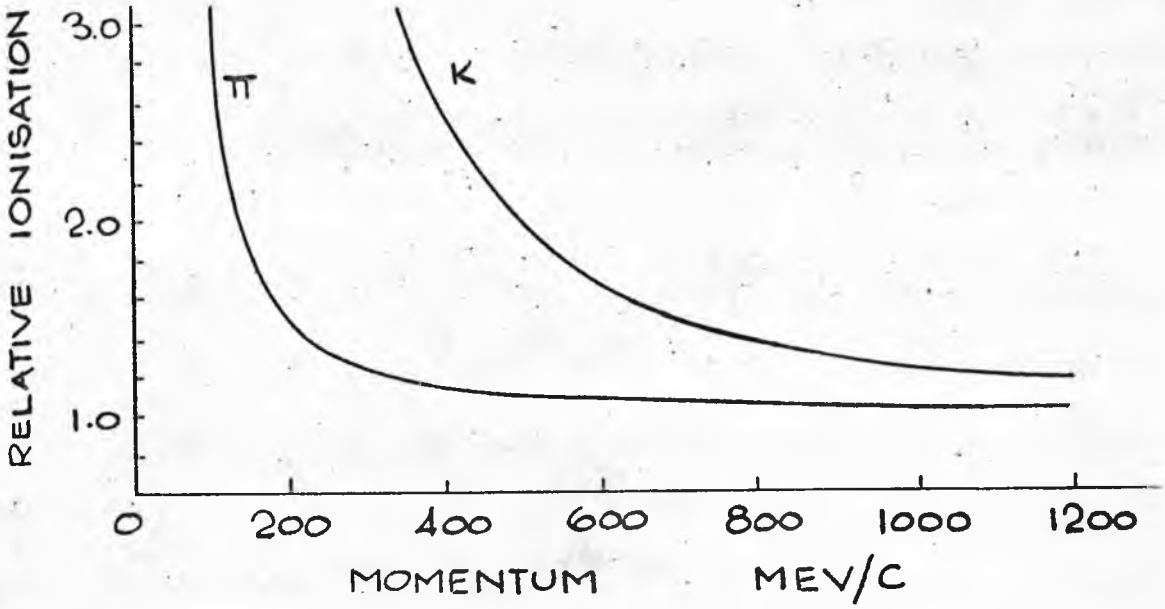

FIG. 2H RELATIVE IONISATION V. MOMENTUM

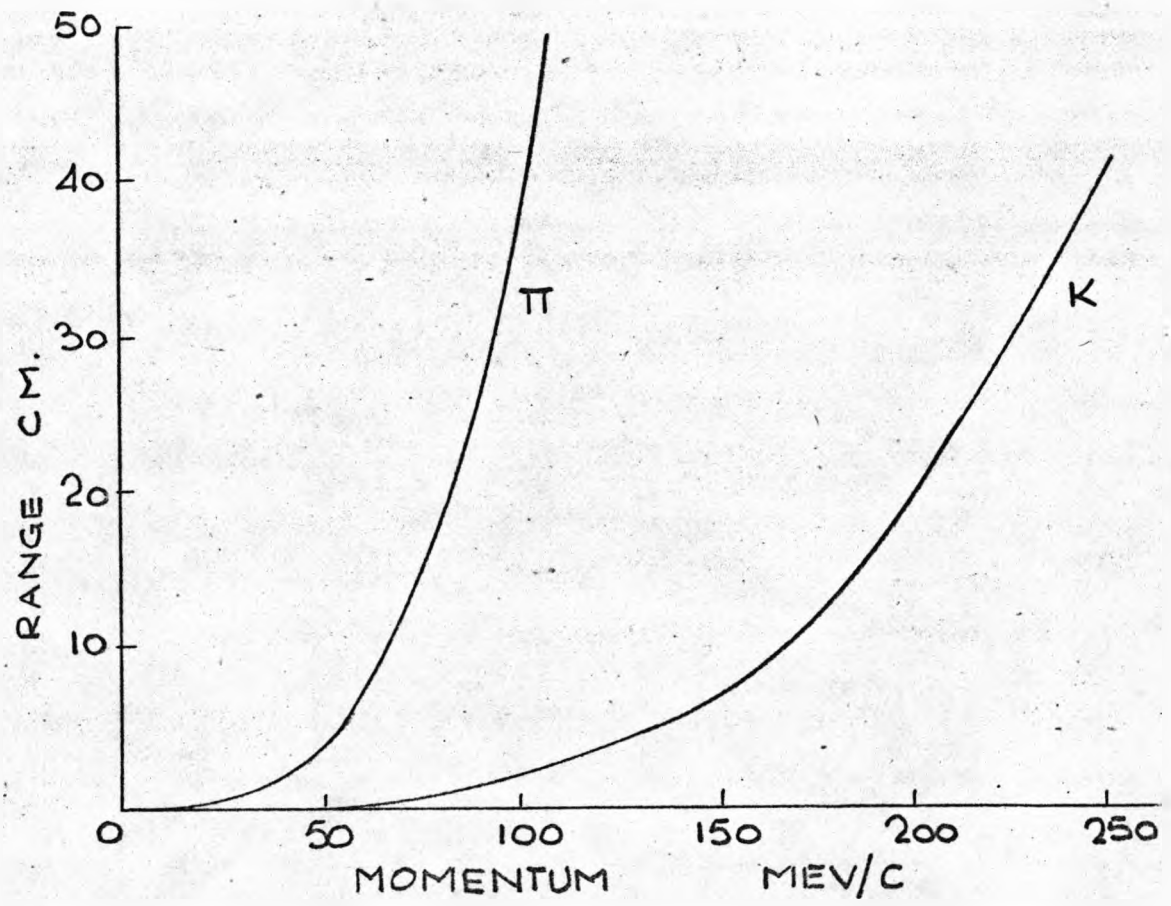

FIG. 2I RANGE IN LIQUID HYDROGEN V. MOMENTUM

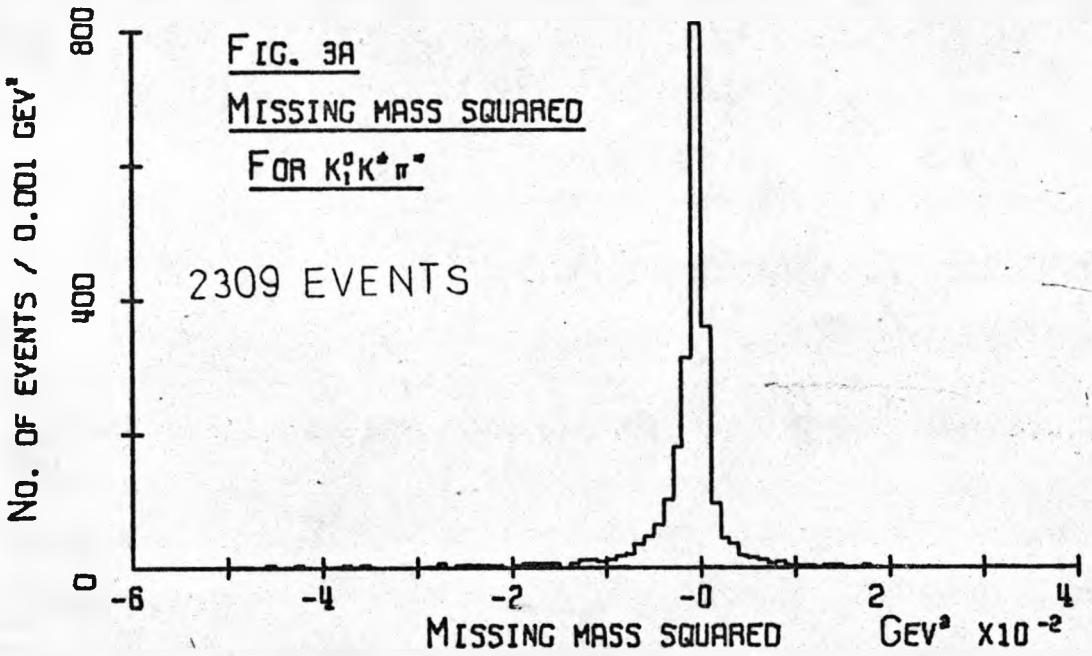
FIG. 3A
MISSING MASS SQUARED
FOR $K_1^0 K^* \pi^-$
2309 EVENTS
No. OF EVENTS / 0.001 GEV²
800
400
0
-6
-4
-2
-0
2
4
MISSING MASS SQUARED GEV² X10⁻²

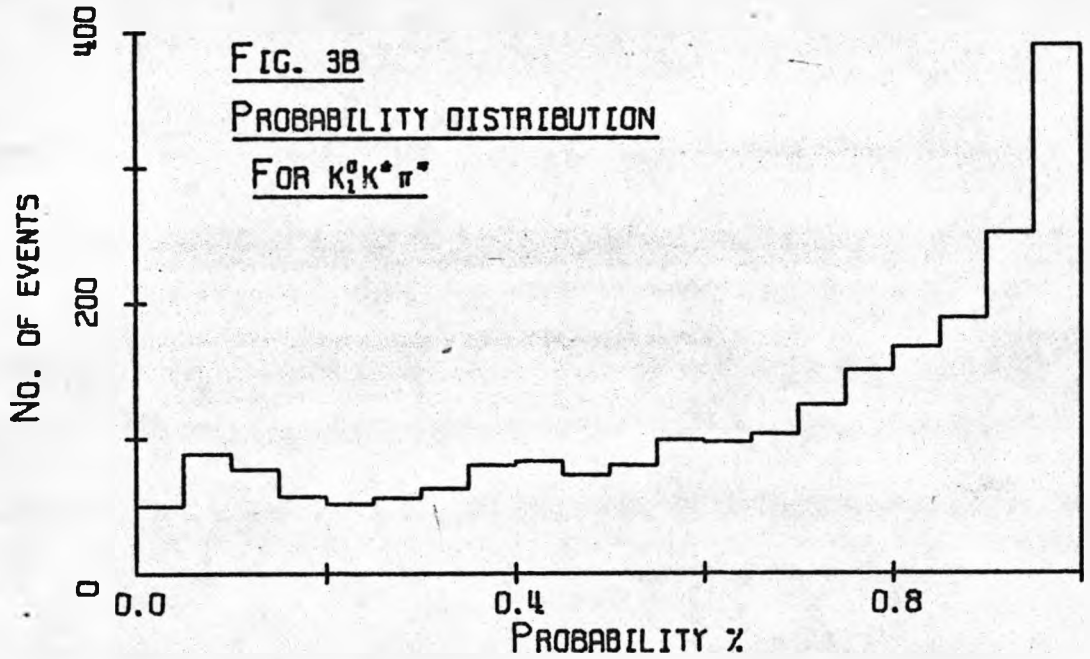
FIG. 3B
PROBABILITY DISTRIBUTION
FOR $K_1^0 K^* \pi^-$
No. OF EVENTS
400
200
0
0.0
0.4
0.8
PROBABILITY %

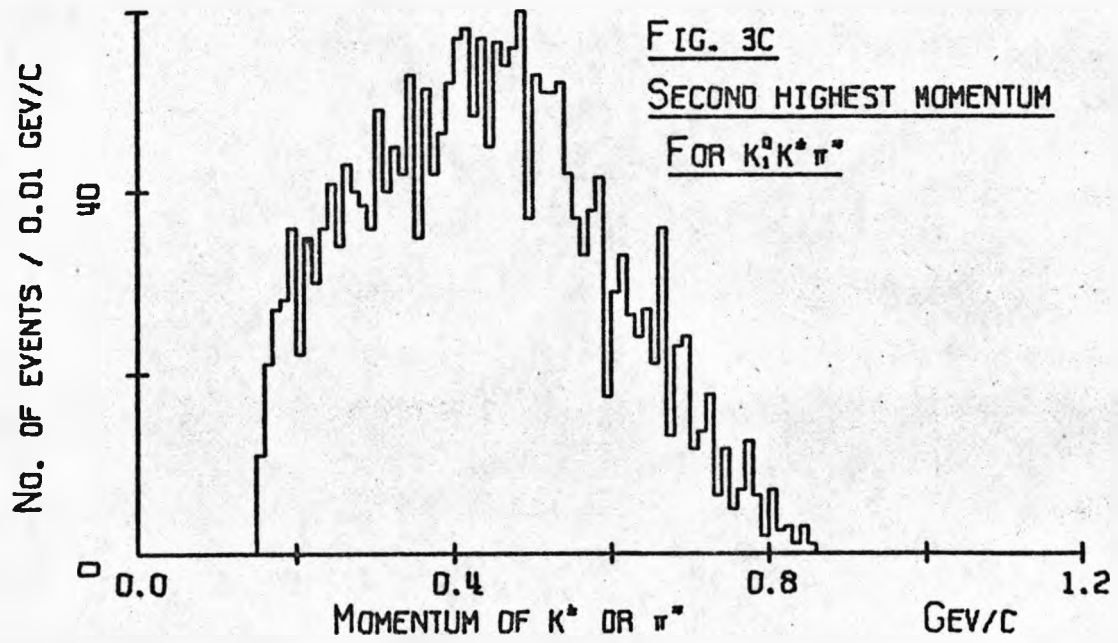
FIG. 3C
SECOND HIGHEST MOMENTUM
FOR $K_1^0 K^* \pi^-$
No. OF EVENTS / 0.01 GEV/C
40
0
0.0
0.4
0.8
1.2
MOMENTUM OF K^* OR π^- GEV/C

FIG. 3D MISSING MASS SQUARED FOR $K_1^0 K_1^0 \pi^+ \pi^-$

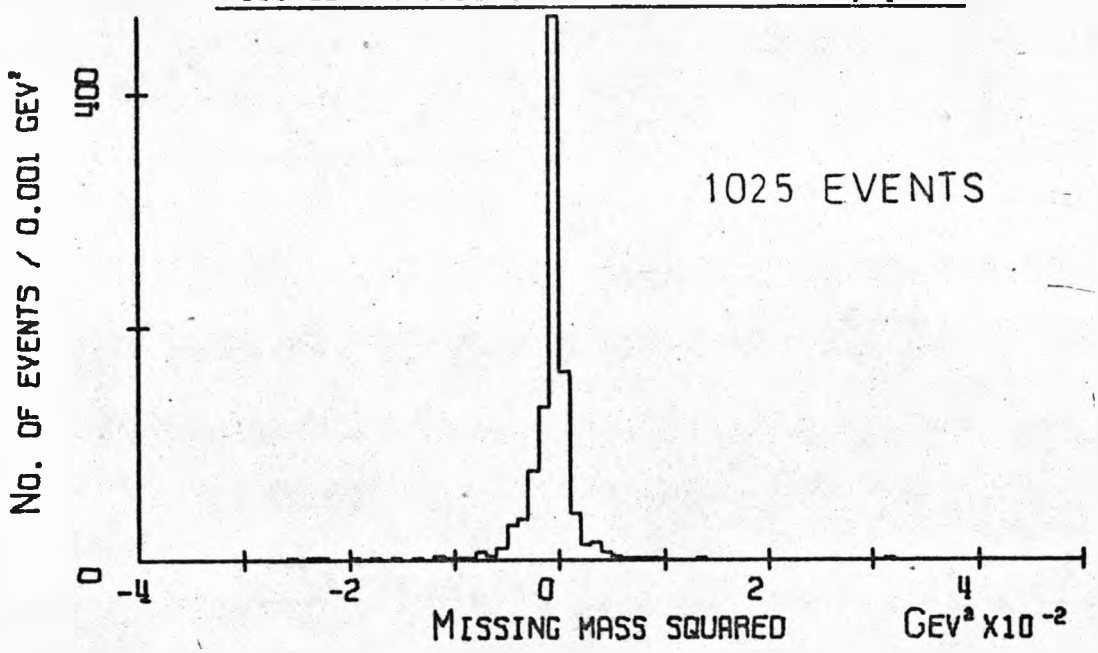

FIG. 3E PROBABILITY DISTRIBUTION FOR $K_1^0 K_1^0 \pi^+ \pi^-$

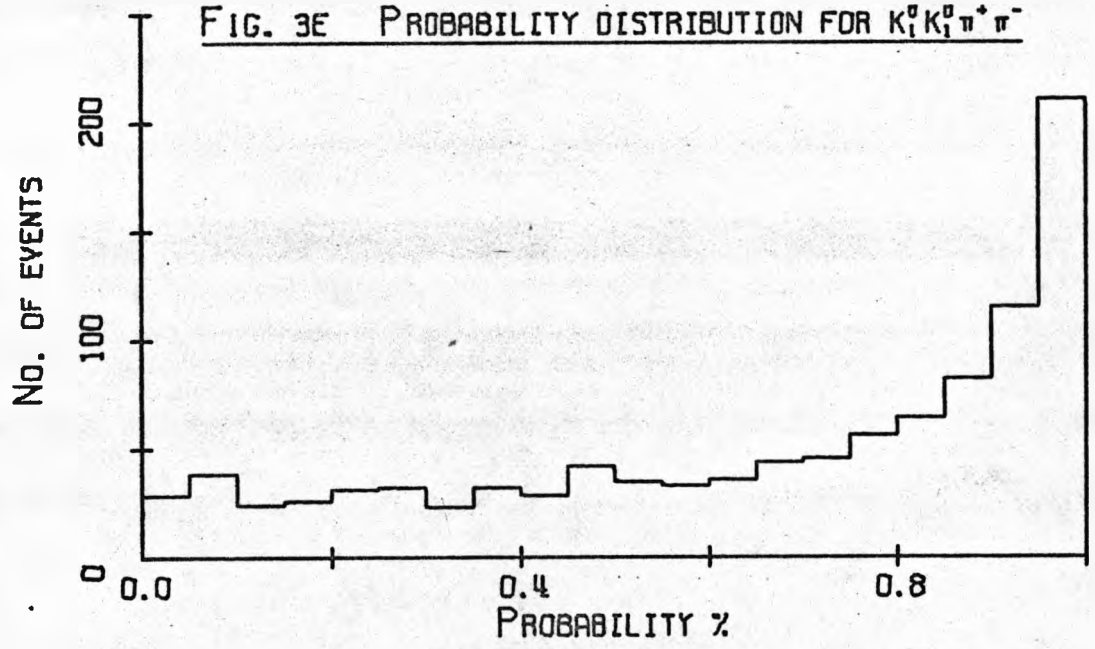

FIG. 3F MISSING MASS SQUARED FOR $K_1^0 (K^0) \pi^+ \pi^-$

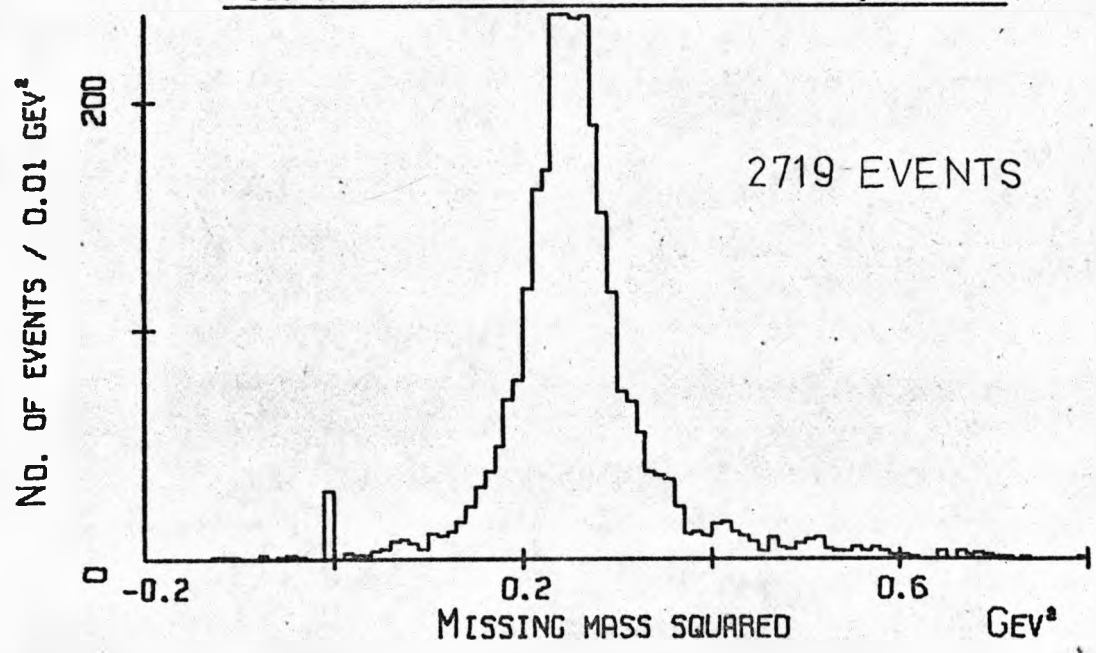

FIG. 3G PROBABILITY DISTRIBUTION FOR K_1^0 (K^0) $\pi^+\pi^-$

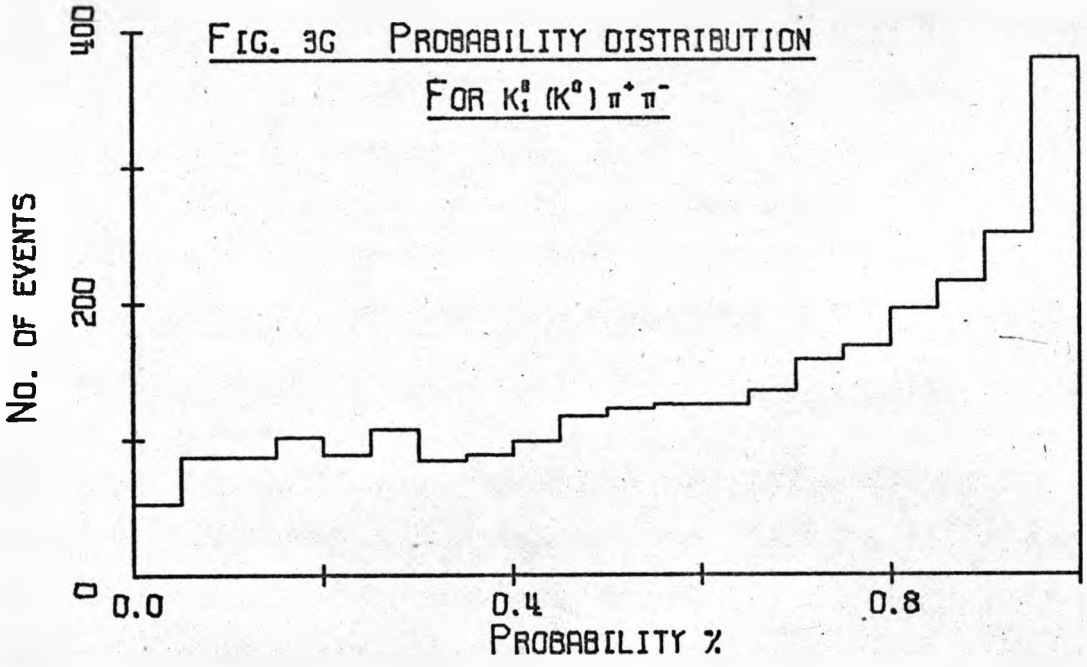

FIG. 3H SECOND HIGHEST MOMENTUM FOR K_1^0 (K^0) $\pi^+\pi^-$

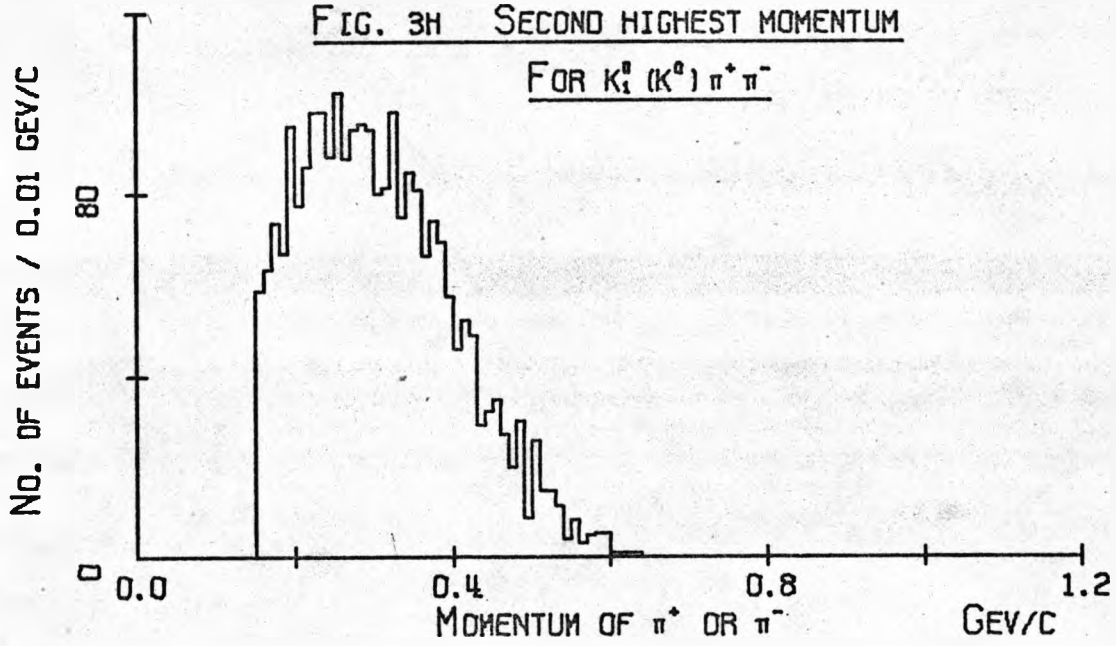

FIG. 3I MISSING MASS SQUARED FOR $K_1^0 K^+ \pi^- \pi^0$

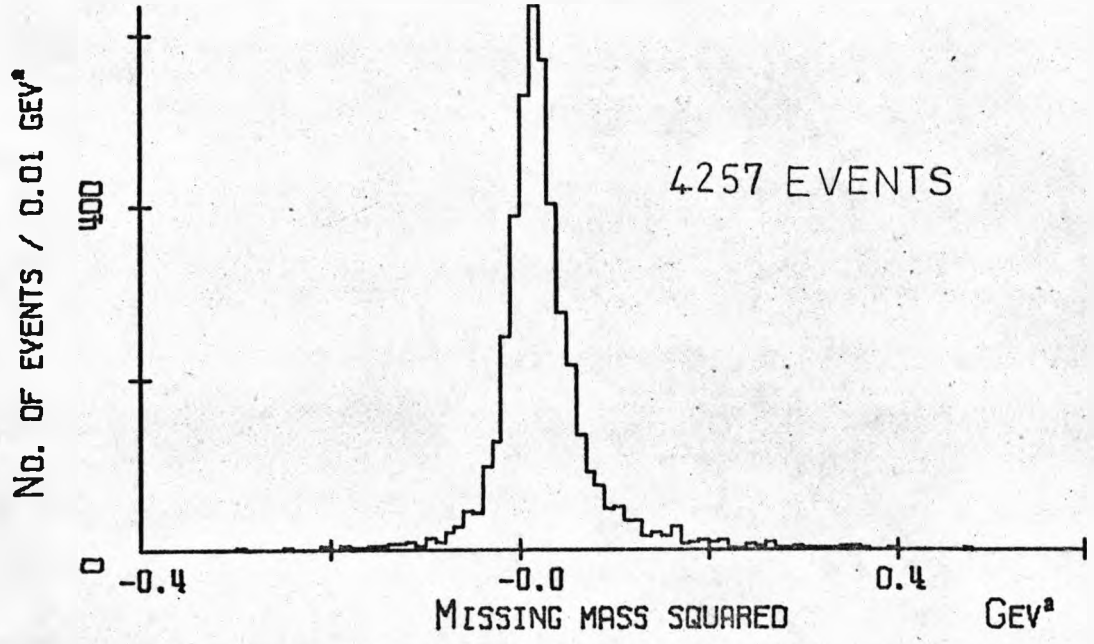

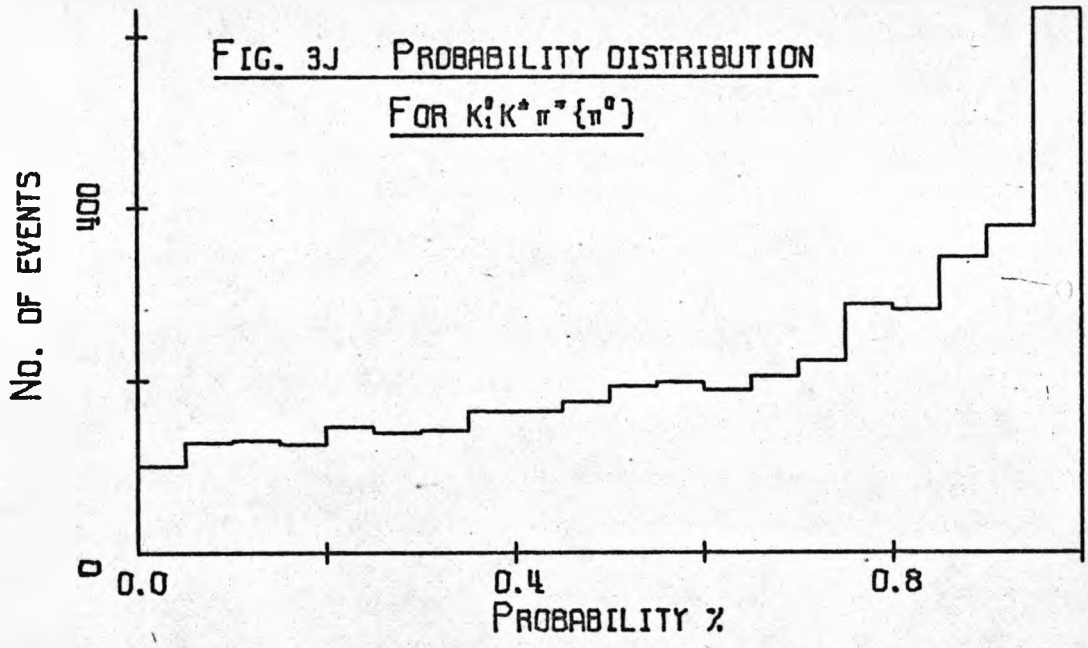

FIG. 3J PROBABILITY DISTRIBUTION FOR $K_1^0 K^* \pi^- (\pi^0)$

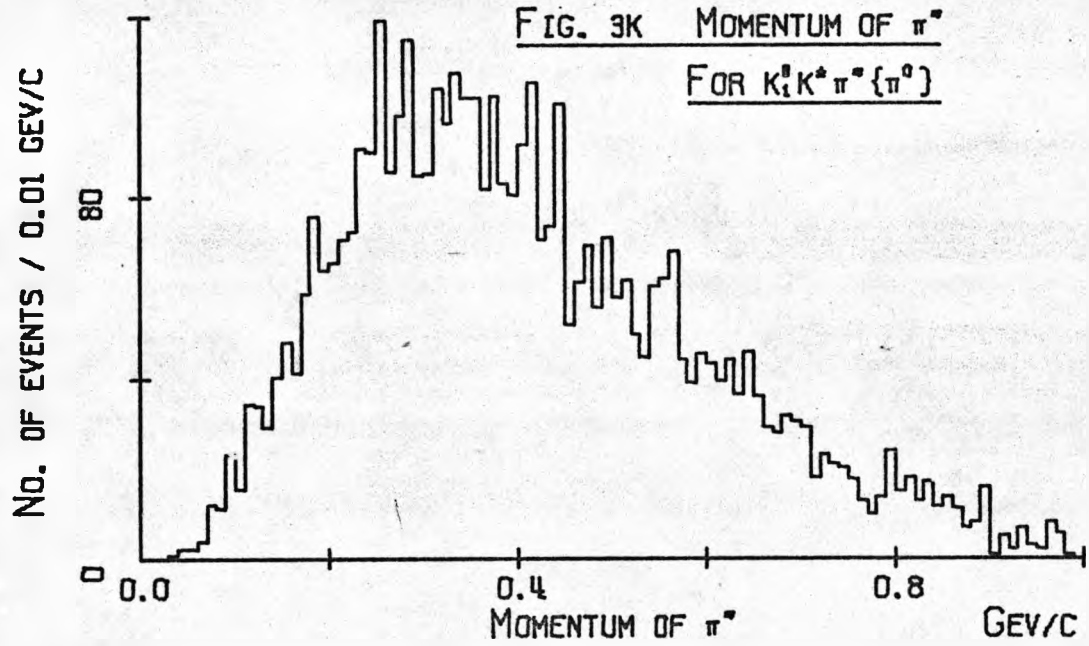

FIG. 3K MOMENTUM OF π^- FOR $K_1^0 K^* \pi^- (\pi^0)$

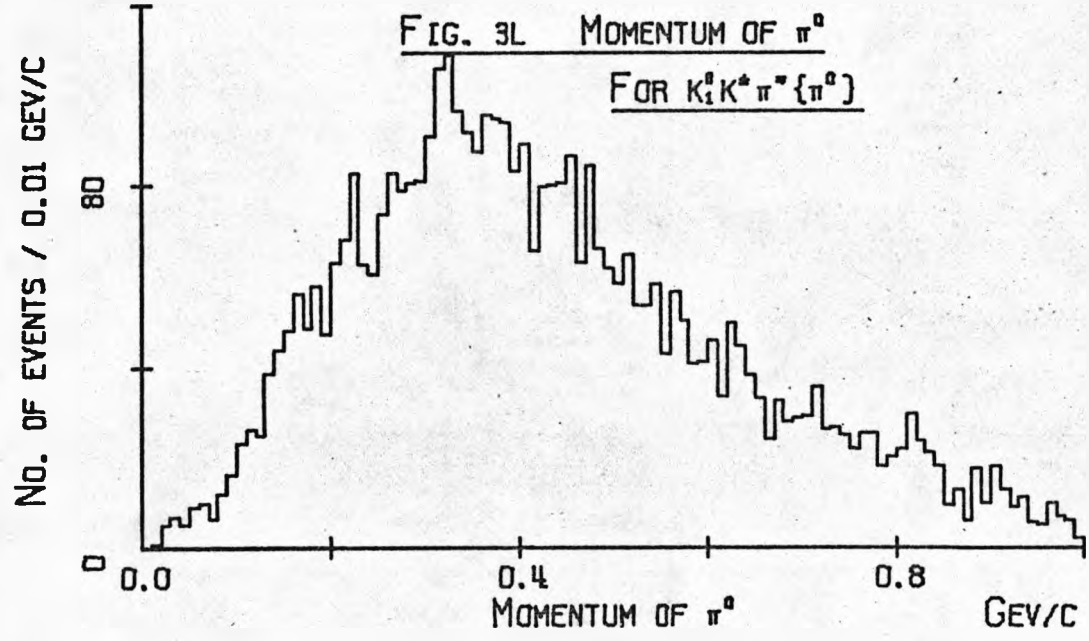

FIG. 3L MOMENTUM OF π^0 FOR $K_1^0 K^* \pi^- (\pi^0)$

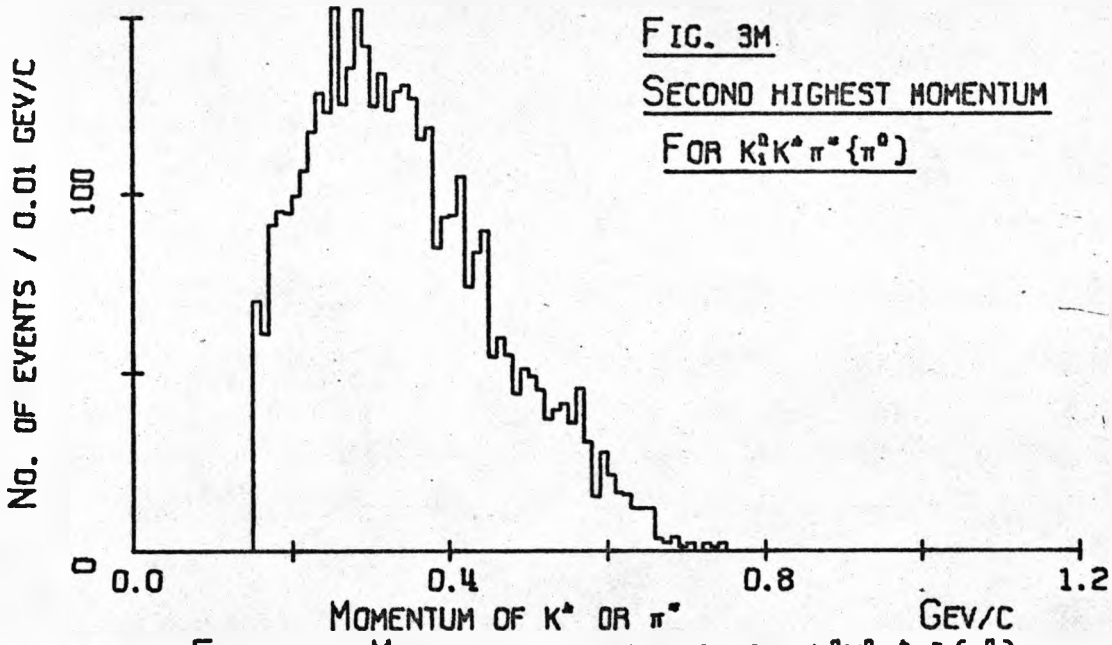

FIG. 3M
SECOND HIGHEST MOMENTUM
FOR $K_1^0 K^* \pi^* (\pi^0)$

FIG. 3N MISSING MASS SQUARED FOR $K_1^0 K_1^0 \pi^+ \pi^- (\pi^0)$

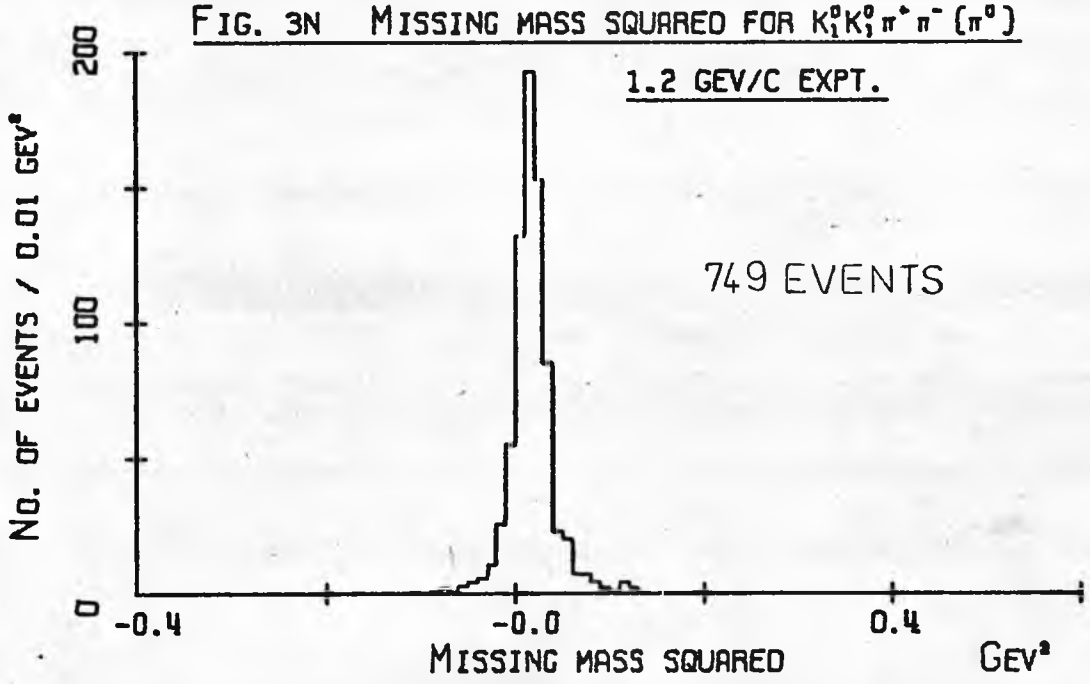

FIG. 3O MISSING MASS SQUARED FOR $K_1^0 K_1^0 \pi^+ \pi^- (\pi^0)$

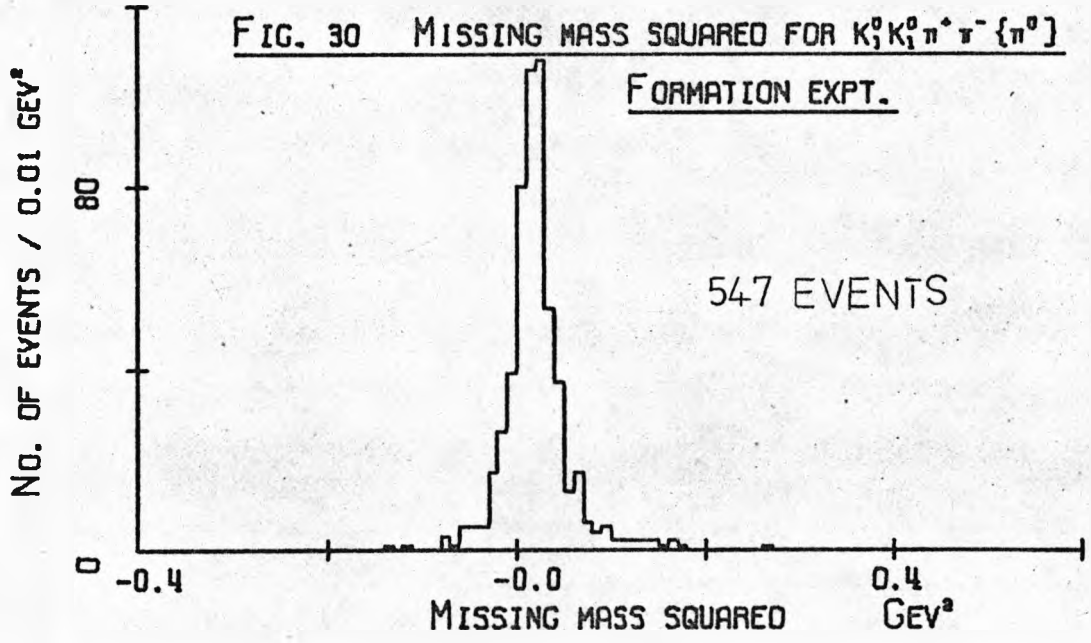

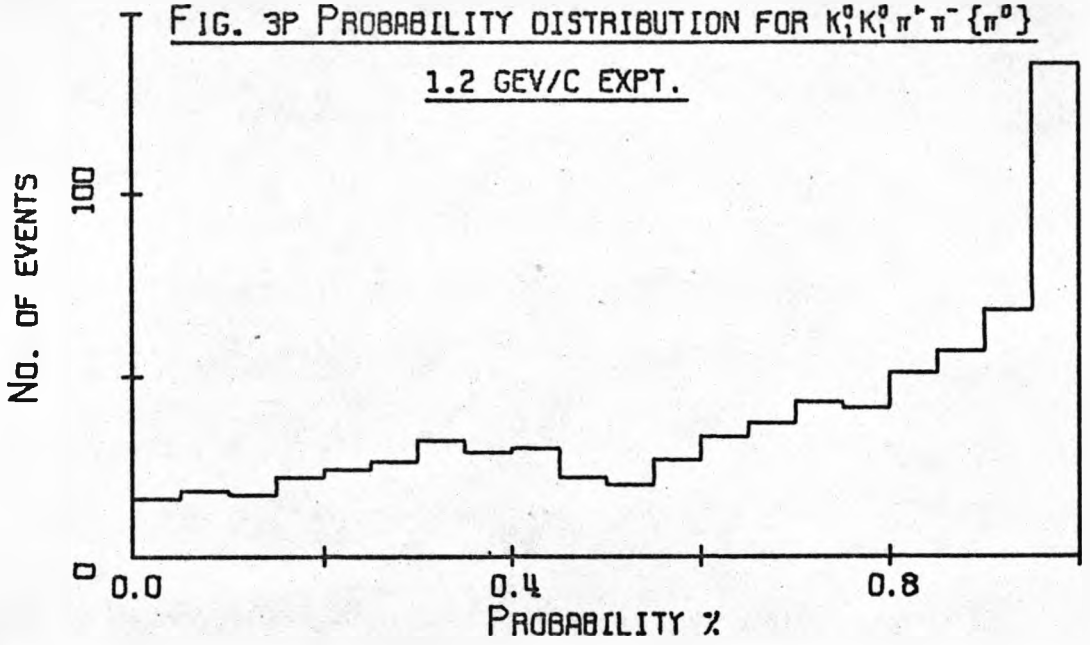
FIG. 3P PROBABILITY DISTRIBUTION FOR $K_1^0 K_1^0 \pi^+ \pi^- \{\pi^0\}$
1.2 GEV/C EXPT.
No. OF EVENTS
100
0
0.0
0.4
0.8
PROBABILITY %

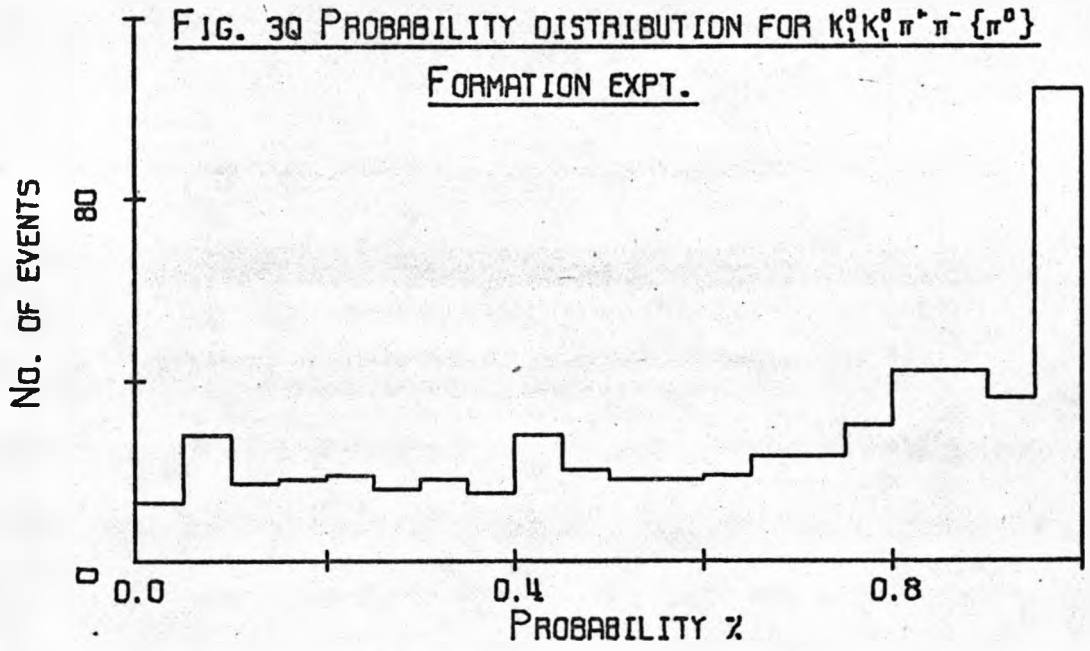
FIG. 3Q PROBABILITY DISTRIBUTION FOR $K_1^0 K_1^0 \pi^+ \pi^- \{\pi^0\}$
FORMATION EXPT.
No. OF EVENTS
80
0
0.0
0.4
0.8
PROBABILITY %

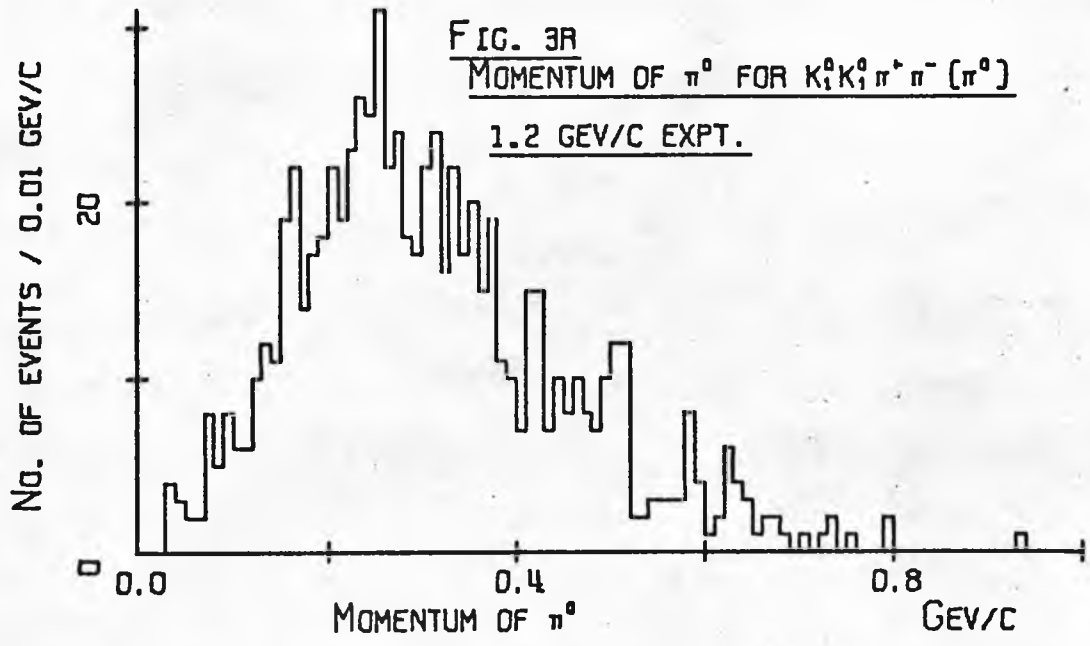
FIG. 3R
MOMENTUM OF π^0 FOR $K_1^0 K_1^0 \pi^+ \pi^- \{\pi^0\}$
1.2 GEV/C EXPT.
No. OF EVENTS / 0.01 GEV/C
20
0
0.0
0.4
0.8
MOMENTUM OF π^0
GEV/C

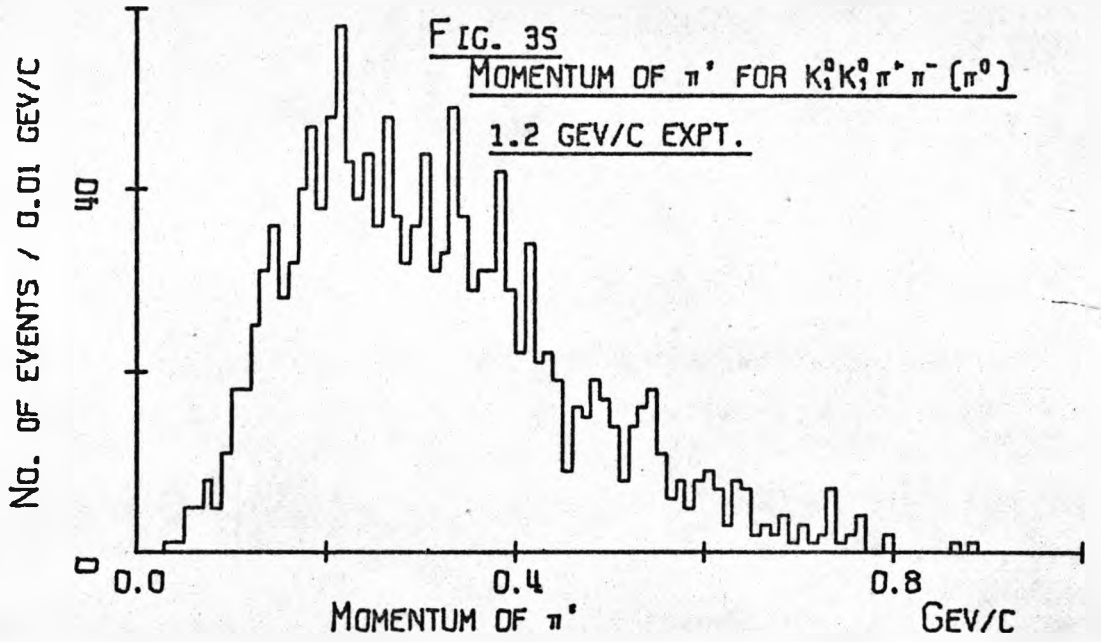
FIG. 3S
MOMENTUM OF π⁺ FOR K₁⁰K₁⁰π⁺π⁻(π⁰)
1.2 GEV/C EXPT.
NO. OF EVENTS / 0.01 GEV/C
40
0
0.0
0.4
0.8
MOMENTUM OF π⁺
GEV/C

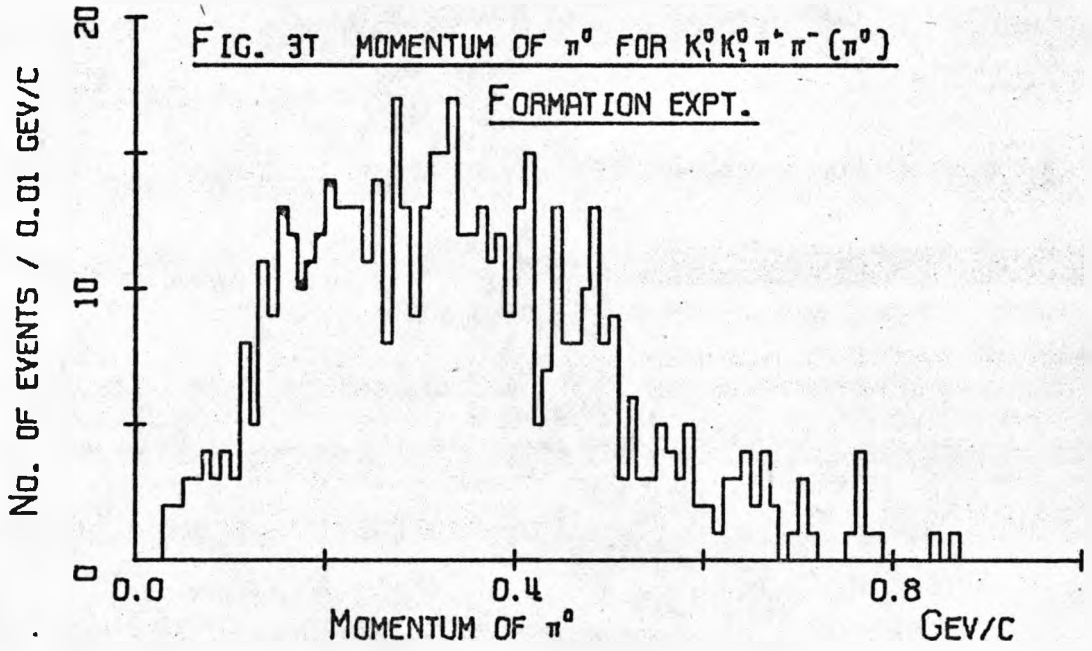
FIG. 3T MOMENTUM OF π⁰ FOR K₁⁰K₁⁰π⁺π⁻(π⁰)
FORMATION EXPT.
NO. OF EVENTS / 0.01 GEV/C
20
10
0
0.0
0.4
0.8
MOMENTUM OF π⁰
GEV/C

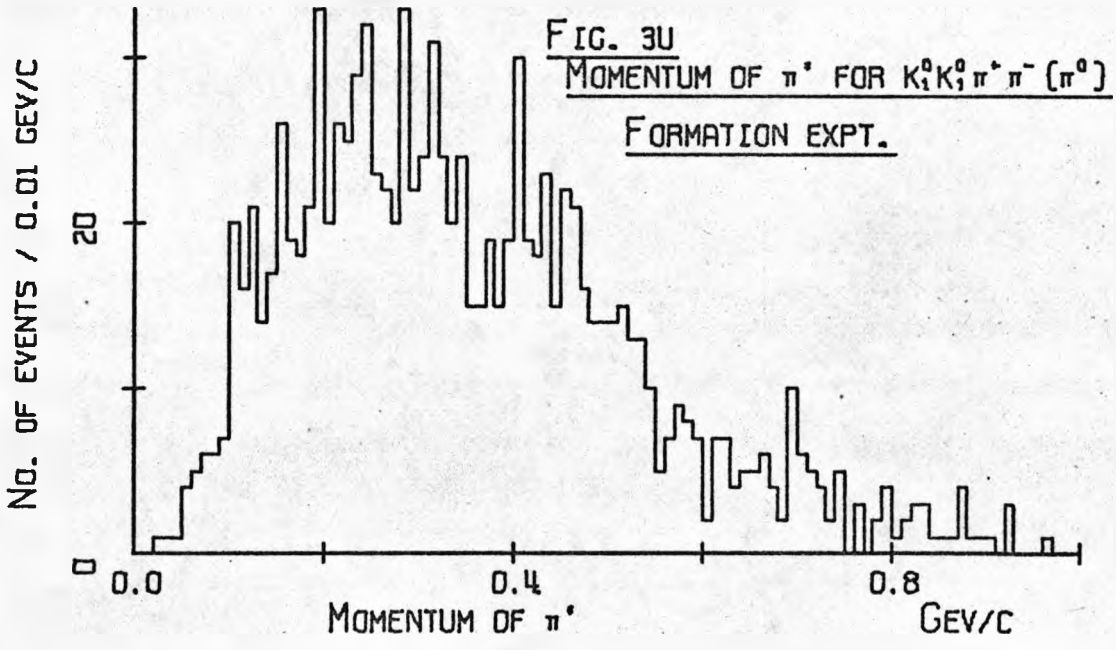
FIG. 3U
MOMENTUM OF π⁺ FOR K₁⁰K₁⁰π⁺π⁻(π⁰)
FORMATION EXPT.
NO. OF EVENTS / 0.01 GEV/C
20
0
0.0
0.4
0.8
MOMENTUM OF π⁺
GEV/C

FIG. 3V

DEVIATION FROM EXPECTED BEAM DIRECTION

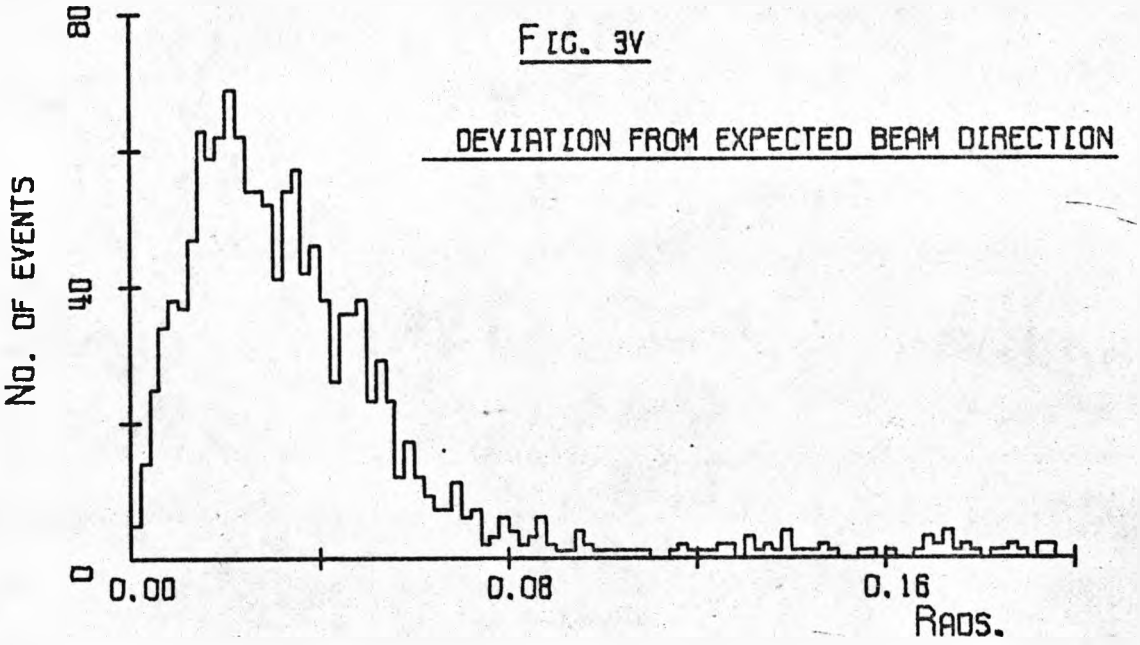

FIG. 3W

$PP \to K_1^0 K_2^0 \pi^+ \pi^-$

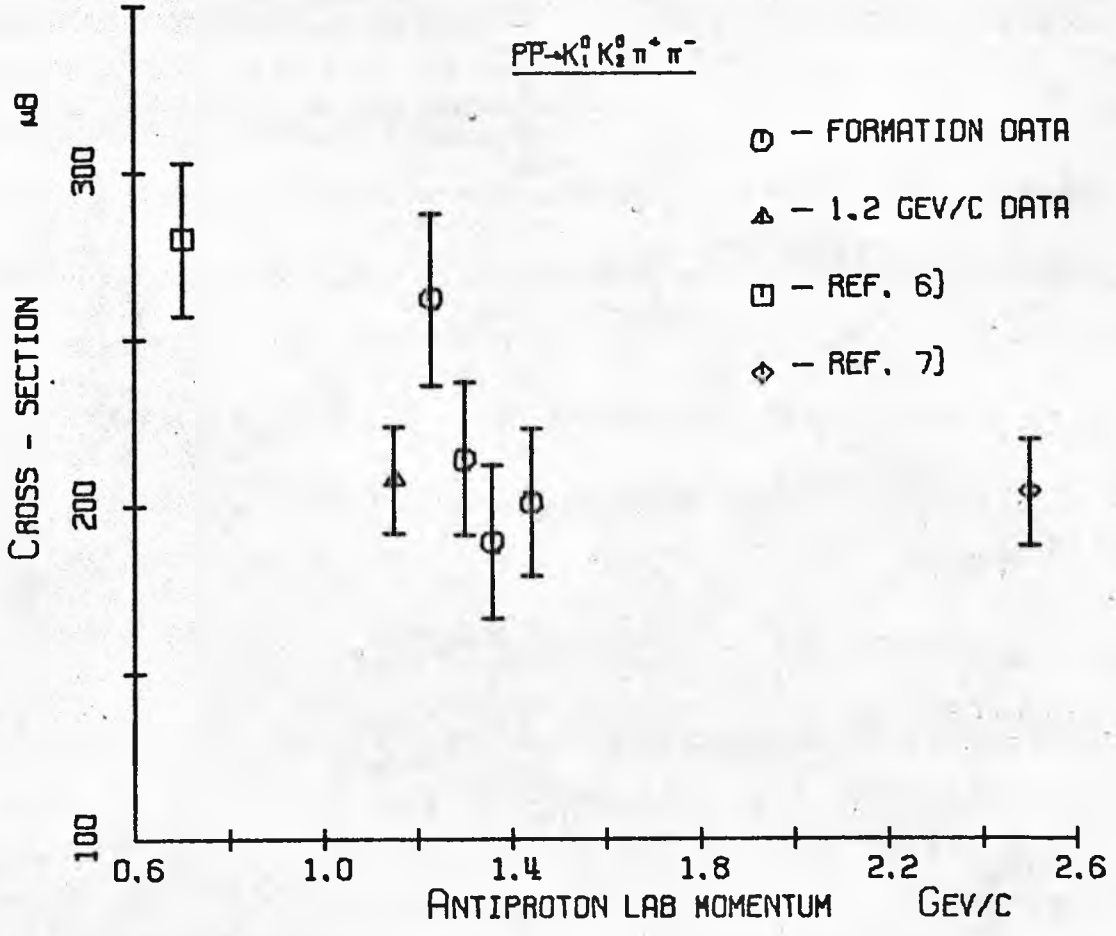

FIG. 3X

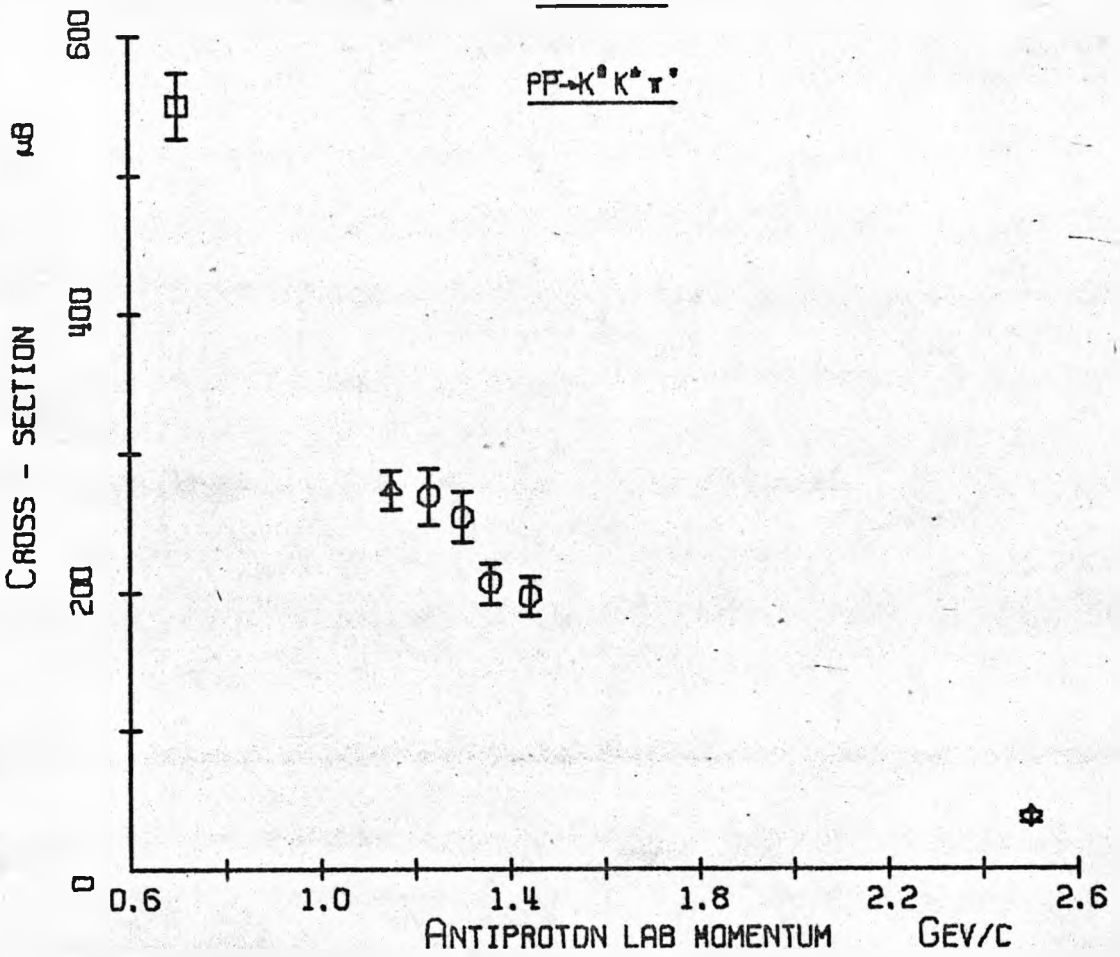
$\bar{P}P \to K^0 K^+ \pi^-$
CROSS - SECTION
μB
600
400
200
0
0.6
1.0
1.4
1.8
2.2
2.6
ANTIPROTON LAB MOMENTUM
GEV/C

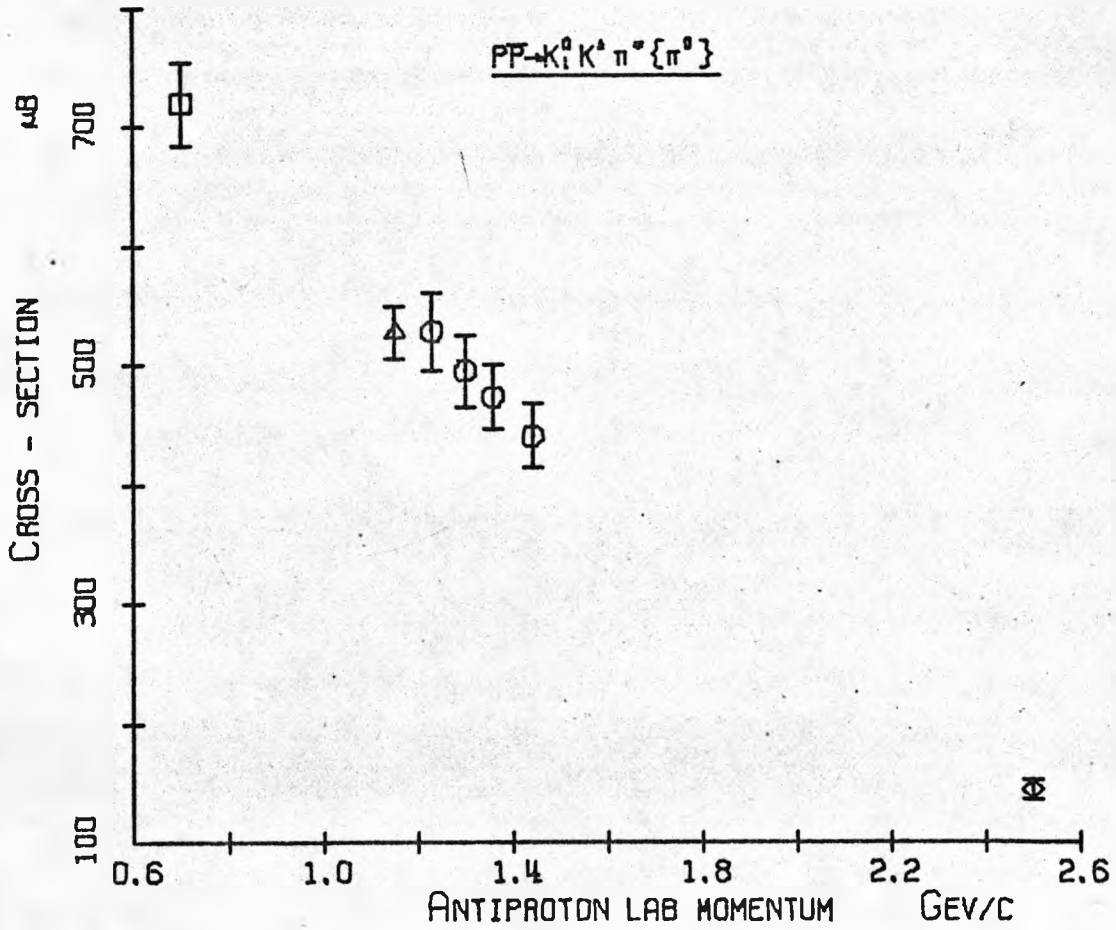
$\bar{P}P \to K_1^0 K^+ \pi^- \{\pi^0\}$
CROSS - SECTION
μB
700
500
300
100
0.6
1.0
1.4
1.8
2.2
2.6
ANTIPROTON LAB MOMENTUM
GEV/C

FIG. 3Y

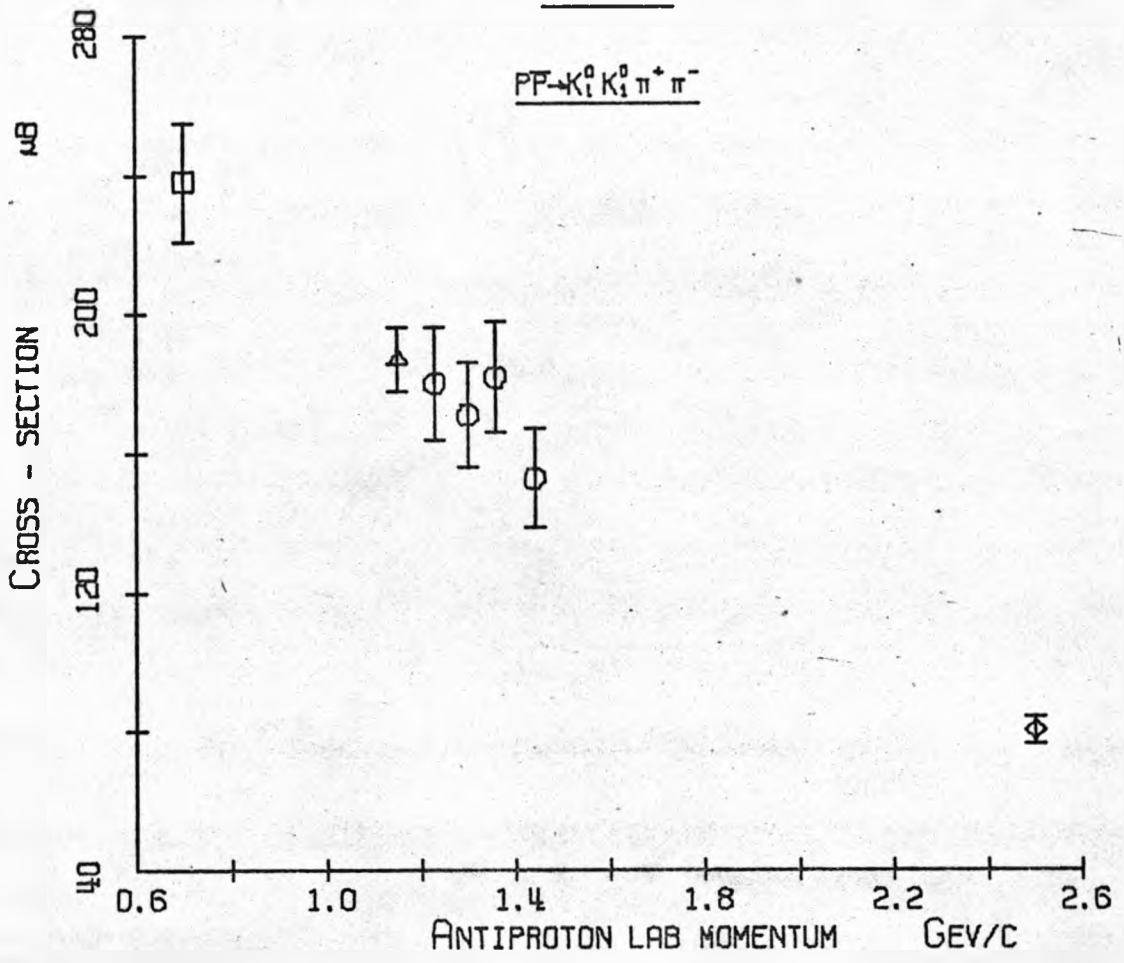
$\bar{P}P \to K_1^0 K_1^0 \pi^+ \pi^-$
CROSS - SECTION
μB
280
200
120
40
0.6
1.0
1.4
1.8
2.2
2.6
ANTIPROTON LAB MOMENTUM
GEV/C

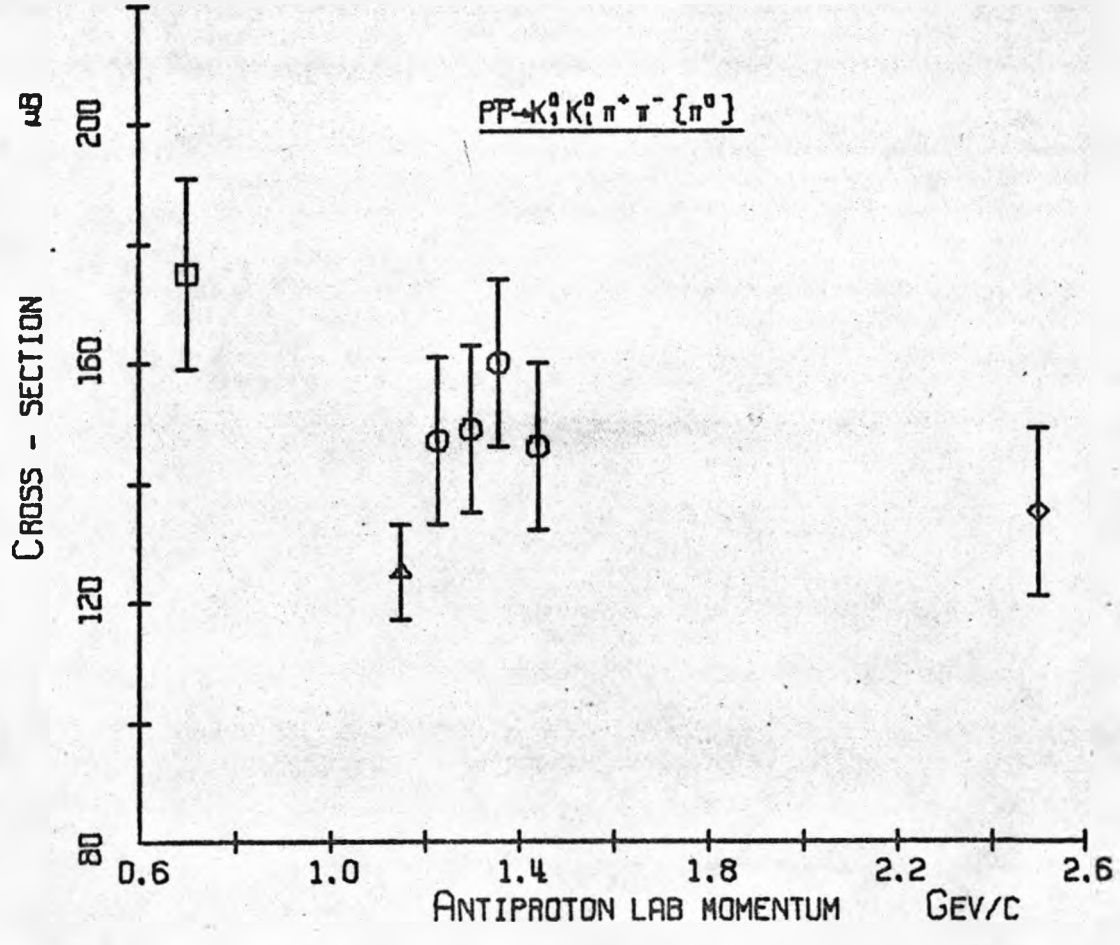
$\bar{P}P \to K_1^0 K_1^0 \pi^+ \pi^- \{\pi^0\}$
CROSS - SECTION
μB
200
160
120
80
0.6
1.0
1.4
1.8
2.2
2.6
ANTIPROTON LAB MOMENTUM
GEV/C

FIG. 5A PRODUCTION DALITZ PLOT FOR $\bar{p}p \to K_1^0 K^* \pi^+$

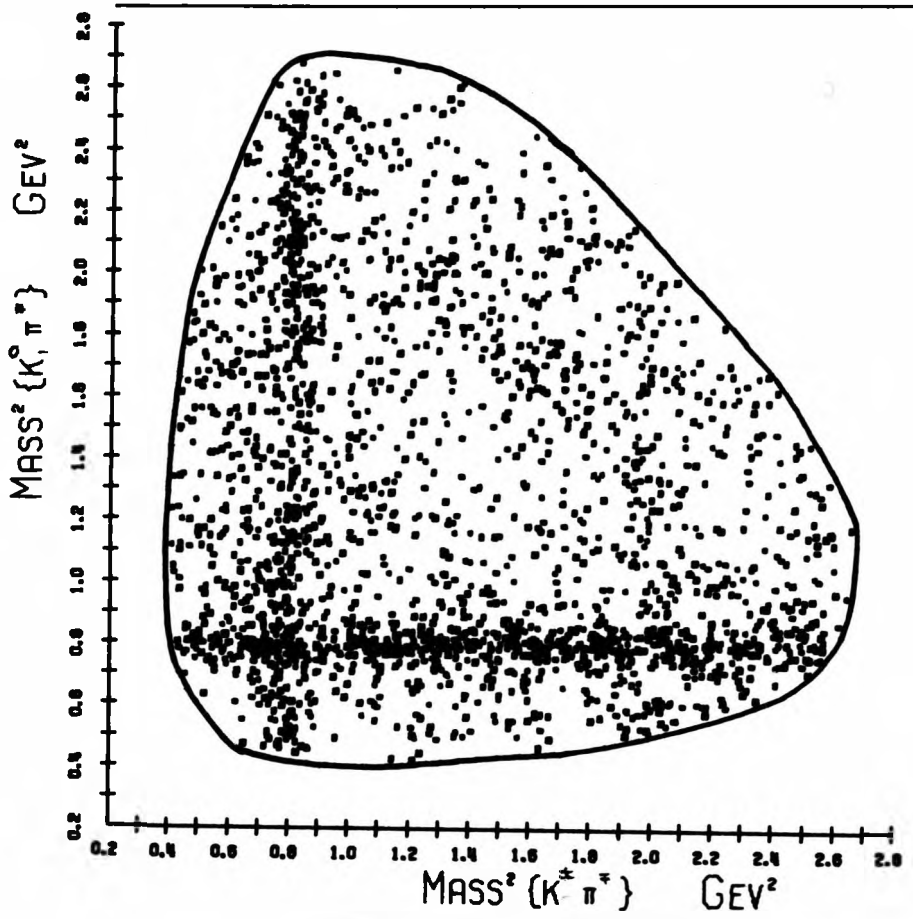

FIG. 5B DALITZ PLOT (CONTOUR)

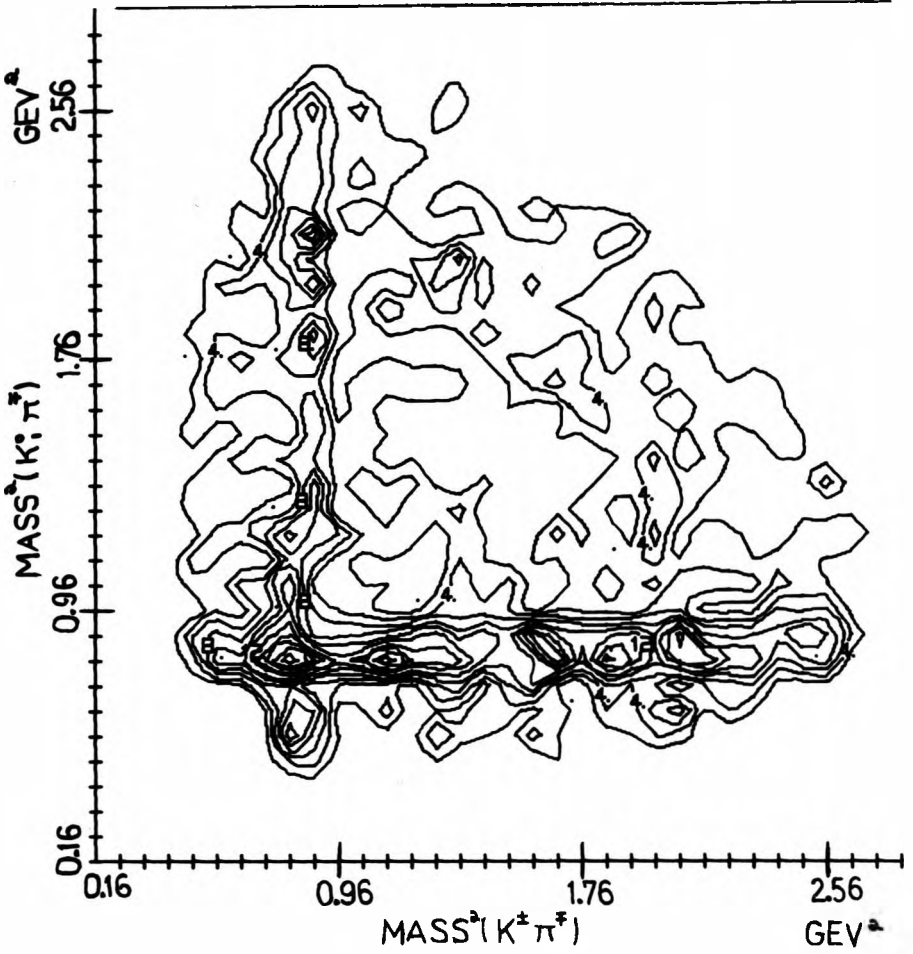

FIG. 5C $K_1^0 K^{\pm}\pi^{\mp}$ DISTRIBUTIONS

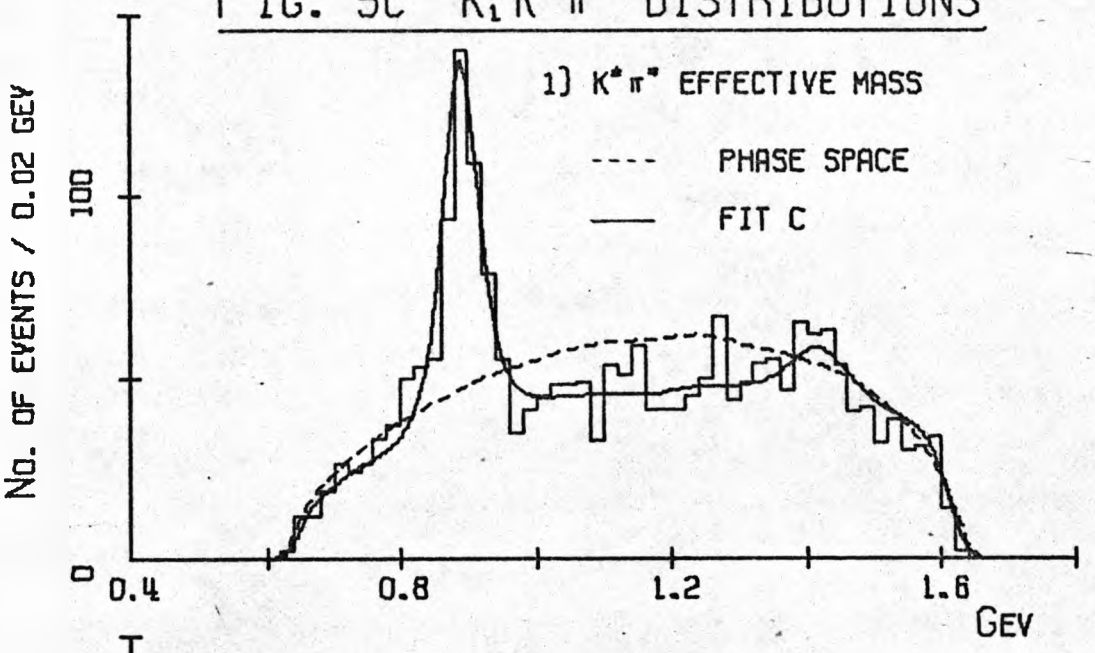

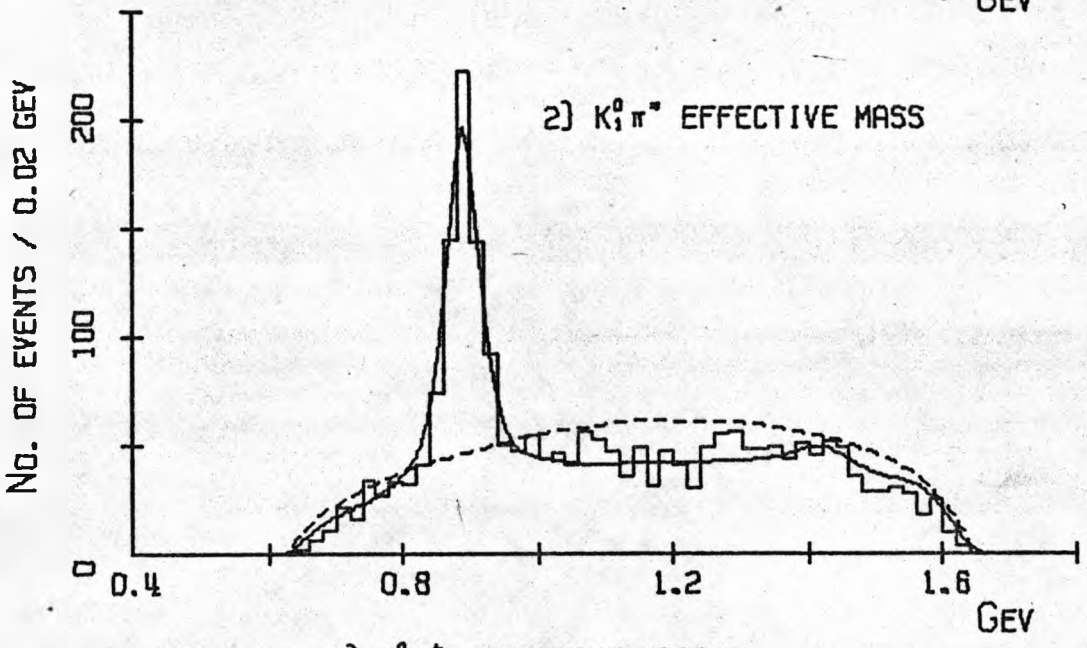

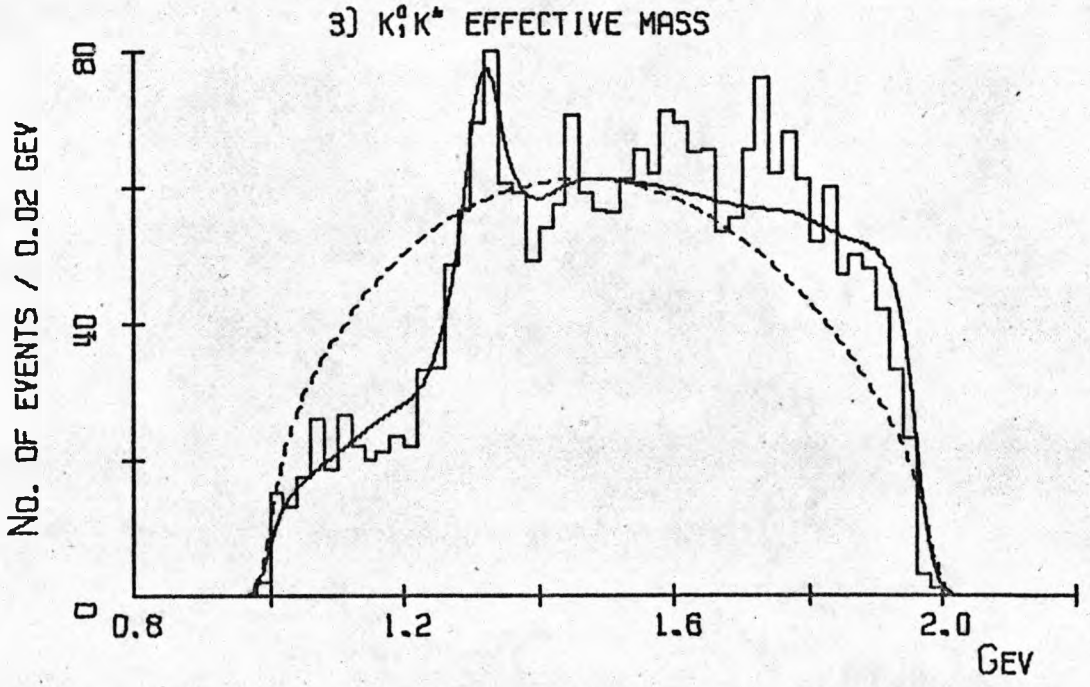

FIG. 5C {CONTD.}

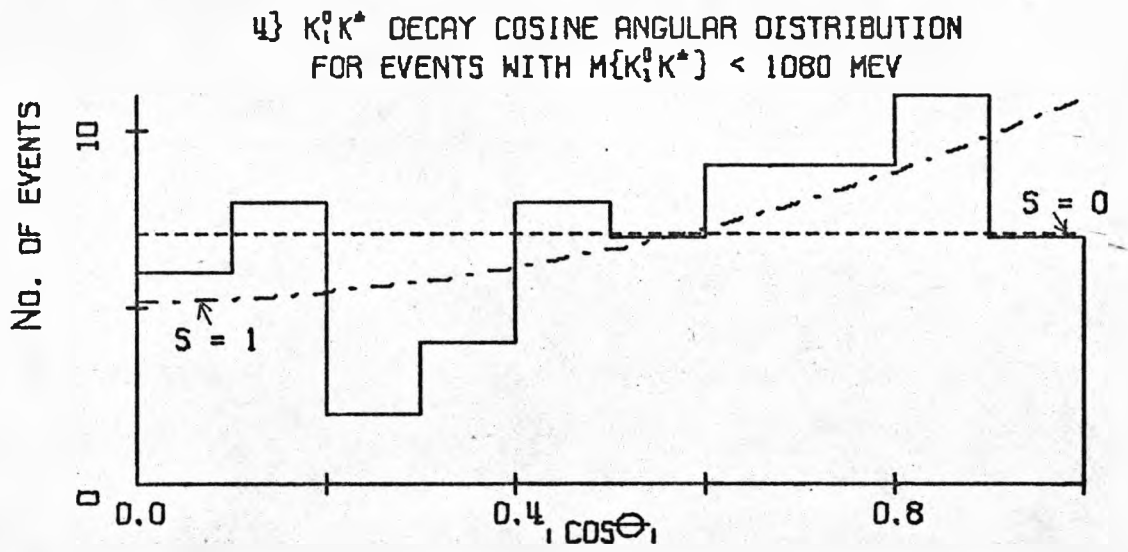

FIG. 5D $K_1^0K^*\pi^*\{\pi^0\}$ DISTRIBUTIONS

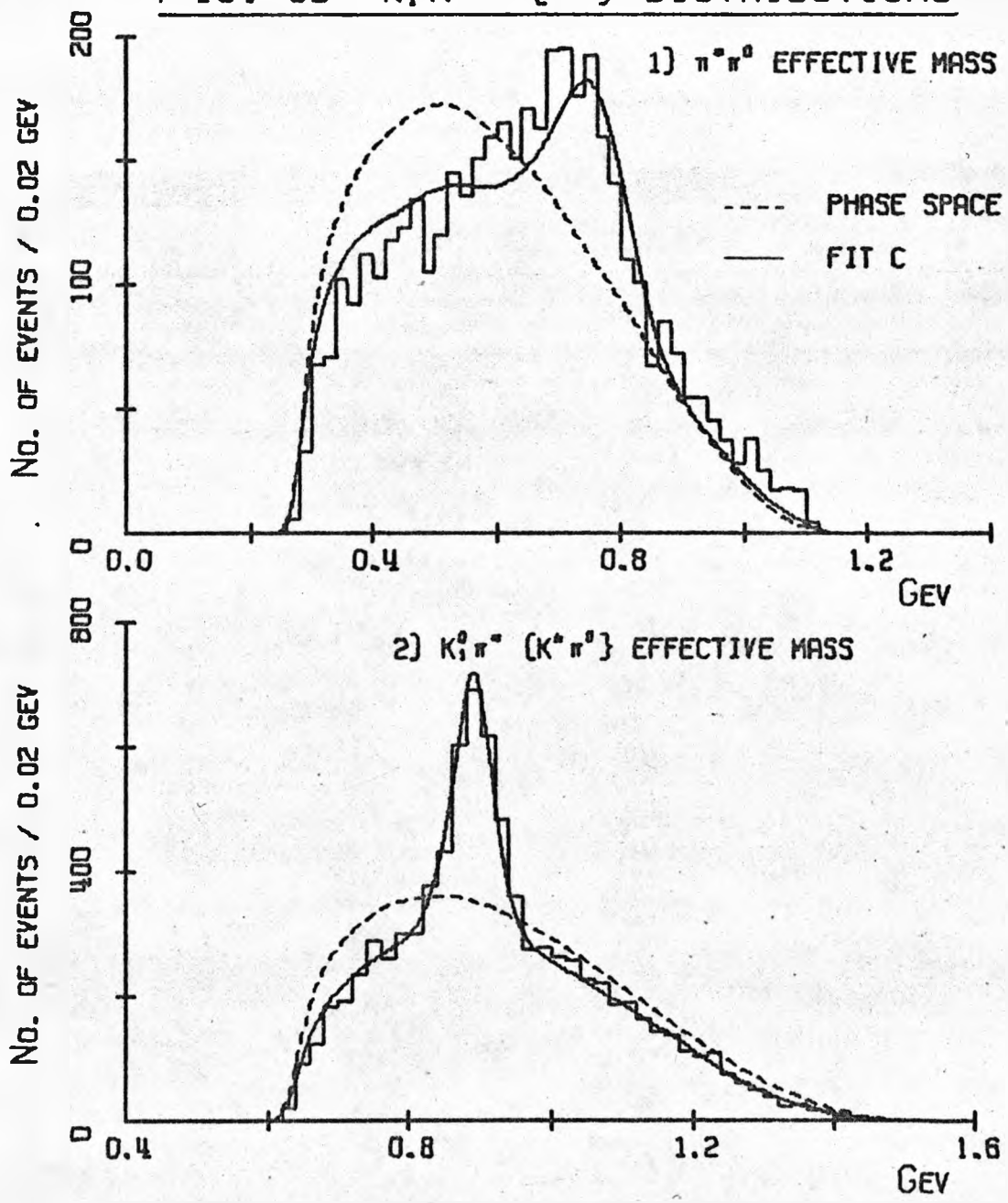

FIG. 5D {CONTD.}

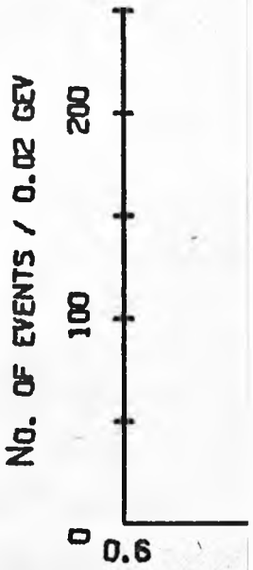
No. OF EVENTS / 0.02 GEV
200
100
0
0.6

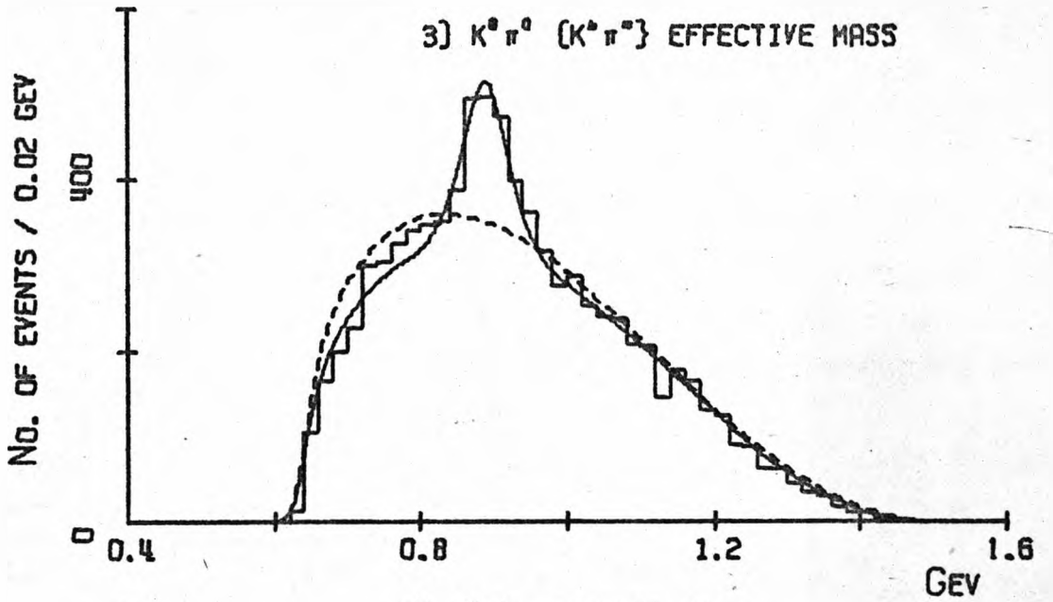
3) K*π° (K*π°) EFFECTIVE MASS
No. OF EVENTS / 0.02 GEV
400
0
0.4
0.8
1.2
1.6
GEV

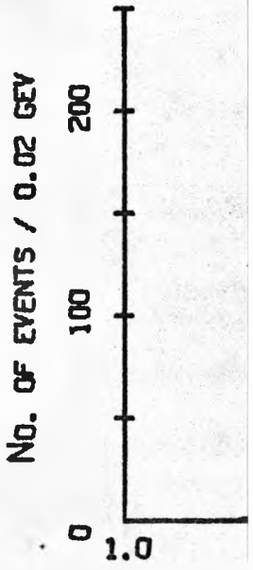
No. OF EVENTS / 0.02 GEV
200
100
0
1.0

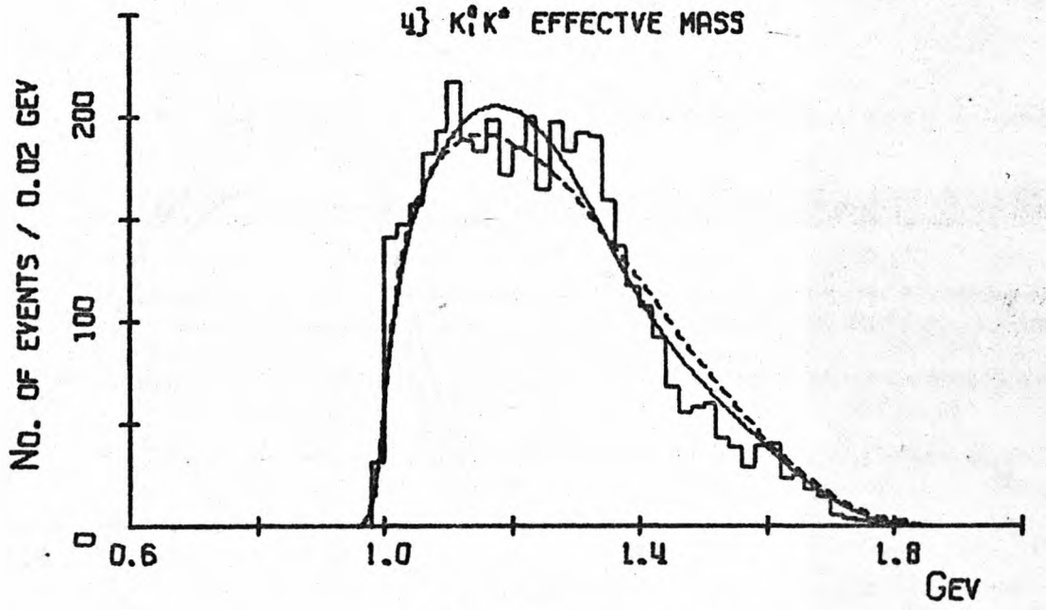
4) K°K* EFFECTVE MASS
No. OF EVENTS / 0.02 GEV
200
100
0
0.6
1.0
1.4
1.8
GEV

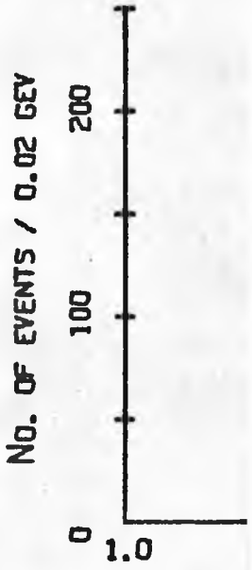
No. OF EVENTS / 0.02 GEV
200
100
0
1.0

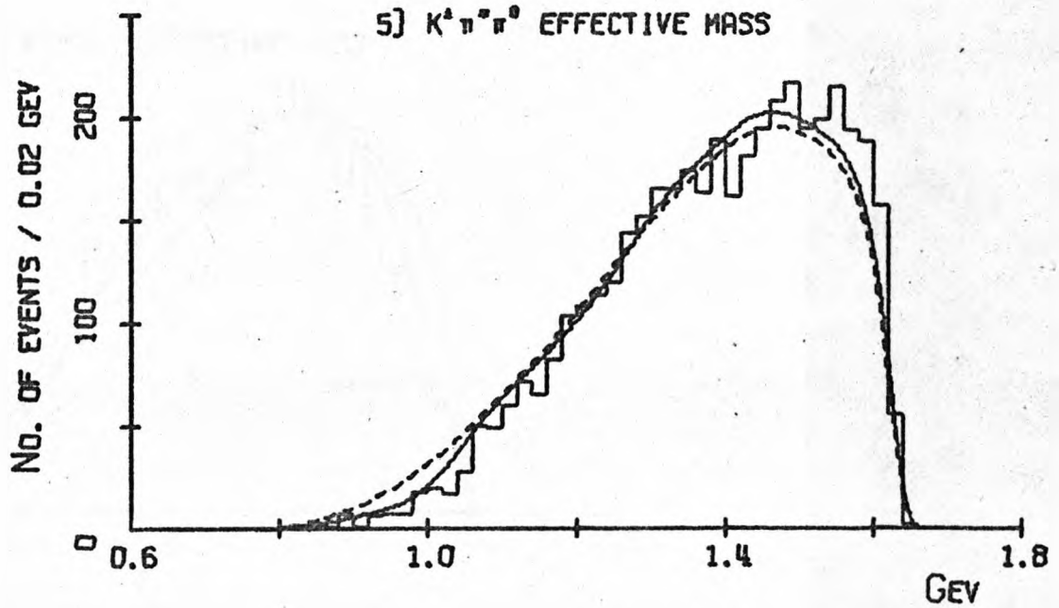
5) K*π°π° EFFECTIVE MASS
No. OF EVENTS / 0.02 GEV
200
100
0
0.6
1.0
1.4
1.8
GEV

FIG. 5D {CONTD.}

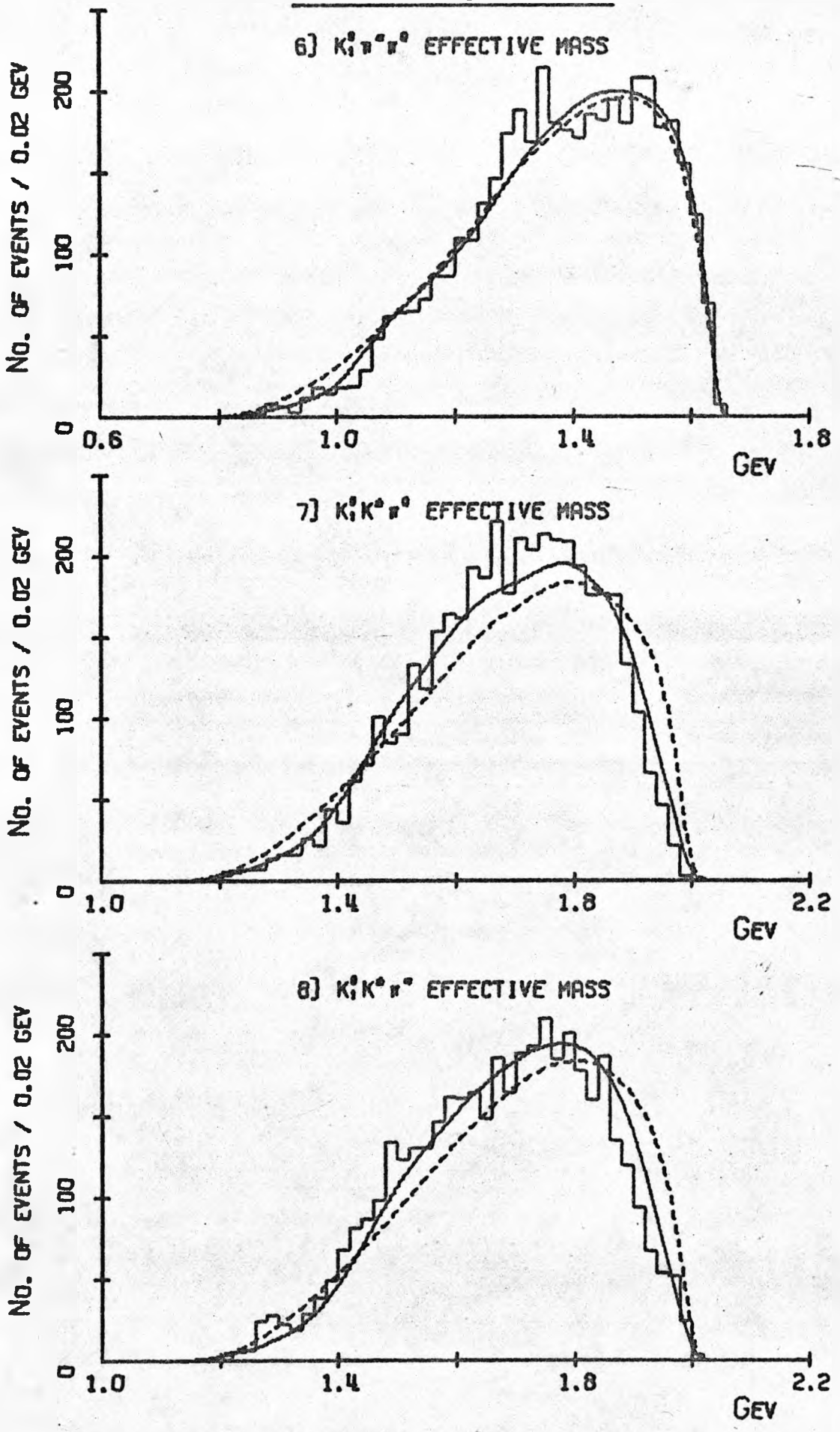
6] $K_1^0\pi^+\pi^0$ EFFECTIVE MASS
No. OF EVENTS / 0.02 GEV
0
100
200
0.6
1.0
1.4
1.8
GEV
7] $K_1^0K^+\pi^0$ EFFECTIVE MASS
No. OF EVENTS / 0.02 GEV
0
100
200
1.0
1.4
1.8
2.2
GEV
8] $K_1^0K^+\pi^-$ EFFECTIVE MASS
No. OF EVENTS / 0.02 GEV
0
100
200
1.0
1.4
1.8
2.2
GEV

FIG. 5E SCATTER PLOT FOR $\bar{P}P \to K_1^0 K^* \pi^* \{\pi^0\}$

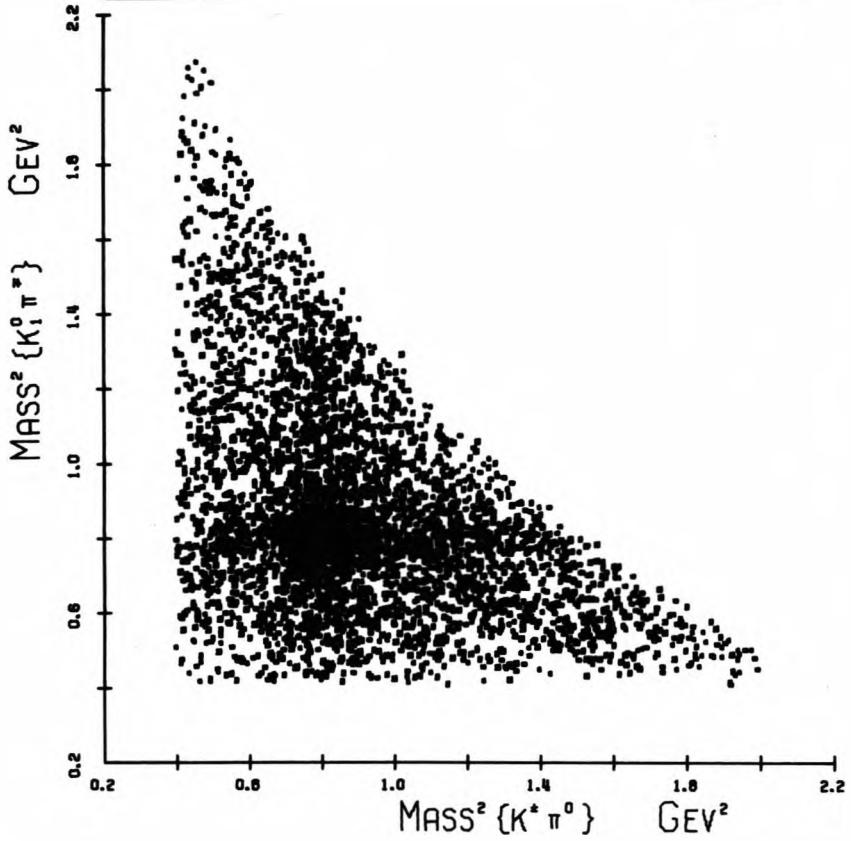

FIG. 5E (CONTD.)

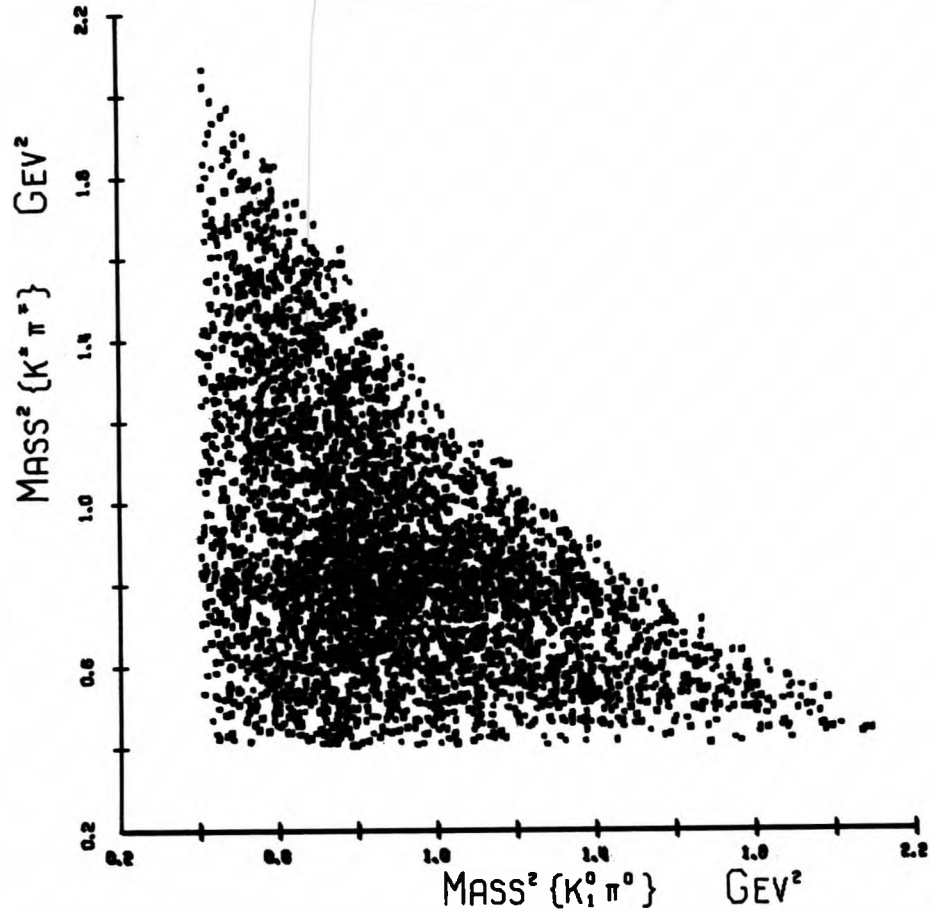

FIG. 5E (CONTD.)

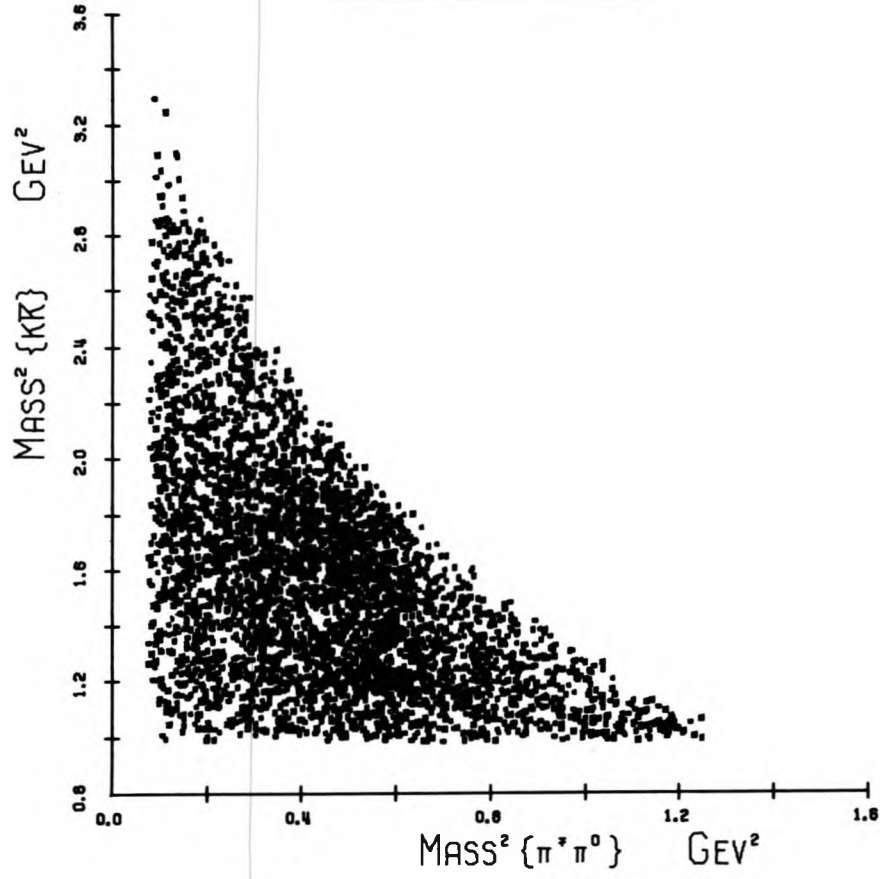

FIG. 5F $K^0_1 K^* \pi^* \{\pi^0\}$ DISTRIBUTIONS

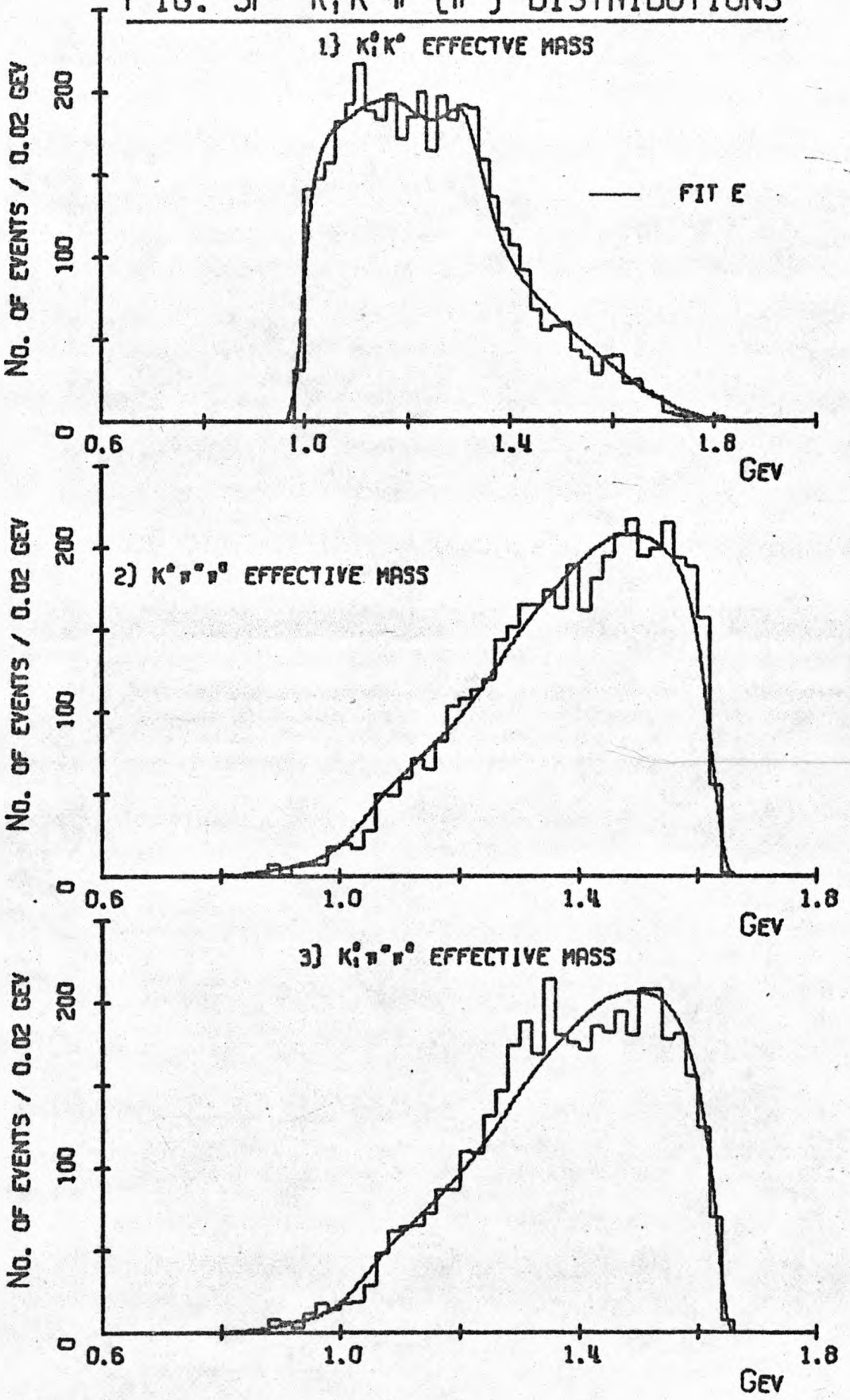

FIG. 5F {CONTD.}

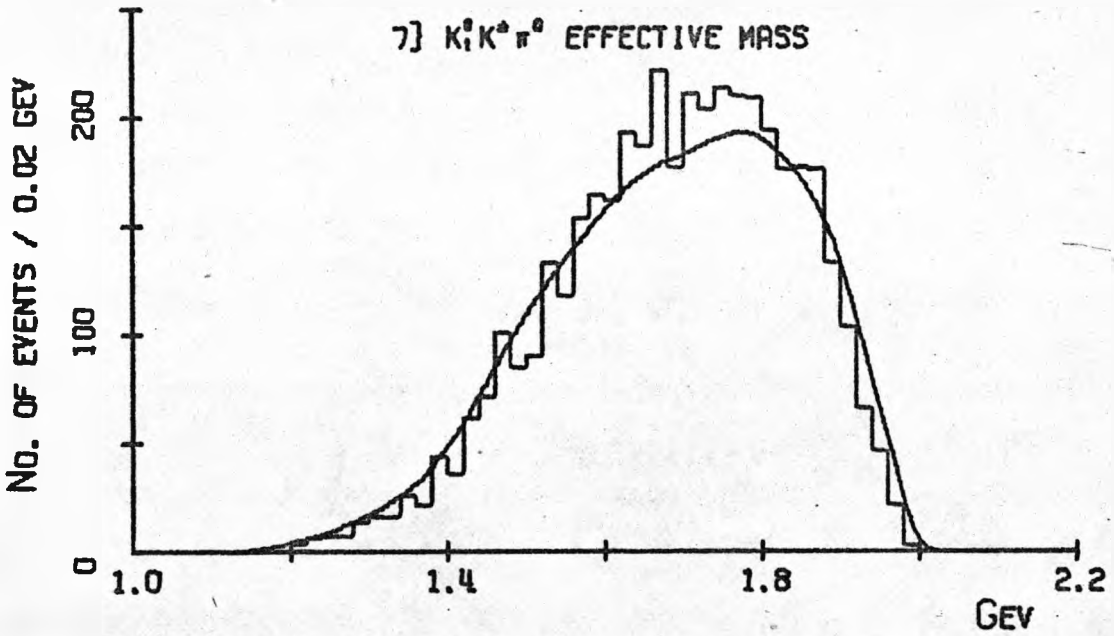

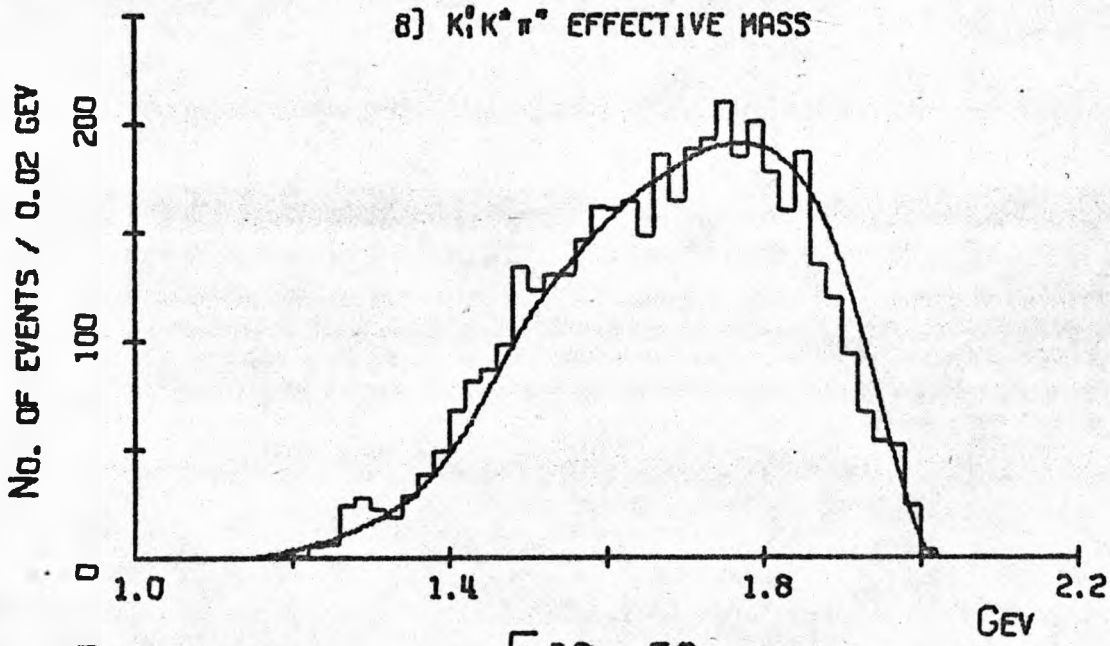

FIG. 5G

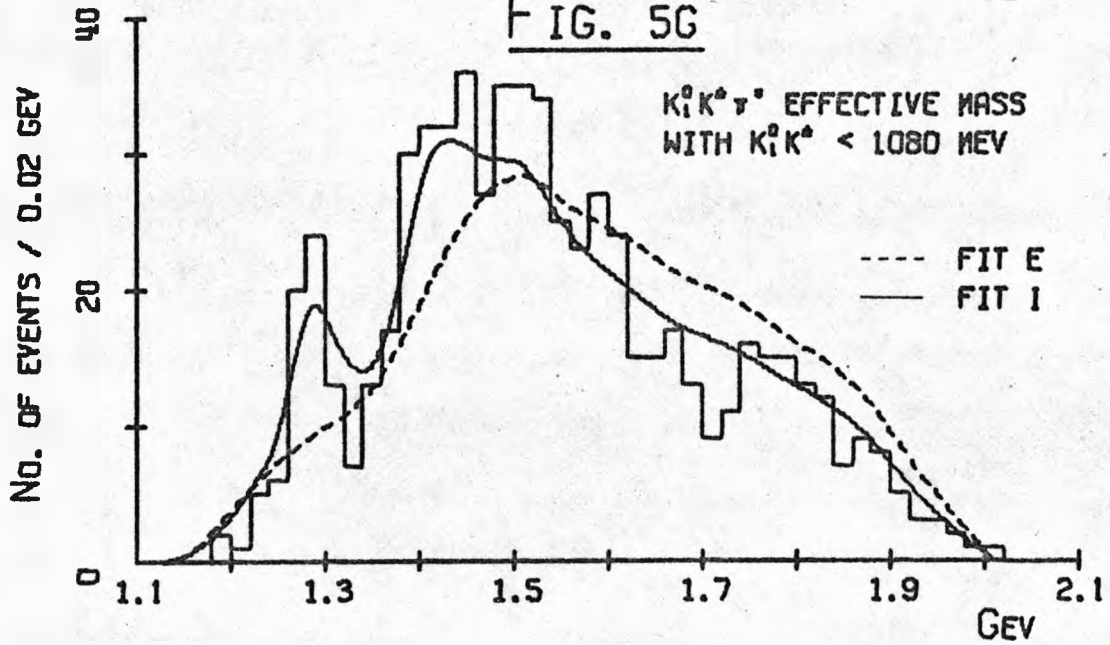

FIG. 5H $K^0_1 K^* \pi^- \{\pi^0\}$ DISTRIBUTIONS

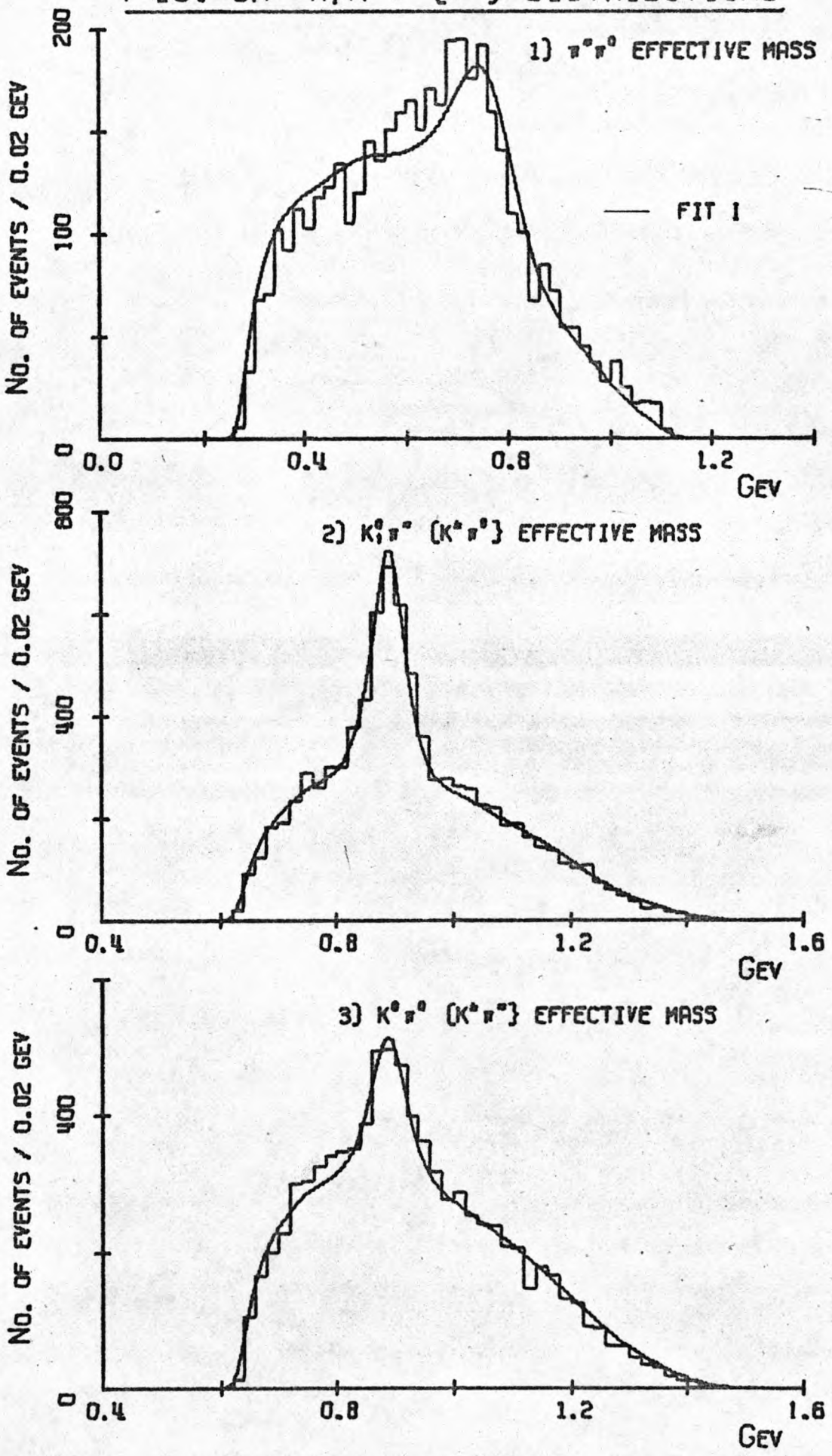

FIG. 5H (CONTD.)

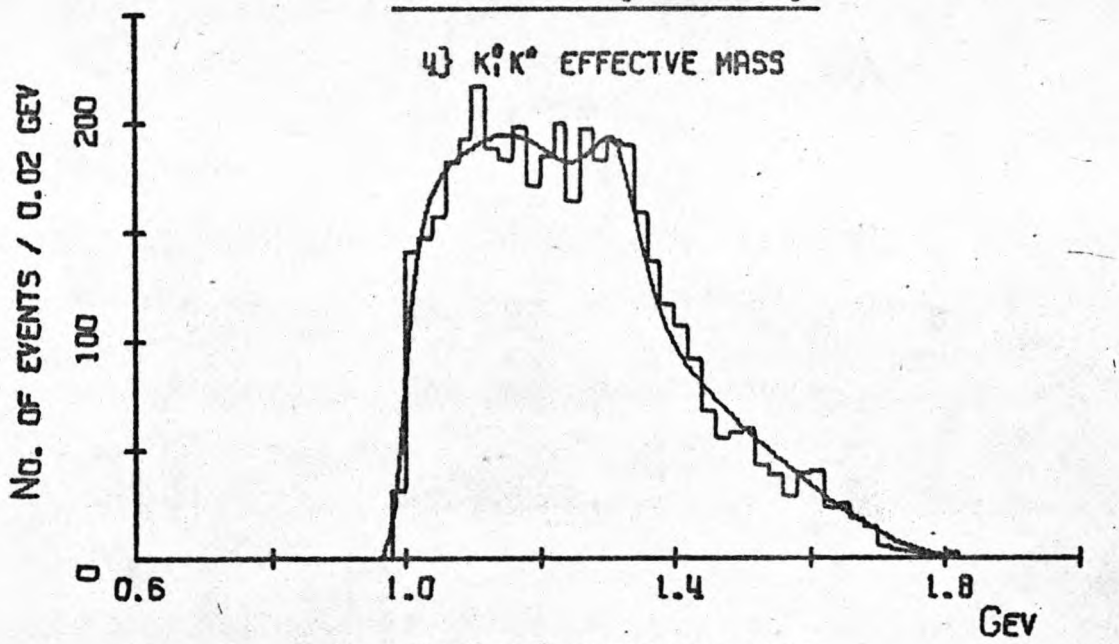
4) $K_1^0 K^+$ EFFECTVE MASS
No. OF EVENTS / 0.02 GEV
0
100
200
0.6
1.0
1.4
1.8
GEV

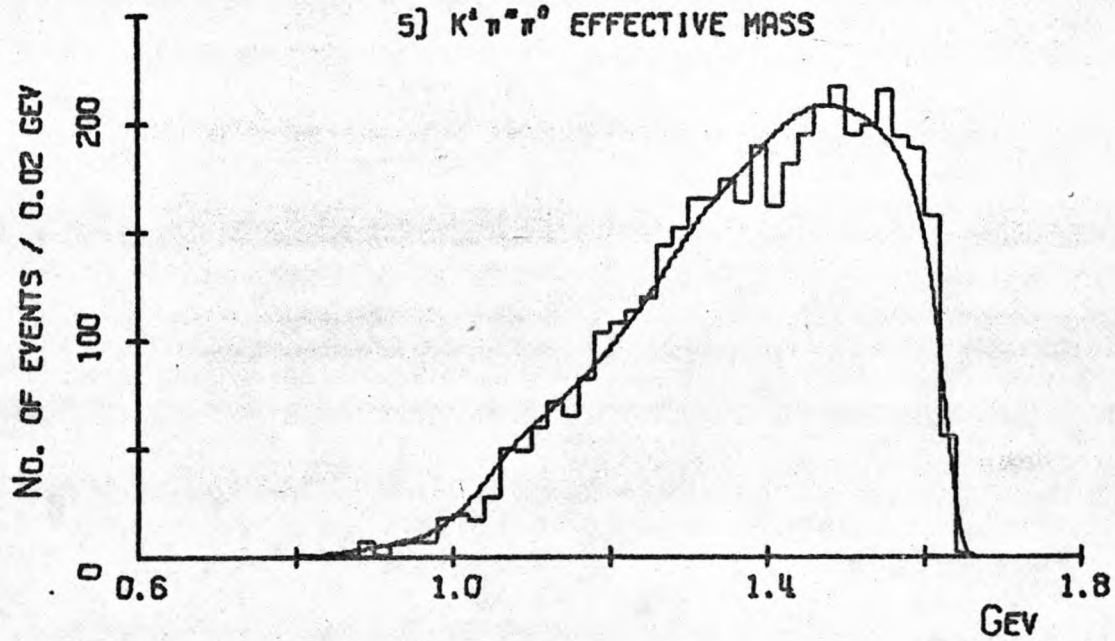
5] $K^+\pi^-\pi^0$ EFFECTIVE MASS
No. OF EVENTS / 0.02 GEV
0
100
200
0.6
1.0
1.4
1.8
GEV

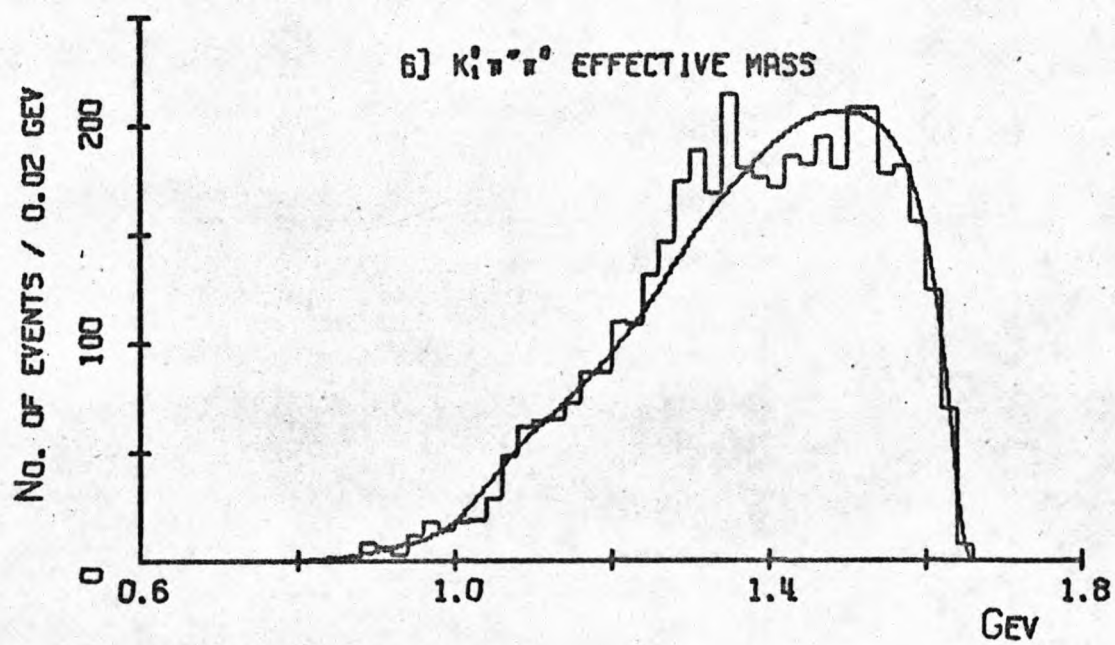
6] $K_1^0\pi^-\pi^0$ EFFECTIVE MASS
No. OF EVENTS / 0.02 GEV
0
100
200
0.6
1.0
1.4
1.8
GEV

FIG. 5H {CONTD.}

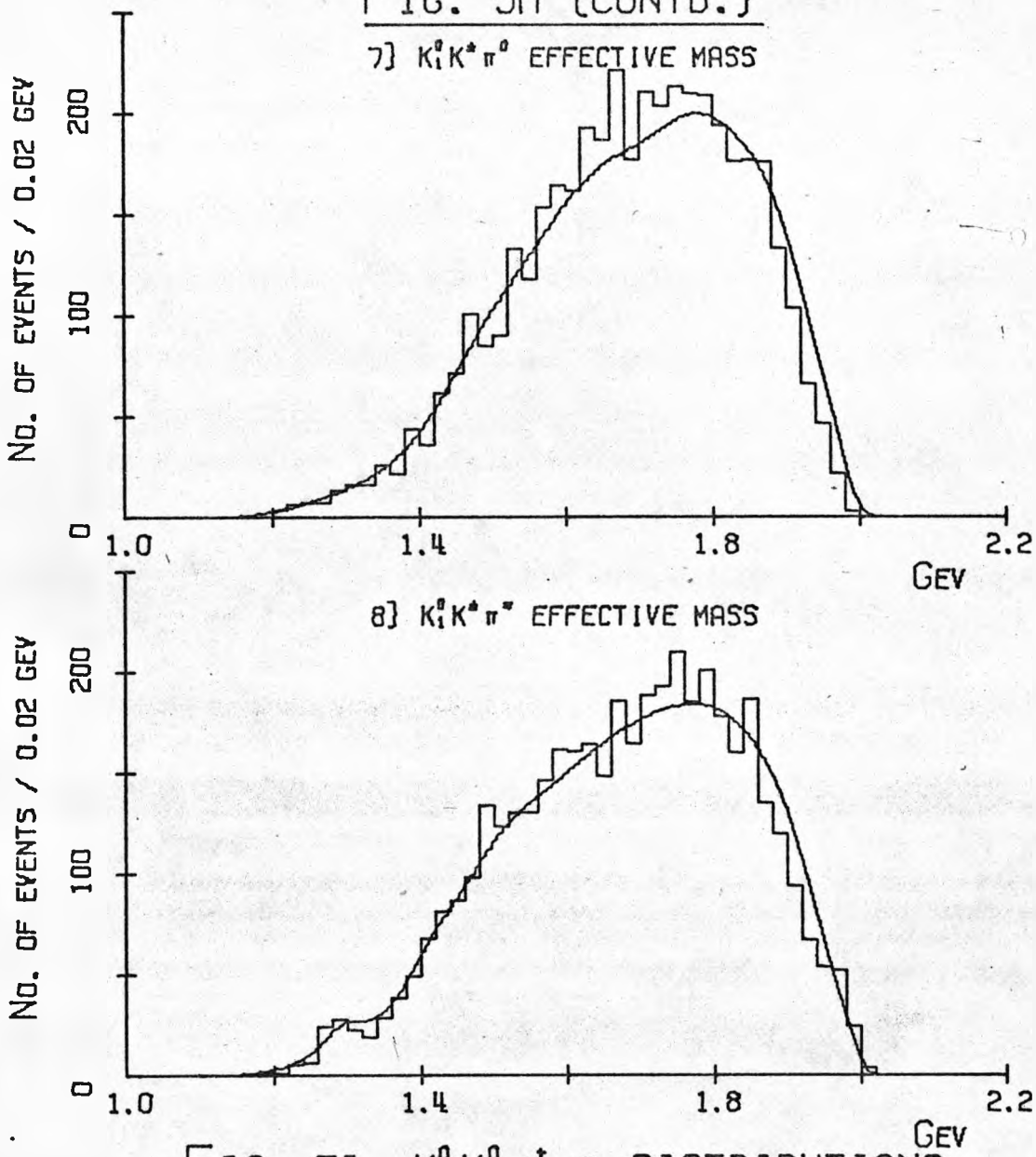

FIG. 5I $K_1^0 K_1^0 \pi^+ \pi^-$ DISTRIBUTIONS

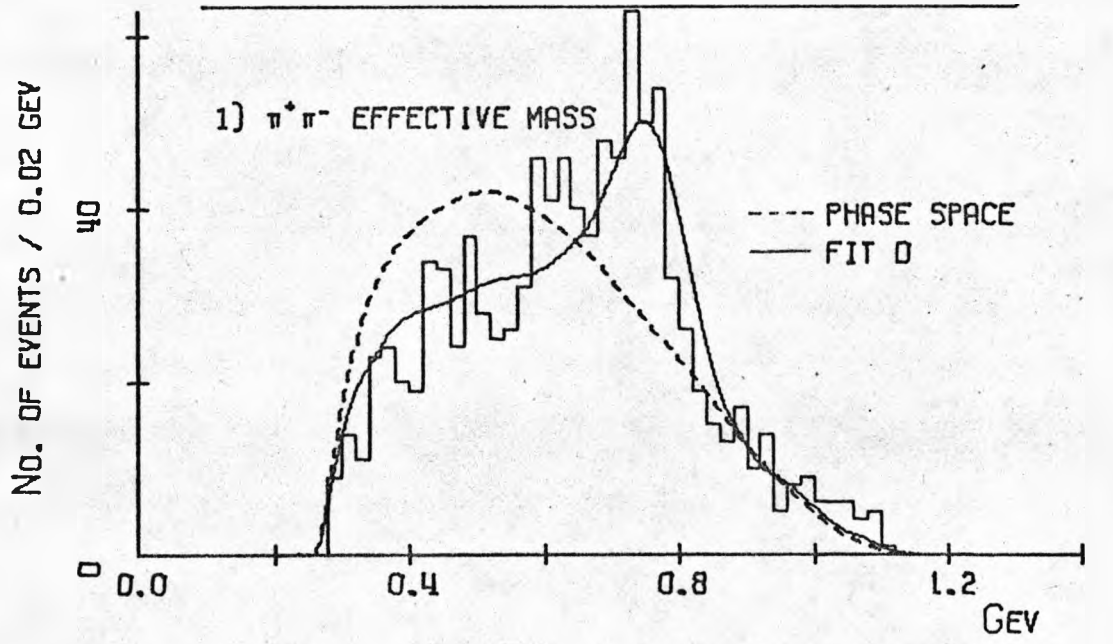

FIG. 5I (CONTD.)

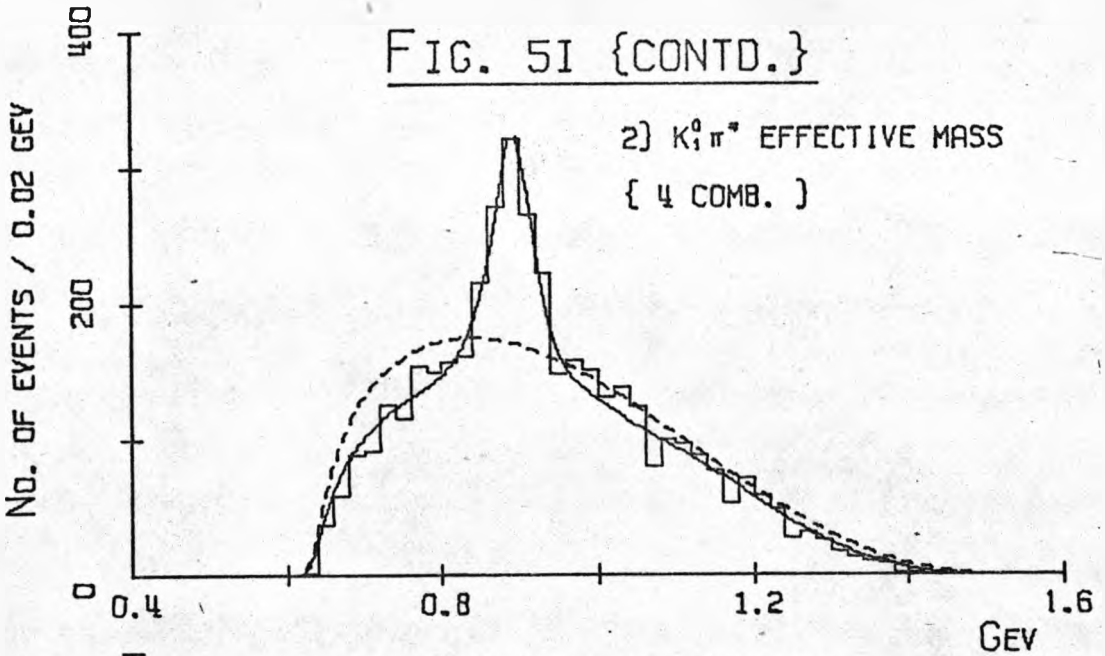
2) $K^0_1\pi^+$ EFFECTIVE MASS
{ 4 COMB. }
No. OF EVENTS / 0.02 GEV
400
200
0
0.4
0.8
1.2
1.6
GEV

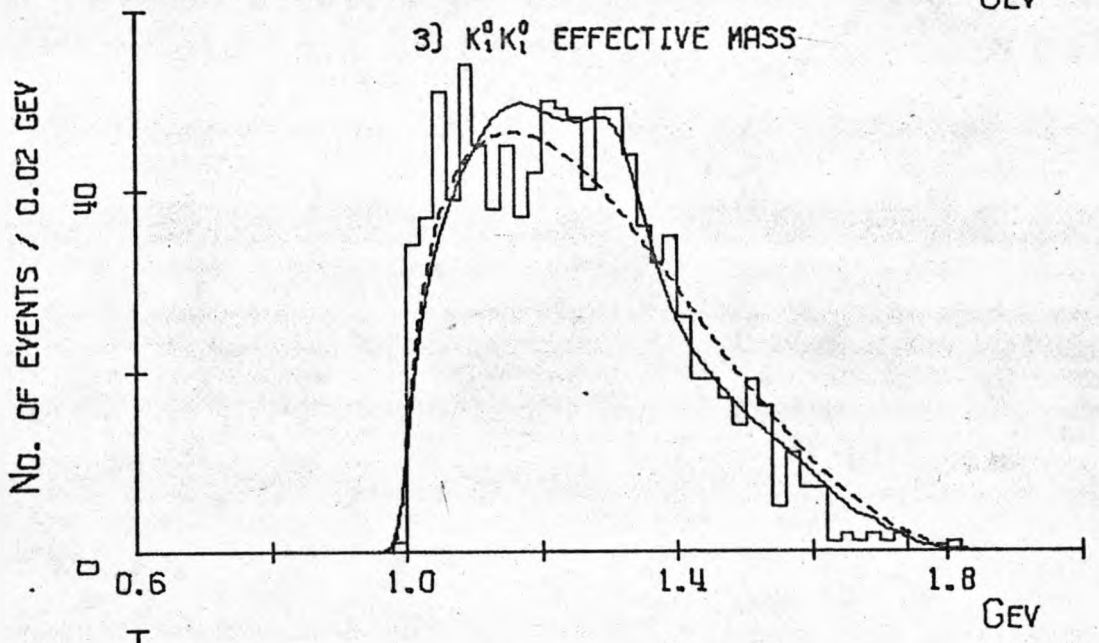
3) $K^0_1K^0_1$ EFFECTIVE MASS
No. OF EVENTS / 0.02 GEV
40
0
0.6
1.0
1.4
1.8
GEV

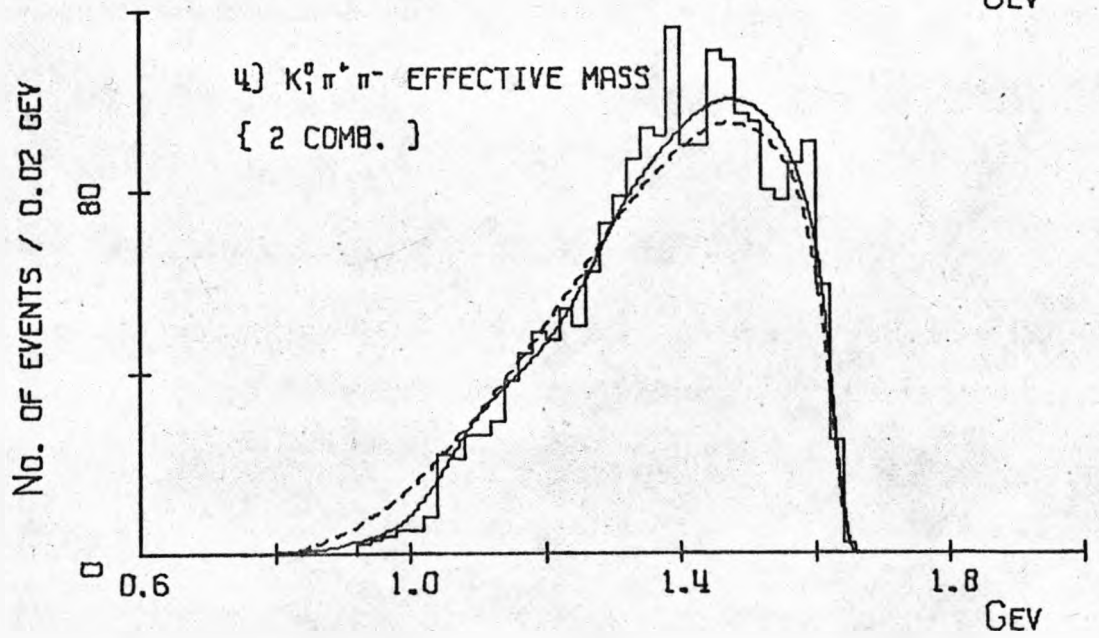
4) $K^0_1\pi^+\pi^-$ EFFECTIVE MASS
{ 2 COMB. }
No. OF EVENTS / 0.02 GEV
80
0
0.6
1.0
1.4
1.8
GEV

FIG. 5I (CONTD.)

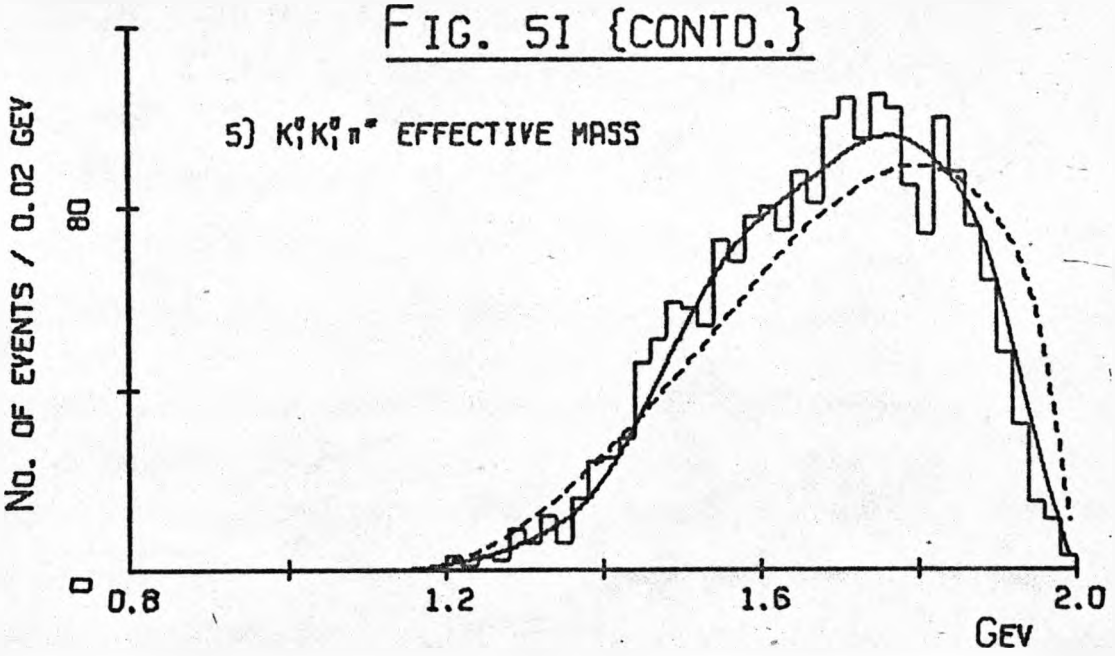

FIG. 5K

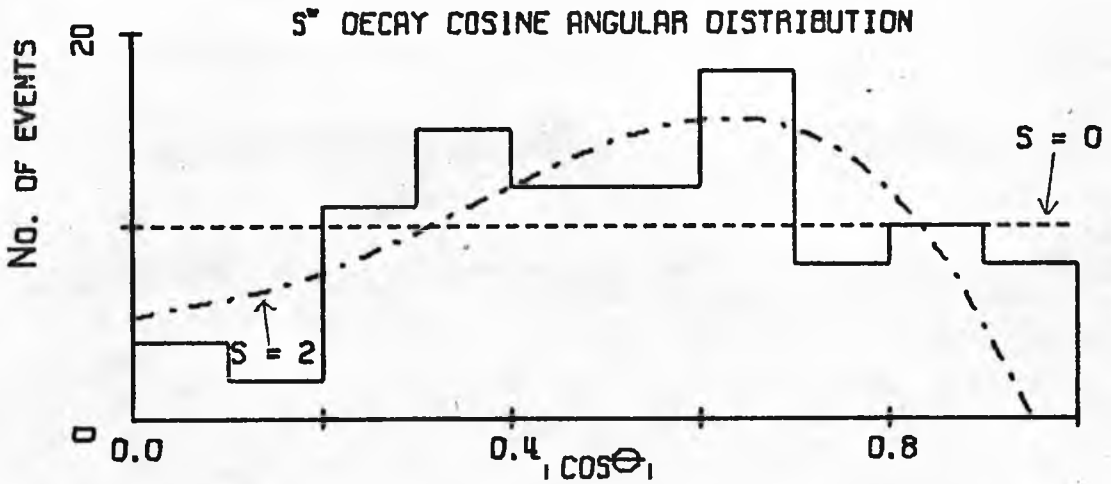

FIG. 5L

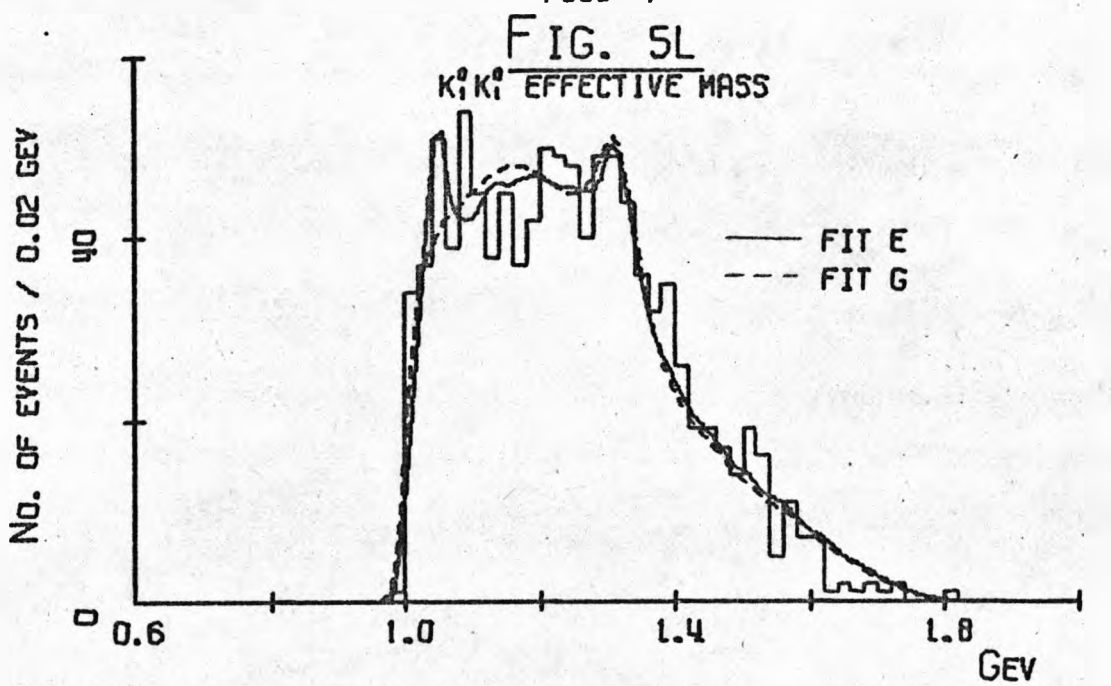

FIG. 5J SCATTER PLOT FOR $\bar{P}P \to K_1^0 K_1^0 \pi^+ \pi^-$

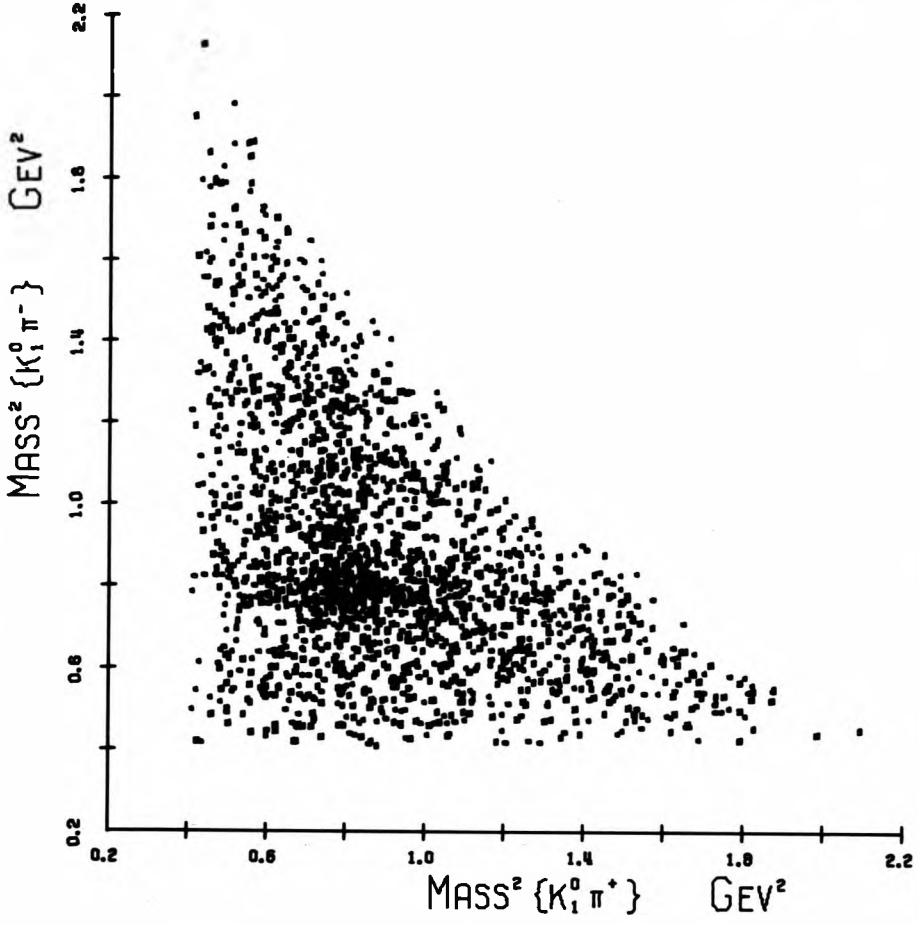

FIG. 5J (CONTD.)

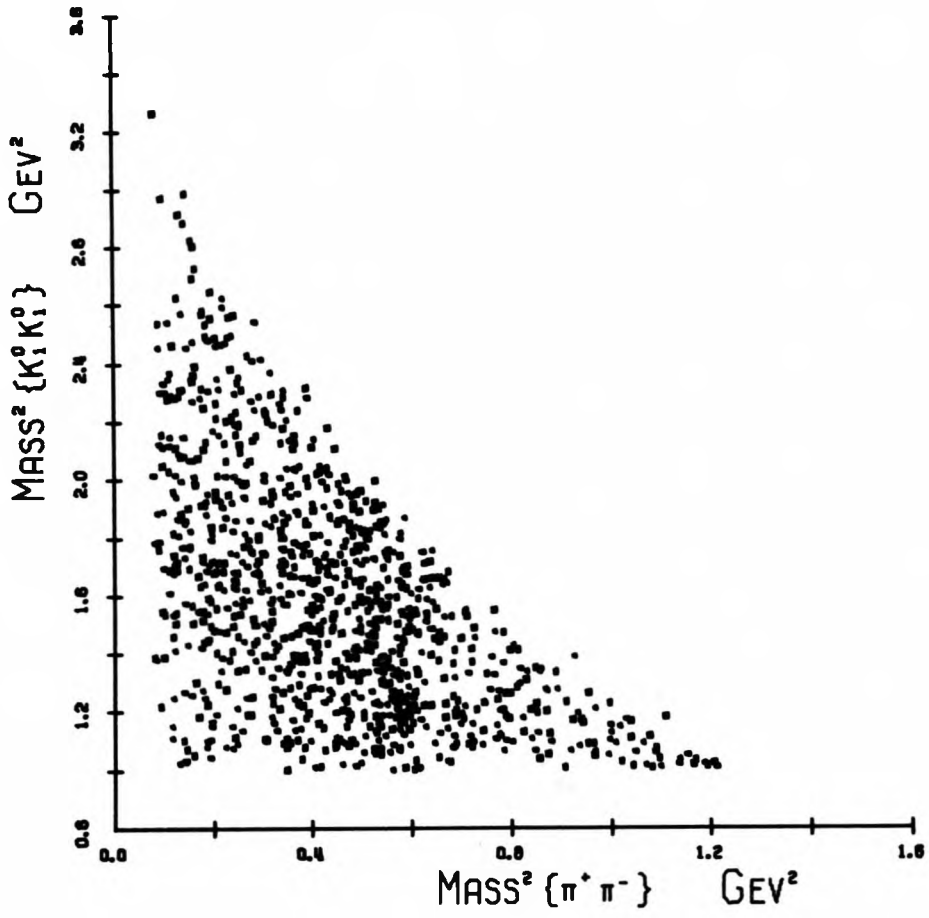
MASS² {K₁⁰K₁⁰} GEV²
3.6
3.2
2.8
2.4
2.0
1.6
1.2
0.8
0.0
0.4
0.8
1.2
1.6
MASS² {π⁺π⁻} GEV²

FIG. 5M $K_1^0 K_1^0 \pi^+ \pi^-$ DISTRIBUTIONS

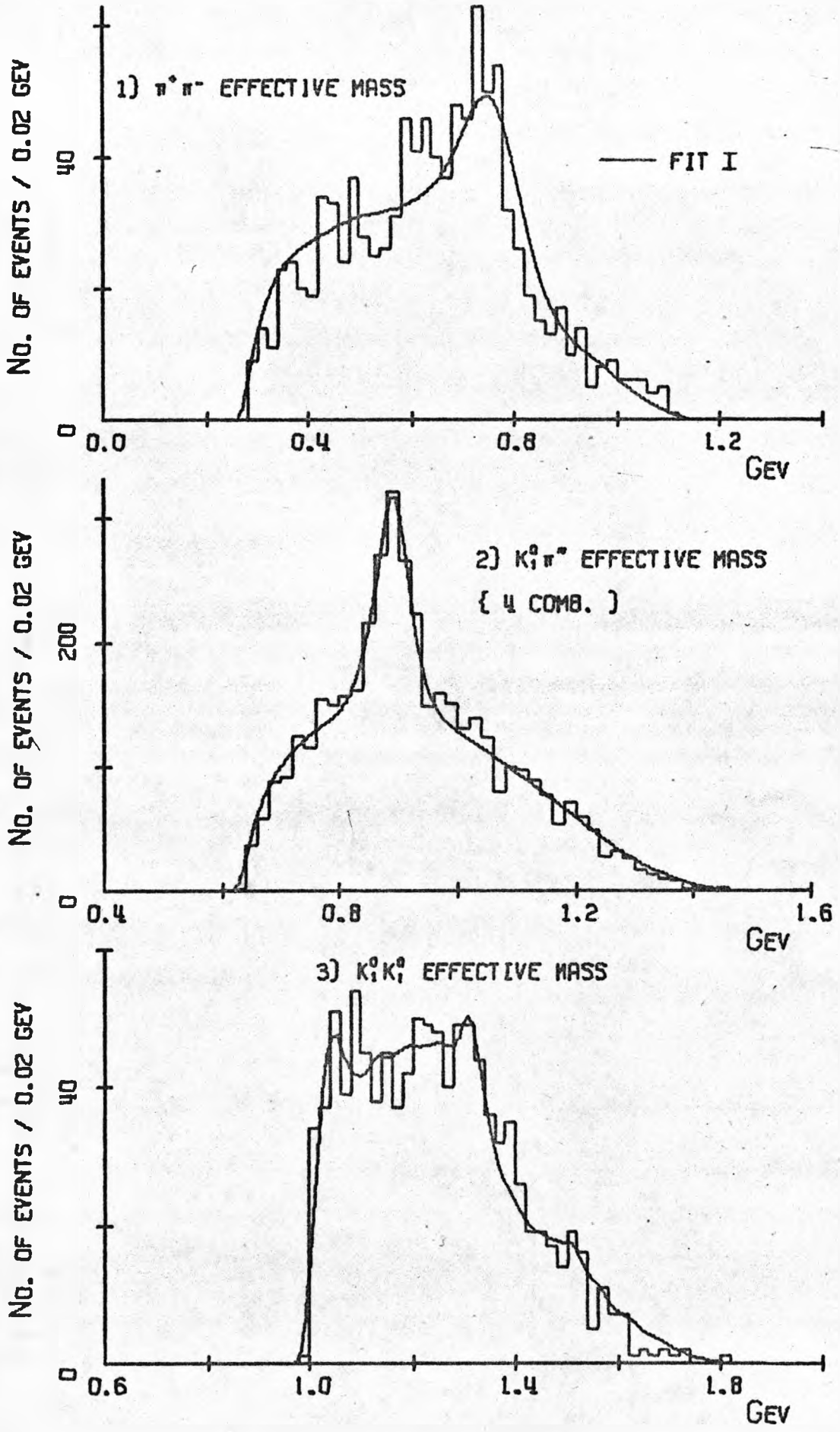

FIG. 5M {CONTD.}

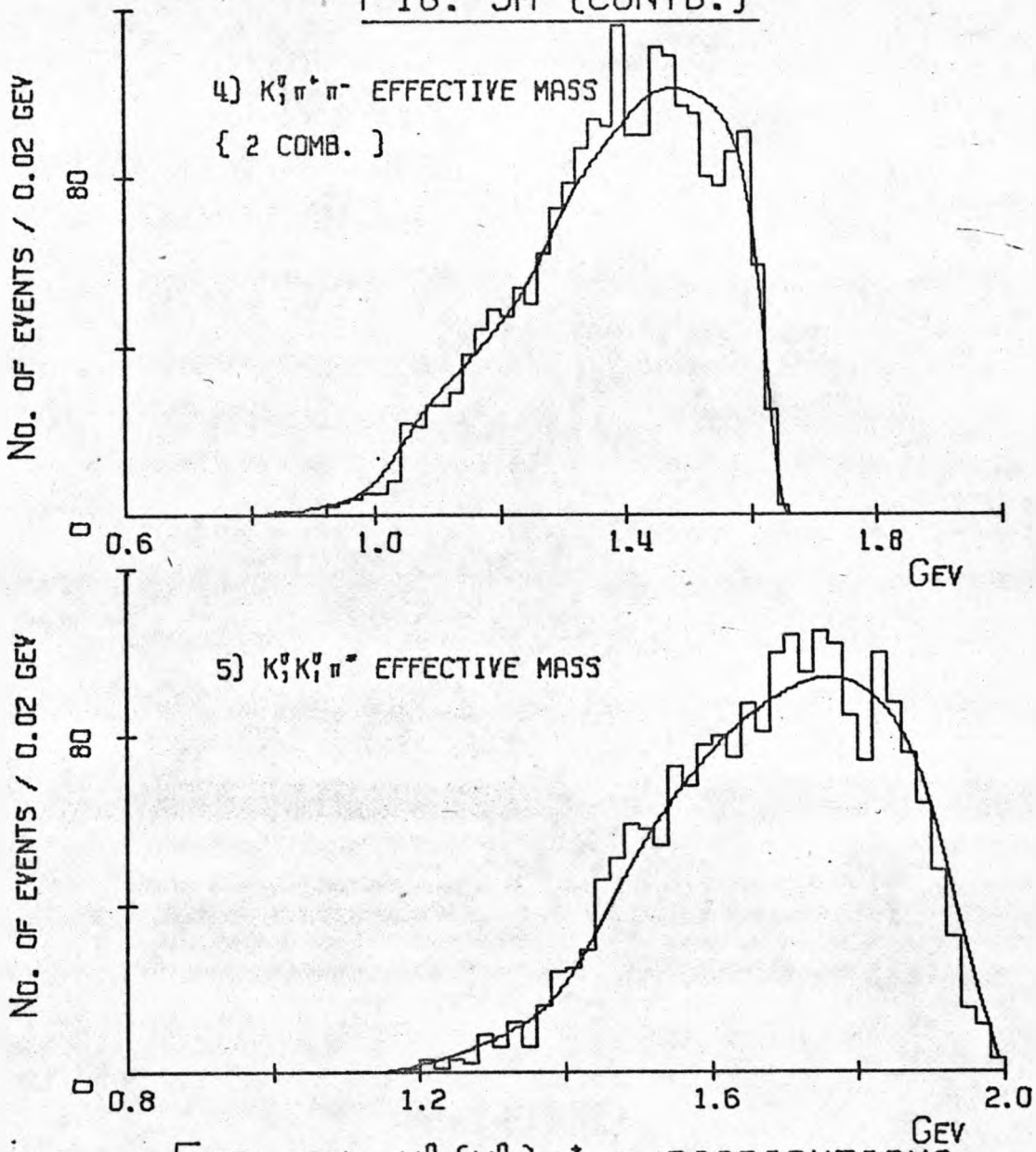

FIG. 5N $K^0_1\{K^0\}\pi^+\pi^-$ DISRIBUTIONS

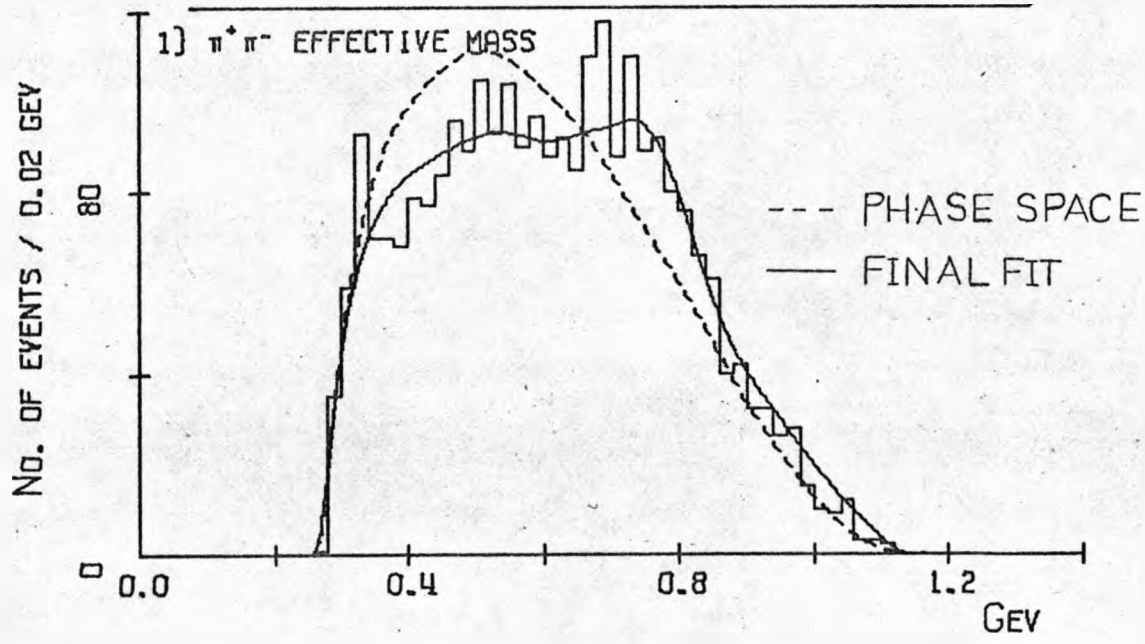

FIG. 5N {CONTD.}

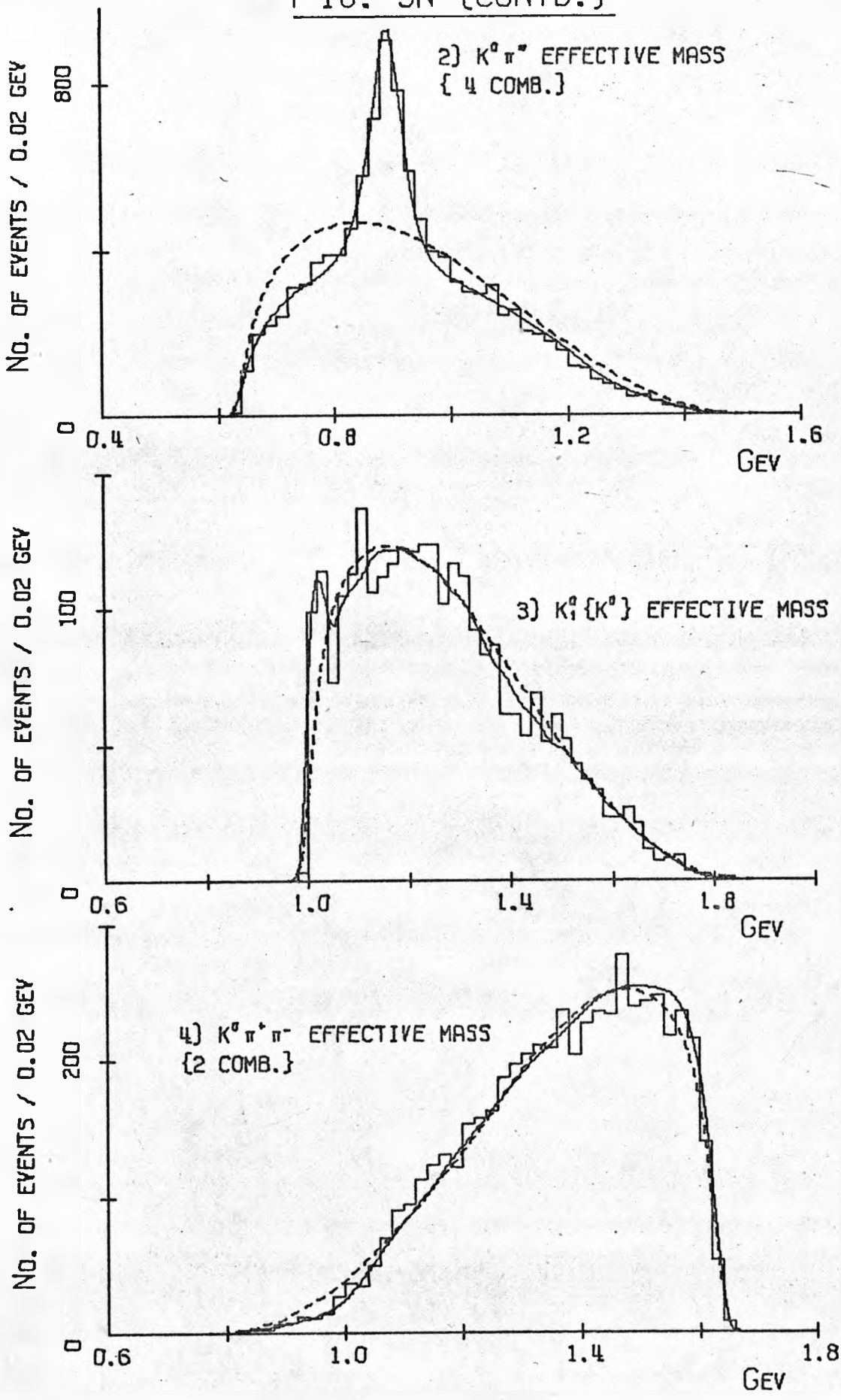
2) $K^0\pi^+$ EFFECTIVE MASS
{ 4 COMB.}
No. OF EVENTS / 0.02 GEV
800
0
0.4
0.8
1.2
1.6
GEV
3) $K_1^0\{K^0\}$ EFFECTIVE MASS
No. OF EVENTS / 0.02 GEV
100
0
0.6
1.0
1.4
1.8
GEV
4) $K^0\pi^+\pi^-$ EFFECTIVE MASS
{2 COMB.}
No. OF EVENTS / 0.02 GEV
200
0
0.6
1.0
1.4
1.8
GEV

FIG. 5N {CONTD.}

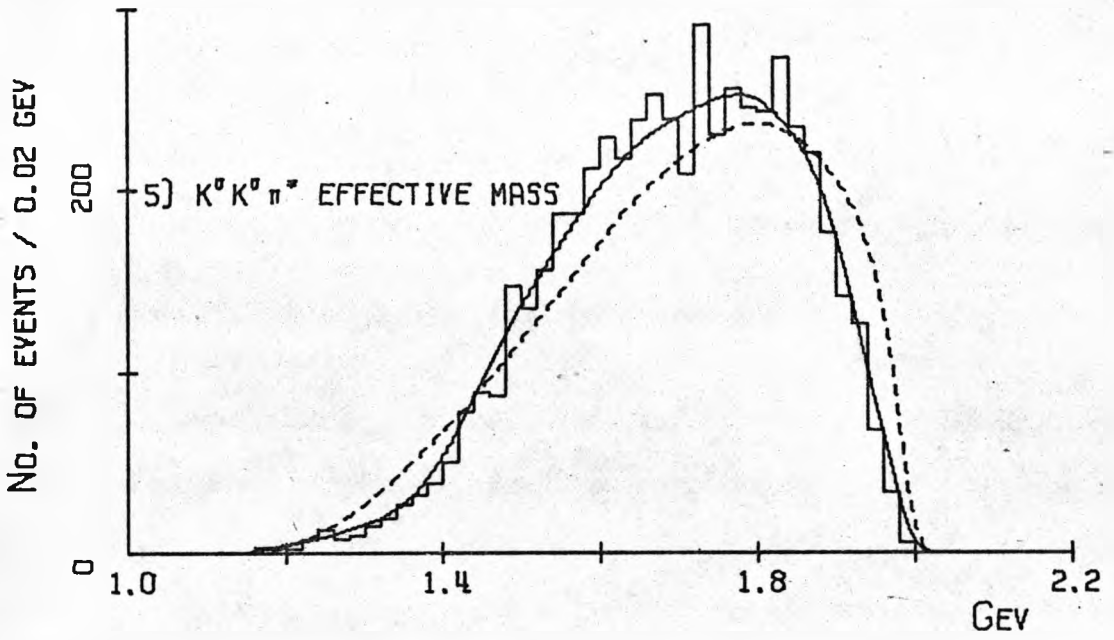

FIG. 5P $P\bar{P} \rightarrow K_1^0 K_1^0 \pi^+ \pi^- \{\pi^0\}$

CROSS-SECTION VARIATION WITH INCIDENT $\bar{P}$ LAB MOMENTUM

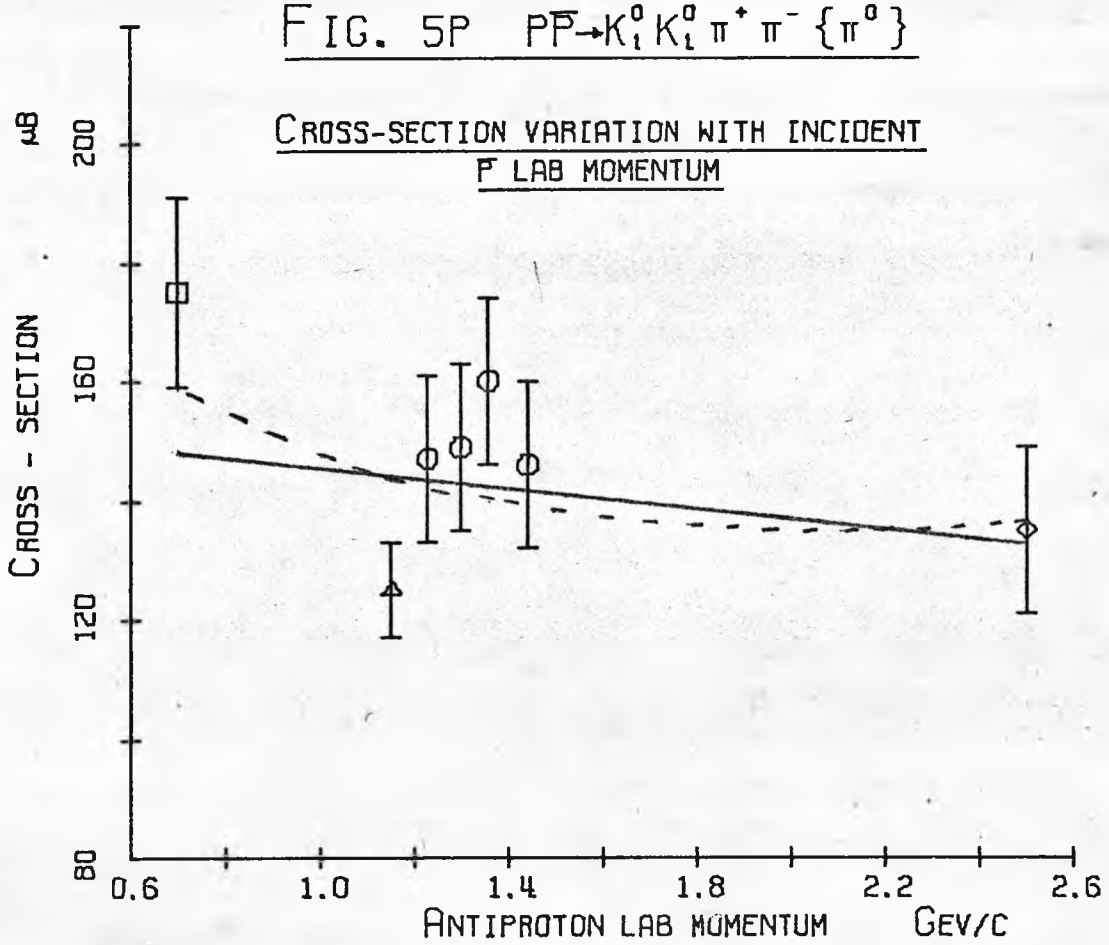

FIG. 50 SCATTER PLOT FOR $\bar{P}P \to K^0_1 \{K^0\} \pi^+ \pi^-$

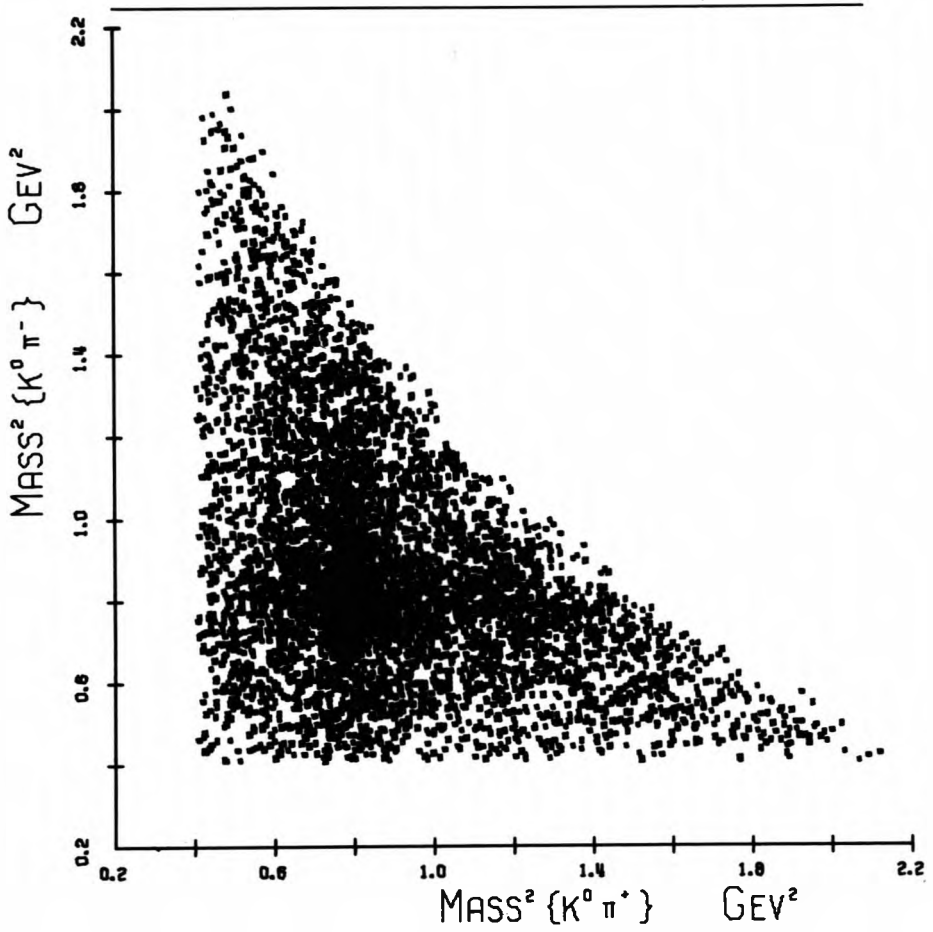

FIG. 50 (CONTD.)

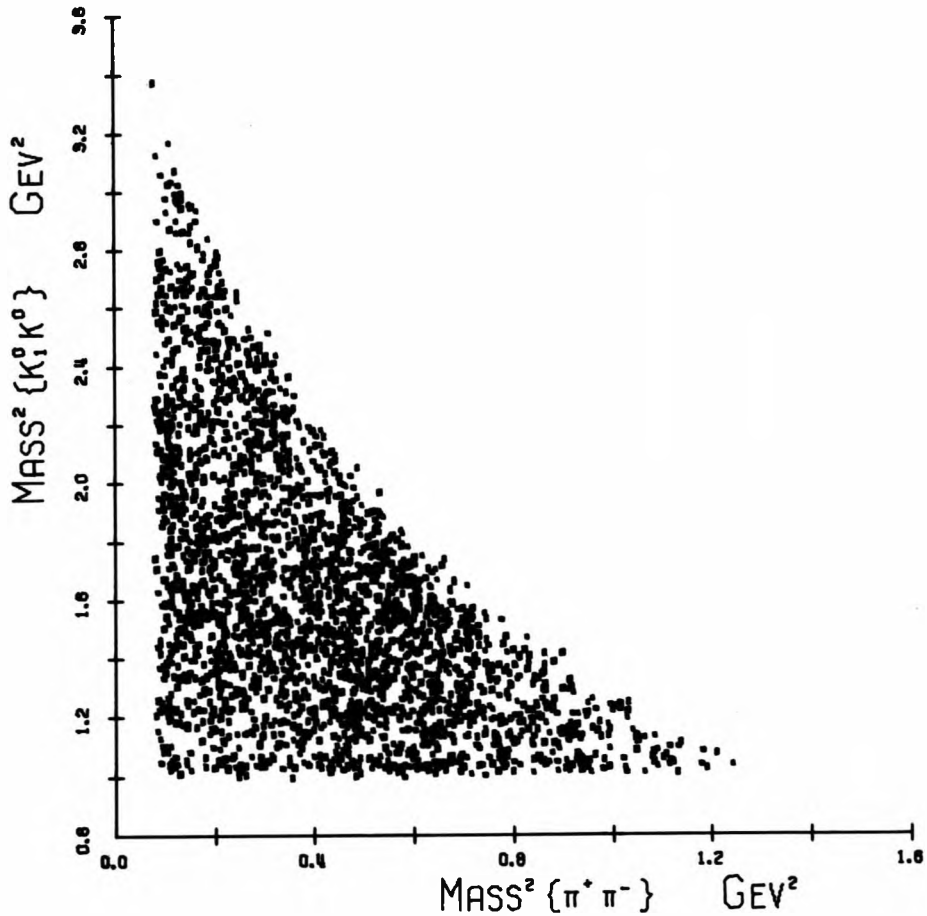
MASS² (K⁰, K⁰) GEV²
3.6
3.2
2.8
2.4
2.0
1.6
1.2
0.8
0.0
0.4
0.8
1.2
1.6
MASS² (π⁺ π⁻) GEV²

FIG. 5Q $\pi^+\pi^-\pi^0$ EFFECTIVE MASS DISTRIBUTIONS

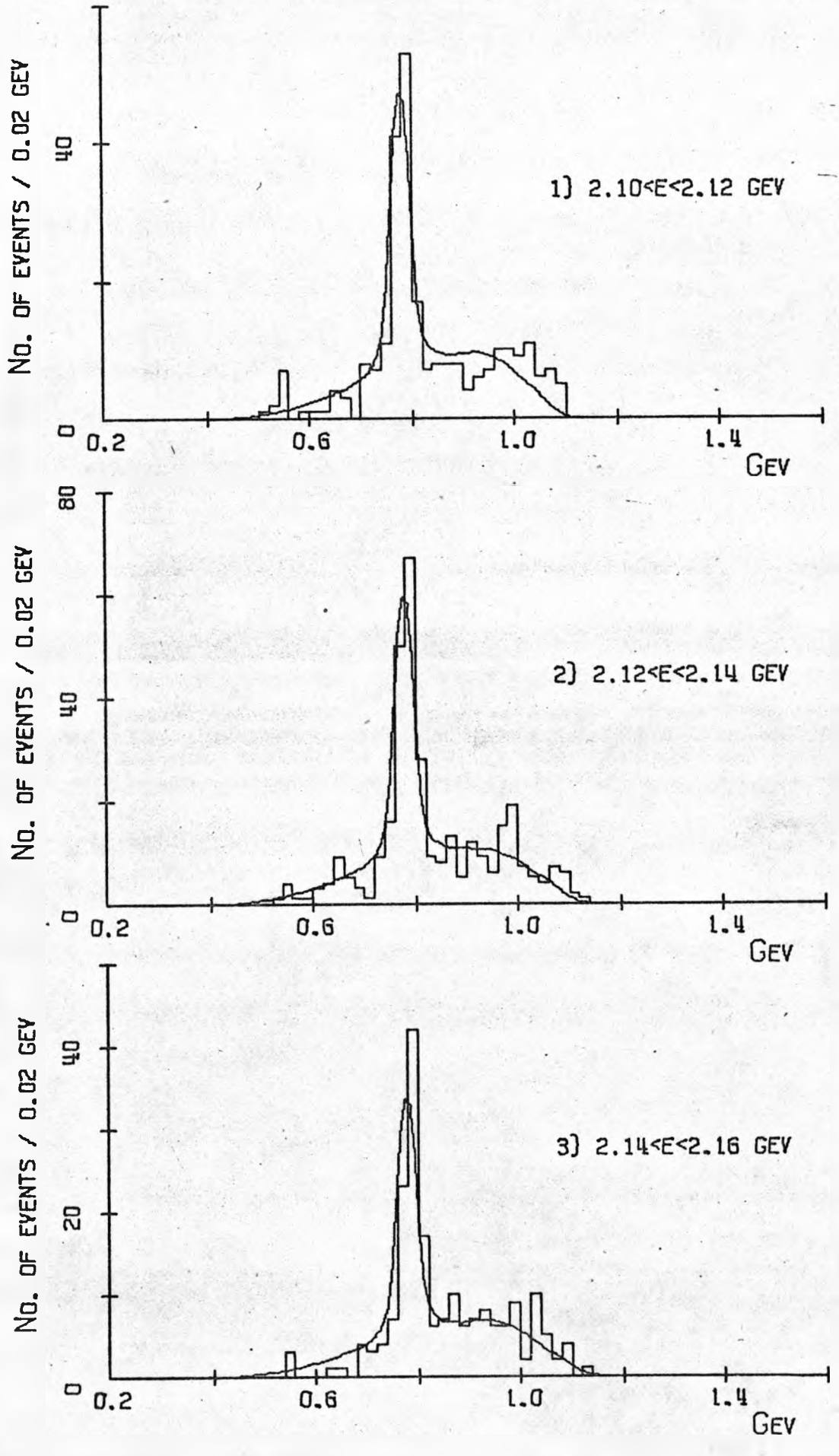

FIG. 5Q {CONTD.}

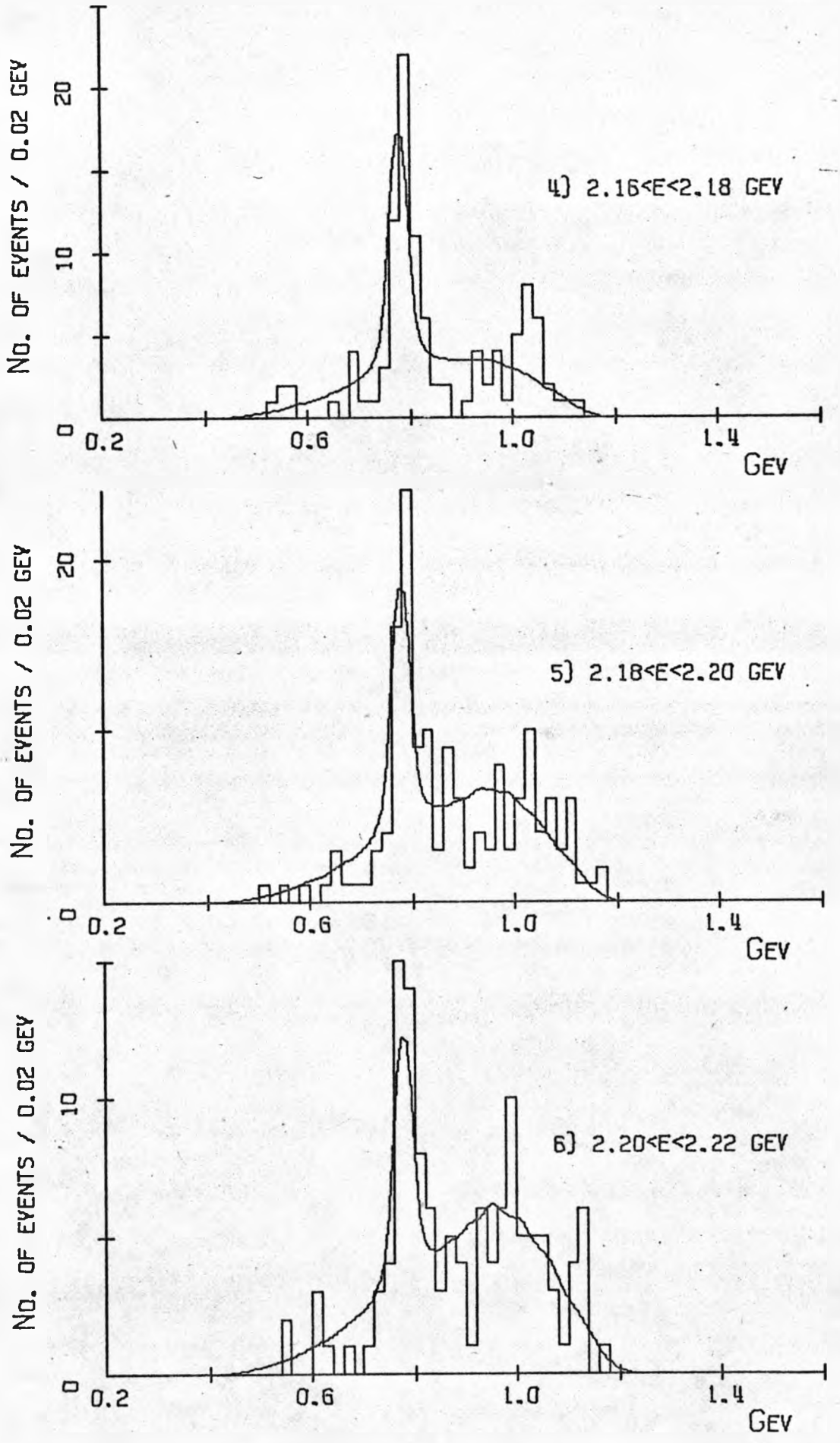
No. OF EVENTS / 0.02 GEV
20
10
0
0.2
0.6
1.0
1.4
GEV
4) 2.16<E<2.18 GEV
No. OF EVENTS / 0.02 GEV
20
0
0.2
0.6
1.0
1.4
GEV
5) 2.18<E<2.20 GEV
No. OF EVENTS / 0.02 GEV
10
0
0.2
0.6
1.0
1.4
GEV
6) 2.20<E<2.22 GEV

FIG. 5Q {CONTD.}

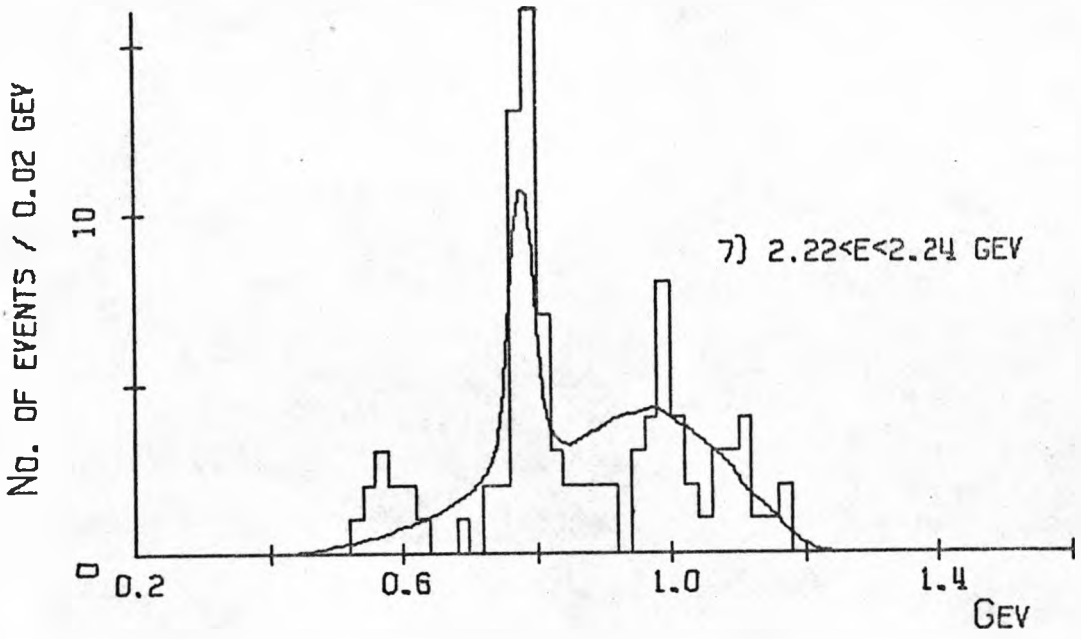

FIG. 5R $\bar{P}P \rightarrow K_1^0 K_1^0 \omega^0$

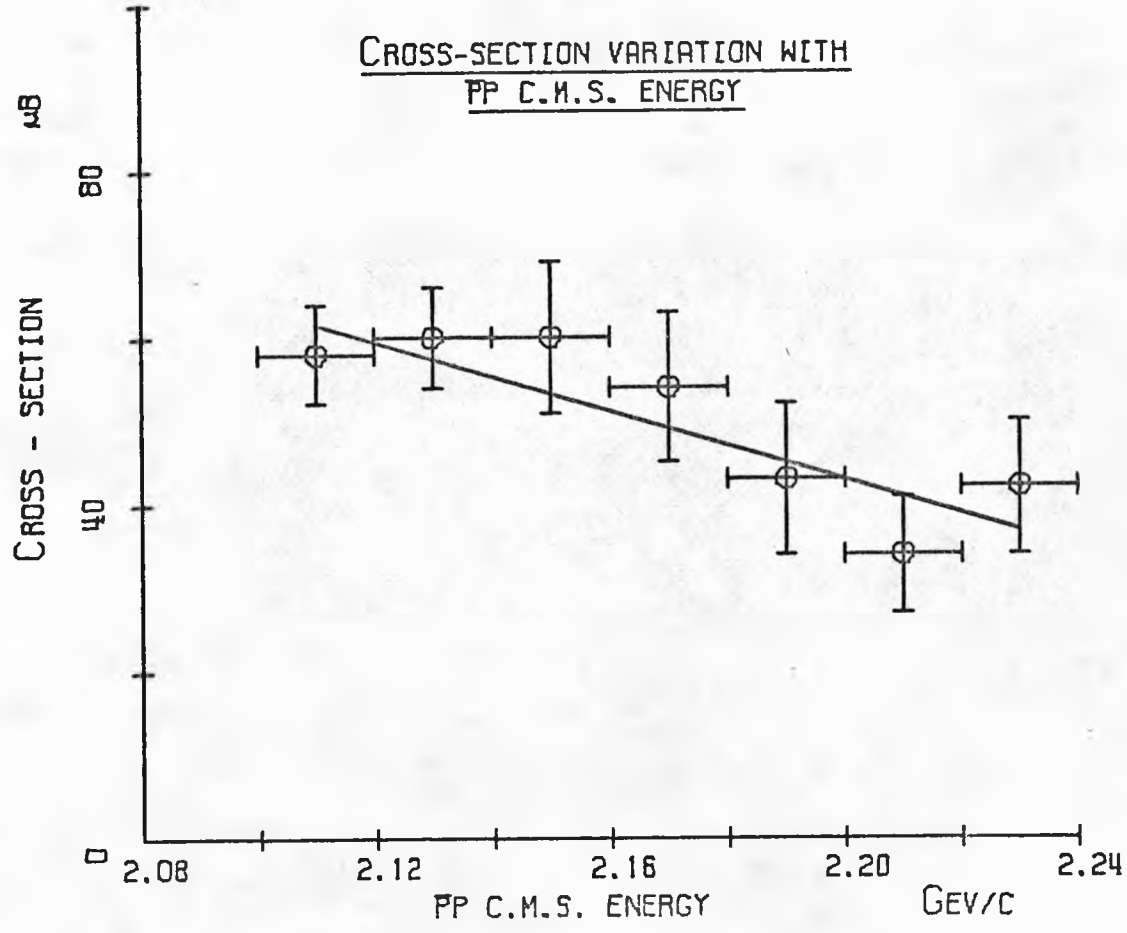

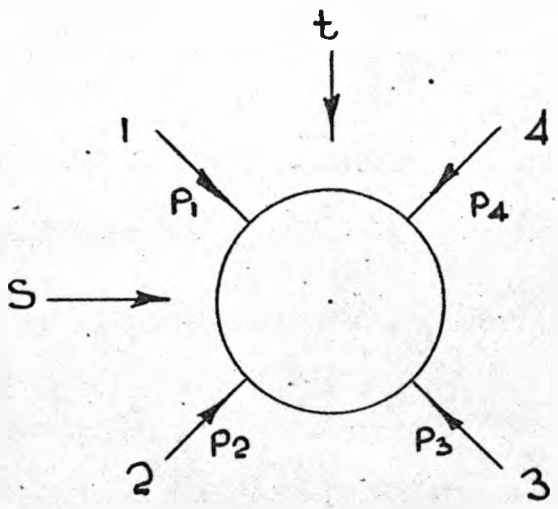

FIG. 6 A THE MANDELSTAM VARIABLES

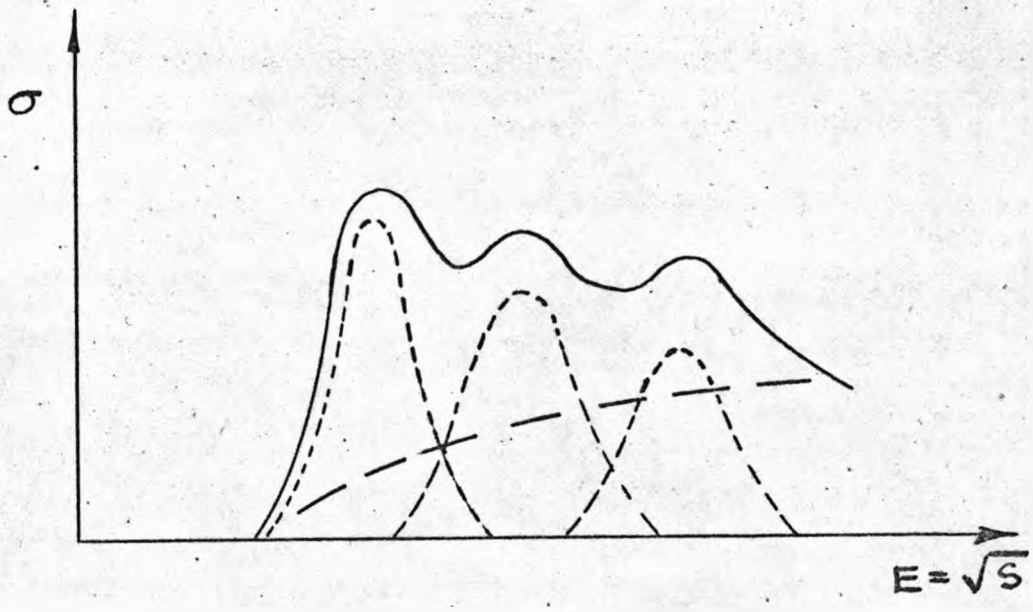

FIG. 6B TYPICAL VARIATION OF CROSS-SECTION WITH ENERGY IN THE LOW ENERGY REGION.

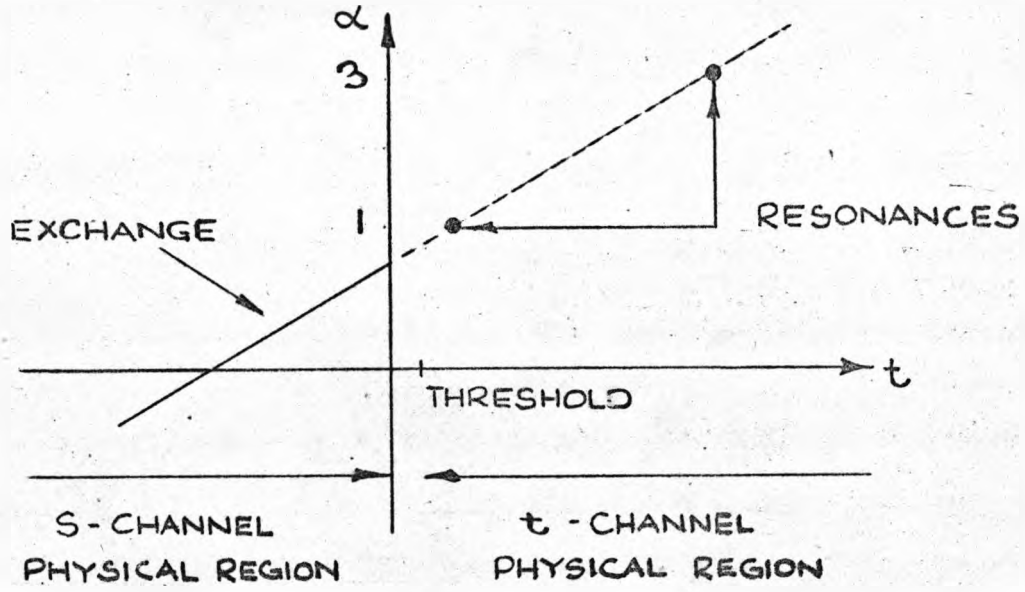

FIG. 6C A CHEW - FRAUTSCHI DIAGRAM

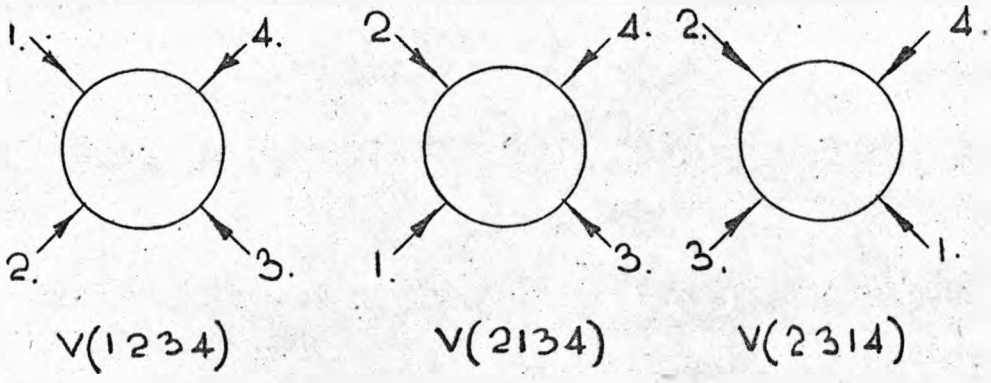

FIG. 6D DIAGRAMS FOR THE VENEZIANO AMPLITUDE

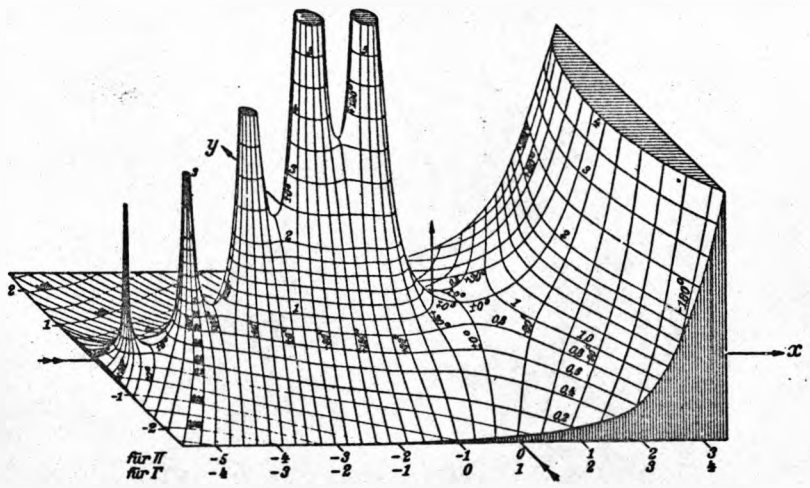

FIG.6E RELIEF DIAGRAM OF $\Gamma(Z)$
WHERE $Z = X + iY$

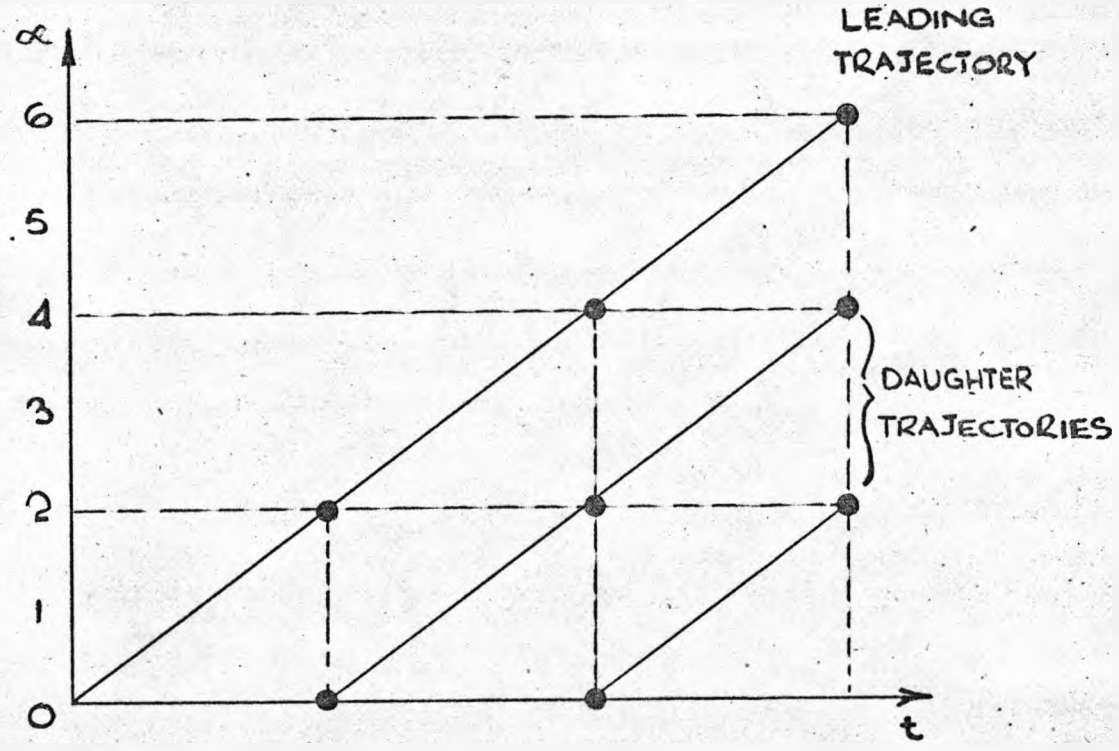

FIG.6F LEADING TRAJECTORY AND DAUGHTER SEQUENCE

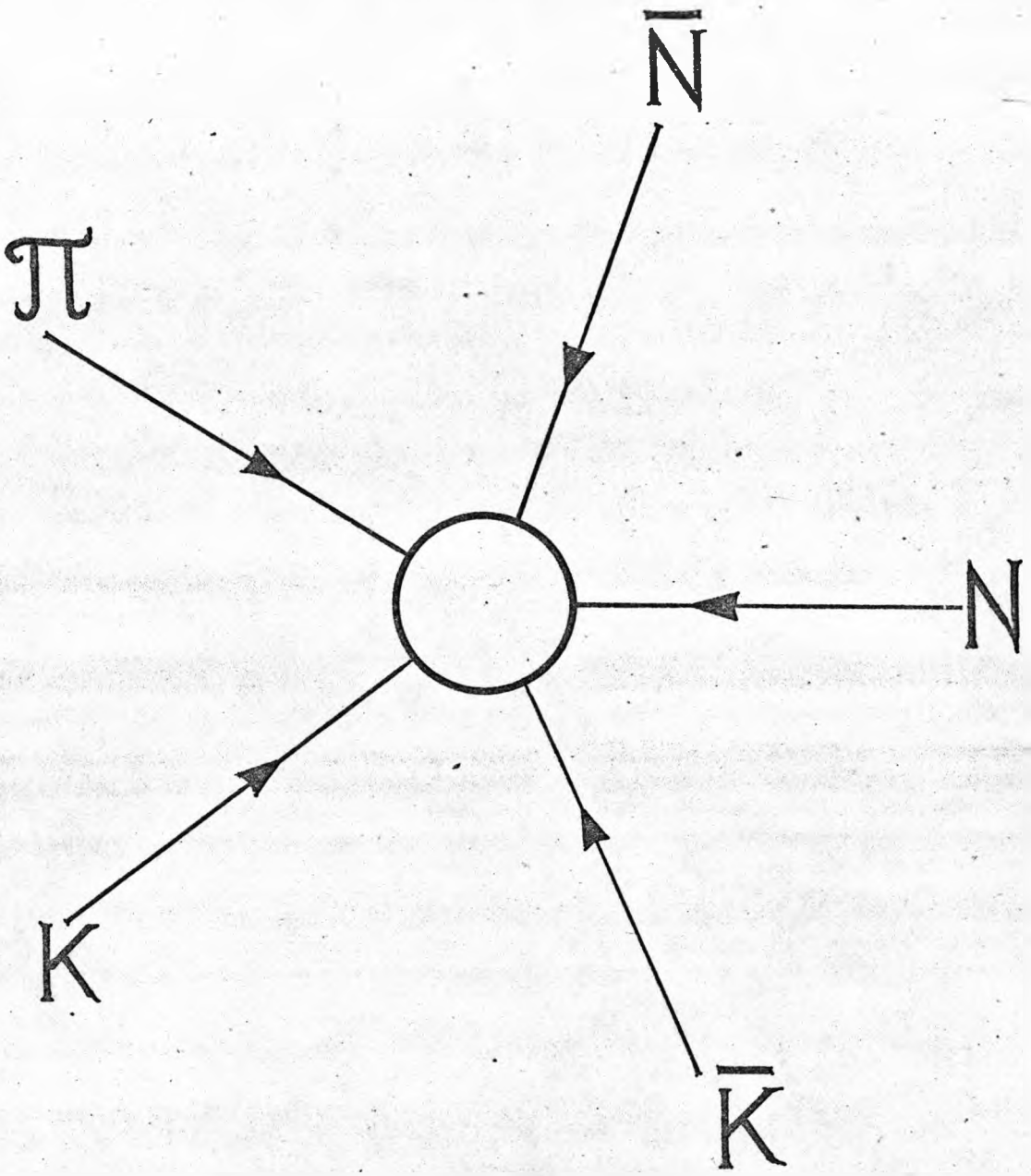

Figure. 6G.

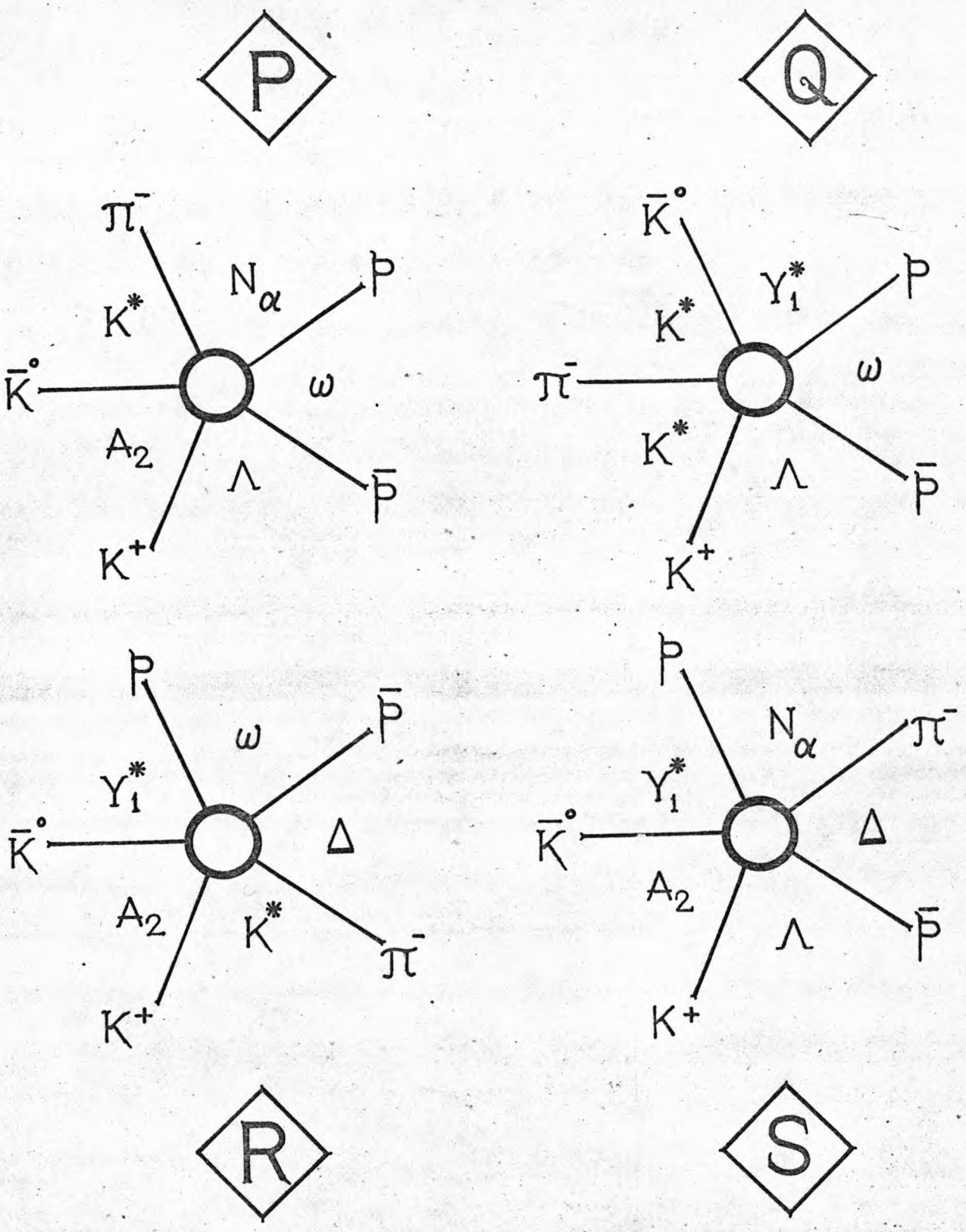
P
π^-
K^*
$\bar{K}^\circ$
A_2
K^+
N_α
ω
Λ
p
$\bar{p}$
Q
$\bar{K}^\circ$
K^*
π^-
K^*
K^+
Y_1^*
ω
Λ
p
$\bar{p}$
R
p
Y_1^*
$\bar{K}^\circ$
A_2
K^+
ω
Δ
K^*
$\bar{p}$
π^-
S
p
Y_1^*
$\bar{K}^\circ$
A_2
K^+
N_α
Δ
Λ
π^-
$\bar{p}$

Figure. 6H.

FIG. 6I 1.1 GEV/C DISTRIBUTIONS

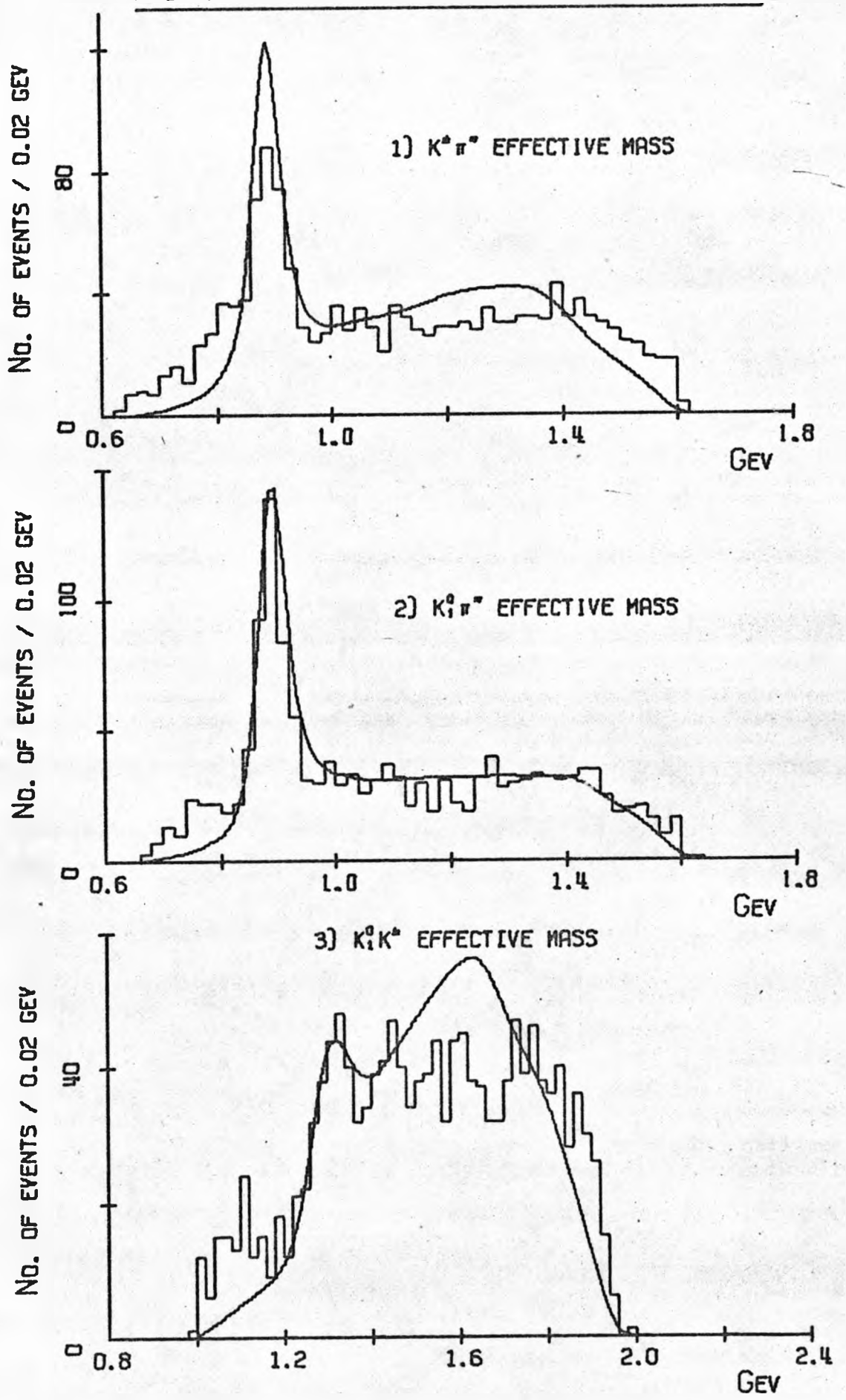

FIG. 6J 1.1 GEV/C DISTRIBUTIONS

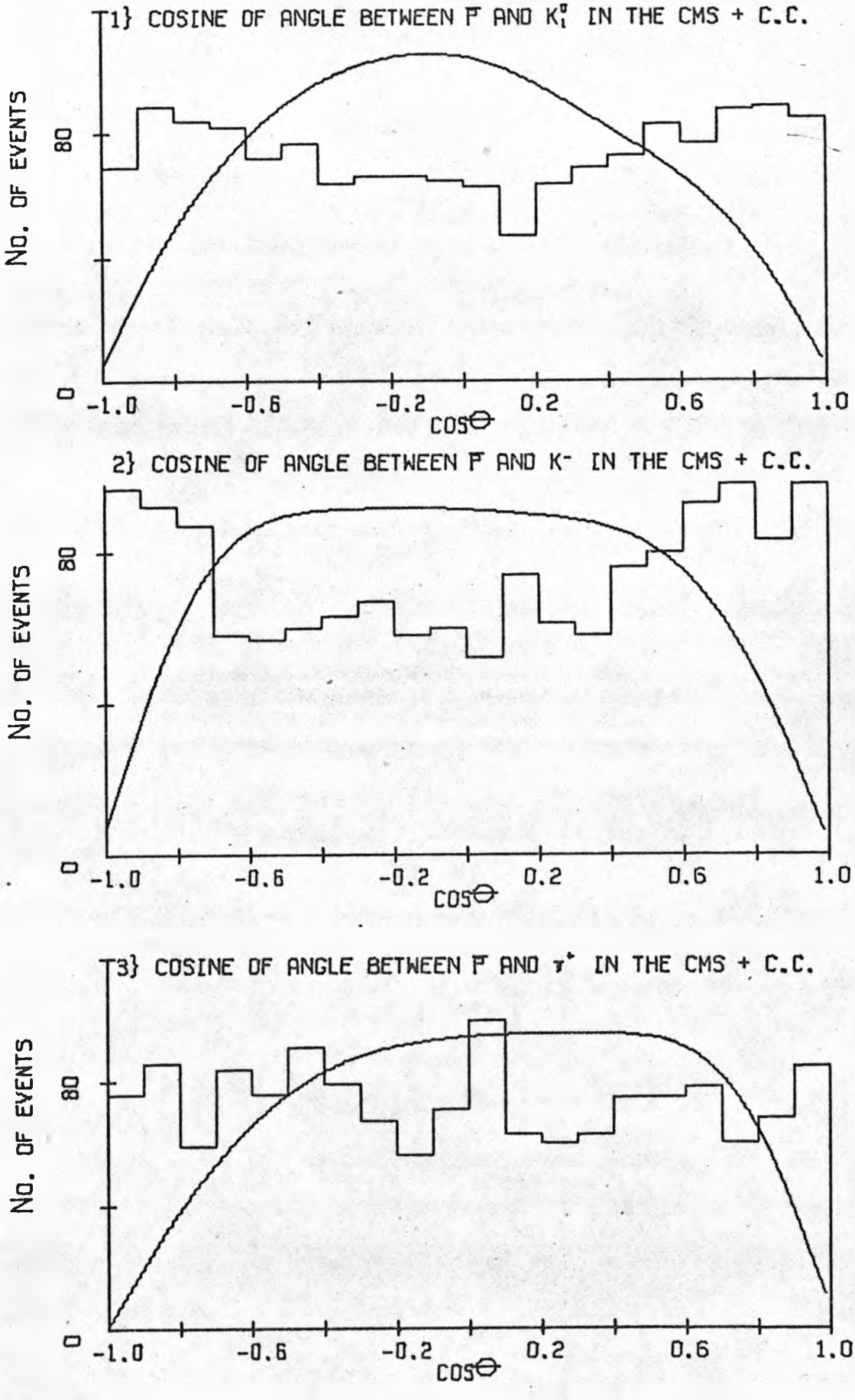

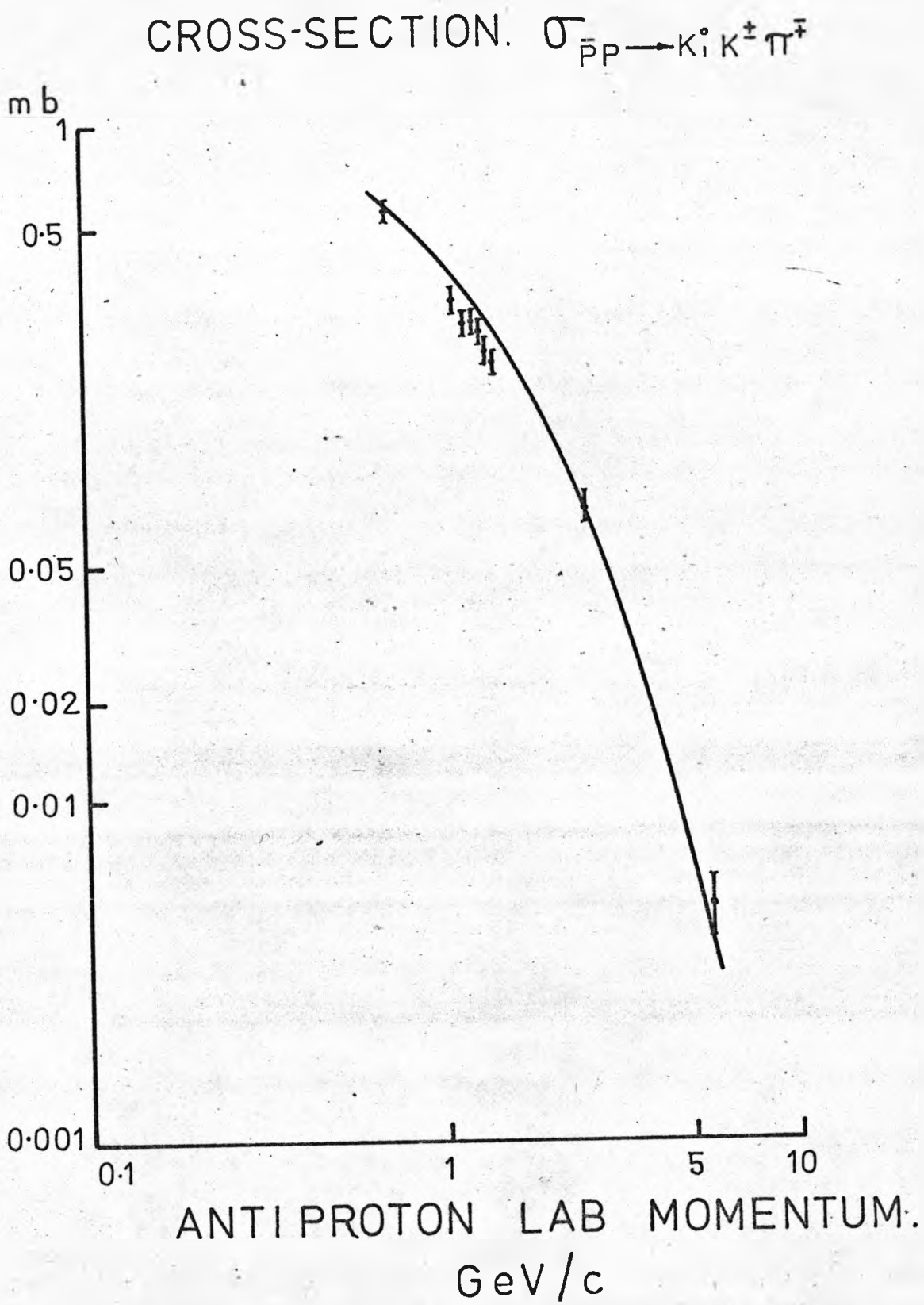
CROSS-SECTION. $\sigma_{\bar{p}p \to K^{\circ}_{1} K^{\pm} \pi^{\mp}}$
mb
1
0·5
0·05
0·02
0·01
0·001
0·1
1
5
10
ANTI PROTON LAB MOMENTUM.
GeV/c

Figure . 6.K.

FIG. 6L 1.1 GEV/C DISTRIBUTIONS

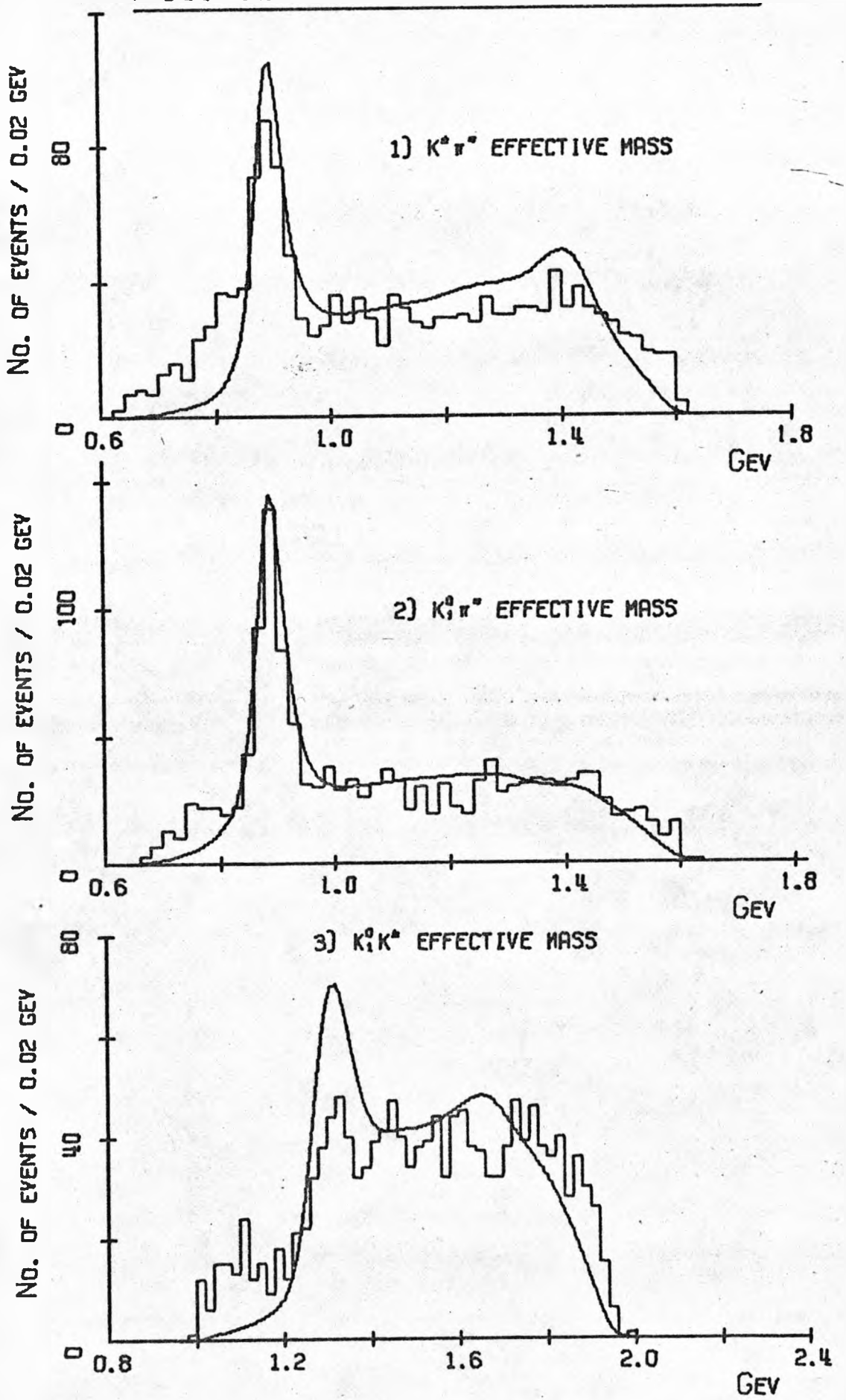

FIG. 6M 1.1 GEV/C DISTRIBUTIONS

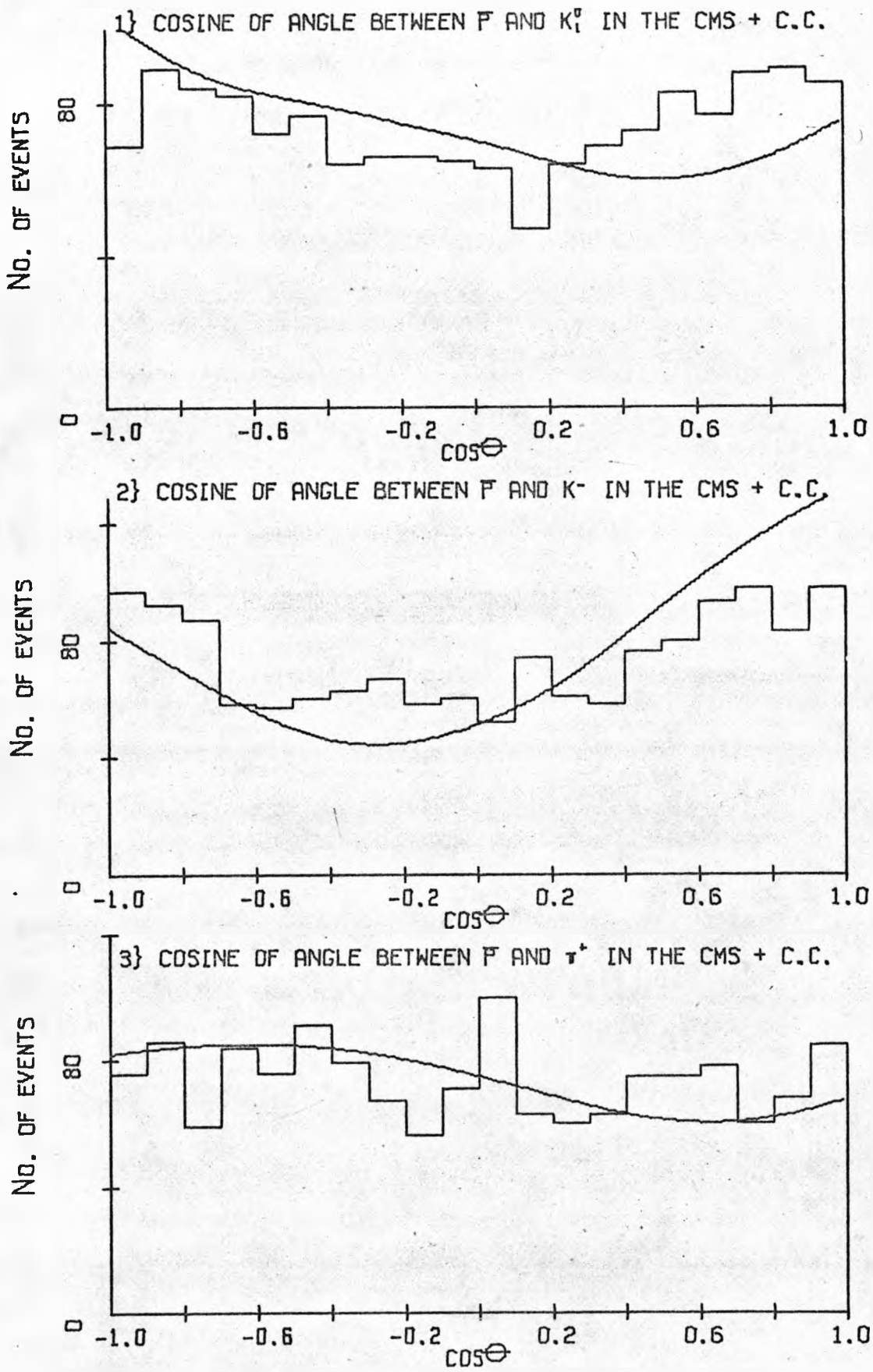

FIG. GN 1.1 GEV/C DISTRIBUTIONS

RESONANCE DECAY ANGLES

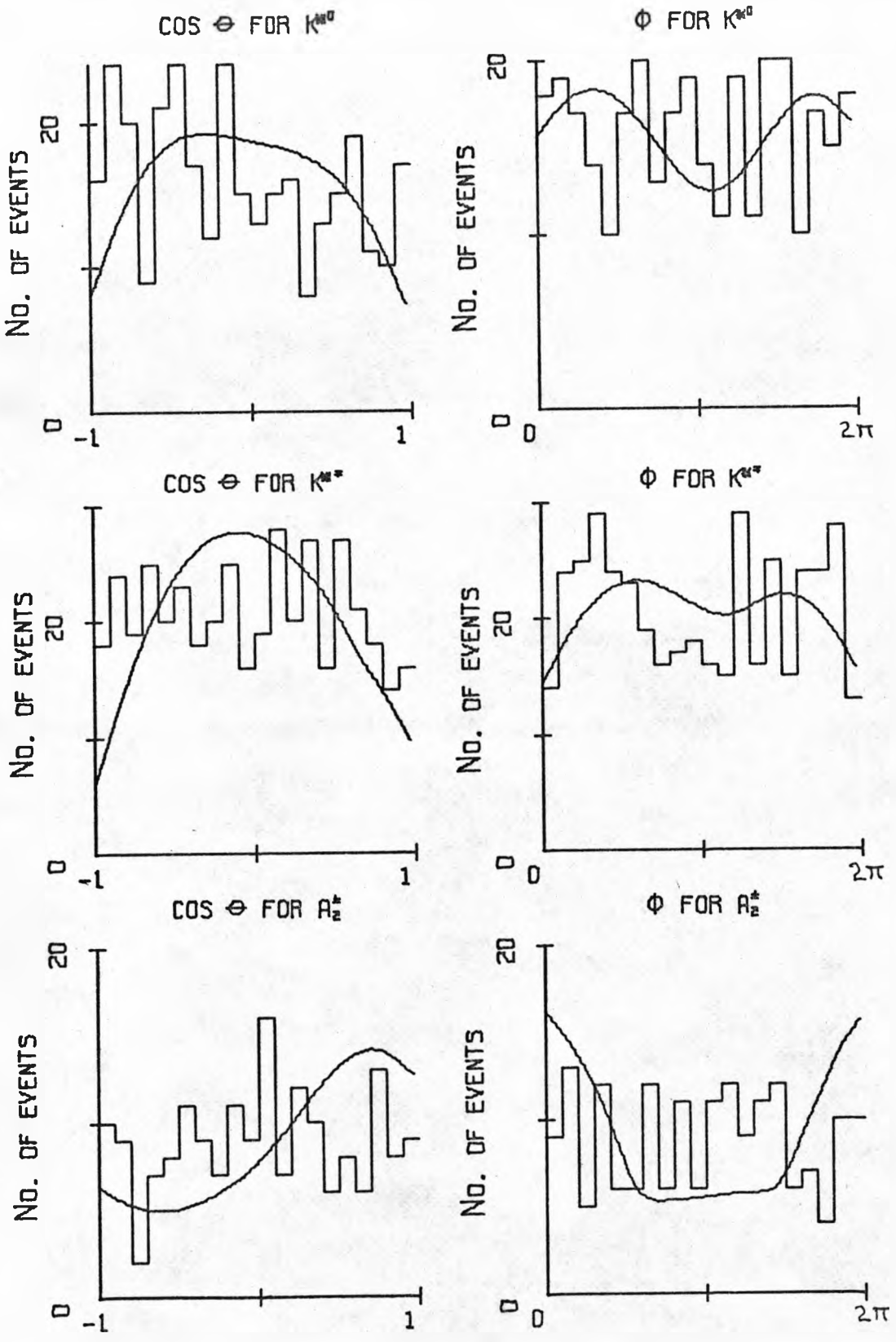

FIG. 60 2.5 GEV/C DISTRIBUTIONS

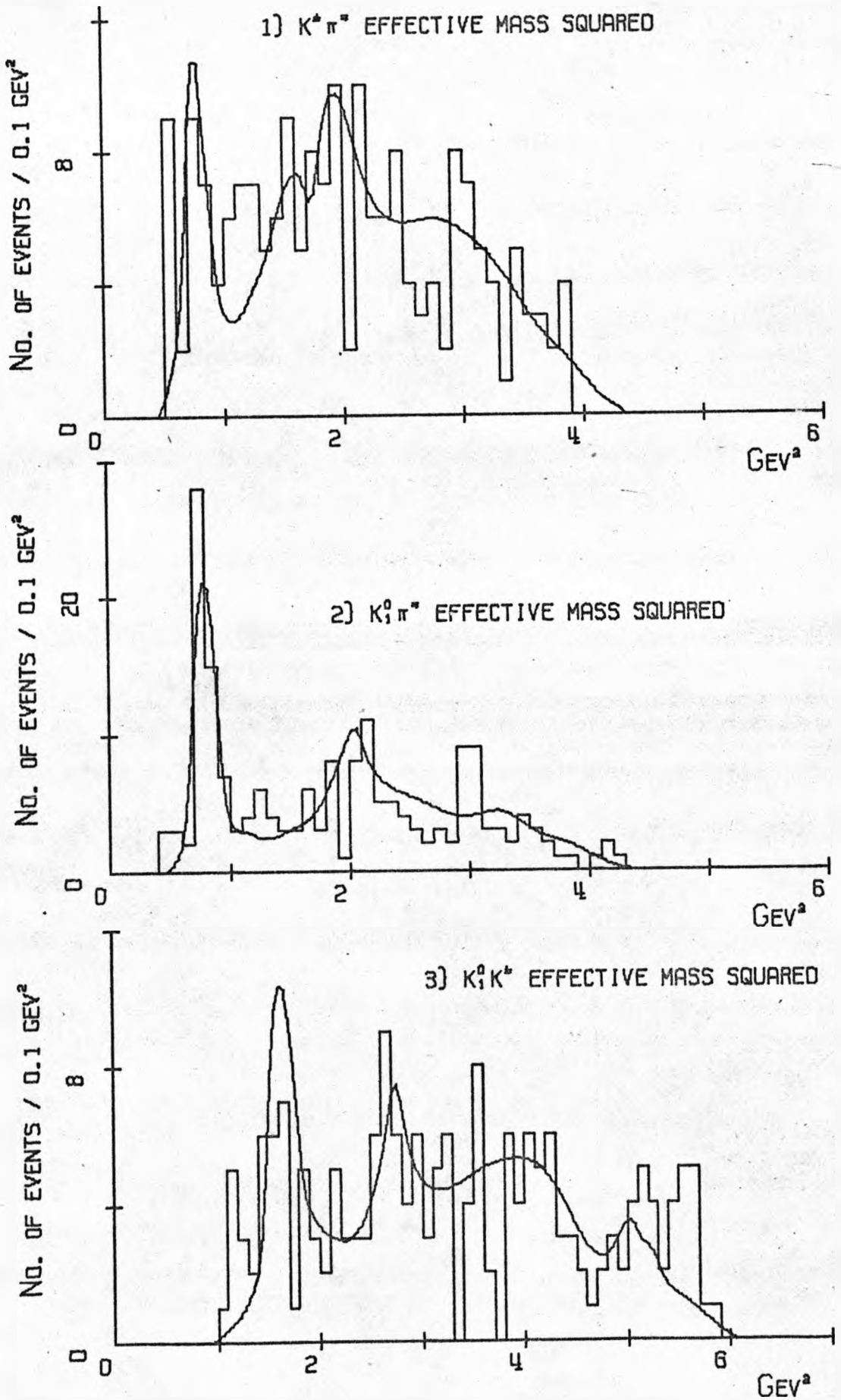

FIG. 6P 2.5 GEV/C DISTRIBUTIONS

1} COSINE OF ANGLE BETWEEN P AND K^0_1 IN THE CMS + C.C.

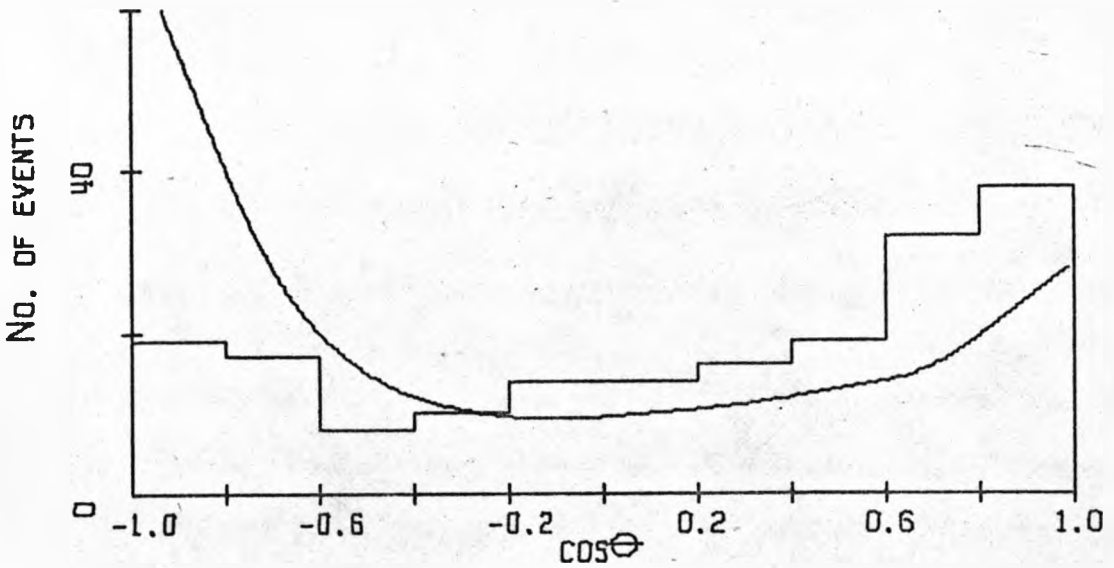

2} COSINE OF ANGLE BETWEEN $\bar{P}$ AND K^- IN THE CMS + C.C.

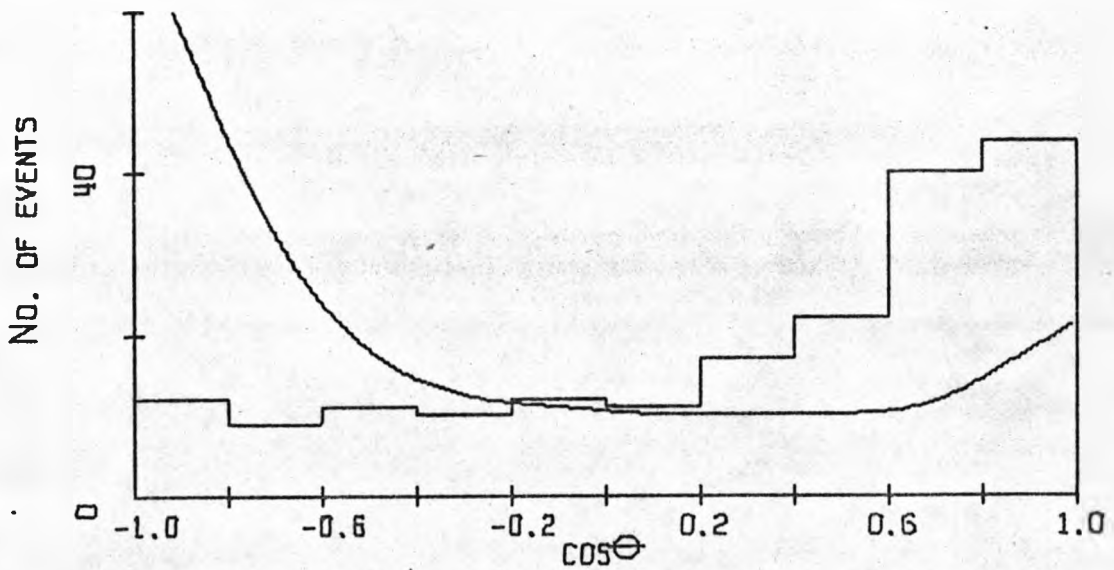

3} COSINE OF ANGLE BETWEEN P AND π^+ IN THE CMS + C.C.

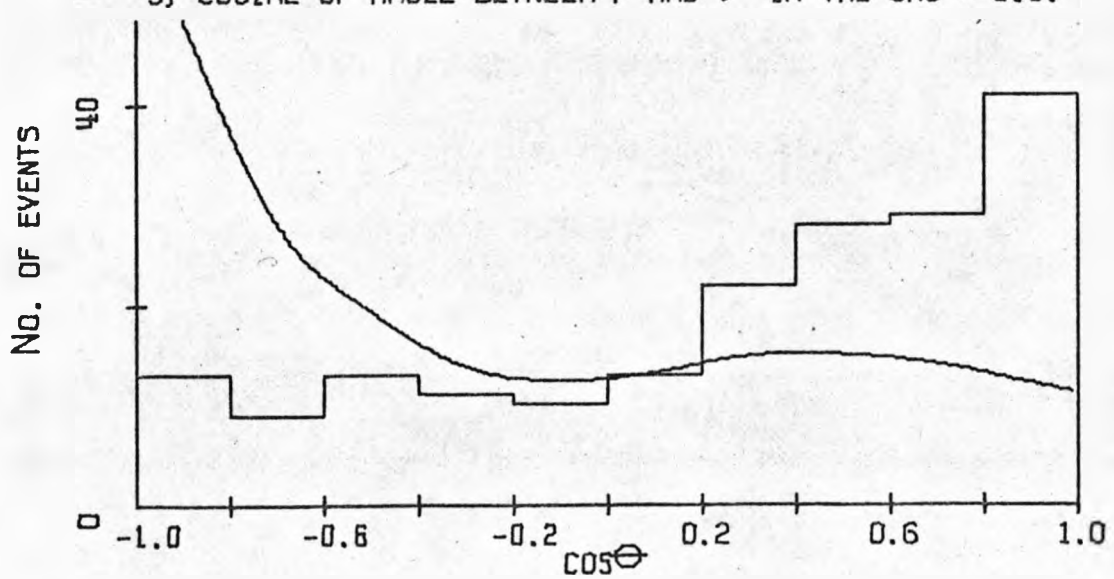

FIG. 6Q 5.7 GEV/C DISTRIBUTIONS